UNIVERSITY OF NOVA GORICA
GRADUATE SCHOOL

MODELLING OF CONTINUOUS CASTING OF STEEL UNDER THE INFLUENCE OF ELECTROMAGNETIC FIELD WITH MESHLESS METHOD

DISSERTATION

Katarina Mramor

Mentor: Prof. Dr. Božidar Šarler

Nova Gorica, 2014

UNIVERZA V NOVI GORICI
FAKULTETA ZA PODIPLOMSKI ŠTUDIJ

MODELIRANJE KONTINUIRNEGA ULIVANJA JEKLA POD VPLIVOM MAGNETNEGA POLJA Z BREZMREŽNO METODO

DISERTACIJA

Katarina Mramor

Mentor: Prof. Dr. Božidar Šarler

Nova Gorica, 2014

Acknowledgements

First, I would like to thank my supervisor Prof. Dr. Božidar Šarler for his guidance and perseverance. I would also like to thank the committee members, Prof. Dr. Matjaž Hriberšek, Asoc. Prof. Dr. Miha Kovačič and Prof. Dr. Jan Sladek, for their remarks on my thesis.

Special thanks go to my co-workers from the Laboratory for Multiphase Processes at University of Nova Gorica and Laboratory for Simulation of Materials and Processes from Institute of Metals and Technology for countless suggestions, discussions and ideas, especially Dr. Robert Vertnik whose advice and guidance about the pre-existing numerical model have greatly facilitated my work.

My special thanks are extended to the staff of the Štore Steel d.o.o. company, especially Dr. Robert Vertnik, for providing all the necessary data, relevant for developing the numerical model of their billet casting machine.

I am particularly grateful to my employer, Centre of Excellence for Biosensors, Instrumentation and Process Control, for their understanding and support during my Ph.D. studies. The Centre of Excellence for Biosensors, Instrumentation and Process Control is an operation financed by the European Union, European Regional Development Fund and Republic of Slovenia, Ministry of Education, Science and Sport.

This doctoral study was partly co-financed by the European Union and by the European Social Fund respectively. The co-financing was carried out within the Human resources development operational programme for years 2007–2013, 1. Developmental priorities: Encouraging entrepreneurship and adaptation; preferential directives 1.3: Scholarship schemes.

The least direct but perhaps the most valuable help came from my friends and family. I would like to thank them for their support, understanding and patience, and most importantly their encouragement.

Modelling of Continuous Casting of Steel under the Influence of Electromagnetic Field with Meshless Method

Abstract

The purpose of this dissertation is to extend and explore the behaviour of a novel meshless method, namely the Local Radial Basis Function Collocation Method (LRBFCM) [Šarler and Vertnik, 2006], in the solution of a steady, laminar, and turbulent thermal fluid flow influenced by the magnetic field. The technological problem under consideration is focused on the influence of the magnetic field in the continuous casting of steel. The problem is defined by coupled mass, momentum, energy, turbulent kinetic energy, dissipation rate and induction equations, that are solved in two dimensions (2D) by local collocation with multiquadric radial basis functions on five nodded overlapping sub-domains and explicit time-stepping. The problem includes liquid-solid phase change phenomena and is characterized by three regions: the pure solid, the pure liquid and the mushy region between. Whereas the treatment of the pure solid and the pure liquid regions is straightforward, the treatment of the mushy region is much more complex since it combines both phases. The liquid-solid phase transformation is modelled by the mixture continuum model [Bennon and Incropera, 1987b]. The alloy solidification region, which might be divided into the slurry zone and the porous zone, is in this dissertation treated as a porous zone solely. As only the porous zone with stationary porous state is considered in this dissertation, it is modelled by the Darcy's law and the Kozeny-Carman [Carman, 1948] relation which supposes a constant value for the morphology of the porous media. The Reynolds time averaging [Reynolds, 1895] is used to devise a low-Reynolds k-ε turbulence model for the incompressible turbulent fluid flow. The Abe-Kondoh-Nagano [Abe et al., 1995] model is used to set the turbulence closures in the additional turbulent kinetic energy and dissipation rate equations. The velocity-pressure coupling is solved by the fractional step method [Chorin, 1967]. The Maxwell's equations are applied to calculate the effect of the externally applied magnetic field. The governing equations are discretized in their strong formulation and the adaptive upwind technique [Lin and Atluri, 2000; Gu and Liu, 2006] is used to approximate

the convection terms.

The accuracy of the method has been tested on several well known benchmark test cases both with and without the magnetic field. These verifications additionally serve as means to asses and set the free numerical parameters of the method used. The LRBFCM has been tested for a wide range of dimensionless parameters such as Prandtl (Pr), Hartmann (Ha), Reynolds (Re), Grasshof (Gr) and Rayleigh (Ra) numbers. The lid-driven cavity benchmark test case [Mramor et al., 2013a] is used to asses the performance of different radial basis functions (RBFs) and pressure-velocity coupling schemes. Numerical predictions are calculated for Re ranging from 100 to 3200. The natural convection in a square cavity under the influence of externally applied magnetic field [Mramor et al., 2013b] is used to determine the accuracy of the addition of magnetic field equations and corresponding boundary and initial conditions to the fully coupled problem of heat and fluid flow. The results are calculated for Ra ranging from 10^3 to 10^6, Pr 0.14 and 0.71, Gr ranging from 10^4 to 10^6 and Ha ranging from 0 to 100. The reference Hartmann flow case is chosen to test the in- and out-flow boundary conditions in the presence of the externally applied magnetic field against the analytical solution. The calculations were performed for Pr 0.71, Re 100, and Ha ranging from 0 to 1000. The backward facing step with magnetic field problem is selected to test the precision of the separation and reattachment positions. The analysis for the backward facing step problem under the influence of the externally applied magnetic field [Mramor et al., 2014a] is implemented for Pr 0.71, Re ranging from 300 to 800 and Ha ranging from 0 to 100. The results in all of the above mentioned examples have been verified against either the previously published results or by comparison with results calculated with the commercial fluid dynamics software (Fluent [ANSYS, 2013]) and are in good agreement.

The numerical model for continuous casting of steel [Vertnik and Šarler, 2006] is upgraded for the application of the magnetic field for magnetic breaking. The initial and boundary conditions are described and set to the values obtained from the Štore Steel billet continuous caster. The geometry and the material properties of steel are simplified for verification purposes. The results for the simplified model are verified by comparison with the Fluent code. The realistic magnetic field is calculated for various coil arrangements and the parametric study is performed for both the simplified and the realistic magnetic field. The sensitivity of magnetic field strength, position, and range is investigated for velocity, temperature and concentration fields. The tests show, that the upgraded numerical model is applicable on a wide range of laminar and turbulent fluid flow with including solidification, both with and without the presence of the magnetic field.

It is shown that the novel LRBFCM is able to successfully, accurately and reliably solve the equations of coupled magnetic and thermo-fluid problems for uniform and non-uniform node arrangements. Advantages of the LRBFCM method are its simplicity, accuracy, and straightforward implementation of the algorithm on non-uniform node arrangements as well as for involved physics. In the future, the discussion will be extended to the three dimensional (3D) problems with different magnetic field configurations, such as Electromagnetic Stirring (EMS) in order to simulate a wider range of continuous casting processes of steel with

externally applied magnetic fields.

Key words

laminar flow, turbulent flow, natural convection, forced convection, solidification, magnetic field, coupled systems, multiphysics problems, meshless methods, collocation, multiquadrics, radial basis functions, explicit time scheme, fractional step method, verification, simulation, continuous casting of steel

Modeliranje kontinuirnega ulivanja jekla pod vplivom elektromagnetnega polja z brezmrežno metodo

Povzetek

Namen te disertacije je razširiti in raziskati obnašanje nove brezmrežne metode, imenovane lokalna kolokacijska metoda radialnih baznih funkcij (LRBFCM) [Šarler and Vertnik, 2006], pri reševanju ustaljenega, laminarnega in turbulentnega termičnega toka tekočine pod vplivom magnetnega polja. Obravnavani tehnološki problem je osredotočen na vpliv magnetnega polja pri procesu kontinuiranega ulivanja jekla. Problem določajo sklopljene ohranitvene enačbe za maso, gibalno količino, energijo, turbulentno kinetično energijo, hitrost disipacije ter indukcijo, ki jih rešujemo v dveh dimenzijah z lokalno kolokacijo in uporabo multikvadričnih radialnih baznih funkcij na pet točkovnih prekrivajočih se poddomenah z eksplicitno časovno shemo. Problem vključuje kaplevito-trdne fazne spremembe in je določen s tremi regijami: popolnoma trdno področje, popolnoma kapljevito področje ter kašasto področje med obema. Medtem ko je obravnava popolnoma trdnega ter popolnoma kapljevitega področja neposredna, je obravnava kašastega področja mnogo bolj zapletena, saj le-to obsega tako trdno kot tudi kapljevito fazo. Kapljevito-trdni fazni prehod je modeliran z modelom kontinuumske mešanice [Bennon and Incropera, 1987b]. Območje strjevanja zlitine, ki ga lahko razdelimo na kašasti in porozni del, je v tej disertaciji obravnavano kot zgolj porozen medij. Ker je v tej disertaciji obravnavano le porozno območje s stacionarnim poroznim stanjem, je le-to modelirano z Darcyjevim zakonom ter Kozeny-Carmanovo [Carman, 1948] relacijo, ki predvideva konstantno vrednost morfologije poroznega materiala. Reynoldsovo časovno povprečenje [Reynolds, 1895] je uporabljeno za izdelavo $k - \varepsilon$ turbulentnega modela za nizka Re števila za tok nestisljive turbulentne tekočine. Abe-Kondoh-Nagano [Abe et al., 1995] model je uporabljen za nastavitev turbulentnih parametrov v zaključnih enačbah za turbulentno kinetično energijo in hitrost disipacije. Hitrostno-tlačna sklopitev je rešena z metodo delnih korakov [Chorin, 1967]. Za izračun vpliva zunanjega magnetnega polja so uporabljene Maxwellove enačbe. Ohranitvene enačbe so bile diskretizirane v močni obliki, za približek konvekcijskih členov pa je uporabljena adaptivna privetrna tehnika [Lin and Atluri, 2000; Gu and Liu, 2006].

Točnost metode je bila preverjena na več dobro znanih referenčnih testnih

primerih, tako z kot tudi brez magnetnega polja. Ta preverjanja so dodatno služila za oceno in nastavitev prostih numeričnih parametrov uporabljane metode. LRBFCM je bila preverjena na širokem spektru brezdimenzijskih parametrov, kot so Prandtlovo (Pr), Hartmanovo (Ha), Reynoldsovo (Re), Grashofovo (Gr), in Rayleighovo (Ra) število. Referenčni testni primer za gnani tok v kotanji [Mramor et al., 2013a] je uporabljen za oceno obnašanja različnih radialnih baznih funkcij ter sklopitvene sheme za hitrost in tlak. Numerične napovedi so bile izračunane za Re v razponu od 100 do 3200. Referenčni test za naravno konvekcijo v kotanji pod vplivom zunanjega magnetnega polja [Mramor et al., 2013b] je bil uporabljen za določitev točnosti pri vključitvi enačb magnetnega polja v že obstoječi model ter preverjanju ustreznosti robnih ter začetnih pogojev pri popolnoma sklopljenem modelu temperaturnega in hitrostnega polja. Rezultati so bili izračunani za Ra v razponu od 10^3 do 10^6, Pr števili 0.14 in 0.71, Gr v razponu od 10^4 do 10^6 ter Ha v razponu od 0 do 100. Referenčni primer Hartmanovega toka je bil izbran za testiranje robnih ter začetnih pogojev za dotok in odtok v prisotnosti zunanjega magnetnega polja ter primerjavo z analitično rešitvijo. Izračuni so bili narejeni za Pr 0.71 in Re 100, za Ha v razponu od 0 do 1000. Tok tekočine čez nazaj obrnjeno stopnico z magnetnim poljem je bil izbran za ugotavljanje točnosti položaja točk, kjer se tok odlepi in nazaj prilepi. Analiza toka preko nazaj obrnjene stopnice pod vplivom zunanjega magnetnega polja [Mramor et al., 2014a] je bila izdelana za Pr 0.71 in Re v razponu od 300 do 800 ter Ha v razponu od 0 do 100. Rezultati vseh zgoraj omenjenih primerov so bili preverjeni ali s poprej objavljenimi rezultati ali z rezultati izračunanimi s komercialnim programom (Fluent[ANSYS, 2013]) in se dobro ujemajo.

Numerični model za kontinuirano ulivanje jekla [Vertnik and Šarler, 2006] je bil nadgrajen z aplikacijo magnetnega polja za magnetno zaviranje. Začetni in robni pogoji so opisani in nastavljeni glede na vrednosti naprave za kontinuirano ulivanje gredic v podjetju Štore Steel. Geometrija in snovne lastnosti jekla so poenostavljene zaradi preverjanja. Rezultati primera s poenostavljenim magnetnim poljem so preverjeni z izračuni narejenimi s programom Fluent. Realistično magnetno polje je izračunano za različne položaje tuljave, parametrična študija pa je narejena tako za poenostavljeno magnetno polje kot tudi za realistično magnetno polje. Občutljivost moči, položaja in dosega magnetnega polja je preverjena za hitrostno, temperaturno in koncentracijsko polje. Testi kažejo, da je dopolnjen numerični model primeren za uporabo na širokem naboru problemov za laminaren in turbulenten tok s strjevanjem tako z kot tudi brez prisotnosti magnetnega polja.

Pokazano je, da lahko z novo LRBFCM uspešno, točno in zanesljivo rešujemo sklopljene enačbe magnetnega in termo-tekočinskega polja za enakomerne in neenakomerne porazdelitve računskih točk. Prednosti LRBFCM metode so njena preprostost, točnost, in enostavna izvedba tako za algoritem na neenakomerno porazdeljenih točkah kot tudi za vpleteno fiziko. V prihodnosti nameravamo razpravo razširiti na obravnavo tri dimenzionalnih problemov za različne postavitve magnetnega polja, kot je na primer elektromagnetno mešanje z namenom simulirati širši spekter procesov kontinuiranega ulivanja jekla z zunanjimi magnetnimi polji.

Ključne besede

laminarni tok, turbulentni tok, naravna konvekcija, prisilna konvekcija, strjevanje, magnetno polje, sklopljeni sistemi, večfizikalni problemi, brezmrežne metode, kolokacija, multikvadriki, radialne bazne funkcije, eksplicitna časovna shema, metoda delnih korakov, verifikacija, simulacija, kontinuirno ulivanje jekla

Contents

List of Symbols **V**

List of Figures **XV**

List of Tables **XXIII**

1 Introduction **1**
1.1 Continuous Casting of Steel 2
1.2 Magnetohydrodynamic Processes in Continuous Casting of Steel . 6
1.2.1 Literature Review of Electromagnetic Field Modelling . . 8
1.3 Meshless Numerical Methods 12
1.3.1 Radial Basis Function Collocation Method 12
1.4 Objectives of the Dissertation 15
1.4.1 Performed Work 15
1.4.2 Originality and Advantages 16
1.5 Overview of the Dissertation 17

2 Physical Model **19**
2.1 Fluid Dynamics 19
2.1.1 Mass Conservation Equation 20
2.1.2 Momentum Conservation Equation 20
2.1.3 Energy Conservation Equation 22
2.1.4 Species Conservation Equation 23
2.2 Solidification 24
2.2.1 Microsegregation 24
2.2.2 Macrosegregation 26
2.2.3 Mixture Continuum Model 26
2.3 Turbulence 29
2.3.1 Low-Re k-ε Turbulence Model 32
2.4 Magnetohydrodynamics 33
2.4.1 Low Magnetic Reynolds Number 35
2.4.2 External Magnetic Field 36
2.5 Final Multiphysics Model 36
2.5.1 Final Set of Governing Equations 36
2.5.2 Boundary Conditions 37
2.5.3 Initial Conditions 39

3 Local Radial Basis Function Collocation Method 41
3.1 Node Distribution and Influence Domain Selection 41
3.2 Approximation Function 43
3.2.1 Radial Basis Functions 44
3.2.2 Collocation 49
3.3 Solving Partial Differential Equations with Radial Basis Functions 50

4 Solution Procedure 51
4.1 Distribution of Computational Nodes 51
4.2 Time Discretization 53
4.3 Solution Procedure for the General Transport Equation 56
4.4 Pressure - Velocity Coupling 59
4.5 Solution of Electromagnetic Field Equations 61
4.6 Description of the Multiphysics Solution Procedure 61
4.7 Convergence Criteria 63
4.8 Numerical Implementation 65
4.8.1 Solution of Poisson's Equation 65

5 Benchmark Test Cases for Fluid Flow and Magnetic Field 67
5.1 Dimensionless Form of Governing Equations 68
5.2 Lid Driven Cavity Problem 71
5.2.1 Problem Description 71
5.2.2 Governing Equations and Numerical Parameters 71
5.2.3 Results and Discussions 72
5.2.4 Summary and Conclusions 79
5.3 Natural Convection in a Rectangular Enclosure with Magnetic Field 79
5.3.1 Problem Description 79
5.3.2 Governing Equations 80
5.3.3 Results and Discussions 82
5.3.4 Summary and Conclusions 91
5.4 Hartmann Flow 91
5.4.1 Problem Description 91
5.4.2 Governing Equations 92
5.4.3 Results and Discussions 93
5.4.4 Summary and Conclusions 95
5.5 Forced Convection in a Backward Facing Step Channel with Magnetic Field 95
5.5.1 Problem Description 95
5.5.2 Governing Equations 96
5.5.3 Results and Discussions 97
5.5.4 Summary and Conclusions 108

6 Continuous Casting of Steel 111
6.1 Model Assumptions 111
6.2 Geometry 113
6.3 Magnetic Field 113
6.3.1 Magnetic Field due to Rectangular Coils 116

6.3.2 Influence of Temperature on Magnetic Behaviour of Molten Steel . . . 124
6.3.3 Magnetization due to the Iron Core in Solenoids . . . 124
6.4 Magnetic Field in the Continuous Casting Problem . . . 126
6.5 Node Arrangement . . . 127
6.6 Initial and Boundary Conditions . . . 128
6.6.1 Initial Conditions . . . 129
6.6.2 Boundary Conditions . . . 131
6.7 Numerical Examples . . . 132
6.7.1 A: Simple Predetermined Magnetic Field . . . 135
6.7.2 B: Coil Magnetic Field - Temperature, Velocity . . . 158
6.7.3 C: Coil Magnetic Field - Temperature, Velocity, Concentration . . . 188
6.8 Overview of Calculated Examples . . . 197

7 Summary and Conclusions 199
7.1 Performed Work . . . 199
7.2 Conclusions . . . 200
7.2.1 Industrial Relevance . . . 201
7.3 Suggestions for Future Work . . . 201
7.3.1 Numerical Modelling Upgrades . . . 201
7.3.2 Physical Modelling Upgrades . . . 202
7.4 Publications . . . 203

A Turbulence Modelling Classification 207

B Dimensionless Governing Equations 211
B.1 Dimensionless Governing Equations for Lid Driven Cavity . . . 211
B.2 Dimensionless Governing Equations for Natural Convection in Cavity under the Influence of External Magnetic Field . . . 212
B.3 Dimensionless Governing Equations for Hartmann Flow . . . 212
B.4 Dimensionless Governing Equations for Backward Facing Step . . . 213

C Magnetic Field Square Loop 215

D Sensitivity Study for Simple Magnetic Field 217

List of Symbols

Latin symbols

a	side of a rectangular coil loop
a_b	billet width
$\mathbf{A}$	vector potential
b	side of a rectangular coil loop, wire length
Bt	Batchlor number
$\mathbf{B}$	magnetic flux density
$\mathbf{B}_{corr}$	magnetic flux correction
c	shape parameter in multiquadrics
c_p	specific heat at constant pressure
$c_{1\varepsilon}$, $c_{2\varepsilon}$, $c_{3\varepsilon}$, c_μ	closure coefficients in k-ε equations
C	concentration
C_E	solute concentration in eutectic alloy
Cu	Courant number
d_2	SEN diameter
D	diffusion coefficient
$D_{k-\varepsilon}$	additional source term in k equation
$E_{k-\varepsilon}$	additional source term in ε equation
$\mathbf{E}$	electric field density
f	function in definition of boundary conditions
f_1, f_2	closure coefficients in ε equation
f_L, f_S	mass fractions of liquid and solid

f_μ	damping function in μ_t equation
$\mathbf{f}$	force per unit volume (force density)
$\mathbf{f}_b$	body force density
$\mathbf{f}_{bu}$	buoyancy force density
$\mathbf{f}_{EM}$	Lorentz force density
$\mathbf{f}_g$	gravitational force density
$\mathbf{f}_{gbu}$	gravitational force density corrected for the buoyancy
$\mathbf{f}_p$	pressure force density
$\mathbf{f}_{pi}$	phase interaction force density
$\mathbf{f}_s$	surface force density
$\mathbf{f}_\tau$	viscous friction force density
$\mathbf{f}_{tbu}$	thermal buoyancy force density
$\mathbf{F}$	force
$\mathbf{F}_{EM}$	Lorentz force
g_L, g_S	volume fraction of liquid and solid
$\mathbf{g}$	gravitational acceleration
G	diffusion number for von-Neumann stability criteria
G_k	turbulent term due to the buoyancy force k equation
Gr	Grashof number
h	enthalpy
h_{ST}	enthalpy source term
h_m	melting enthalpy
h_{mc}, h_{sc}	heat transfer coefficient for mould and for spray cooling
H	dimension of computational domain; height
Ha	Hartmann number
$\mathbf{H}$	magnetic field strength
$\mathbf{i}_x$, $\mathbf{i}_y$, $\mathbf{i}_z$	unit vectors in x, y, z directions
$\mathbf{I}$	electric current

$\underline{\underline{\mathbf{I}}}$	identity tensor
$\mathbf{j}$	volumetric current density
$\mathbf{j}_C$	solute flux
$\mathbf{J}$	electric current density
k	turbulent kinetic energy
k_p	equilibrium partition coefficient
K	permeability
K_0	permeability constant
ℓ	characteristic length
l_m	mould height
l_{EM}	electromagnet height
l_{mEM}	electromagnet placement height
$d\mathbf{l}$	differentiation of integration length
L	dimension of the domain; length
m	mass
$\mathbf{m}$	magnetic dipole momentum
$\mathbf{M}$	magnetisation
$\mathbf{n}$	normal vector
$\mathcal{N}$	interaction parameter
N	total number of computational nodes
N_{basis}	number of basis functions in a influence domain
N_{domain}	number of nodes in an influence domain
N_N, N_M	number of coils in x and y direction
N_Ω, N_Γ	number of the domain and boundary nodes
N_s	number of nodes between two points
Nu	Nusselt number
p	pressure
$\mathbf{p}$	central node of the influence domain

$\mathbf{p}_j$	support node
P_k	production term in k equation
Pr	Prandtl number
Pr_M	magnetic Prandtl number
Pr_t	turbulent Prandtl number
q	heat flux
r	distance between two nodes in an influence domain
$\hat{\mathbf{r}}$	unit position vector
$\mathbf{r}$	position vector
Ra	Rayleigh number
Re	Reynolds number
Re_M	magnetic Reynolds number
Re_t	local turbulent Reynolds number
$d\mathbf{s}$	differential of wire segment length
S_Φ	source term in general transport equation
Sc	Schmidt number
St	Stuart number
t	time
Δt	time step
$t^\wr$	time interval
T	temperature
T_C, T_H	cold and hot temperatures
T_{Currie}	Currie temperature
T_E	eutectic temperature
T_m	melting temperature
u	refinement parameter in node arrangement
v_c	characteristic velocity
$v_{x(MAX)}$	center-line velocity

v_{cast}	casting velocity
$\mathbf{v}$	velocity vector
$\mathbf{v}^\star$	intermediate velocity vector
$\mathbf{v}_\varepsilon$	Kolmogorov velocity scale vector
V	volume
w_1, w_2	weights in definition of boundary conditions
x, y, z	Cartesian coordinates
y^+	non-dimensional distance to the wall
$y_{refined}$	refined node distribution in y direction
$y^{norm}_{refined}$	refined normalized node distribution in y direction
$y_{uniform}$	uniform node distribution in y direction
$y^{norm}_{uniform}$	uniform normalized node distribution in y direction

Greek symbols

α_T	thermal diffusivity
α_{Tt}	thermal eddy diffusivity
$\boldsymbol{\alpha}$	vector of radial basis function expansion coefficients
β	compressibility coefficient in artificial compressibility method
β_C, β_T	solute and thermal expansion coefficients
Γ	boundary
δ_{ij}	Kronecker delta
ε	dissipation rate
ε_0	permittivity of free space
ε_C, ε_T, ε_v, ε_p, ε_k, ε_ε	iteration criteria for the solute concentration, temperature, velocity, pressure, turbulent kinetic energy, and dissipation rate
ϵ_{ijl}	Levi-Civita symbol
θ	approximation function
${}_l\theta$	data value
$\boldsymbol{\theta}$	vector of data

Θ	dimensionless temperature
κ	bulk viscosity
λ	thermal conductivity
μ	fluid viscosity
μ_0	permeability of free space
μ_{iron}	magnetic permeability of iron
μ_M	magnetic permeability
μ_r	relative permeability
μ_{steel}	magnetic permeability of steel
μ_t	turbulent dynamic viscosity
ν	kinematic viscosity
ν_t	turbulent kinematic viscosity
ρ	density
ρ^*	partial density
ρ_e	charge density
σ	electrical conductivity
σ_T, σ_C, σ_k, σ_ε	energy, solute, turbulent kinetic energy and dissipation rate closure coefficients in conservation equations
$\underline{\underline{\boldsymbol{\sigma}}}$	stress tensor
τ_w	wall shear stress
$\boldsymbol{\tau}$	viscous friction
$\underline{\underline{\boldsymbol{\tau}}}$	deviatoric stress tensor
ϕ	electric potential
ϕ_v	velocity potential
ϕ_w	diameter of the wire
Φ	dependent variable
χ	magnetic diffusivity
χ	susceptibility

ψ	radial basis function
ψ_{CON}	conical radial basis function
ψ_{CU}	cubic radial basis function
ψ_{GA}	Gaussian radial basis function
ψ_{IMQ}	inverse multiquadric radial basis function
ψ_{IQ}	inverse quadric radial basis function
ψ_{MQ}	multiquadric radial basis function
ψ_{TPS}	thin plane spline radial basis function
Ψ	stream function
$\mathbf{\Psi}$	collocation matrix
Ω	domain

Acronyms

1D	one dimensional
2D	two dimensional
3D	three dimensional
AC	alternating current
ACM	artificial compressibility method
AKN	Abe-Kondoh-Nagano turbulence model
BC	boundary condition
BEM	boundary element method
CBS	characteristic base split
CC	continuous casting
CCM	Chebyshev collocation method
CFD	computational fluid dynamics
CON RBF	conical radial basis function
CU RBF	cubic radial basis function
CVF	Compaq visual fortran
DC	direct current

DCC	direct-chill casting
DES	detached eddy simulations
DNS	direct numerical simulation
DSM	differential stress model
EM	electromagnetic
EMBR	electromagnetic brakers
EMLA	electromagnetic level accelerator
EMLS	electromagnetic level stabilizer
EMRS	electromagnetic rotary stirrer
EMS	electromagnetic stirrers
EVM	eddy-viscosity model
FCM	flow control mould
FDM	finite difference method
FEM	finite element method
FEMS	final electromagnetic stirrers
FSM	fractional step method
FVM	finite volume method
GA RBF	Gaussian radial basis function
GRBFCM	global radial basis function collocation method
IMQ RBF	inverse multiquadric radial basis function
IQ RBF	inverse quadric radial basis function
LAPACK	linear algebra package
LBM	lattice Boltzman method
LES	large eddy simulation
LIRBFCM	local indirect radial basis function collocation method
LMAPS	local method of approximate particular solutions
LRBFCM	local radial basis function collocation method
MEMS	mould electromagnetic stirrers

MGM	multi grid method
MHD	magnetohydrodynamics
MKL	math kernel library
MLPGM	meshless local Petrov-Galerkin method
MLRPIM	meshfree local radial point interpolation method
MMEMS	multi-mode electromagnetic stirrers
MQ	multiquadric
N-S	Navier-Stokes
NAFEMS	national agency for finite element methods and standards
NLEVM	non-linear eddy-viscosity model
PARDISO	parallel direct sparse solver
PDE	partial differential equations
PISO	pressure implicit with splitting of operators method
PV	pressure-velocity
RANS	Reynolds-averaged Navier-Stokes
RANS-SST	Reynolds-averaged Navier-Stokes shear stress transport
RBF	radial basis function
RBFCM	radial basis function collocation method
RNG	re-normalisation group
SEMS	strand electromagnetic stirrers
SEN	submerged entry nozzle
SGS	sub-grid scale
SIMPLE	semi-implicit method for pressure linked equations
SIMPLER	semi-implicit method for pressure linked equations revised
SMEMS	slab mould electromagnetic stirrers
SPIM	smoothed point interpolation method
TPS RBF	thin plane spline radial basis function
UDV	ultrasonic Doppler velocimetry

WALE	wall adapting local eddy-viscosity

Subscripts

$_0$	initial value
$_\perp$	perpendicular component
$_\parallel$	parallel component
$_{BC}$	boundary condition
$_C$	solutal
$_{i,\ j,\ l,\ n}$	counters
$_k$	turbulent kinetic energy
$_L$	liquid phase, liquidus
$_{MIN}$	minimum
$_{MAX}$	maximum
$_r$	relative
$_{ref}$	reference value
$_{sc}$	spray cooling
$_S$	solid phase, solidus
$_t$	turbulent
$_T$	thermal
$_w$	wall
$_{x,\ y,\ z}$	Cartesian coordinates
$_\varepsilon$	dissipation rate

Superscripts

$'$	dimensionless
$\overline{\zeta}$	mean value of general variable
$\urcorner$	fluctuating part
^{T}	transposed

List of Figures

1.1 The amount of produced crude steel since 1900 and the amount of continuously cast steel. Data from [WSA, 2013]. 2
1.2 Types of CC of steel devices. R_1, R_2, R_3, and R stand for casting device radius. Figure based on [Pass, 2013] 3
1.3 A scheme of the curved CC process. 4
1.4 Semi-finished steel products. Left: blooms (courtesy of Accolade Photography [Accolade-Photography, 2013]). Right: billets (courtesy of Štore Steel d.o.o. [Štore Steel, d. o. o., 2013]). 4
1.5 A detail of tundish and mould. 5
1.6 Types of EMS configurations. 8
1.7 Types of the EMBR configurations (Figure based on [ABB, 2013]). I. Conventional EMBR, II. EMBR ruler, III. FCM. 9

2.1 The linearised simplification of the concentration - temperature phase diagram for a binary alloy. 25
2.2 The extent of the modelling for different types of turbulence models. 30
2.3 Schematic representation of general boundary conditions for magnetic field. 39

3.1 Node arrangement configurations. 42
3.2 Five nodded influence domain. 43
3.3 Overlapping influence domains. 43
3.4 MQ RBF with the shape parameter $c = 0.5$. 44
3.5 IQ RBF with the shape parameter $c = 0.5$. 45
3.6 IMQ RBF with the shape parameter $c = 0.5$. 46
3.7 GA RBF with the shape parameter $c = 0.5$. 46
3.8 CON RBF with the shape parameter $c = 0.5$. 47
3.9 CU RBF with the shape parameter $c = 0.5$. 48
3.10 TPS RBF with the shape parameter $c = 0.5$. 48

4.1 Flow chart of solution procedure. 52
4.2 Refinement steps of the node refinement process in y direction. . . 52
4.3 A more complex refinement steps of the node refinement process in y direction. 53
4.4 Explicit time discretization scheme. 54
4.5 Implicit time discretization scheme. 55
4.6 Semi-implicit time discretization scheme. 55

4.7 Flow chart for solving velocity and pressure. 61
4.8 Flow chart for solving electromagnetic effects. 62
4.9 Block diagram of the entire solution procedure. 64

5.1 Computational scheme of a 2D cavity with boundary conditions. 72
5.2 Scheme of the node arrangement (41x41, $u = 1.2$) for the computational domain of a 2D cavity. 73
5.3 Positions of vertical and horizontal lines through the geometric center of a square cavity. 73
5.4 Comparison of dimensionless velocities at different node densities for the Re=1000. 74
5.5 Comparison of dimensionless velocities for Re=100, calculated with LRBFCM with the results of [Ghia et al., 1982]. 75
5.6 Comparison of dimensionless velocities for Re=400, calculated with LRBFCM and Fluent, and the results of [Ghia et al., 1982]. . . . 75
5.7 Comparison of dimensionless velocities for Re=1000, calculated with LRBFCM and the results of [Ghia et al., 1982]. 76
5.8 Comparison of dimensionless velocities for Re=3200, calculated with LRBFCM and the results of Ghia et al. [1982]. 76
5.9 Comparison of the results with two different RBF types (MQ and IMQ). 77
5.10 Comparison of dimensionless velocities for different PV coupling schemes. 78
5.11 Comparison of dimensionless velocities for different β. 79
5.12 Scheme of a 2D differentially heated cavity with initial and boundary conditions. 82
5.13 Case 2. Nu as function of four different node arrangements (41x41, 61x61, 81x81 and 101x101) at Gr = 10^4 and Pr=0.71. 84
5.14 Case 2. Comparison of dimensionless velocities v'_x for Gr = 10^4 (left) and Gr = 10^6 (right) along the horizontal line through the center of the cavity. 85
5.15 Case 2. Comparison of dimensionless temperatures Θ for Gr = 10^4 (left) and Gr = 10^6 (right) along the horizontal line through the center of the cavity. 85
5.16 Case 3. Comparison of dimensionless temperatures Θ for Gr = 10^4 (left) and Gr = 10^5 (right) along the horizontal line through the center of the cavity. 86
5.17 Case 3. Comparison of dimensionless temperatures Θ for Gr = 10^6 along the horizontal line through the center of the cavity. 87
5.18 Case 3. Comparison of v'_x along the horizontal (left) and v'_y along the vertical (right) lines through the center of the cavity for Gr = 10^4 as a function of different Ha. 87
5.19 Case 3. Comparison of v'_x along the horizontal (left) and v'_y along the vertical (right) lines through the center of the cavity for Gr = 10^5 as a function of different Ha. 87

5.20 Case 3. Comparison of v'_x along the horizontal (left) and v'_y along the vertical (right) lines through the center of the cavity for Gr = 10^6 as a function of different Ha. 88
5.21 Case 3. Comparison of streamlines at various Gr (Gr = 10^4,Gr = 10^5) and Ha (0, 10, 50). The streamlines are equidistantly spaced. 89
5.22 Case 3. Comparison of streamlines at various Gr (Gr = 10^5, Gr = 10^6) and Ha (0, 10, 50, 100, 200). The streamlines are equidistantly spaced. 89
5.23 Isotherms at various Gr (Gr = 10^4, Gr = 10^5) and Ha (0, 10, 50) at Pr=0.14. The isotherms are equidistantly spaced, the minimum is at T_C (right boundary) and the maximum is at T_H (left boundary). 90
5.24 Isotherms at various Gr (Gr = 10^5, Gr = 10^6) and Ha (0, 10, 50, 100, 200) at Pr=0.14. The isotherms are equidistantly spaced, the minimum is at T_C (right boundary) and the maximum is at T_H (left boundary). 91
5.25 Scheme with initial and boundary conditions. 93
5.26 Node arrangement with 39x99 nodes. 94
5.27 Comparison of dimensionless velocities for different node arrangements for Re = 800. 94
5.28 Comparison of velocity profiles for different Ha. 95
5.29 Geometry of the backward facing step problem. 98
5.30 Scheme of the backward facing step problem with initial and boundary conditions. 98
5.31 Scheme of 301x101 node arrangement. 99
5.32 Comparison of dimensionless outlet velocities for different node arrangements for Re = 800 and Ha = 0. 99
5.33 Comparison of v'_x (left) and v'_y (right) at two different positions ($x' = 7$ and $x' = 15$) for Re = 800 and Ha = 0, and 301x101 node arrangement. 100
5.34 Comparison of outlet velocities for Re = 300, 400, 500, 600, 700, and 800 and Ha = 0 for 301x101 node arrangement. 100
5.35 Comparison of wall shear stresses for the upper (N) and the lower (S) walls with reference results (G N) and (G S) [Gartling, 1990]) at Re = 800. 101
5.36 Comparison of wall shear stresses and reattachment positions for 301x101 node arrangement, Ha = 0 and Re ranging from 300 to 800 (step 100). 101
5.37 Streamlines for Re = 300 and Ha = 0, 5, 10, 50, and 100 (from the top to the bottom) for 301x101 node arrangement. 103
5.38 Streamlines for Re = 600 and Ha = 0, 5, 10, 50, and 100 (from the top to the bottom) for 301x101 node arrangement. 104
5.39 Streamlines for Re = 800 and Ha = 0, 5, 10, 50, and 100 (from the top to the bottom) for 301x101 node arrangement. 104
5.40 Comparison of the vertical cross sections for v'_x (left) and v'_y (right) for Re = 800 and Ha = 10. 105

5.41 Comparison of the final velocities at the outlet for Re = 300, and Ha = 0, 5, 10, 50, and 100. 105
5.42 Comparison of the final velocities at the outlet for Re = 600, and Ha = 0, 5, 10, 50, and 100. 105
5.43 Comparison of the final velocities at the outlet for Re = 800, and Ha = 0, 5, 10, 50, and 100. 106
5.44 Comparison of the maximum outlet velocities at the outlet for different Re and Ha. 107
5.45 Comparison of the wall shear stresses calculated with the LRBFCM and reference results calculated with Fluent for Re = 800 and Ha = 10 for the upper (N) and the lower (S) walls. 107
5.46 Wall shear stress for Re = 300 and Ha = 0, 5, 10, 50 and 100. . . 108
5.47 Wall shear stress for Re = 600 and Ha = 0, 5, 10, 50 and 100. . . 108
5.48 Wall shear stress for Re = 800 and Ha = 0, 5, 10, 50 and 100. . . 108

6.1 Scheme of a simplified model for CC of steel. 114
6.2 Scheme of a simplified computational domain model of CC of steel. 114
6.3 Square coils layout. 115
6.4 A 2D approximation of the wire arrangement for a simplified model of CC process. 115
6.5 Finite, straight, current carrying wire with length b. 116
6.6 Magnetic field (ln(B)) of a finite straight wire with length b. . . . 116
6.7 Finite, straight, current carrying wire with length b. Rotations from the left to the right: 0°, 180°, 90° and 270°. 118
6.8 Square loop with sides $a = b$. 119
6.9 Magnetic field of a square loop. 119
6.10 Schematic picture of parallel square loops. Left: scheme. Right: side view. 120
6.11 Magnetic field of N_N square parallel loops. 120
6.12 Parallel square loops arrangement. 121
6.13 Square solenoid 2D model arrangement. 121
6.14 Orientation of magnetic field in a realistic coil arrangement with four coils. 122
6.15 Orientation of magnetic field in two coil arrangement. 122
6.16 Magnetic field of $N_N \times N_M$ square loops placed at a distance d. . 122
6.17 Magnetic field of $N_M \times N_N$ infinite square coils. 123
6.18 Temperature dependence of permeability of 51CrV4 steel for four different cooling rates taken from JMatPro database. 125
6.19 Magnetic field of two parallel iron core solenoids, each with $N_N \times N_M$ infinite square coils. 126
6.20 Levels of the refinement in the computational domain. 128
6.21 Node arrangement at the top of the computational domain. See TOP section in Fig. 6.20. 129
6.22 Node arrangement detail at the end of the mould. See MIDDLE section in Fig. 6.20. 129

6.23 Node arrangement at the bottom of the computational domain. See BOTTOM section in Fig. 6.20. 130
6.24 Positions of plotting cross-sections. The dashed line represents plotting cross-section along y axis. 134
6.25 Positions of plotting cross-sections. The dashed line represents plotting cross-sections along x axis. 134
6.26 An example of a simple magnetic field with $l_m = -0.8$ m and $l_{EM} = 0.1$ m. 135
6.27 Temperature at simplified magnetic field. 136
6.28 Temperature at simplified magnetic field at cross-section -1.8 m. 136
6.29 Temperature at simplified magnetic field. Left: cross-section at 0.07 m. Right: cross-section at 0.14 m. 137
6.30 Absolute velocity field at simplified magnetic field. 137
6.31 Absolute velocity at simplified magnetic field at cross-section -1.8 m. 138
6.32 Absolute velocity at simplified magnetic field. Left: 0.07 m. Right: 0.14 m. 138
6.33 Comparison of absolute velocity magnitudes for the cases with and without magnetic field. 139
6.34 Comparison of absolute velocity magnitudes for the cases with and without magnetic field. Left: cross-section at -0.8 m. Right: cross-section at -0.9 m. 139
6.35 Comparison of absolute velocity magnitudes for the cases with and without magnetic field at cross-section -1.8 m. 139
6.36 Comparison of streamlines between FVM and LRBFCM simulations with and without magnetic field. I: Fluent $B_x = 0$ T. II: $B_x = 0$ T. III: Fluent $B_x = 3.5 \cdot 10^{-2}$ T. IV: $B_x = 3.5 \cdot 10^{-2}$ T. . . 140
6.37 Comparison of temperature field between FVM and LRBFCM simulations with and without magnetic field. I: Fluent $B_x = 0$ T. II: $B_x = 0$ T. III: Fluent $B_x = 3.5 \cdot 10^{-2}$ T. IV: $B_x = 3.5 \cdot 10^{-2}$ T. . . 141
6.38 Comparison of velocity field between FVM and LRBFCM simulations with and without magnetic field. I: Fluent $B_x = 0$ T. II: $B_x = 0$ T. III: Fluent $B_x = 3.5 \cdot 10^{-2}$ T. IV: $B_x = 3.5 \cdot 10^{-2}$ T. . . 142
6.39 Comparison of profiles for strand length of $l = 1.8$ m and $l = 2.6$ m. Left: temperature profile at 0.14 m. Right: velocity profile at -1.8 m. 143
6.40 Comparison of temperature and velocity fields as a function of computational domain length. Left: temperature field. Right: velocity field. 144
6.41 Comparison of temperature profiles along x direction. Left: -0.9 m. Right: -1.8 m. 145
6.42 Comparison of temperature profiles along y direction. Left: 0.07 m. Right: 0.14 m. 145
6.43 Temperature field $(T(\mathbf{B}) - T(\mathbf{B} = 0))$ as a function of magnetic field magnitude. I: $B_x = 2.6 \cdot 10^{-3}$ T. II: $B_x = 2.6 \cdot 10^{-2}$ T. III: $B_x = 2.6 \cdot 10^{-1}$ T. IV: $B_x = 2.6$ T. 146

6.44 Comparison of velocity profiles along x direction. Left: -0.8 m. Right: -0.9 m. 147
6.45 Comparison of velocity profiles along x direction at cross-section -1.8 m. 148
6.46 Velocity field $(\mathbf{v}(\mathbf{B}) - \mathbf{v}(\mathbf{B} = 0))$ as a function of EM magnitudes. I: $B_x = 2.6 \cdot 10^{-3}$ T. II: $B_x = 2.6 \cdot 10^{-2}$ T. III: $B_x = 2.6 \cdot 10^{-1}$ T. IV: $B_x = 2.6$ T. 149
6.47 Comparison of temperature profiles along x direction. Left: 0.07 m. Right: 0.14 m. 150
6.48 Comparison of velocity profiles along y direction. Left: -0.8 m. Right: -0.9 m. 150
6.49 Comparison of velocity profiles along y direction at -1.8 m. . . . 151
6.50 Temperature field $(T(\mathbf{B}) - T(\mathbf{B}_0))$ as a function of magnetic field position. I: $l_{mEM} = -0.6$ m. II: $l_{mEM} = -0.7$ m. III: $l_{mEM} = -0.9$ m. 152
6.51 Velocity field $(\mathbf{v}(\mathbf{B}) - \mathbf{v}(\mathbf{B}_0))$ as a function of EM positions. I: $l_{mEM} = -0.6$ m. II: $l_{mEM} = -0.7$ m. III: $l_{mEM} = -0.9$ m. 153
6.52 Comparison of temperature profiles along x direction. Left: 0.07 m. Right: 0.14 m. 154
6.53 Comparison of velocity profiles along y direction. Left: -0.8 m. Right: -0.9 m. 154
6.54 Comparison of velocity profiles along y direction at -1.8 m. . . . 155
6.55 Temperature field $(T(\mathbf{B}) - T(\mathbf{B}_0))$ as a function of magnetic field position. I: -0.8 m $< l_{EM} < -1.0$ m. II: -0.8 m $< l_{EM} < -0.95$ m. III: -0.8 m $< l_{mEM} < -0.85$ m. 156
6.56 Velocity field $(\mathbf{v}(\mathbf{B}) - \mathbf{v}(\mathbf{B}_0))$ as a function of magnetic field range. I: -0.8 m $< l_{EM} < -1.0$ m. II: -0.8 m $< l_{EM} < -0.95$ m. III: -0.8 m $< l_{mEM} < -0.85$ m. 157
6.57 Left: the vertical cross-sections of the coil magnetic field. Right: the horizontal cross-sections of the coil magnetic field. 158
6.58 Magnetic field of the default coil configuration. 159
6.59 Temperature fields. Left: vertical cross-sections. Right: horizontal cross-sections. 160
6.60 Velocity fields. Left: vertical cross-sections. Right: horizontal cross-sections. 160
6.61 Liquid fraction. Left: horizontal cross-sections. Right: vertical cross-sections. 161
6.62 Temperature fields. Left: without magnetic field. Right: with magnetic field. 162
6.63 Velocity fields. Left: without magnetic field. Right: with magnetic field. 163
6.64 Magnetic field as a function of the span distance a_d. Left: $a_d = 0.00$ m. Middle: $a_d = 0.05$ m. Right: $a_d = 0.075$ m. 165
6.65 Temperature profiles. Left: -0.8. Right: -1.8 m. 166
6.66 Temperature profiles. Left: $x = 0.07$ m. Right: $x = 0.14$ m. 166

6.67 Temperature field as a function of a_d. Left: $a_d = 0.00$ m. Middle: $a_d = 0.05$ m. Right: $a_d = 0.075$ m. 167
6.68 Velocity profiles at $y = -0.4$ m, -0.8 m, -0.9 m, and -1.8 m. . . 168
6.69 Velocity profiles at $x = 0.07$ m and 0.14 m. 168
6.70 Velocity field as a function of a_d. Left: $a_d = 0.00$ m. Middle: $a_d = 0.05$ m. Right: $a_d = 0.075$ m. 169
6.71 Magnetic field as a function of electric current. Left: $I = 12.5$ A. Middle: $I = 25.0$ A. Right: $I = 50.0$ A. 171
6.72 Temperature profiles. Top left: -0.4 m. Top right: -0.8 m. Bottom left: -0.9 m. Bottom right: -1.8 m. 172
6.73 Temperature profiles. Left: $x = 0.07$ m. Right: $x = 0.14$ m. 172
6.74 Temperature field electric current. Left: $I = 12.5$ A. Middle: $I = 25.0$ A. Right: $I = 50.0$ A. 173
6.75 Velocity profiles. Top left: -0.4 m. Top right: -0.8 m. Bottom left: -0.9 m. Bottom right: -1.8 m. 174
6.76 Velocity profiles. Left: $x = 0.07$ m. Right: $x = 0.14$ m. 174
6.77 Velocity field as a function of electric current. Left: $I = 12.5$ A. Middle: $I = 25.0$ A. Right: $I = 50.0$ A. 175
6.78 Magnetic field as a function of N_N. Left: $N_N = 20$. Middle: $N_N = 25$. Right: $N_N = 30$. 177
6.79 Temperature profiles. Top left: -0.4 m. Top right: -0.8 m. Bottom left: -0.9 m. Bottom right: -1.8 m. 178
6.80 Temperature profiles. Left: $x = 0.07$ m. Right: $x = 0.14$ m. 178
6.81 Temperature field as a function of N_N. Left: $N_N = 20$. Middle: $N_N = 25$. Right: $N_N = 30$. 179
6.82 Velocity profiles. Top left: -0.4 m. Top right: -0.8 m. Bottom left: -0.9 m. Bottom right: -1.8 m. 180
6.83 Velocity profiles. Left: $x = 0.07$ m. Right: $x = 0.14$ m. 180
6.84 Velocity field as a function of N_N. Left: $N_N = 20$. Middle: $N_N = 25$. Right: $N_N = 30$. 181
6.85 Magnetic field as a function of N_M. Left: $N_M = 9$. Middle: $N_M = 10$. Right: $N_M = 11$. 183
6.86 Temperature profiles. Top left: -0.4 m. Top right: -0.8 m. Bottom left: -0.9 m. Bottom right: -1.8 m. 184
6.87 Temperature profiles. Left: $x = 0.07$ m. Right: $x = 0.14$ m. 184
6.88 Temperature field as a function of N_M. Left: $N_M = 9$. Middle: $N_M = 10$. Right: $N_M = 11$. 185
6.89 Velocity profiles. Top left: -0.4 m. Top right: -0.8 m. Bottom left: -0.9 m. Bottom right: -1.8 m. 186
6.90 Velocity profiles. Left: $x = 0.07$ m. Right: $x = 0.14$ m. 186
6.91 Velocity field as a function of N_M. Left: $N_M = 9$. Middle: $N_M = 10$. Right: $N_M = 11$. 187
6.92 Temperature fields. Left: vertical cross-sections of the temperature field. Right: horizontal cross-sections of the temperature field. . . 189
6.93 Velocity fields. Left: vertical cross-sections of the velocity field. Right: horizontal cross-sections of the velocity field. 189

6.94 Liquid fraction. Left: vertical cross-sections of the liquid fraction. Right: horizontal cross-sections of the liquid fraction. 190
6.95 Concentration fields. Left: vertical cross-sections of the concentration fields. Right: horizontal cross-sections of the concentration fields. 190
6.96 Streamlines. Left: without magnetic field. Right: with magnetic field. 192
6.97 Temperature field. Left: without magnetic field. Right: with magnetic field. 193
6.98 Velocity field. Left: without magnetic field. Right: with magnetic field. 194
6.99 Concentration field. Left: without magnetic field. Right: with magnetic field. 195
6.100Heat flux. 196

A.1 Classification of turbulence modelling. 209

D.1 Temperature field at different EM field magnitudes. I: $B_x = 2.6 \cdot 10^{-3}$ T. II: $B_x = 2.6 \cdot 10^{-2}$ T. III: $B_x = 2.6 \cdot 10^{-1}$ T. IV: $B_x = 2.6$ T. 218
D.2 Velocity field at different EM field magnitudes. I: $B_x = 2.6 \cdot 10^{-3}$ T. II: $B_x = 2.6 \cdot 10^{-2}$ T. III: $B_x = 2.6 \cdot 10^{-1}$ T. IV: $B_x = 2.6$ T. . 219
D.3 Temperature field at different EM field positions. I: $l_{mEM} = -0.6$ m. II: $l_{mEM} = -0.7$ m. III: $l_{mEM} = -0.8$ m. IV: $l_{mEM} = -0.9$ m. 220
D.4 Velocity field at different EM field positions. I: $l_{mEM} = -0.6$ m. II: $l_{mEM} = -0.7$ m. III: $l_{mEM} = -0.8$ m. IV: $l_{mEM} = -0.9$ m. . . 221
D.5 Temperature field at different EM field ranges. I: $-0.8\text{ m} < l_{EM} < -1.0$ m. II: $-0.8\text{ m} < l_{EM} < -0.95$ m. III: $-0.8\text{ m} < l_{mEM} < -0.9$ m. IV: $-0.8\text{ m} < l_{mEM} < -0.85$ m. 222
D.6 Velocity field at different EM field ranges. I: $-0.8\text{ m} < l_{EM} < -1.0$ m. II: $-0.8\text{ m} < l_{EM} < -0.95$ m. III: $-0.8\text{ m} < l_{mEM} < -0.9$ m. IV: $-0.8\text{ m} < l_{mEM} < -0.85$ m. 223

List of Tables

4.1 Terms in general transport equation. 57

5.1 Minimum and maximum velocities along the horizontal line (y'=0.5) and the vertical line (x'=0.5) that pass through the geometric center of the cavity. 77
5.2 Iteration times with the values of minimum velocities in the x and y direction for different values of β. 79
5.3 Case 1. Comparison of LRBFCM predictions with previous solutions for Pr=0.71 and various Ra numbers. 83
5.4 Case 2. Comparison of present predictions with previous works in terms of Nu for Pr=0.71 and various Ha and Gr numbers. 84
5.5 Case 3. Tabulated dimensionless velocities for Gr = 10^6, Ha = 0 and 50, obtained with LRBFCM. 88
5.6 Comparison of extreme velocity values at the outlet for Re = 800 and Ha = 0 for 201x51, 301x101, 401x151, and 501x201 node arrangements. 99
5.7 Extreme velocity values for the outlet velocity profiles for Re 300 to 800 (step 100) and Ha = 0. 100
5.8 Reattachment positions for Ha = 0 and various Re numbers. . . . 102
5.9 Extreme values of v'_x and v'_y for 301x101 node arrangement, Re = 300, and Ha = 0, 5, 10, 50, and 100. 103
5.10 Extreme values of v'_x and v'_y for 301x101 node arrangement, Re = 600, and Ha = 0, 5, 10, 50, and 100. 106
5.11 Extreme values of v'_x and v'_y for 301x101 node arrangement, Re = 800, and Ha = 0, 5, 10, 50, and 100. 106
5.12 Reattachment positions for various Re and Ha numbers. 109

6.1 Geometry parameters of the simplified CC process. 113
6.2 Parameters for magnetic field. 126
6.3 Thermophysical properties of steel used in the computation. . . . 133
6.4 Overview of calculated examples. 197

1 Introduction

Steel is a material, that, since the iron age, presents a key driver to the world's economy. It presents one of the major components in construction (bridges, buildings), power, transport (infrastructure), automotive (cars, planes, ships), health and machine goods industries. It is found in products that vary from appliances, tools, computers, steel cans, and weapons, to surgical and safety equipment. As the demand for such products increases so does the production of steel. The amount of crude steel produced has risen from 28.3 million tons in 1900 to 848.9 million tons in 2000 [WSA, 2013]. The growth of production has been especially quick in the past decade as the quantity of product has nearly doubled in the past dozen years (848.9 Mt in 2000, 1511 Mt in 2012 [WSA, 2013]). Steel is also a material that can easily be recycled and thus presents another advantage especially in recent years when the ecological awareness is gaining importance.

The most efficient process to solidify molten metal into solid semi-finished products is the Continuous Casting (CC) process. Currently, over 95% [WSA, 2013] of all steel grades are obtained with this technique. The process enables mass production of a high quality material at low cost and energy consumption. The growth of steel production and the amount of steel produced by the continuous casting process is presented in Fig. 1.1. To further improve the process, a magnetic field is applied during the phase of solidification. It serves to refine the grain structure and to reduce the amount of impurities as well as the amount of trapped gas bubbles in the metal.

Very high temperatures ($\sim 1500°C$) of liquid steel and inaccessibility of the mold region during the casting process make the measurements of the temperature and the velocity fields inside the mould extremely difficult. In order to better understand the behaviour of the melt and to further optimize the influence of magnetic field in the CC process of steel, a mathematical model has been devised in the present dissertation. The model enables us to consider the changes in geometry of the casting machine, various physical phenomena and process parameters at low cost and reasonable time efficiency. Due to the complexity of the geometry and physics, and due to the presence of the moving and deforming boundaries, a novel Local Radial Basis Function Collocation Method (LRBFCM) [Šarler and Vertnik, 2006], is used to solve the mathematical model. The LRBFCM performs well in complicated geometries as it eliminates the problem of mesh generation. To ensure the confident usage of the developed computational models, a rigours validation against measurements or benchmark test cases is required. In this dissertation, the designed computational model and the chosen numerical method are assessed against the results obtained with Computational Fluid Dynamics

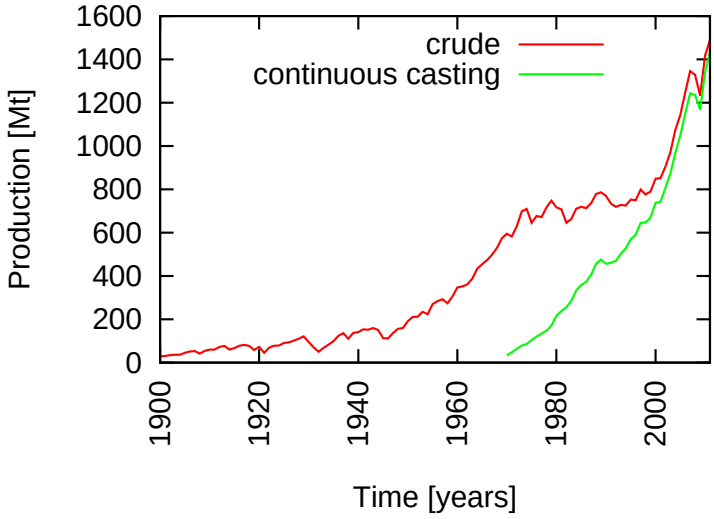

Figure 1.1: The amount of produced crude steel since 1900 and the amount of continuously cast steel. Data from [WSA, 2013].

(CFD) software Fluent [ANSYS, 2013] for four benchmark test cases: the lid driven cavity, the free convection in a rectangular cavity under the influence of magnetic field, the Hartman flow, and the free convection in a backward facing step under the influence of magnetic field, and for CC process model.

1.1 Continuous Casting of Steel

CC [Irving, 1993] is the most common process [WSA, 2013] and the most effective technique to produce steel. Among different types of CC units such as vertical, vertical with bending, radial, curved, etc. [Pass, 2013] (Fig. 1.2), a curved CC device, depicted in the Fig. 1.3, is considered in present computational model.

In the CC process (Fig. 1.3), the molten metal is transformed into simple semi-finished solid shapes such as slabs, billets and blooms for subsequent processing. The process begins by pouring the molten steel from a ladle into a tundish, which holds enough material for the flow to be continuous even when the ladle is exchanged. The liquid steel than flows from the tundish through a Submerged Entry Nozzle (SEN) into a copper mould. The walls of the mould are cooled with water and the outer layers of steel solidify. The solid shell, when thick enough, acts as a container for liquid steel. It is continuously withdrawn from the bottom of the mould. The material is transferred from the vertical to the horizontal position by the support rollers and is further cooled by water sprays, radiation, natural convection and heat transfer from the material to the support rolls. The solidified shell grows in thickness throughout the cooling process until the whole strand is solidified, which happens at the metallurgical length. The process is fully continuous as the material is transferred from the vertical to the horizontal position without the need to stop the caster.

The completely solidified strand is cut either into slabs, billets or blooms (Fig 1.4). These semi-finished materials differ from one to another in the shape of the

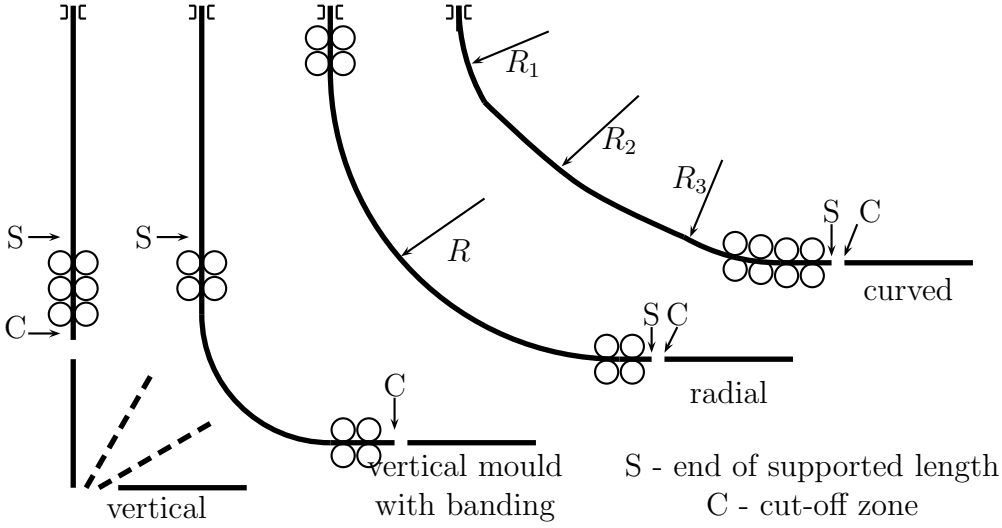

Figure 1.2: Types of CC of steel devices. R_1, R_2, R_3, and R stand for casting device radius. Figure based on [Pass, 2013]

strand cross section [OutoKumpu, 2013]. Slabs are rectangular, with a width up to 3 m, a height up to 32 cm and length up to 15 m. The cross-section of billets is either circular or square, with typical dimension up to 50 cm and length up to 12 m. The blooms have rectangular shape with width and height up to 50 cm and length up to 12 m.

A tundish is a tank that contains the supply of steel which is then poured through a nozzle into the CC mould [Thomas, 2001]. The tundish is repeatedly fed from the ladle to ensure that the flow to the mould is continuous. The speed of the molten steel flow through the nozzle is controlled with a stopper rod.

The mould (Fig. 1.5) is the most important part of the casting machine as the most crucial physical phenomena occur here. The molten steel enters the mould at high velocities through the nozzle ports. The high velocities cause the turbulent flow behaviour. The turbulent jet thus formed, proceeds across the mould towards the solidifying shell, where it impinges against its walls. The jet, carrying the superheated material, erodes the solidifying shell and can cause a breakout if it hits the shell at its weaker regions. Typically, two recirculation zones are formed as the flow is further separated by the jet. Consequently, the flow moves in two directions: upwards toward the top surface and downwards toward the interior of the strand. The recirculating zones influence the motion of the inclusion particles and bubbles, as well as the entrapment of the liquid flux into the steel.

A mould powder is added to the top free surface to prevent chemical reactions between the steel surface and the surrounding area. The mould powder also provides effective thermal insulation. The high temperature of the steel melts the powder into a liquid flux, which floats on the top surface of the molten steel. The part of the liquid flux that comes into contact with the cold mould walls re-solidifies and forms a solid flux rim, which restricts the heat transfer at the

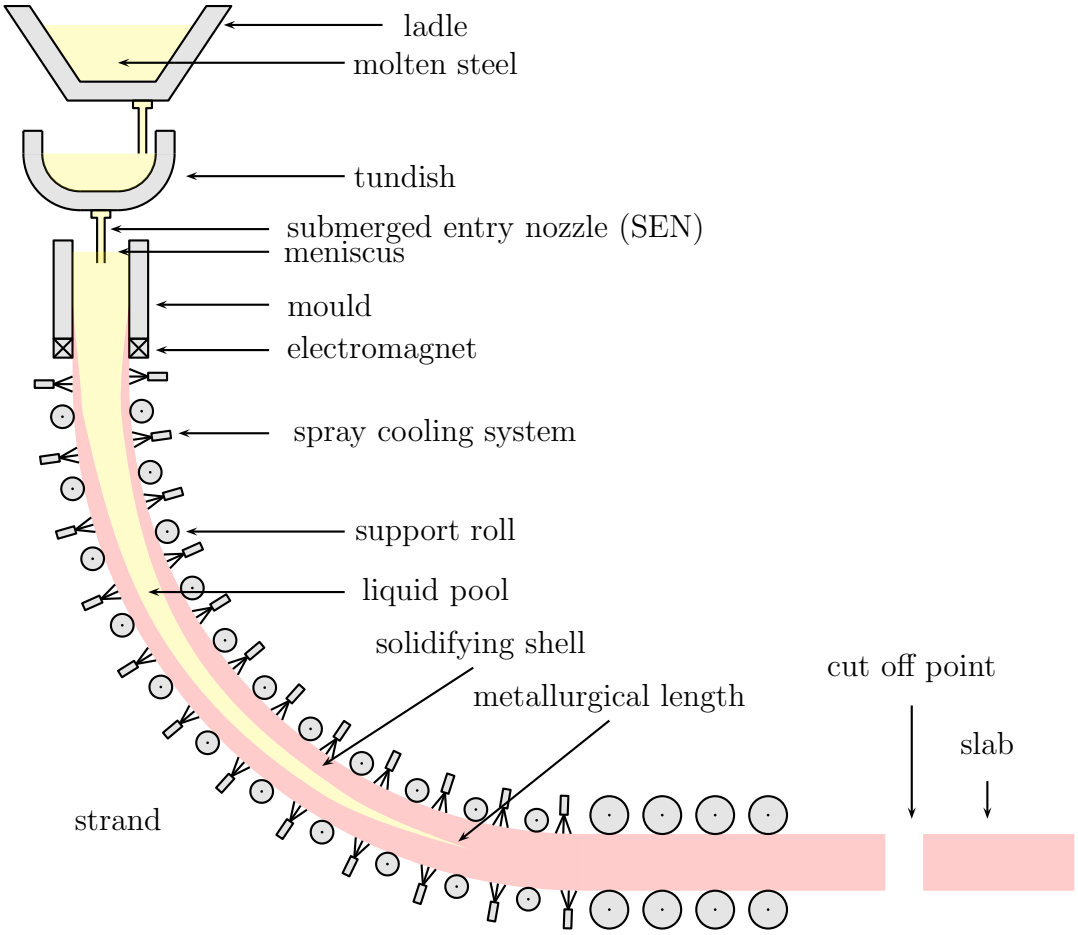

Figure 1.3: A scheme of the curved CC process.

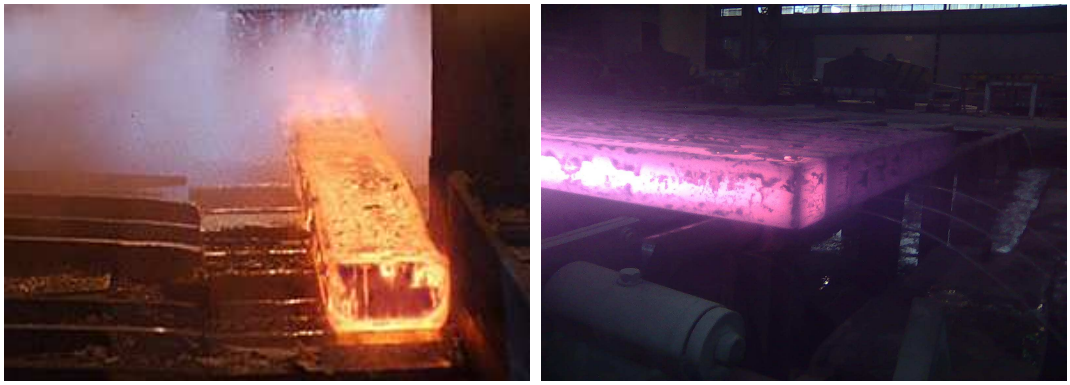

Figure 1.4: Semi-finished steel products. Left: blooms (courtesy of Accolade Photography [Accolade-Photography, 2013]). Right: billets (courtesy of Štore Steel d.o.o. [Štore Steel, d. o. o., 2013]).

meniscus. The rest of the liquid flux is absorbed into the gap between the mould wall and the solidified strand. Here it supports the uniform heat transfer and together with the periodic oscillating motion of the mould, prevents the material from sticking to the mould walls. As a result of the mould oscillation, the so

called oscillation marks are created. These periodic indentations affect the heat transfer and can cause the material to crack.

The liquid flow along the top surface of the mould is an important parameter that can greatly influence the quality of the steel. If the horizontal velocity along the interface is too low, it can generate inadequate liquid flux coverage which leads to various surface defects. On the other hand, when the horizontal surface velocity is too large, the shear flow and the vortices that may occur as a consequence, may entrain the flow into the liquid steel. The entrapped liquid then moves along with the steel flow, and can later, assuming that it is captured in the solid shell, cause problems in the final product. The liquid flux layer tends to be thinner at the places where the vertical jet impinges the top free surface. The time variations that are caused by the transient fluctuations in the flow can at the detrimental spots result in mould powder entrapment. The impurities that enter the steel flow through the SEN exit present another problem. These impurities consist of particles of various shapes and sizes. They either move with the fluid flow up towards the surface or become entrapped inside the solidifying shell. When the later happens, the impurities can form defects in the final product.

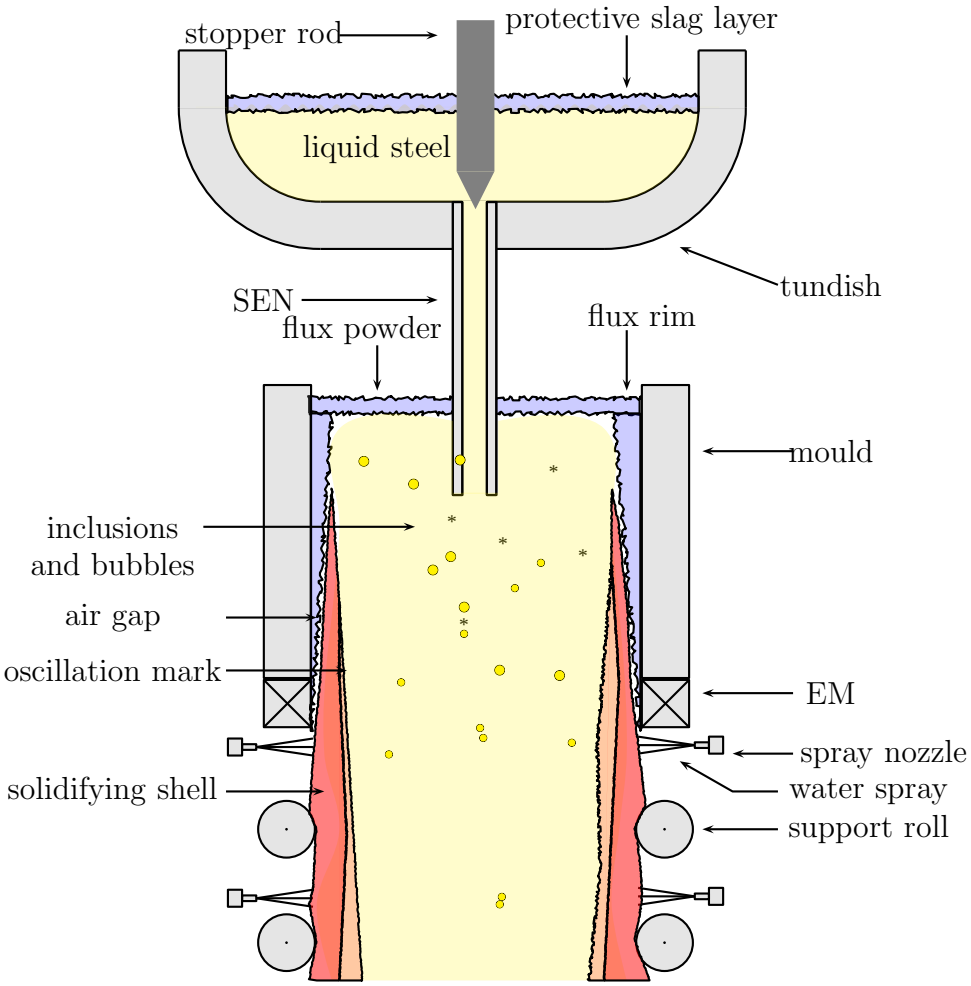

Figure 1.5: A detail of tundish and mould.

Variations in the composition during the solidification, called macrosegrega-

tion, are one of the major reasons for internal defects. This phenomenon occurs in the mushy solidification zone and can range in scale from a couple of millimetres to several meters. It is caused by forced, natural and solute convection and refers to a transport of the liquid and the solid phases on a scale much larger than a dendrite arm. The variation of composition within the dendrite structure, especially the redistribution of the solute during solidification on micro level, is called microsegregation. It occurs, because the solubility of the alloying elements is different in the solid and the liquid phases [Dantzig and Rappaz, 2009]. Usually, the solute has a higher solubility in the liquid phase than in the solid phase. The solute is therefore repelled back into the liquid phase, where consequently the concentration of the solute increases. The continuous growth of the solid phase leads to higher concentrations of the solute in the liquid steel and depleted concentrations of the solute in the solidified steel. The respective macrosegregation, results in non-uniform mechanical properties of the cast products. To further improve the CC process of steel and to avoid defects in the final product, Electromagnetic (EM) field is introduced to the process.

1.2 Magnetohydrodynamic Processes in Continuous Casting of Steel

Although the CC process of steel is cost efficient, with high yield and productivity, as well as good quality of the material, the process is further optimized by introducing the EM field. The EM field affects the turbulent flow field, the heat transfer and the solidification. The outcome of the EM field is the EM force, which causes the stirring of the molten steel flow or the breaking of the ensuing solid structure. By varying the EM field, and consequently the EM force, the amount of defects in the material is reduced. The EM field is usually applied in the mould, where the solidification takes place. This is the most critical area of the process, since the liquid and the solid coexist together and can be easily influenced by the magnetic field. In general, the methods of applying the EM field to the CC process are divided into two major groups [ABB, 2013; Cukierski and Thomas, 2008]: Electromagnetic Stirrers (EMS) and Electromagnetic Brakers (EMBR) as the EM field either stirs or brakes the flow.

Electromagnetic Stirrers

The EMS systems utilize the Alternating Current (AC) to generate a continuously changing EM field [Cukierski and Thomas, 2008]. The EMS systems can be divided by the position of their placement into three categories: the Mould Electromagnetic Stirrers (MEMS), the Strand Electromagnetic Stirrers (SEMS), and the Final Electromagnetic Stirrers (FEMS) (Fig. 1.6).

The MEMS is placed, as its' name suggests, in the mould. In general there are two types of MEMS: the Slab Mould Electromagnetic Stirrers (SMEMS) and the Multi-Mode Electromagnetic Stirrers (MMEMS). The SMEMS employ two magnets on each side of the mould near the meniscus in order to activate and

uphold the circulation of the flow around the mould perimeter. The circulation of the flow homogenizes temperature in the meniscus and thus improves the quality of the finished slab. The MMEMS use two stirrers placed near the SEN outlets. This EMS system has three modes of operation: the Electromagnetic Level Stabilizer (EMLS), the Electromagnetic Level Accelerator (EMLA), and the Electromagnetic Rotary Stirrer (EMRS). The low frequency alternating magnetic field is applied in the case of the EMLS mode [Kubo et al., 2004]. It has been developed to stabilize the molten steel flow as the velocity at the surface is reduced and the meniscus profile is flattened due to the flow opposing forces. The direction of the flow is strongly dependent on the intensity of the imposed field. If the enforced magnetic field is strong, the current flows towards the mould walls, whereas if the enforced magnetic field is weak, the current flows towards the nozzle. The EMLA mode [Kubo et al., 2007] employs the alternating magnetic field with a low frequency, which stimulates the flow to move from the nozzle to the side of the mould. The purpose of this type of the EMS is to accelerate the molten steel flow, particularly when the mould is wide or the casting speed is low. The EMRS mode [Pardeshi et al., 2008] employs the rotating magnetic field, which generates a swirling flow. The swirling flow encourages mixing and the liquid phase consequently becomes more homogeneous. The benefits of the MEMS are increased equiaxed zone, equalized crust, and reduced air holes, pinholes, and inclusions in the surface and the subsurface [Kemeida Electric Co., 2013].

The SEMS is placed in the strand. A high placement on the strand reduces the possibility of the brake-outs whereas a lower placement improves the V segregation [Ergolines, 2013]. The SEMS changes the initial coarse columnar grains to a more fine grained structure, which means that the centreline segregation, the center porosity and the internal cracks are reduced [ABB, 2013], and the equiaxed zone is increased [Kemeida Electric Co., 2013].

The FEMS employs a rotating magnetic field and is placed at the end of the strand, just before the metallurgical length. It is usually employed in billet and bloom casting. The metallurgical effects of the FEMS are the reduced central segregation, central porosity and shrinkage, as well as refinement of the equiaxed zone [Kemeida Electric Co., 2013].

Electromagnetic Brakers

The EMBR systems employ coils to generate the Direct Current (DC). Thus generated static magnetic field can be effectively used to control the liquid steel flow and to slow down the mainstream flow. The EMBR ensures uniform temperature and casting speed over the entire strand width [ABB, 2013]. The most common configurations of the EMBR are the conventional or level EMBR, the EMBR ruler and the Flow Control Mould (FCM) (Fig. 1.7) [ABB, 2013; Cukierski and Thomas, 2008; Timmel et al., 2010].

The level EMBR consists of two thin magnets placed on the opposite sides of the mould that act locally across the strand width and create finite, rectangular regions of transverse EM field below the SEN ports. This arrangement is used to stabilize the jet exiting the nozzle ports in order to decrease the velocity in the meniscus and the fluctuations in the meniscus profile.

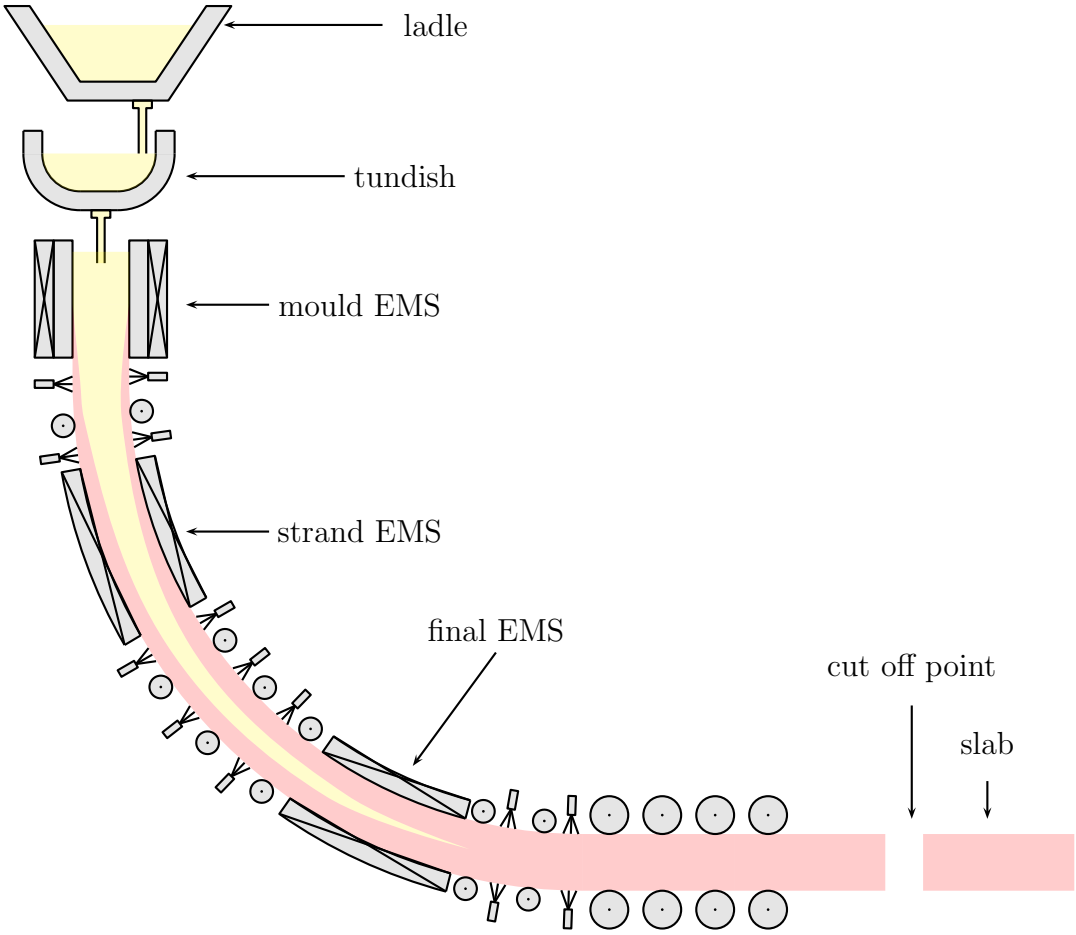

Figure 1.6: Types of EMS configurations.

The EMBR ruler uses two magnets on the opposite sides of the mould that span the entire width of the mould and create one magnetic field just below the SEN ports. As in the case of the conventional EMBR, the aim of this configuration is to slow, diffuse and suppress the penetration depth of the jet exiting the SEN ports and to stabilize the meniscus velocity and the fluctuations of the profile.

The FCM configuration consists of two parallel magnets that span the entire width of the mould [ABB, 2013]. The magnetic fields thus created affect the flow in the meniscus and below the SEN ports. The purpose of this system is to control the fluid flow exiting the nozzle as well as at the meniscus. The FCM configuration is most commonly applied to decrease the overall velocities in the mould.

1.2.1 Literature Review of Electromagnetic Field Modelling

The EM field affects turbulent flow, as well as the heat transfer and the solidification and therefore has to be carefully considered when constructing a mathematical model. In the mathematical model, Maxwell equations that describe EM

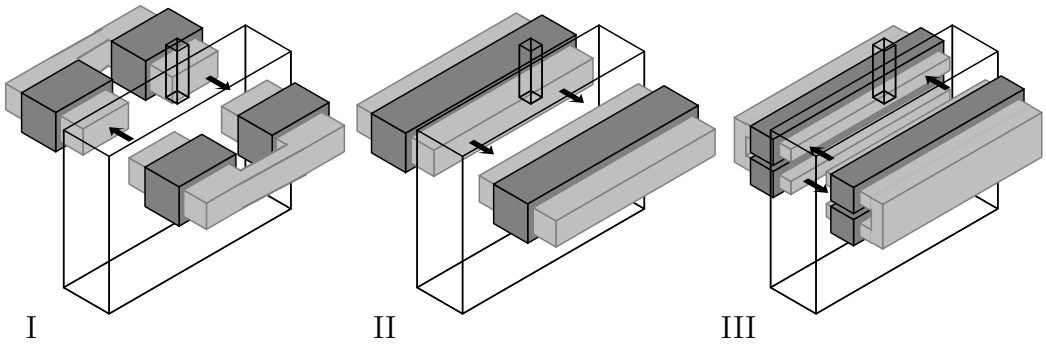

Figure 1.7: Types of the EMBR configurations (Figure based on [ABB, 2013]). I. Conventional EMBR, II. EMBR ruler, III. FCM.

field are coupled with the conservation equations of mass, momentum, energy, turbulent kinetic energy and dissipation rate for the fluid flow. The attempts that have been made to describe the fluid flow influenced by the magnetic field are listed below in a chronological order.

The research in the EMS in CC began as early as 1983, when Birat and Chone [Birat and Chone, 1982] provided the initial guidelines for tailoring the stirring systems by stating that the EMS reduces the centreline macrosegregation.

In 1986, Spitzer and co-workers [Spitzer et al., 1986] calculated the 3D flow field with a rotational EMS of round steel strands and examined the influence of the stirrer position, the stirring length and the EM parameters on the flow field. In their model, Maxwell equations were coupled with Navier-Stokes equations and k-ε turbulence model. Davidson and Boysan [Davidson and Boysan, 1987] considered the EMRS flow and gave a review on the One Dimensional (1D) models of stirring in which the axial variation in stirring force is ignored. They considered the secondary flow, which sweeps the momentum into the unforced region, where it diffuses and dissipates the angular momentum.

In 1989, Ilegbusi and Szekely [Ilegbusi and Szekely, 1989] modelled fluid flow in a Newtonian and a non-Newtonian system subjected to the rotational EMS. In their model the k-ε turbulence model was used to model the effective viscosity in Newtonian fluids and the constitutive relations were used to connect the shear stress to the rate of the strain in the non-Newtonian fluids.

In 1992, Yao [Yao et al., 1992] performed a first computational study of a Three Dimensional (3D) EMBR system.

In 1994, Takeuchi and co-workers [Takeuchi et al., 1994] presented flow control techniques of the EMBR and the EMS in Nippon Steel and explained the interference between the fluid flow and the EM field. Choudhary and Mazumdar [Choudhary and Mazumdar, 1994] developed a Two Dimensional (2D) mathematical model of CC of steel. The Partial Differential Equations (PDE) with appropriate boundary conditions were solved with a control volume based Finite Difference Method (FDM) by incorporating a Semi-Implicit Method for Pressure Linked Equations (SIMPLE) [Patankar and Spalding, 1972] algorithm.

In 1996, Gardin with his associates [Gardin et al., 1996], studied the influence of the EMBR on liquid steel flow in a curved CC process and discovered that the brake suppresses the movement of the fluid and decreases the enthalpy exchange between the various fluid layers. Ishii and his colleagues [Ishii et al., 1996] numerically studied the AC magnetic field and found that this kind of magnetic field suppresses the velocity of the molten steel below the meniscus. It was demonstrated that the flexibility and effectiveness of the EMLS are better than those of the EMBR.

In 1997, Hwang and co-workers [Hwang et al., 1997] modeled the influence of the EMBR on the fluid flow, the induced current, the argon gas fraction in the molten steel flow, and the meniscus shape. To numerically solve the mathematical model, the Finite Volume Method (FVM) was used.

In 1998, Yang and co-workers [Yang et al., 1998] developed a 3D model to describe the fluid flow, the solute redistribution, the heat transfer and the solidification in the CC process, in which the blockage of fluid flow by the columnar dendrites in the mushy zone, the change in liquidus temperature with liquid concentration and the double diffusive convection are considered. The same year, Harada [Harada et al., 1998] developed a novel application of the EM, where two steels with different chemical compositions are poured into the mould through two nozzles with different submergences.

The following year, El-Kaddah and Natarajan [El-Kaddah and Natarajan, 1999] examined the effect of the frequency and current of the stirrer on the fluid flow in a horizontal EMS arrangement. The devised 3D model shows that the frequency and the current of the stirrer affect the primary horizontal flow in the EMS range and the upward flow in the region above the EMS.

In 2000, Li and associates [Li et al., 2000] reported that the application of a static EM field can significantly suppress the buoyancy. The k-ε model was used to describe the turbulent flow and the EM force was incorporated in the Navier-Stokes equations to account for the effect of the FCM. Kim and co-workers [Kim et al., 2000] investigated the effect of the EMBR on the turbulent melt flow, the temperature fields, and the macroscopic segregation by incorporating a low-Reynolds k-ε turbulence model to account for the the turbulence effects, and employing the enthalpy porosity relation to suppress the velocity in the mushy region. They found that the temperature in the free-surface region and the temperature gradients near the solidifying shell were increased and that the transfer of superheat to the narrow face was decreased.

In 2002, Trindade and co-workers [Trindade et al., 2002] introduced a Finite Element Method (FEM) based method to simulate the EMRS.

In the following year, Ha and his associates [Ha et al., 2003] simulated the 3D flow, the heat transfer, and the solidification of steel in the CC process with the EMBR and found out, that the EMBR effectively damps and controls the local flows.

In 2004, Kubo and colleagues [Kubo et al., 2004] used a 2D model to simulate the EMLS to evaluate the surface velocity and its connection to the entrapment of surface powder and to track the argon gas bubbles injected through the SEN. The same year, Natarajan and El-Kaddah [Natarajan and El-Kaddah, 2004] used

the segregated FEM to simulate the sub-mould EM stirring in CC of steel. They have shown, that the EM force generates a strong rotational flow within the stirrer and a strong secondary flow beyond the stirrer, which promotes mixing past the area of stirrers. They concluded that the frequency of the applied magnetic field controls the range of stirring. Wang and co-workers [Wang et al., 2004], calculated the influence of the EMBR in the CC of steel with the FDM and the SIMPLER (SIMPLE Revised) [Patankar, 1980] algorithm. They proposed a staggered grid arrangement to discretisize the governing equations for the fluid flow and the EM field and confirmed that the EMBR reduces the flow velocities, relives the shear stress at the mould face and represses the fluctuations on the free surface.

In 2006, Li and co-workers [Li et al., 2006] determined the optimal position of the FEMS, by calculating the thickness of the solidifying shell in a bloom. They concluded that the inner porosity and composition of the segregation can be influenced with the EMS.

In 2007, Kubo with his associates [Kubo et al., 2007], carried out a simulation to investigate the effect of the EMLA on the molten steel flow and measured the velocities of the steel flow. It was discovered that the EMLA reduces the number of inclusions in the solidifying shell and decreases the temperature drop at the meniscus. Na and co-workers [Na et al., 2007] investigated the deformation of initial shell in CC mould under the influence of a high frequency EM field using a numerical model. The results showed, that the thickness of the initial solidification shell, the temperature of strand surface and the temperature of the copper mould increase, whereas the viscosity decreases, because of the internal heating.

In 2008, Cukierski and Thomas [Cukierski and Thomas, 2008] used a 3D steady state, k-ε model of fluid flow under the influence of the local EMBR to investigate the influence of the EMBR on the SEN submergence depth. Haiqi and associates [Haiqi et al., 2008] used a 3D FVM to investigate the metallurgical effects of the EMBR. The results of the numerical simulation confirmed that the EMBR can effectively control the molten steel flow. Javurek and his co-workers [Javurek et al., 2008] modelled the MEMS and confirmed that the rotary effect of the MEMS impacts the number of inclusions in the steel, decreases the size of the dendritic structures and increases the number of the equiaxed grains.

In 2010, Timmel and colleagues [Timmel et al., 2010], investigated the flow structures under the influence of a DC magnetic field. The experiments, performed for this purpose in a cold metal laboratory, provide a substantial database for the validation of the numerical results.

The next year, Chaudhary and co-workers [Chaudhary et al., 2011] investigated both the transient and the turbulent features of the fluid flow by combining two steady Reynolds-Averaged Navier-Stokes (RANS) models, a filtered unsteady RANS model and two Large Eddy Simulation (LES) models with the Ultrasonic Doppler Velocimetry (UDV) measurements.

In 2012, Chaudhary and his associates [Chaudhary et al., 2012] applied LES for different configurations of the EMBR ruler applied to the transient turbulent flow. Miao and colleagues [Miao et al., 2012], performed numerical and experimental investigation of fluid flow in the CC mould under the effect of the EMBR.

In order to numerically model the turbulence, the RANS Shear Stress transport (RANS-SST) turbulence model was used. Liu and co-workers [Liu et al., 2012] calculated a 3D model of the EM flow in a round bloom mould under the influence of a low frequency in-mould EMRS.

In 2013, Zhu and colleagues [Zhu et al., 2013] investigated the effect of EMBR and argon gas blowing on the CC process and clarified the relationship between wavy fluctuation height near meniscus and the situation of mould flux entrapment. Ji and co-workers [Ji et al., 2013] used LES to simulate the turbulent flow in a liquid metal model of CC and compared the results with measurements using UDV.

In 2014, Schwarz and Fröhlich [Schwarz and Fröhlich, 2014] performed a simulation of the rise of a bubble in liquid metal with and without magnetic field. Their results showed that the vorticity is significantly damped in the bubble wake.

1.3 Meshless Numerical Methods

Various numerical methods can be used to numerically evaluate a mathematical model. At the moment, the most widely used among them are the FDM [Özişik, 1994], the FEM [Zienkiewicz and Taylor, 1977], the FVM [Versteeg and Malalasekera, 2007], and the Boundary Element Method (BEM) [Hall, 1994]. In case of the CC of steel, the geometry is complex and the problem requires moving and/or deforming boundaries, which can present substantial difficulties for the above mentioned methods. To circumvent the problem of mesh generation, a meshless numerical method, which performs well in complicated geometries, is used and further developed in the present dissertation.

A variety of different meshless methods [Liu, 2010] have been developed in recent years to avoid the problem of polygonisation. Among the most common ones are the Meshless Local Petrov-Galerkin Method (MLPGM) [Atluri and Zhu, 1998], the point interpolation method [Liu and Gu, 2001], the element free Galerkin method [Belytschko et al., 1994], the point assembly method [Liu, 1998], the smoothed particle hydrodynamics [Gingold and Monaghan, 1977; Liu and Liu, 2003], the discrete least square meshless method [Arzani and Afshar, 2006], the Method of Fundamental Solutions (MFS) [Kołodziej, 2001; Golberg and Chen, 1998; Fairweather and Karageorghis, 1998], the Smoothed Point Interpolation Method (SPIM) [Liu and Zhang, 2008], the Meshfree Local Radial Point Interpolation Method (MLRPIM) [Liu et al., 2002], the Radial Basis Function Collocation Method (RBFCM) [Kansa, 1990a,b], LRBFCM [Šarler and Vertnik, 2006], and others. Although each of these methods has advantages for a specific class of problems, the easiest to implement seem to be the methods based on the Radial Basis Functions (RBFs) [Buhmann, 2000] collocation.

1.3.1 Radial Basis Function Collocation Method

The RBF collocation method or Kansa method was developed in 1991 [Kansa, 1990a,b]. In his method a given problem is solved by constructing a global approximation by a set of global approximation functions, most often Multiquadric

(MQ) RBFs. The application of the method to the PDEs leads to a formation of a global stiff dense matrix. The recently developed alternative, which uses the approximation that is constructed locally on a smaller sub-domain, uses local approximation. In highly demanding and complex problems with a huge amount of nodes, the solution of the sparse matrix is simpler and faster than the solution of the global matrix. The accuracy of both methods is similar [Lee et al., 2003], however, the local version is more robust in terms of choosing the RBF shape and the node distribution.

The global RBFM, has been applied to a great variety of problems, including the heat transport [Zerroukat et al., 1998], diffusion [Zerroukat et al., 2000], advection-diffusion, natural convection [Šarler et al., 2001], solid-liquid phase change [Kovacevic et al., 2003] and electromagnetic field [Young et al., 2005].

Lately, the RBFs have been combined with several other numerical methods, such as the FVM based methods (the C^2-continuous control-volume technique [An-Vo et al., 2011a,b; Bustamante et al., 2011], and alternating direction implicit method [An-Vo et al., 2013]), FDM concepts [Wright and Fornberg, 2006; Bayona et al., 2010, 2011] and BEM formulations (e.g. the dual reciprocity method [Chen et al., 1999; Wrobel and Brebbia, 1987], method of fundamental solutions [Golberg and Chen, 1998; Johnston and Fairweather, 1984] and RBF boundary knot method [Hon and Chen, 2003]).

The method has been successfully applied to various scientific and engineering problems. The RBF method [Kansa, 1990a,b] was first used in 1991 to solve the fluid dynamics problems. The fluid flow problems were later expanded [Mai-Duy and Tran-Cong, 2001, 2002; Divo and Kassab, 2007; Mai-Duy et al., 2007b; Mai-Duy and Tanner, 2007; Zhang et al., 2006], and several other types of problems such as heat transport [Ho-Minh et al., 2009] and conduction [Ostrowski et al., 2008; Soleimani et al., 2010], convection [Stevens et al., 2009; Divo and Kassab, 2008] - diffusion problems [Fan et al., 2013; La Rocca et al., 2005], solid mechanics [Mai-Duy et al., 2007a] and electromagnetic problems [Zhang et al., 2007; Karimi and Babazadeh, 2005; Yang et al., 2009], have been tackled.

Literature Review of the Local Radial Basis Function Collocation Method

In this dissertation, the emphasis is on the in-house developed LRBFCM. A short, chronological review of the problems presently calculated with this method, is given below.

The meshfree LRBFCM was first developed for diffusion problem [Šarler and Vertnik, 2006] in 2006. The first application of the method was demonstrated for NAFEMS boundary value problem with the steady temperature field and the Dirichlet, Neumann and Robin boundary conditions on a rectangular cavity, and the initial value problem with the Dirichlet jump on a square cavity. In the same year the method was applied to the convective-diffusive solid-liquid phase change problems on a relatively simple 1D steady state class of problems with a uniform velocity field, and a simplified 2D steady state model of the Direct-Chill Casting (DCC) process [Vertnik and Šarler, 2006]. The solution of the DCC of aluminium alloys problem was subsequently extended for coping with simultaneously moving material and inter-phase boundaries [Vertnik et al., 2006].

A demonstration on how the LRBFCM was developed from the Global Radial Basis Function Collocation Method (GRBFCM) was given in 2007 [Šarler, 2007].

In 2008, several articles were published on the solution of coupled heat transfer and fluid flow problems. The method was tested on the classical 2D de Vahl Davis [de Vahl Davis, 1983] steady natural convection benchmark [Kosec and Šarler, 2008b,c]. The method was also verified on the Darcy porous media problem [Kosec and Šarler, 2008a]. In these tests, the Pressure-Velocity (PV) coupling is calculated iteratively, with entirely local pressure correction, which is predicted from the violation of the local continuity equation.

The following year, a solution of the incompressible turbulent flow [Vertnik and Šarler, 2009b] was presented in a channel and backward facing step problems. The turbulent flow equations were described by the low-Re (Reynolds number) k-ε model with Jones and Launder [Jones and Launder, 1972] closure coefficients, the PV coupling is calculated iteratively, with the Fractional Step Method (FSM) [Chorin, 1967], and the adaptive upwind technique [Lin and Atluri, 2000] is used due to the convection dominated situation. The same year, the LRBFCM was used to calculate the solution of the transient convective–diffusive heat transport in the CC of steel [Vertnik and Šarler, 2009a]. The solution was based on the mixture continuum model and the test case was solved in 2D. Next, the solution of phase change problems was demonstrated [Kosec and Šarler, 2009a,b, 2010] on the example of melting/freezing of a pure substance [Benard et al., 1986]. The numerical procedure is verified on the classical rectangular 2D cavity melting benchmark test [Gobin and Le Quere, 2000].

In 2010, a comparison between the GRBFCM and the LRBFCM on a 2D initial boundary value diffusion-reaction problem with the Dirichlet and Neumann boundary conditions [Yao et al., 2010], and a solution of multiscale solidification modelling of coupled heat, mass, momentum and species transfer problems on macroscopic level was presented along with the phase-field concepts of grain evolution [Šarler et al., 2010] .

In 2011, three different explicit meshless methods using the RBFs were compared [Yao et al., 2011]. Among the Local Method of Approximate Particular Solutions (LMAPS), the LRBFCM, and the Local Indirect Radial Basis Function Collocation Method (LIRBFCM), that were examined on the simple diffusion equation with a Dirichlet jump boundary condition. The LMAPS and the LDRBFCM perform better than the LIDRBFCM on a non-uniform node arrangement, whereas the results for all three methods are similar for uniform node arrangement. The same year, a 2D steady state solution of a coupled turbulent flow and heat transfer in the CC of steel billets in a curved mould geometry [Vertnik and Šarler, 2011] is solved with the LRBFCM. The turbulence is considered by the low-Re k-ε model and the solidification effects on the fluid flow in the mushy region are modelled through the Darcy assumption. The PV coupling is performed by the FSM method. The LRBFCM was later upgraded with the H-adaptive technique [Kosec and Šarler, 2011], which includes the refinement/derefinement of the node arrangement in vicinity of the reference node. The number of the nodes added or removed depends on the topology of the area around the reference node. The upgraded method was tested on the 2D Burgers' equation

[Burgers, 1948].

The same year, the simulation of the macrosegregation phenomena which occurred as a consequence of the solidification of a binary alloy [Kosec et al., 2011] was investigated. A binary Al 4.5% Cu alloy was tackled in a 2D rectangular cavity by incorporating the local PV coupling scheme. The properties of the phases were considered by applying the Lever solidification rule. The mushy zone was modelled by the Darcy law and the assumption of an incompressible Newtonian fluid was made for the liquid phase. Double diffusive effects in the melt were taken into account by incorporating the thermal and solutal Boussinesq hypothesis.

In 2012, the LRBFCM was tested on the 2D transient non-linear coupled Burgers' equations [Burgers, 1948] for large Re [ul Islam et al., 2012]. In the case of mixed boundary conditions, the application of the adaptive upwind technique [Atluri and Shen, 2002; Gu and Liu, 2006] is necessary for stabilization of the method.

In 2013, the LRBFCM method was assessed for hyperbolic partial differential equations [ul Islam et al., 2013]. 1D and 2D benchmark problems with the discontinuities, shock pattern and periodic initial conditions were calculated on a uniform node arrangement. An adaptive upwind technique was used for the stabilization of the method and the scaling technique was used to control the sensitivity of the shape parameter. At the same time, a solution of a low Prandtl number (Pr) natural convection benchmark [Kosec and Šarler, 2013] was calculated as a response to the Call for contributions to a numerical benchmark problem for a 2D columnar solidification of binary alloys [Bellet et al., 2009]. The performance of the method was tested on the natural convection in a rectangular enclosure filled with a low Pr fluid. It was shown that both cases considered, the one with the steady state and the other with the oscillatory solution, can be successively handled with this method.

In 2014, the LRBFCM was extended to the macrosegregation with macrosegregates in binary metallic casts [Kosec and Šarler, 2014]. At the same time, Vertnik and Šarler [Vertnik and Šarler, 2014] solved the recently proposed benchmark problem for CC of steel [Šarler et al., 2012].

1.4 Objectives of the Dissertation

1.4.1 Performed Work

Since 2006 developing meshless numerical method is upgraded to account for the effects of the externally applied EM field. This is achieved by inserting the Lorentz force term into the momentum equation. The EM (Lorentz) force is obtained by first solving the Poisson's equation for the electric potential, and then applying the Maxwell equations in order to get the current density. The simplified geometry of the mould and the SEN of the caster was considered as well as the process parameters such as the casting velocity, casting temperature, mould cooling, magnetic field strength, etc. The following quantities: temperature, velocity, turbulent kinetic energy, dissipation rate, species concentration,

and current density, were calculated as function of the process parameters. The upgraded method is tested first for a benchmark test case for a lid-driven cavity, then for a rectangular cavity in the presence of magnetic field and for a benchmark test for a rectangular cavity with in- and outflow. The method is also tested for the flow over a backward facing step. Finally, the CC problem is addressed with this method. A sensitivity analysis is performed in order to find out the optimal position at which the solenoid should be placed and the optimal magnitude of the magnetic field that should be applied to produce a steel of even better quality.

The research presented in the present work, has so far been published in the following scientific papers [Mramor et al., 2013a,b, 2014a,b] and was presented at the following conferences [Šarler et al., 2012; Mramor et al., 2012; Šarler et al., 2013].

1.4.2 Originality and Advantages

For the first time, the LRBFCM is used for solving the equations of the EM field in the CC process of steel. Further, the LRBFCM is applied for the first time to model the solidification under the influence of the externally applied magnetic field in the CC process of steel.

The use of LRBFCM for the solution of the velocity, temperature and EM fields, along with the species concentration has many advantages. The most notable are:

- There is no need for the domain or surface polygonisation as the mesh generation is not required. The approximation with RBFs is based on computational nodes, only. The calculations can be performed on non-equally distributed nodes that do not need to be geometrically connected, explicitly, mesh is not needed.

- There is no need for numerical integration, as the governing equations are solved in their strong formulation.

- As the value of the RBFs depends only on the distance between the central and (typically four) neighbouring nodes, the method is almost independent of the problem dimension; the same RBFs can be implemented to solve two, three or higher dimensional problems.

- The ability to solve complex problems due to the local nature of the method.

- The method is relatively simple and easy to program.

The contents of the dissertation are important from the scientific and technological points of view. The developments are foreseen to be applied among others, in modelling of the casting process in Štore Steel d.o.o. company.

1.5 Overview of the Dissertation

- In Chap. 2, the main physical phenomena in the CC process are introduced along with the mathematical background for the turbulent fluid flow, segregation and magnetohydrodynamics.
- The meshless numerical method is defined and presented in Chap. 3.
- In Chap. 4, the solution procedure is described in detail and explained.
- In Chap. 5, the numerical method is verified for various benchmark test cases. Among them are the lid driven cavity test, the convection in a cavity under the influence of a magnetic field test, the Hartman flow test, and the backward facing step under the influence of a magnetic field test.
- The simplified model of continuous casting process under the influence of externally applied static magnetic field is presented in Chap. 6. The first part of the chapter describes the computational model with the boundary and the initial conditions, and the computational domain, whereas the second part covers the results obtained for various layouts and the strength of the applied magnetic field, and for two carbon concentrations.
- Finally, Chap. 7 offers the summary of the achievements and the future directions in which the model can be evolved. It also presents possible improvements of the developed numerical models.

2 Physical Model

In this chapter, the fundamental principles and governing equations of the phenomena present in the CC process are explained. The chapter is focused on the formulation of the physical model that at least qualitatively accurately describes the multicomponent fluid flow with solidification under the influence of an externally applied magnetic field. The model has to be detailed enough to account for all the physical phenomena occurring in the CC process and, at the same time, simple enough to be effectively solved numerically.

First, the basic concepts of the mathematical modelling of the fluid flow are described. The solidification process is then reviewed and the macroscopic mixture continuum model is chosen to describe the flow in the porous region. Further, the microscopic species concentration modelling is described and the Lever rule is selected to account for the local concentrations of the individual species in the liquid and solid phases. Next, the fundamentals of turbulence modelling are discussed. The Reynolds time averaging is applied to the equations and the low-Re k-ε model is used to implement the turbulence effects. The description of the magnetic field is then recounted and its influence on the turbulent fluid flow is incorporated by the Maxwell's equations. Lastly, an overview of a complete physical model is given together with the general initial and boundary conditions.

The development of the model presented in this dissertation essentially correlates to the previous work of [Vertnik, 2010], who devised a model for the CC of steel without EM effects. The magnetic field implementation correlates to the work of [Ha et al., 2003; Aboutalebi et al., 2007] and segregation implementation is based on the works of [Bennon and Incropera, 1987a,b; Založnik and Šarler, 2005].

2.1 Fluid Dynamics

The main governing equations for fluid dynamics are the Navier-Stokes (N-S) equations, which are based on the principles of mass and momentum conservation. An energy conservation equation is added to account for the temperature variations in the fluid. In this dissertation, the N-S equations together with the energy equation are presented first for a general and than for an incompressible fluid flow. The state of fluid is completely determined by the fluid velocity $\mathbf{v}(\mathbf{r}, t)$, its pressure $p(\mathbf{r}, t)$, and density $\rho(\mathbf{r}, t)$, all of which are functions of space $\mathbf{r} = x_i\,\mathbf{i}_i$ $(i = 1, 2, 3)$ or $\mathbf{r} = x\,\mathbf{i}_x + y\,\mathbf{i}_y + z\,\mathbf{i}_z$ and time t.

2.1.1 Mass Conservation Equation

The continuity or mass conservation equation in its differential form is written as

$$\frac{\partial \rho}{\partial t} + \nabla \cdot (\rho \mathbf{v}) = 0. \tag{2.1}$$

In the index notation the continuity equation takes the following form

$$\frac{\partial \rho}{\partial t} + \frac{\partial}{\partial x_i}(\rho v_i) = 0. \tag{2.2}$$

If the fluid is incompressible, the density ρ is constant, and Eq. 2.1 becomes

$$\nabla \cdot \mathbf{v} = 0, \tag{2.3}$$

or in the index notation

$$\frac{\partial v_i}{\partial x_i} = 0. \tag{2.4}$$

The Eq. 2.3 is known as the divergence-free or solenoidal condition of the vector field $\mathbf{v}$.

2.1.2 Momentum Conservation Equation

The conservation of momentum is derived from the Newton's second law

$$\frac{d(m\mathbf{v})}{dt} = \mathbf{F}, \tag{2.5}$$

where $\mathbf{F}$, and m represent the force and the mass respectively. By taking into account that the force acts on a volume element of the flow and dividing Eq. 2.5 by $\Delta x \Delta y \Delta z$ the momentum equation is obtained

$$\frac{\partial(\rho \mathbf{v})}{\partial t} + \nabla \cdot (\rho \mathbf{v}\mathbf{v}) = \nabla \cdot \mathbf{f}_s + \mathbf{f}_b, \tag{2.6}$$

where $\mathbf{f} = \mathbf{F}/V$ ($V = \Delta x \Delta y \Delta z$), and is divided into the body forces $\mathbf{f}_b$, and the surface forces $\mathbf{f}_s$. In the index notation, it is written as

$$\frac{\partial(\rho v_i)}{\partial t} + \frac{\partial(\rho v_j v_i)}{\partial x_j} = \frac{\partial f_{si}}{\partial x_j} + f_{bi}. \tag{2.7}$$

Body Force

The body force $\mathbf{f}_b$ is the sum of all the volumetric forces that act on the volume element of the fluid, e.g. gravitational force $\mathbf{f}_g$, buoyancy force $\mathbf{f}_{bu}$, phase interaction force $\mathbf{f}_{pi}$, Lorentz force $\mathbf{f}_{EM}$, etc. The gravitational force is $\mathbf{f}_g = \rho \mathbf{g}$, where $\mathbf{g}$ is the gravitational acceleration. The buoyancy force is defined as $\mathbf{f}_{bu} = \rho_{ref} \mathbf{g}$, where ρ_{ref} is the reference fluid density. By taking into account the density difference due to the temperature and solute variation, and assuming the Boussinesq

approximation $\rho_{ref} = \rho(1 - \beta_T(T - T_{ref}) - \beta_C(C - C_{ref}))$, which essentially states that the density changes are the result of the temperature and concentration differences. They may be neglected except when coupled with gravitational acceleration in the buoyancy force. The following relation is obtained

$$\mathbf{f}_{gbu} = \mathbf{f}_g - \mathbf{f}_{bu} = \rho\mathbf{g} - \rho_{ref}\mathbf{g} = \rho\Big(\beta_T(T - T_{ref}) + \beta_C(C - C_{ref})\Big)\mathbf{g}, \tag{2.8}$$

where $\mathbf{f}_{gbu}$, β_T, T, T_{ref}, β_C, C, and C_{ref} are the buoyancy force, thermal expansion coefficient of the fluid, temperature, reference temperature, solute expansion coefficient, concentration, and reference concentration, respectively. The phase interaction force and the Lorentz body force are considered separately and are described in detail in Sects. 2.2.3 and 2.4.

Surface Forces

As the name suggests, the surface forces $\mathbf{f}_s$ are the total sum of the forces acting on the surface of the volume element of the fluid, i.e. the pressure p ($\mathbf{f}_p$) and viscous friction $\boldsymbol{\tau}$ ($\mathbf{f}_\tau$). The net pressure can be, with the help of the Gauss's theorem, rewritten into the volumetric term. As a result, the pressure term is written as $-\nabla p$. The same can be done for the viscous friction, where the obtained variable is the deviatoric stress tensor $\nabla \cdot \underline{\underline{\boldsymbol{\tau}}}$. Often, the two are combined into the stress tensor $\sigma_{ij} = -p\delta_{ij} + \tau_{ij}$. The constitutive relation between the velocity field and the deviatoric stress tensor is for an incompressible Newtonian fluid prescribed as [Bredberg, 1999]

$$\underline{\underline{\boldsymbol{\tau}}} = \mu\left((\nabla\mathbf{v}) + (\nabla\mathbf{v})^T - \frac{2}{3}\nabla\cdot\mathbf{v}\right) + \kappa\nabla\cdot\mathbf{v}, \tag{2.9}$$

or in the index notation

$$\tau_{ij} = \mu\left(\frac{\partial v_i}{\partial x_j} + \frac{\partial v_j}{\partial x_i} - \frac{2}{3}\delta_{ij}\sum_k \frac{\partial v_k}{\partial x_k}\right) + \kappa\delta_{ij}\sum_k \frac{\partial v_k}{\partial x_k}, \tag{2.10}$$

where μ is the fluid viscosity, and κ is the second viscosity coefficient or bulk viscosity. If the fluid is incompressible, the deviatoric stress tensor is reduced to

$$\underline{\underline{\boldsymbol{\tau}}} = \mu\left((\nabla\mathbf{v}) + (\nabla\mathbf{v})^T\right), \tag{2.11}$$

or in the index notation

$$\tau_{ij} = \mu\left(\frac{\partial v_i}{\partial x_j} + \frac{\partial v_j}{\partial x_i}\right). \tag{2.12}$$

The N-S equation is acquired by inserting the body forces and the surface forces into the momentum equation (Eq. 2.6) and can be written as

$$\begin{aligned}\frac{\partial(\rho\mathbf{v})}{\partial t} + \nabla\cdot(\rho\mathbf{v}\mathbf{v}) &= -\nabla p + \nabla\cdot\Big(\mu\big((\nabla\mathbf{v}) + (\nabla\mathbf{v})^T - \frac{2}{3}\nabla\cdot\mathbf{v}\big) + \kappa\nabla\cdot\mathbf{v}\Big) \\ &+ \rho\mathbf{g}\Big(\beta_T(T - T_{ref}) + \beta_C(C - C_{ref})\Big).\end{aligned} \tag{2.13}$$

For an incompressible flow the momentum equation is reduced to

$$\rho\Big(\frac{\partial(\mathbf{v})}{\partial t}+\nabla\cdot(\mathbf{vv})\Big) = -\nabla p+\nabla\cdot\mu\Big((\nabla\mathbf{v})+(\nabla\mathbf{v})^T\Big) + \rho\mathbf{g}\Big(\beta_T(T-T_{ref})+\beta_C(C-C_{ref})\Big). \tag{2.14}$$

In the index notations Eqs. 2.13 and 2.15 are rewritten as

$$\frac{\partial(\rho v_i)}{\partial t}+\frac{\partial}{\partial x_i}(\rho v_i v_j) = -\frac{\partial p}{\partial x_i}+\frac{\partial}{\partial x_i}\Big(\mu\Big(\frac{\partial v_i}{\partial x_j}+\frac{\partial v_j}{\partial x_j}-\frac{2}{3}\delta_{ij}\nabla\cdot\mathbf{v}\Big)+\kappa\delta_{ij}\nabla\cdot\mathbf{v}\Big) + \rho g\Big(\beta_T(T-T_{ref})+\beta_C(C-C_{ref})\Big) \tag{2.15}$$

and

$$\rho\Big(\frac{\partial v_i}{\partial t}+\frac{\partial}{\partial x_i}(v_i v_j)\Big) = -\frac{\partial p}{\partial x_i}+\frac{\partial}{\partial x_i}\Big(\mu\Big(\frac{\partial v_i}{\partial x_j}+\frac{\partial v_j}{\partial x_i}\Big)\Big) + \rho g\Big(\beta_T(T-T_{ref})+\beta_C(C-C_{ref})\Big). \tag{2.16}$$

2.1.3 Energy Conservation Equation

The first law of thermodynamics, also known as the conservation of energy principle, is used to account for the heat transfer and the temperature differences. The law states that the total energy of the system equals the heat transferred to and generated in the system minus the work done by the system on the surroundings. In this dissertation, the alternative formulation of the energy equation in terms of enthalpy is used

$$\frac{\partial}{\partial t}\big(\rho h\big)+\nabla\cdot\big(\rho\mathbf{v}h\big)=-\nabla\cdot q+h_{ST}, \tag{2.17}$$

where q is the heat flux, and h_{ST} is the enthalpy source term, which accounts for the electromagnetic heating, heating due to nuclear reactions, and work done by deformation. The heat flux is described with the Fourier law of conduction and is defined as

$$q=-\lambda\nabla T, \tag{2.18}$$

where λ is the thermal conductivity. The enthalpy source term accounts for the Joule heating effect and is described in detail in Sect. 2.4. Eq. 2.17 is in the index notation written as

$$\frac{\partial(\rho h)}{\partial t}+\frac{\partial}{\partial x_i}(\rho v_i h)=-\frac{\partial q_i}{\partial x_i}+h_{ST}. \tag{2.19}$$

By inserting Eq. 2.18 into Eq. 2.17 the energy conservation equation becomes

$$\frac{\partial}{\partial t}\big(\rho h\big)+\nabla\cdot\big(\rho\mathbf{v}h\big)=\nabla\cdot\big(\lambda\nabla T\big)+h_{ST} \tag{2.20}$$

or in the index notation

$$\frac{\partial(\rho h)}{\partial t}+\frac{\partial}{\partial x_i}(\rho v_i h)=\frac{\partial}{\partial x_i}\Big(\lambda\frac{\partial T}{\partial x_i}\Big)+h_{ST}. \tag{2.21}$$

For an incompressible flow, Eqs. 2.20 and 2.21 are reduced to

$$\rho\left(\frac{\partial h}{\partial t} + \nabla \cdot (\mathbf{v}h)\right) = \nabla \cdot (\lambda \nabla T) + h_{ST} \tag{2.22}$$

and

$$\rho\left(\frac{\partial h}{\partial t} + \frac{\partial}{\partial x_i}(v_i h)\right) = \frac{\partial}{\partial x_i}\left(\lambda \frac{\partial T}{\partial x_i}\right) + h_{ST}. \tag{2.23}$$

In order to be able to calculate the temperature from the enthalpy, the following constitutive relation is used

$$h = \int_{T_{ref}}^{T} c_p dT, \tag{2.24}$$

where c_p is the specific heat at constant pressure.

2.1.4 Species Conservation Equation

The species conservation equation for the concentration field is written as

$$\frac{\partial(\rho C)}{\partial t} + \nabla \cdot \big(\rho C \mathbf{v}\big) = -\nabla \cdot \mathbf{j}_C, \tag{2.25}$$

where $\mathbf{j}_C$ is the species flux. The $\mathbf{j}_C$, expressed in terms of concentration field, is given with Fick's law

$$\mathbf{j}_C = -D \nabla C, \tag{2.26}$$

where D is the diffusion coefficient. Eq. 2.25 then becomes

$$\frac{\partial(\rho C)}{\partial t} + \nabla \cdot \big(\rho C \mathbf{v}\big) = \nabla \cdot \big(D \nabla C\big). \tag{2.27}$$

In the index notation, the Eq. 2.27 is rewritten as

$$\frac{\partial(\rho C)}{\partial t} + \frac{\partial}{\partial x_i}(\rho C v_i) = \frac{\partial}{\partial x_i}\Big(D \frac{\partial C}{\partial x_i}\Big). \tag{2.28}$$

For the incompressible flow, Eqs. 2.27 and 2.28 become

$$\frac{\partial C}{\partial t} + \nabla \cdot \big(C \mathbf{v}\big) = \nabla \cdot \big(D \nabla C\big), \tag{2.29}$$

and

$$\frac{\partial C}{\partial t} + \frac{\partial}{\partial x_i}(C v_i) = \frac{\partial}{\partial x_i}\Big(D \frac{\partial C}{\partial x_i}\Big). \tag{2.30}$$

2.2 Solidification

Solidification [Kurz and Fischer, 1989; Dantzig and Rappaz, 2009] is a phase transformation process during which a melt is transferred into a solid. During the phase-change a latent heat is released and according to this classification, the solidification of pure substances and the solidification of alloys can be distinguished. Pure substances or eutectic alloys freeze at constant temperature, whereas alloys solidify over an extended temperature range. In this dissertation the solidification of a binary mixture with three different macroscopic phase regions (the liquid zone, the solid zone, and the mushy zone), is considered. The mixture is completely liquid in the liquid zone, where temperature is above the liquidus temperature T_L, and completely solid in the solid zone, where the temperature is below the solidus temperature T_S. In the mushy zone, the mixture is neither solid nor liquid, but a complex morphology of both phases exists. All three zones coincide in the eutectic point, where the melting temperature reaches its minimum, T_E. This is also the place where the solidus line, which shows the change of T_S with the concentration, and the liquidus line, which shows the change of T_L with the concentration, collide. The T_L is calculated as

$$T_L = T_m + (T_E - T_m)\frac{C}{C_E}, \tag{2.31}$$

where C_E is solute concentration in eutectic alloy. The relation between the concentration and the temperature is presented in a phase diagram shown in Fig. 2.1. In this case, a linearised simplification of the phase-change diagram is used instead of one solid phase. Among several models available to describe the relation between the solid fraction and the temperature [Hong, 2004], the linear model is chosen to describe the eutectic alloy, whereas the equilibrium solidification model or lever rule is chosen to describe the binary mixture.

2.2.1 Microsegregation

Microsegregation [Rappaz and Voller, 1990; Kraft and Chang, 1997] describes the solidification of liquid phase on the microlevel. The solubility of the mixture components is not the same for the liquid and for the solid components. The formation of the solid, causes the excess solute to be rejected back into the liquid. The liquid is therefore gradually enriched and consequently the solid layers that are formed later consist of a higher concentration of solute. This results in higher equilibrium concentration at the interface in comparison with the average concentrations of each phase. The concentration gradients in both phases are slightly balanced by the diffusion. The growth of the solid forms the columnar dendrites.

Linear Model

The linear solidification model describes the behaviour of a pure metal or an eutectic alloy during the phase-change process. If the latent heat is evenly distributed over the solidification range $T_S < T < T_L$, the solidus fraction f_S is

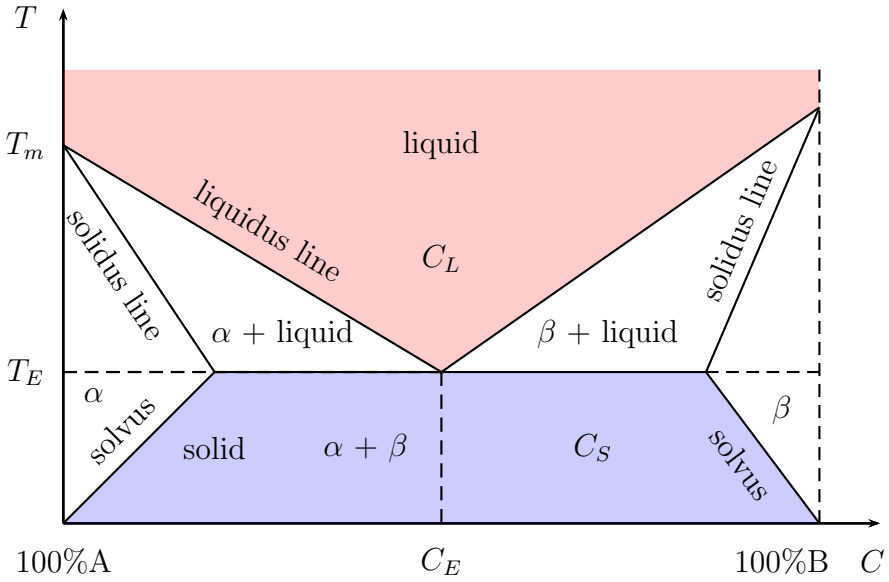

Figure 2.1: The linearised simplification of the concentration - temperature phase diagram for a binary alloy.

given as

$$f_S = \frac{T_L - T}{T_L - T_S}. \tag{2.32}$$

Lever Rule Model

The lever rule, also called the local equilibrium solidification model, assumes that the solid and the liquid phases are in a thermodynamic equilibrium and that the diffusion in solid and liquid is infinitely fast. In the mushy zone, the mixture concentration C is thus

$$f_S\, C_S + f_L\, C_L = C, \tag{2.33}$$

where the C_S and C_L are the concentrations of the solidus and the liquidus, respectively, and f_L is the liquid fraction of the alloy. The total mass fraction in the mushy zone is

$$f_S + f_L = 1. \tag{2.34}$$

C_L is obtained by inserting Eq. 2.33 into Eq. 2.34 and is

$$C_L = \frac{C}{1 + f_S\,(k_p - 1)}. \tag{2.35}$$

In the liquid zone, the mass fractions are $f_L = 1$ and $f_S = 0$ and consequently the concentration is $C = C_L$. In the solid zone, the mass fractions are $f_L = 0$ and $f_S = 1$ and consequently the concentration is $C = C_S$.

The solid fraction as a function of the temperature is given as

$$f_S = \frac{T_L - T}{(1 - k_p)(T_m - T)}, \tag{2.36}$$

where $T_S \leq T \leq T_L$, T_m is melting temperature, and

$$k_p = \frac{C_S}{C_L} \tag{2.37}$$

is the partition coefficient. In a similar way, the f_L can be obtained from Eqs. 2.34 and 2.36 and is

$$f_L = 1 - \frac{T_L - T}{(1 - k_p)(T_m - T)}. \tag{2.38}$$

2.2.2 Macrosegregation

Macrosegregation [Rappaz and Voller, 1990; Beckermann, 2002; Kraft and Chang, 1997] is an inhomogeneous distribution of macroscopic alloy components in metal casting. The variations in chemical composition of the cast material can significantly deteriorate the quality of the material. In order to improve the mechanical and processing characteristics of the product, the macrosegregation must be optimized.

The macrosegregation strongly depends on the microsegregation and on the relative motion of liquid and solid phases. The rejection of solute into the liquid on the microlevel, causes a macroscopic transport of solute. Macrosegregation in the solidified material is thus a consequence of relative motion of solute-rich liquid and solid-lean grains and can be caused either by shrinkage flow, forced flow, natural convection, motion of solid grains or deformation of solid skeleton. Alloys do not freeze at a fixed melting temperature, but solidify over a temperature range and multiple phase compositions. This causes the formation of a mushy region, where liquid and solid phases coexist. The mushy region is further divided into the slurry and porous regions. The porous region consists of the coalesced columnar dendrites, forming a solid porous skeleton. The interdenditic space is filled with liquid, that is either trapped or flowing through the solidified matrix. The slurry region consists of non-coalesced equiaxed dendrites that are floating freely in the liquid flow. The equiaxed dendrites are formed either from heterogeneous nucleation sites or by the brake-off of the columnar dendrites.

2.2.3 Mixture Continuum Model

Solidification is introduced into the mass, momentum, energy and species conservation equations with the mixture continuum model that was first utilized in 1987 [Bennon and Incropera, 1987b]. The model accounts for the interactions between the solid and the liquid phases by including the additional source terms in the conservation equations. The geometry of the phase change boundaries and the solid structures as well as between the microscopic and the macroscopic physical phenomena were not considered. Although the model is implemented by a single-phase numerical procedure, it accounts for all phases that are considered in the physical domain. The model assumes an equilibrium between the solid and the liquid phases and a constant velocity of the solid phase. The continuum is

composed of two distinct phases; the solid phase and the liquid phase, both of which can occupy the same position. The mixture density is defined as

$$\rho = \rho_S^* + \rho_L^*, \tag{2.39}$$

where the indexes $_S$ and $_L$ stand for the solid and the liquid. The partial density $\rho_{L,S}^*$ of each phase is obtained as

$$\rho_S^* = g_S \rho_S, \qquad \rho_L^* = g_L \rho_L, \tag{2.40}$$

where g_S and g_L are the volume fraction of the solid and of the liquid, respectively. The mass fractions of the solid and liquid phases are

$$f_S = \frac{\rho_S^*}{\rho}, \qquad f_L = \frac{\rho_L^*}{\rho}. \tag{2.41}$$

The average mixture velocity is then

$$\mathbf{v} = \frac{1}{\rho}\left(\rho_S^* \mathbf{v}_S + \rho_L^* \mathbf{v}_L\right) = f_S \mathbf{v}_S + f_L \mathbf{v}_L, \tag{2.42}$$

where $\mathbf{v}_S$ and $\mathbf{v}_L$ are the velocity of the solid phase and the velocity of the liquid phase, respectively. In a similar way, the mixture body force, the mixture thermal conductivity, the mixture enthalpy, the mixture species concentration and the mixture mass diffusion coefficient are written as

$$\mathbf{f}_b = \frac{1}{\rho}\left(\rho_S^* \mathbf{f}_{bS} + \rho_L^* \mathbf{f}_{bL}\right) = f_S \mathbf{f}_{bS} + f_L \mathbf{f}_{bL}, \tag{2.43}$$

$$\lambda = g_S \lambda_S + g_L \lambda_L, \tag{2.44}$$

$$h = \frac{1}{\rho}\left(\rho_S^* h_S + \rho_L^* h_L\right) = f_S h_S + f_L h_L, \tag{2.45}$$

$$C = \frac{1}{\rho}\left(\rho_S^* C_S + \rho_L^* C_L\right), \tag{2.46}$$

and

$$D = \frac{1}{\rho}\left(\rho_S^* D_S + \rho_L^* D_L\right) = f_S D_S + f_L D_L. \tag{2.47}$$

By inserting these equations into the mass (Eq. 2.1), momentum (Eq. 2.6), energy (Eq. 2.17) and species (Eq. 2.27) conservation equations the complete set of mixture continuum model equations is obtained.

Phase Interaction Force

The interaction between phases in the mushy region is described with phase interaction force. In this dissertation, the mushy region is modelled with a permeable solid matrix, which can either be stationary or moving with the velocity of the system. Such morphology is analogous to the flow through porous media [Nield and Bejan, 2006], which is described by Darcy's law. The Darcy's law for porous

media states that the phase interaction force is proportional to the relative velocity

$$\mathbf{f}_{pi} = \frac{\mu_L}{K} g_L \mathbf{v}_r, \tag{2.48}$$

where μ_L, K, and $\mathbf{v}_r$ are the viscosity of liquid, permeability, and relative velocity, respectively. $\mathbf{v}_r$ is defined as the difference between the velocity of the liquid and the velocity of the porous solid

$$\mathbf{v}_r = (\mathbf{v}_L - \mathbf{v}_S). \tag{2.49}$$

The permeability is modelled by the Kozeny-Carman model [Carman, 1948; Viskanta, 1990; Dullien, 1991; Aboutalebi et al., 1995]

$$K = \frac{f_L^3}{K_0\big(1+f_L\big)^2}, \tag{2.50}$$

where K_0 is the permeability constant. Identities $f_L\mathbf{v}_r = \mathbf{v} - \mathbf{v}_S$ and $g_L = (\rho/\rho_L)f_L$ are applied to the Eq. 2.48, which, for a constant velocity of the solid phase, such as in the case of the CC, and by further assuming that the phase densities are constant, becomes [Bennon and Incropera, 1987b]

$$\mathbf{f}_{pi} = -\frac{\mu_L K_0\big(1+f_L\big)^2}{f_L^3}\frac{\rho}{\rho_L}\Big(\mathbf{v} - \mathbf{v}_S\Big). \tag{2.51}$$

The conservation equations of the unified incompressible mixture continuum model are thus

$$\nabla \cdot \mathbf{v} = 0, \tag{2.52}$$

$$\begin{aligned} \frac{\partial(\rho\mathbf{v})}{\partial t} + \nabla\cdot(\rho\mathbf{v}\mathbf{v}) &= -\nabla p + \nabla\cdot\Big(\mu_L\frac{\rho}{\rho_L}\big((\nabla\mathbf{v}) + (\nabla\mathbf{v})^T\big)\Big) \\ &- \mu_L\frac{K_0(1+f_L)^2}{f_L^3}\frac{\rho}{\rho_L}\big(\mathbf{v}-\mathbf{v}_S\big) \\ &+ \rho\mathbf{g}\big(\beta_T(T-T_{ref}) + \beta_C(C-C_{ref})\big), \end{aligned} \tag{2.53}$$

$$\begin{aligned} \frac{\partial(\rho h)}{\partial t} + \nabla\cdot\big(\rho\mathbf{v}h\big) &= \nabla\cdot(\lambda\nabla T) \\ &+ \nabla\Big(\rho f_S\big(h_L - h_S\big)\big(\mathbf{v}-\mathbf{v}_S\big)\Big), \end{aligned} \tag{2.54}$$

and

$$\begin{aligned} \frac{\partial(\rho C)}{\partial t} + \nabla\cdot\big(\rho C\mathbf{v}\big) &= \nabla\cdot\Big(\rho\big(f_S D_S\nabla C_S + f_L D_L \nabla C_L\big)\Big) \\ &+ \nabla\cdot\Big(\rho f_L\big(\mathbf{v}-\mathbf{v}_L\big)\big(C_L - C\big) + \rho f_S\big(\mathbf{v}-\mathbf{v}_S\big)\big(C_S - C\big)\Big). \end{aligned} \tag{2.55}$$

The constitutive relation for the temperature - enthalpy (Eq. 2.24) is transferred into [Šarler and Kuhn, 1998; Šarler and Kuhn, 1998, 1999]

$$h_S = \int_{T_{ref}}^{T} c_{pS} dT, \tag{2.56}$$

and

$$h_L = \int_{T_{ref}}^{T_S} c_{pS} dT + \int_{T_S}^{T} c_{pL} dT + h_m = h_S(T) + \int_{T_S}^{T} \big(c_{pL} - c_{pS}\big) dT + h_m, \tag{2.57}$$

where c_{pS}, c_{pL}, and h_m are the specific heat at constant pressure for the solid, the specific heat at constant pressure for the liquid, and melting enthalpy respectively.

2.3 Turbulence

The turbulence [Wilcox, 1998] describes random fluctuations of various flow properties, such as pressure and velocity, in space and time. Turbulent flow is characterized by irregular, random and chaotic fluid motion which increases diffusivity. It occurs at high Re and is always 3D. The largest eddies obtain their kinetic energy from the mean flow and by breaking up transfer of the energy to slightly smaller eddies. The transfer of kinetic energy is successively transferred to increasingly smaller eddies until the viscous stresses are large enough to enable the kinetic energy to dissipate into the internal energy. Even the smallest eddies however, are always large enough that the flow can still be treated as a continuum. This transfer of energy from the largest to the smallest eddies is called an energy cascade.

In general, turbulent models are divided into three groups, according to the extent of modelling (Fig. 2.2) that is used in each approach: the Direct Numerical Simulation (DNS), the LES, and the RANS based models. Apart from these three major groups for turbulence modelling, several hybrid models, such as the Detached Eddy Simulations (DES) model, also exist. These models attempt to combine the best aspects of the RANS and the LES solution methodologies in a single model. A detailed scheme of turbulence models is given in Appx. A.

Even though the turbulent flow is always 3D, it can be treated as 2D when the equations are time averaged. In this dissertation, the Reynolds time averaging [Reynolds, 1895]

$$\overline{\psi(t')} = \lim_{t' \to \infty} \frac{1}{t'} \int_{t}^{t+t'} \psi(\mathbf{r}, t) dt, \tag{2.58}$$

where $\overline{\psi}$ is the averaged quantity, and t' is a time interval much longer than the longest time scale of the turbulent flow, is used to derive the governing equations.

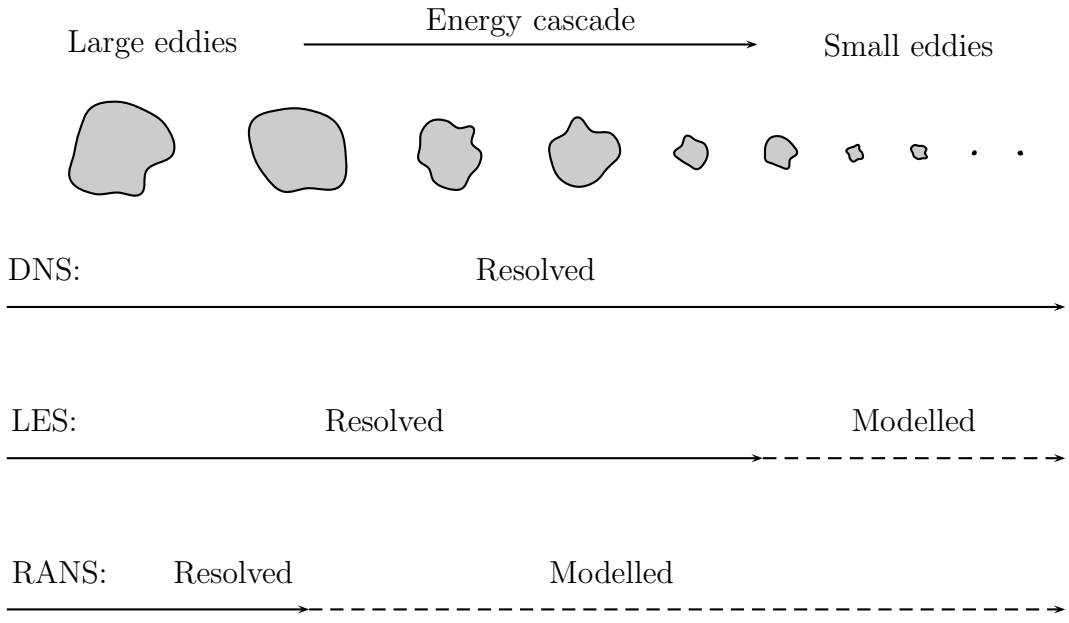

Figure 2.2: The extent of the modelling for different types of turbulence models.

The averaging operation (Eq. 2.58) allows the averaging quantity to be split into the mean $\overline{\psi}$ and the fluctuating part $\psi^{\urcorner}$

$$\psi = \overline{\psi} + \psi^{\urcorner}. \tag{2.59}$$

Once the time averaging is applied to the conservation equations of the continuum mixture model (Eqs. 2.52 - 2.55), a new set of conservation equations is obtained

$$\nabla \cdot \mathbf{v} = 0, \tag{2.60}$$

$$\begin{aligned} \frac{\partial(\rho\mathbf{v})}{\partial t} + \nabla\cdot(\rho\mathbf{v}\mathbf{v}) &= -\nabla p + \nabla\cdot\Big(\big(\mu_L\frac{\rho}{\rho_L} + \mu_t\big)\big((\nabla\mathbf{v}) + (\nabla\mathbf{v})^T\big)\Big) \\ &- \frac{2}{3}\nabla(\rho k) - \mu_L\frac{K_0(1+f_L)^2}{f_L^3}\frac{\rho}{\rho_L}\big(\mathbf{v}-\mathbf{v}_S\big) \\ &+ \rho\mathbf{g}\big(\beta_T(T-T_{ref}) + \beta_C(C-C_{ref})\big), \end{aligned} \tag{2.61}$$

$$\begin{aligned} \frac{\partial(\rho h)}{\partial t} + \nabla\cdot\big(\rho\mathbf{v}h\big) &= \nabla\cdot(\lambda\nabla T) \\ &+ \nabla\cdot\Big(\rho f_S\big(h_L - h_S\big)\big(\mathbf{v}-\mathbf{v}_S\big)\Big) \\ &+ \nabla\cdot\Big(f_L\frac{\mu_t}{\sigma_T}\nabla h_L\Big), \end{aligned} \tag{2.62}$$

and

$$\begin{aligned}\frac{\partial(\rho C)}{\partial t}+\nabla\cdot\big(\rho C\mathbf{v}\big) &= \nabla\cdot\Big(\rho f_S D_S\nabla C_S+\rho f_L D_L\nabla C_L\Big)\\ &+ \nabla\cdot\Big(\rho\big(\mathbf{v}-\mathbf{v}_S\big)\big(C_L-C\big)\Big)\\ &+ \nabla\cdot\Big(\frac{f_L\mu_t}{\sigma_C}\nabla C_L\Big),\end{aligned} \tag{2.63}$$

where μ_t, k, σ_T and σ_C are the turbulent dynamic viscosity, turbulent kinetic energy, closure coefficient for energy and closure coefficient for species concentration. Most of the terms in these equations are the same as those in the original mixture continuum model (Eqs. 2.52 - 2.55); the only terms that do change are the ones in which the dot product of fluctuating velocity appears $\overline{\mathbf{v}^{\urcorner}\mathbf{v}^{\urcorner}}$. This term is called the Reynolds stress tensor [Bredberg, 1999] and is a fundamental problem in turbulence modelling. As the primary objective of this dissertation is not a detailed turbulence modelling, only a short description of relevant quantities (such as the turbulent kinetic energy) that are necessary to complete our model are given.

In order to complete the set of governing equations, two additional transport equations are added, one for the turbulent kinetic energy and one for the dissipation rate.

Turbulent Kinetic Energy Equation

The turbulent kinetic energy k is defined as the trace $\mathrm{tr}(\overline{\mathbf{v}^{\urcorner}\mathbf{v}^{\urcorner}})$ of the Reynolds stress tensor

$$k=\frac{1}{2}tr\big(\overline{\mathbf{v}^{\urcorner}\mathbf{v}^{\urcorner}}\big). \tag{2.64}$$

The conservation equation for turbulent kinetic energy equation can be derived from the Reynolds stress equation [Bredberg, 1999]

$$\begin{aligned}\frac{\partial(\rho k)}{\partial t}+\nabla\cdot(\rho\mathbf{v}k) &= \nabla\cdot\Big(\big(\mu_L\frac{\rho}{\rho_L}+\frac{\mu_t}{\sigma_k}\big)\nabla k\Big)+P_k+G_k-\rho\varepsilon\\ &+ \rho D_{k-\varepsilon}+\mu_L\frac{K_0(1+f_L)^2}{f_L^3}\frac{\rho}{\rho_L}k,\end{aligned} \tag{2.65}$$

where σ_k, P_k, G_k, ε, and $D_{k-\varepsilon}$ stand for the closure coefficient for turbulent kinetic energy, the production term, the turbulent term due to the buoyancy force, the dissipation rate and the additional source term. The production term is defined as

$$P_k=\mu_t\nabla\overline{\mathbf{v}}:\big(\nabla\overline{\mathbf{v}}+(\nabla\overline{\mathbf{v}})^T\big), \tag{2.66}$$

or in index notation

$$P_k=\mu_t\left(2\left(\frac{\partial v_i}{\partial x_j}\right)^2+\left(\frac{\partial v_i}{\partial x_j}+\frac{\partial v_j}{\partial x_i}\right)^2\right), \tag{2.67}$$

where the turbulent dynamic viscosity μ_t is defined as

$$\mu_t=\rho c_\mu f_\mu\frac{k^2}{\varepsilon}, \tag{2.68}$$

and c_μ and f_μ represent the closure coefficient and the damping function. The G_k describes the generation of turbulence due to the buoyancy force and is defined as

$$G_k = -\mathbf{g}\beta_T \frac{\nu_t}{\mathrm{Pr}_t}\frac{\partial T}{\partial y}, \tag{2.69}$$

where ν_t and Pr_t are the turbulent dynamic viscosity and turbulent Prandtl number.

Dissipation Rate

The dissipation rate ε is defined as

$$\varepsilon = \overline{\nu \nabla \mathbf{v}^{\urcorner} \nabla \mathbf{v}^{\urcorner}}, \tag{2.70}$$

or in the index notation

$$\varepsilon = \overline{\nu \frac{\partial v_i^{\urcorner}}{\partial x_j}\frac{\partial v_i^{\urcorner}}{\partial x_j}}. \tag{2.71}$$

The dissipation rate equation is

$$\begin{aligned} \frac{\partial(\rho\varepsilon)}{\partial t} + \nabla\cdot(\rho\mathbf{v}\varepsilon) &= \nabla\Big(\big(\mu_L\frac{\rho}{\rho_L} + \frac{\mu_t}{\sigma_\varepsilon}\big)\nabla\varepsilon\Big) \\ &+ \big(c_{1\varepsilon}f_1(P_k + c_{3\varepsilon}G_k) - c_{2\varepsilon}f_2\rho\varepsilon\big)\frac{\varepsilon}{k} \\ &+ \rho E_{k-\varepsilon} + \mu_L\frac{K_0(1+f_L)^2}{f_L^3}\frac{\rho}{\rho_L}\varepsilon, \end{aligned} \tag{2.72}$$

where σ_ε, $c_{1\varepsilon}$, $c_{3\varepsilon}$, f_1, $c_{2\varepsilon}$, and f_2 are the closure coefficients, while $E_{k-\varepsilon}$ is the additional source term. Coefficient $c_{3\varepsilon}$ is calculated from the following equation [Henkes et al., 1991]

$$c_{3\varepsilon} = \tanh\Big|\frac{\overline{\mathbf{v}_\parallel}}{\overline{\mathbf{v}_\perp}}\Big|, \tag{2.73}$$

where $\overline{\mathbf{v}_\parallel}$ and $\overline{\mathbf{v}_\perp}$ are the parallel and the perpendicular velocity components.

A detailed derivation of the Reynolds stresses along with the description of various turbulence models can be found in [Wilcox, 1998] and [Bredberg, 1999]. Among many different possible forms of the RANS based models, that can be used to model this tensor, the two-equation Abe-Kondoh-Nagano (AKN) [Abe et al., 1994, 1995] low-Re k-ε turbulence model is applied in this dissertation.

2.3.1 Low-Re k-ε Turbulence Model

In the k-ε turbulence model the additional relations are given for the unknowns in the k and ε transport equations. The standard k-ε model was designed for a fully turbulent flow with high turbulent Re numbers, and cannot accurately predict the behaviour of the flow near the wall, where turbulence is low. In our case, the behaviour of the flow near the wall (boundary) is important and thus the low-Re turbulent model has to be applied. The high and the low Re models refer to the local turbulent Reynolds number Re_t, which varies through the domain.

When the wall is approached the viscous diffusion becomes dominant, whereas the turbulent diffusion can be neglected and thus the Re_t is high in the fully turbulent flow and low near the wall. Different low-Re models [Launder and Sharma, 1974; Abe et al., 1994; Jones and Launder, 1972; Abid et al., 1995] use different closure coefficients.

Abe-Kondoh-Nagano Turbulence Model

The closure coefficients for the AKN model are $c_\mu = 0.09$, $c_{\varepsilon 1} = 1.40$, $c_{\varepsilon 2} = 1.40$, $\sigma_k = 1.50$, and $\sigma_\varepsilon = 1.90$. The source terms $D_{k-\varepsilon}$ and $E_{k-\varepsilon}$ are equal to zero. The damping functions f_μ and f_2 are defined with equations

$$f_\mu = \left(1 - e^{-\frac{y^+}{14}}\right)^2 \left(1 + \frac{5}{Re_t^{0.75}} e^{-\left(\frac{\mathrm{Re}_t}{200}\right)^2}\right), \tag{2.74}$$

and

$$f_2 = \left(1 - e^{\left(-\frac{y^+}{3.1}\right)}\right)^2 \left(1 - 0.3 e^{-\left(\frac{\mathrm{Re}_t}{6.5}\right)^2}\right), \tag{2.75}$$

and f_1 is set to 1.0. The y^+ is the non-dimensional distance to the wall and is defined as

$$y^+ = \frac{\rho \overline{\mathbf{v}_\varepsilon} n_y}{\mu}, \tag{2.76}$$

where $\overline{\mathbf{v}_\varepsilon} = (\nu\varepsilon)^{1/4}$, and n_y stand for the Kolmogorov velocity scale, and the normal distance.

2.4 Magnetohydrodynamics

Magnetohydrodynamics (MHD) [Davidson, 2001; Cullity and Graham, 2011] is an academic discipline, concerned with the motion of electrically conducting and non-magnetic fluids under the influence of the magnetic field. The complete set of the MHD equations includes the mass conservation equation, the momentum conservation equation, the energy conservation equation, the Maxwell's equations and the Ohm's law.

Maxwell's Equations

The Maxwell's equations are a set of PDEs that together with the Lorentz force law and the conservation law, describe all of the electrodynamics. The four Maxwell's equations are

$$\nabla \cdot \mathbf{E} = \frac{\rho_e}{\varepsilon_0}, \tag{2.77}$$

$$\nabla \cdot \mathbf{B} = 0, \tag{2.78}$$

$$\nabla \times \mathbf{E} = -\frac{\partial \mathbf{B}}{\partial t}, \tag{2.79}$$

$$\nabla \times \mathbf{B} = \mu_0 \left(\mathbf{J} + \varepsilon_0 \frac{\partial \mathbf{E}}{\partial t}\right), \tag{2.80}$$

with $\mathbf{E}$, ρ_e, ε_0, $\mathbf{B}$, μ_0, $\mathbf{J}$ standing for electric field density, charge density, permittivity of free space, magnetic flux density, permeability of free space and electric current density, respectively. The Maxwell's equations consist of the Gauss's law (Eq. 2.77) the Gauss's law for magnetism (Eq. 2.78), the Faraday's induction law (Eq. 2.79) and the Ampere's law with the Maxwell's correction (Eq. 2.80). In index notation Eq. 2.77-2.80 are

$$\sum_{i=1}^{3} \frac{\partial E_i}{\partial x_i} = \frac{\rho_e}{\varepsilon_0}, \tag{2.81}$$

$$\sum_{i=1}^{3} \frac{\partial B_i}{\partial x_i} = 0, \tag{2.82}$$

$$\frac{\partial}{\partial x_i} E_j \epsilon_{ijl} = -\frac{\partial B_i}{\partial t}, \tag{2.83}$$

and

$$\frac{\partial}{\partial x_i} B_j \epsilon_{ijl} = \mu_0 \left(J_i + \varepsilon_0 \frac{\partial E_i}{\partial t} \right), \tag{2.84}$$

where ϵ_{ijl} is Levi-Civita symbol.

Ohm's Law

The Ohm's law is written as

$$\mathbf{J} = \sigma(\mathbf{E} + \mathbf{v} \times \mathbf{B}), \quad \text{or in index notation} \quad J_i = \sigma(E_i + \epsilon_{ijl}\, v_i\, B_j), \tag{2.85}$$

when the fluid is in motion and the external magnetic field is applied. σ stands for the electric conductivity.

Charge Conservation Equation

In addition to the Maxwell's equations and the Ohm's law, the charge conservation equation

$$\nabla \cdot \mathbf{J} = -\frac{\partial \rho_e}{\partial t}, \quad \text{or in index notation} \quad \frac{\partial J_i}{\partial x_i} = -\frac{\partial \rho_e}{\partial t} \tag{2.86}$$

and the Lorentz's force

$$\mathbf{F}_{EM} = \mathbf{J} \times \mathbf{B}, \quad \text{or in index notation} \quad F_{EMi} = \epsilon_{ijl} J_i\, B_j \tag{2.87}$$

are used to describe the total system of the electromagnetism in the MHD. As the charge density is constant in the MHD, the charge conservation equation is simplified to

$$\nabla \cdot \mathbf{J} = 0, \quad \text{or in index notation} \quad \frac{\partial J_i}{\partial x_i} = 0. \tag{2.88}$$

In general, the magnetic flux density and the electric field density can be written as functions of a vector potential $\mathbf{A}$ and a scalar potential ϕ. The potentials are

$$\mathbf{B} = \nabla \times \mathbf{A}, \quad \text{or in index notation} \quad B_i = \epsilon_{ijl} \frac{\partial}{\partial x_i} B_j \tag{2.89}$$

and

$$\mathbf{E} = -\nabla\phi - \frac{\partial \mathbf{A}}{\partial t}, \quad \text{or in index notation} \quad E_i = -\frac{\partial \phi}{\partial x_i} - \frac{\partial A_i}{\partial t}. \tag{2.90}$$

In this dissertation, the assumption is made that $\mathbf{B}$ and $\mathbf{E}$ are steady. Consequently, the Faraday's induction law (Eq. 2.79) and the Ampere's law (Eq. 2.80) become $\nabla \cdot \mathbf{E} = 0$ and $\nabla \times \mathbf{B} = \mu_0 \mathbf{J}$. By inserting these two equations into the conservation law (Eq. 2.88), the electric flux (Eq. 2.90) is reduced to

$$\mathbf{E} = -\nabla\phi, \quad \text{or in index notation} \quad E_i = -\frac{\partial \phi}{\partial x_i}. \tag{2.91}$$

By further substituting Eq. 2.91 into Eq. 2.88, the Poisson's equation for electric potential ϕ is obtained

$$\nabla^2\phi = \nabla \cdot (\mathbf{v} \times \mathbf{B}), \quad \text{or in index notation} \quad \frac{\partial^2 \phi}{\partial x_i^2} = \sum_{i=1}^{3} \frac{\partial\, \epsilon_{ijl}\, v_i\, B_j}{\partial x_i}. \tag{2.92}$$

This limits our discussion to EMBR.

Lorentz Force

In order to account for the magnetic field effect, the Lorentz body force term

$$\mathbf{f}_{EM} = \frac{\mathbf{F}_{EM}}{V} = \mathbf{j} \times \mathbf{B}, \tag{2.93}$$

where $\mathbf{j} = \mathbf{J}/V$, is added in the momentum equation (Eq. 2.62).

Joule Heating Term

In general, the additional enthalpy source term called the Joule heating term

$$h_m = \frac{|\mathbf{j}|^2}{\sigma} \tag{2.94}$$

needs to be added to the energy equation (Eq. 2.63), in order to account for the heating caused by the externally applied magnetic field. However, in the case of CC of steel this term is sufficiently small to be neglected.

2.4.1 Low Magnetic Reynolds Number

The coupling of the magnetic $\mathbf{B}$ and the velocity $\mathbf{v}$ fields is done through the Lorentz force. The magnetic field affects the velocity field and vice versa, the velocity field affects the magnetic field. The extent to which the fields are coupled can be expressed by the magnetic Reynolds number Re_m. In case of laboratory experiments and industrial processes, particularly those including liquid metals, $\mathrm{Re}_m \ll 1$ [Davidson and Boysan, 1987]. This means that the effect of the $\mathbf{B}$ on $\mathbf{v}$ is significant, whereas the effect of $\mathbf{v}$ on $\mathbf{B}$ can be neglected. In the MHD, the

approximation of low Re_m indicates that the induced currents are negligible in comparison with the imposed magnetic field $\mathbf{B}$.

Magnetic field can affect the velocity field in three different ways: it can either suppress the bulk motion, excite the bulk motion or alter the structure of the boundary layers. To ensure that the magnetic field is unaffected by the velocity, the approximation of low Re_m is applied.

2.4.2 External Magnetic Field

The external magnetic field can be either given with a fixed constant value or calculated. The magnetic field is calculated from the Biot-Savart law

$$\mathbf{B}(\mathbf{r}) = \frac{\mu_0}{4\pi} \int \frac{I d\mathbf{l} \times \hat{\mathbf{r}}}{r^2} = \mu_0 \mathbf{H}; \quad \hat{\mathbf{r}} = \frac{\mathbf{r}}{r}, \tag{2.95}$$

which states that the magnetic field at position $\mathbf{r}$ is generated by the electric current $\mathbf{I}$. $d\mathbf{l}$ stands for the integration length, and $\mathbf{H}$ is the magnetic field strength. When the magnetic field is measured in the material, one has to account for the specific properties of the medium. In that case, the magnetic field is

$$\mathbf{B} = \mu_M \mathbf{H} = \mu_0 \big(\mathbf{H} + \mathbf{M}\big), \tag{2.96}$$

where μ_M represents the magnetic permeability of the material and $\mathbf{M}$ the magnetisation. The magnetisation is a function of the magnetic flux density

$$\mathbf{M} = \chi \mathbf{H}, \tag{2.97}$$

where the susceptibility is defined as

$$\chi = \mu_r - 1 = \frac{\mu_M}{\mu_0} - 1. \tag{2.98}$$

χ depends on the relative permeability μ_r of the material.

2.5 Final Multiphysics Model

The physical model consists of the governing equations and the constitutive relations, along with the initial and boundary conditions that enable us to solve them. In this chapter, the equations are presented in their final form.

2.5.1 Final Set of Governing Equations

The governing equations that consider the turbulent fluid flow, the temperature and the magnetic field, as well as the segregation and the species concentration are, in their final form, presented below.

$$\nabla \cdot \mathbf{v} = 0, \tag{2.99}$$

$$\begin{aligned}\frac{\partial(\rho\mathbf{v})}{\partial t}+\nabla\cdot(\rho\mathbf{v}\mathbf{v}) &= -\nabla p+\nabla\cdot\Big(\big(\mu_L\frac{\rho}{\rho_L}+\mu_t\big)\big((\nabla\mathbf{v})+(\nabla\mathbf{v})^T\big)\Big)\\ &- \frac{2}{3}\nabla(\rho k)-\mu_L\frac{K_0(1+f_L)^2}{f_L^3}\frac{\rho}{\rho_L}\big(\mathbf{v}-\mathbf{v}_S\big)\\ &+ \rho\mathbf{g}\big(\beta_T(T-T_{ref})+\beta_C(C-C_{ref})\big)+\mathbf{j}\times\mathbf{B},\end{aligned} \tag{2.100}$$

$$\begin{aligned}\frac{\partial(\rho h)}{\partial t}+\nabla\cdot\big(\rho\mathbf{v}h\big) &= \nabla\cdot(\lambda\nabla T)\\ &+ \nabla\cdot\Big(\rho f_S\big(h_L-h_S\big)\big(\mathbf{v}-\mathbf{v}_S\big)\Big)\\ &+ \nabla\cdot\Big(f_L\frac{\mu_t}{\sigma_T}\nabla h_L\Big)+\frac{|\mathbf{j}|^2}{\sigma},\end{aligned} \tag{2.101}$$

$$\begin{aligned}\frac{\partial(\rho C)}{\partial t}+\nabla\cdot\big(\rho C\mathbf{v}\big) &= \nabla\cdot\Big(\rho f_S D_S\nabla C_S+\rho f_L D_L\nabla C_L\Big)\\ &+ \nabla\cdot\Big(\rho\big(\mathbf{v}-\mathbf{v}_S\big)\big(C_L-C\big)\Big)\\ &+ \nabla\cdot\Big(\frac{f_L\mu_t}{\sigma_C}\nabla C_L\Big),\end{aligned} \tag{2.102}$$

$$\begin{aligned}\frac{\partial(\rho k)}{\partial t}+\nabla\cdot(\rho\mathbf{v}k) &= \nabla\cdot\Big(\big(\mu_L\frac{\rho}{\rho_L}+\frac{\mu_t}{\sigma_k}\big)\nabla k\Big)+P_k+G_k-\rho\varepsilon\\ &+ \rho D_{k-\varepsilon}+\mu_L\frac{K_0(1+f_L)^2}{f_L^3}\frac{\rho}{\rho_L}k,\end{aligned} \tag{2.103}$$

$$\begin{aligned}\frac{\partial(\rho\varepsilon)}{\partial t}+\nabla\cdot(\rho\mathbf{v}\varepsilon) &= \nabla\cdot\Big(\big(\mu_L\frac{\rho}{\rho_L}+\frac{\mu_t}{\sigma_\varepsilon}\big)\nabla\varepsilon\Big)\\ &+ \big(c_{1\varepsilon}f_1(P_k+c_{3\varepsilon}G_k)-c_{2\varepsilon}f_2\rho\big)\frac{\varepsilon}{k}\\ &+ \rho E_{k-\varepsilon}+\mu_L\frac{K_0(1+f_L)^2}{f_L^3}\frac{\rho}{\rho_L}\varepsilon.\end{aligned} \tag{2.104}$$

2.5.2 Boundary Conditions

In the solution of the PDEs either Dirichlet, Neuman or Robin boundary conditions (BC) can be used. The Dirichlet BC prescribe the value of the function on the surface

$$f=f(\mathbf{r},t). \tag{2.105}$$

The Neuman BC prescribe the value of the normal derivative of the function on the surface:

$$\frac{\partial f}{\partial\mathbf{n}}=f(\mathbf{r},t). \tag{2.106}$$

The Robin BC is the weighted sum of the Dirichlet and the Neuman BC

$$w_1 f+w_2\frac{\partial f}{\partial\mathbf{n}}=f(\mathbf{r},t), \tag{2.107}$$

where w_1 and w_2 represent the weights. Geometrically, five different boundaries: inlet, outlet, wall, free surface and symmetry, are considered in the present dissertation. Which of the boundary conditions is prescribed on the specific boundary for the velocity, temperature, turbulent kinetic energy, dissipation rate, species concentration and current density is listed below. The schematic view of the boundary conditions is shown in Fig. 2.3.

Velocity Field

Dirichlet BC are prescribed on the inlet and the wall for both velocity components, and on the symmetry line for the velocity component perpendicular to the boundary. The Neuman BC are prescribed and set to zero for both velocity components on the outlet boundary, and on the symmetry line for the velocity component parallel to the boundary.

Temperature Field

Dirichlet BC are set for temperature field on the inlet. Neuman BC are prescribed and set to 0 for the temperature field on the symmetry line and on the outlet. On the wall either of the three possible BC can be used to calculate the temperature.

Pressure

Neuman BC are prescribed for the pressure on the inlet, symmetry and wall

$$\mathbf{n} \cdot \nabla p = \frac{\rho}{\Delta t} \mathbf{n}(\mathbf{v}^\star - \mathbf{v}_w), \tag{2.108}$$

where $\mathbf{v}^\star$ is an intermediate velocity field and $\mathbf{v}_w$ is the velocity of the wall. At the outlet, Dirichlet BC is prescribed. The pressure on the outlet is equal to ambivalent pressure and is set to 0.

Turbulent Kinetic Energy

Dirichlet BC are set for the turbulent kinetic energy at the inlet and at the wall, where no-slip condition is applied. The Neuman BC are used on the symmetry line and at the outlet and are set to 0.

Dissipation Rate

Dirichlet BC are set for the dissipation rate at the inlet and at the wall, where no-slip condition implies that the value of the dissipation rate is 0. On the symmetry line and at the outlet the Neuman BC are applied and set to 0.

Magnetic Field and Scalar Potential

The BC for the electric current density are determined by the electric conductivity of the wall and of the fluid, the applied magnetic field and the velocity. The Dirichlet BC are used for the values of magnetic field on all of the boundaries.

The values are calculated with the Biot-Savart equation (Eq. 2.95). Either of the BC types can be used to calculate the scalar potential. The boundaries can be either insulating, conducting or perfectly conducting. The scalar potential is determined with the Neuman BC, when the boundary is insulating

$$\frac{\partial \phi}{\partial \mathbf{n}} = (\mathbf{v} \times \mathbf{B})_{BC} \cdot \mathbf{n} = 0, \tag{2.109}$$

with the Dirichlet BC when the boundary is perfectly conducting, $\phi = 0$, and with the Robin BC, when the boundary is conducting.

Species Concentration

Dirichlet BC are prescribed for the species concentration on the walls. The Neuman BC are prescribed for species concentration and set to 0 on the inlet, outlet, free surface and symmetry line.

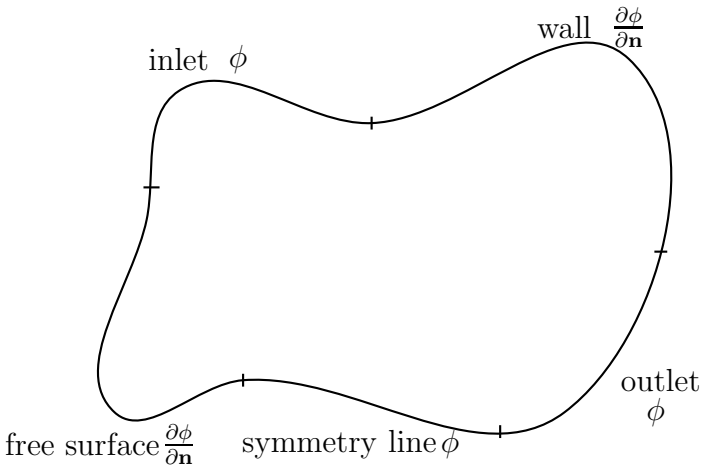

Figure 2.3: Schematic representation of general boundary conditions for magnetic field.

2.5.3 Initial Conditions

The initial conditions have to be either set or prescribed for each of the transport variables.

Velocity

Initial values for the velocity field are calculated from

$$\mathbf{v} = \nabla \phi_v, \tag{2.110}$$

where the velocity potential ϕ_v is obtained by solving the Laplace equation

$$\nabla^2 \phi_v = 0, \tag{2.111}$$

and applying the boundary conditions defined in the previous section (Sect. 2.5.2).

Temperature

Initial values for temperature are prescribed and set to a constant value T_0.

Pressure

Initial values for pressure are set to ambivalent pressure which is in turn set to 0.

k and ε

Initial values for k and ε are prescribed and set to a constant uniform value.

Magnetic Field

Initial values for magnetic field B_0 are calculated from the Biot-Savart equation (Eq. 2.95). The values for the scalar potential are calculated from Poisson's equation (Eq. 2.92), by using boundary conditions defined in the previous section (Sect. 2.5.2).

Species concentration

Initial value for species concentrations are set to a constant, predefined value.

3 Local Radial Basis Function Collocation Method

Meshless methods are the numerical simulation algorithms that in general use a set of arbitrarily distributed nodes, both in the domain Ω and on its boundary Γ, to represent the solution of a physical phenomenon. One of the simplest among them is the LRBFCM [Šarler and Vertnik, 2006]. The general idea behind this meshless method is to construct the approximation function on the local group of nodes, the so-called influence domain, where in collocation version the number of points matches the number of basis functions. On the other hand, in the least squares approximation version, the number of points exceeds the number of basis functions. Once the approximation function is constructed, it can be applied to the PDEs in the form of the strong formulation that describes the problem under consideration. However, it can also serve as a basis for weak formulation. In this chapter, the formulation of the LRBFCM is explained and presented. The construction of node arrangement is presented along with the selection of the local influence domain. The approximation function is given along with a selection of commonly used RBFs. Further, the collocation and the application of the method to the solution of the PDEs are explained.

3.1 Node Distribution and Influence Domain Selection

For the purposes of this work three different node arrangements (Fig. 3.1) are distinguished: the uniform node arrangement, where the nodes are equidistantly spaced and coincide with coordinate directions, the totally random node arrangement, where the distances and angles between the nodes are arbitrary, and the non-uniform node arrangement, where the distances between the nodes are not equal, but the angles are. The problem of the uniform node arrangement is the huge amount of nodes that have to be added to the entire computational domain in order to refine the small part of the domain that requires a higher node density. Such node arrangement can quickly become impractical, especially in terms of computational efficiency. Truly meshless methods imply that the node discretisation inside the computational domain can be arbitrary and that a background mesh is not needed. However, the randomly scattered nodes inside the domain may not present the optimal coverage of the domain and might be either

too scarce or too dense in certain parts of the domain. For this reason, a non-uniform node arrangement is an appropriate alternative and is therefore chosen for the purposes of this work.

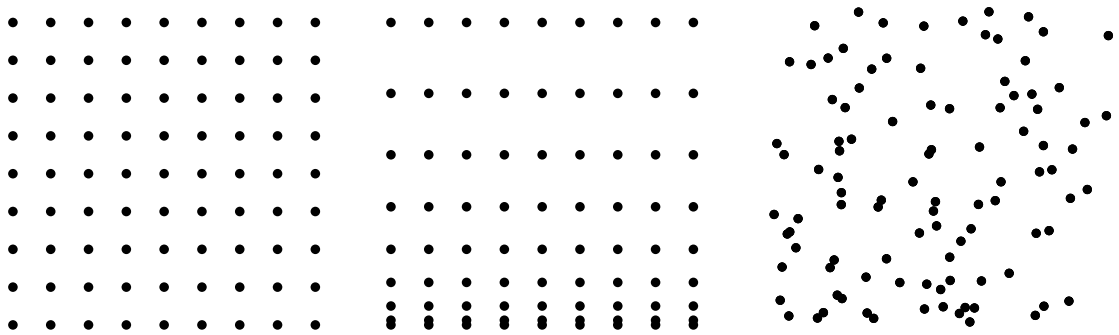

Figure 3.1: Node arrangement configurations. Left: uniform node arrangement. Middle: non-uniform node arrangement. Right: random node arrangement.

The computational domain consists of N nodes, of which N_Ω nodes lay inside the domain and N_Γ on its boundary. The total number of nodes in the computational domain is thus

$$N = N_\Omega + N_\Gamma. \tag{3.1}$$

The computational domain is divided into N_Ω overlapping influence domains or sub-domains. For an arbitrary node, chosen inside the computational domain, the influence domain is defined as a local group of neighbouring nodes that are used as a support for approximation to the chosen node. Each of the influence domains consists of N_{domain} in general non-equally spaced nodes ${}_l\mathbf{p}_i$, where $l = 1, \ldots, N_\Omega$ stands for the influence domains and i for the influence domain nodes ($i = 1, \ldots, N_{domain}$). The simplest five nodded influence domains consist of the central node and the four neighbouring nodes that are used to calculate the desired values in the central node. An example of such an influence domain is depicted in Fig. 3.2. Throughout this dissertation, the five-nodded influence domains are used.

In order to calculate the values in all of the domain nodes inside of the computational domain, the influence domains have to overlap, which means that the support node in one influence domain is the central or calculation node in the neighbouring influence domain. The overlapping of the influence domains in presented in Fig. 3.3. By making an assumption that all of the influence domains have to follow the same construction rules, it might not be possible to include some of the boundary nodes into the influence domain (for example the corner nodes as seen in Fig. 3.2). Such nodes are either defined as a BC or obtained by interpolation.

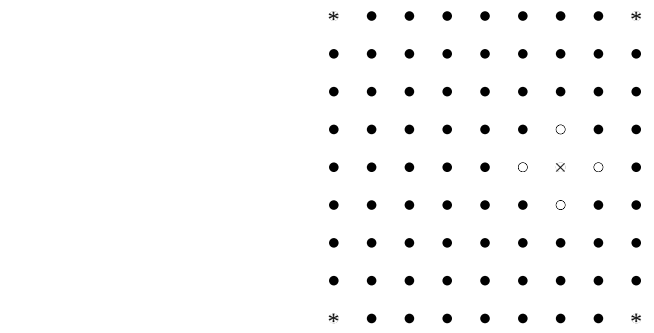

Figure 3.2: Five nodded influence domain. The calculation point is depicted with x, the supporting nodes are depicted with o, and the corner nodes are depicted with *.

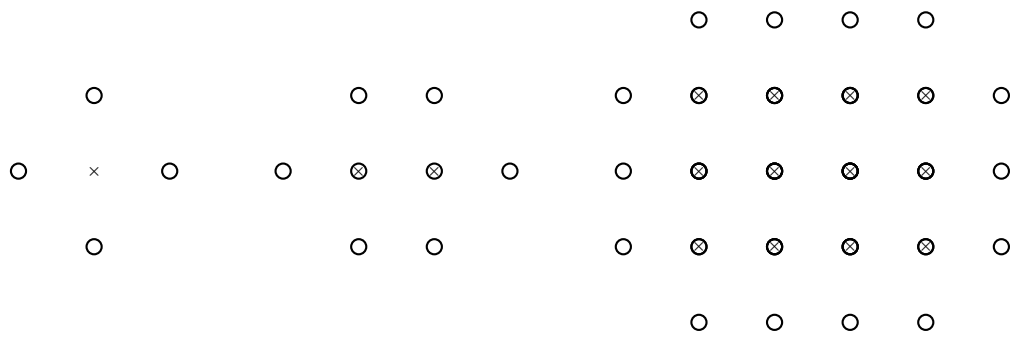

Figure 3.3: Overlapping influence domains. Left: five nodded influence domain. Middle: two overlapping influence domains. Right: computational domain with overlapping influence domains. o represents the support node. x represents the central node. $\otimes$ represents the overlapping of central and support nodes.

3.2 Approximation Function

The approximation function θ is constructed on a local influence domain l and is represented as a linear combination of the weighted basis functions ψ

$$ {}_l\theta(\mathbf{p}) = \sum_{i=1}^{N_{basis}} {}_l\psi_i(\mathbf{p})\, {}_l\alpha_i, \tag{3.2} $$

where ${}_l\alpha_i$, N_{basis}, ${}_l\psi_i$, and $\mathbf{p} = x\mathbf{i}_x + y\mathbf{i}_y + z\mathbf{i}_z$ represent the expansion coefficient, the number of basis functions, the shape function, and the support node in influence domain l, and $l = 1, \ldots, N_{domain}$. The distance between point and node j $({}_l\mathbf{p}_j = {}_lx_j\,\mathbf{i}_x + {}_ly_j\,\mathbf{i}_y + {}_lz_j\,\mathbf{i}_z)$ in influence domain l is defined as

$$ {}_lr_j = \left|\left|{}_l\mathbf{p} - {}_l\mathbf{p}_j\right|\right| = \sqrt{(x - {}_lx_j)^2 + (y - {}_ly_j)^2 + (z - {}_lz_j)^2}, \tag{3.3} $$

where $||\cdot||$ is the Euclidian norm. The basis functions that can appear in the formulation of the approximation function are the polynomials, the RBFs, the Fourier basis functions and several others. In this dissertation, the RBFs are chosen.

3.2.1 Radial Basis Functions

In general, the RBFs [Buhmann, 2003] can be divided into two groups: the infinitely smooth RBFs and the piecewise smooth RBFs. The most common RBF types among the former are the MQ RBF [Hardy, 1971], the Inverse Quadric (IQ) RBF, the Inverse Multiquadric (IMQ) RBF, and the Gaussian (GA) RBF. The Conical (CON), Cubic (CU), and Thin Plane Spline (TPS) RBFs are the most common RBF forms among the piecewise smooth RBFs. The most common of the above mentioned RBF forms are described bellow, together with their first and second derivatives.

Multiquadric Radial Basis Function

The MQ RBF is defined as

$$\psi_{MQ}(r) = \sqrt{r^2 + c^2}, \tag{3.4}$$

where c stands for the shape parameter. The parameter c controls the shape of the function. It is either predetermined to some fixed non-zero real value or set as a part of the solution. The first derivatives of the MQ are calculated from

$$\frac{\partial \psi_{MQ}}{\partial r} = r\,(r^2 + c^2)^{-\frac{1}{2}}, \tag{3.5}$$

and the second derivatives of MQ are

$$\frac{\partial^2 \psi_{MQ}}{\partial r^2} = (r^2 + c^2)^{-\frac{1}{2}} - r^2\,(r^2 + c^2)^{-\frac{3}{2}}. \tag{3.6}$$

The MQ RBFs are presented in Fig. 3.4 as a function of a shape parameter. Unless otherwise stated, the MQ RBFs are used in this dissertation.

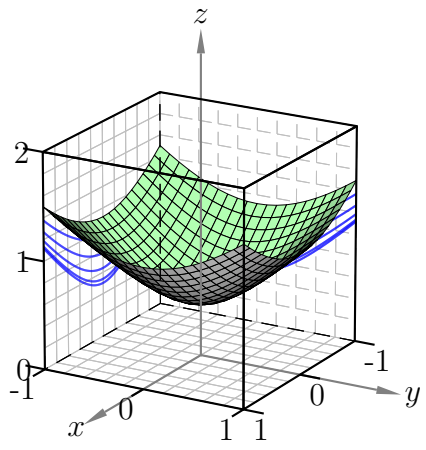

Figure 3.4: MQ RBF with the shape parameter $c = 0.5$.

Inverse Quadric Radial Basis Function

The IQ RBF shown in Fig. 3.5 is defined as

$$\psi_{IQ}(r) = \frac{1}{r^2 + c^2}. \tag{3.7}$$

The first derivatives of the IQ RBFs are

$$\frac{\partial \psi_{IQ}}{\partial r} = -2\, r\, (r^2 + c^2)^{-2}, \tag{3.8}$$

and the second derivatives of the IQ RBFs are

$$\frac{\partial^2 \psi_{IQ}}{\partial r^2} = -2(r^2 + c^2)^{-2} + 8\, r^2\, (r^2 + c^2)^{-3}. \tag{3.9}$$

The IQ RBFs are depicted in Fig. 3.5.

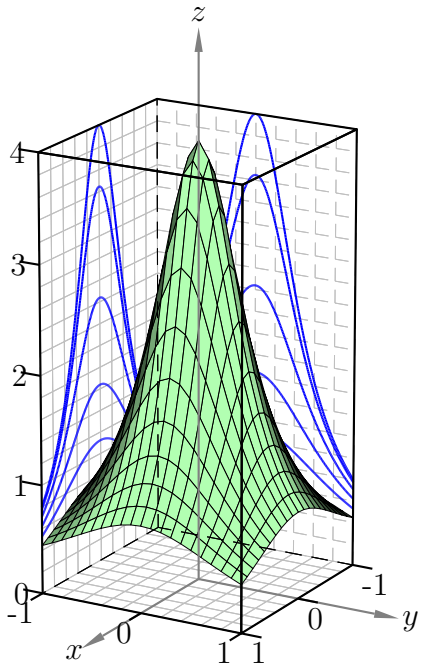

Figure 3.5: IQ RBF with the shape parameter $c = 0.5$.

Inverse Multiquadric Radial Basis Function

The IMQ RBF is defined as

$$\psi_{IMQ}(r) = \frac{1}{\sqrt{r^2 + c^2}}, \tag{3.10}$$

with the first derivative

$$\frac{\partial \psi_{IMQ}}{\partial r} = -r\, (r^2 + c^2)^{-\frac{3}{2}}, \tag{3.11}$$

and the second derivative

$$\frac{\partial^2 \psi_{IMQ}}{\partial r^2} = -(r^2 + c^2)^{-\frac{3}{2}} + 3\, r^2 (r^2 + c^2)^{-\frac{5}{2}}. \tag{3.12}$$

The IMQ RBF for $c = 0.5$ is plotted in Fig. 3.6.

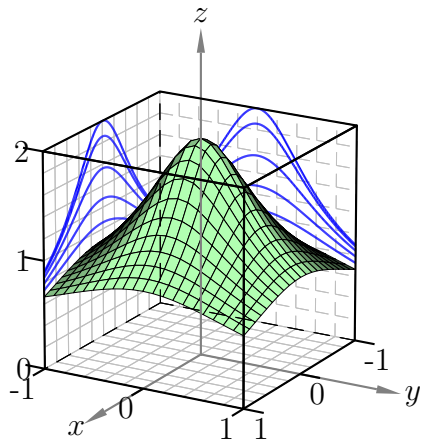

Figure 3.6: IMQ RBF with the shape parameter $c = 0.5$.

Gaussian Radial Basis Function

The GA RBF that are depicted in Fig. 3.7 are written as

$$\psi_{GA}(r) = e^{-(c\,r)^2}. \tag{3.13}$$

The first derivative of the GA RBF is

$$\frac{\partial \psi_{GA}}{\partial r} = -2\,c^2\,r\,e^{-(c\,r)^2}, \tag{3.14}$$

and the second derivative of the GA RBF is

$$\frac{\partial^2 \psi_{GA}}{\partial r^2} = \left(4\,c^4\,r^2 - 2\,c^2\right) e^{-(c\,r)^2}. \tag{3.15}$$

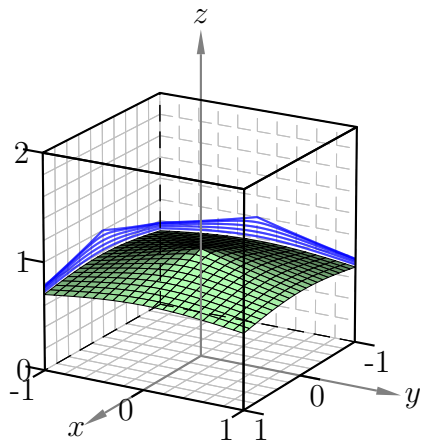

Figure 3.7: GA RBF with the shape parameter $c = 0.5$.

Conical Radial Basis Function

The CON RBF shown in Fig. 3.8 is defined as

$$\psi_{CON}(r) = r + c, \tag{3.16}$$

with the first derivative

$$\frac{\partial \psi_{CON}}{\partial r} = 1, \tag{3.17}$$

and the second derivative

$$\frac{\partial \psi_{CON}}{\partial r} = 0. \tag{3.18}$$

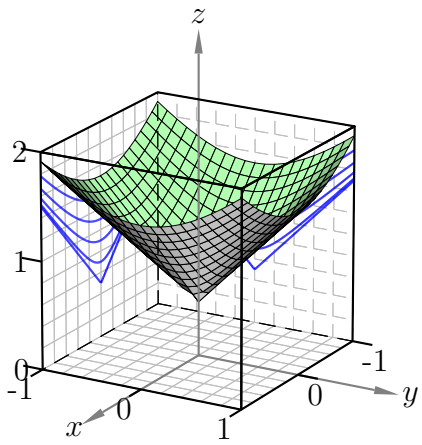

Figure 3.8: CON RBF with the shape parameter $c = 0.5$.

Cubic Radial Basis Function

The CU RBF is written as

$$\psi_{CU}(r) = (\sqrt{r^2 + c^2})^3. \tag{3.19}$$

Its first derivative is

$$\frac{\partial \psi_{CU}}{\partial r} = 3\, r\, \sqrt{r^2 + c^2}, \tag{3.20}$$

and its second derivative is

$$\frac{\partial^2 \psi_{CU}}{\partial r^2} = 3\, \sqrt{r^2 + c^2} + \frac{3r^2}{r^2 + c^2}. \tag{3.21}$$

The CU RBF is plotted in Fig. 3.9 for shape parameter $c = 0.5$.

Thin Plane Spline Radial Basis Function

The TPS RBF is defined as

$$\psi_{TPS}(r) = (r^2 + c^2)\, \ln\left(\sqrt{r^2 + c^2}\right), \tag{3.22}$$

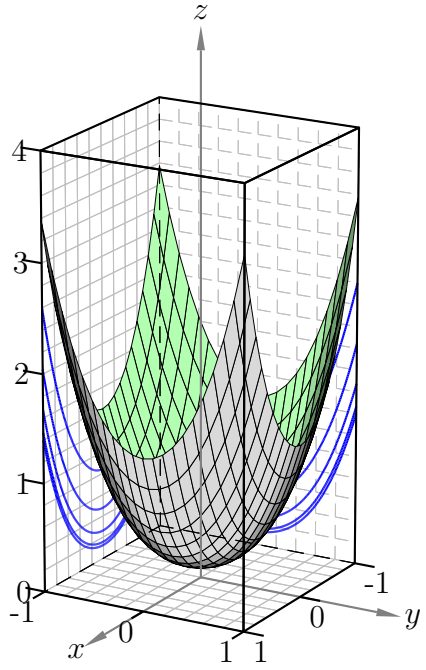

Figure 3.9: CU RBF with the shape parameter $c = 0.5$.

with the first derivative written as

$$\frac{\partial \psi_{TPS}}{\partial r} = \frac{1}{2}\big(r \, \ln\left(r^2 + c^2\right) + r\big), \tag{3.23}$$

and its second derivative written as

$$\frac{\partial \psi_{TPS}}{\partial r^2} = \frac{1}{2}\big(\ln\left(r^2 + c^2\right) + \frac{2\,r^2}{r^2 + c^2} + 1\big). \tag{3.24}$$

The TPS RBF is presented in Fig. 3.10 for $c = 0.5$.

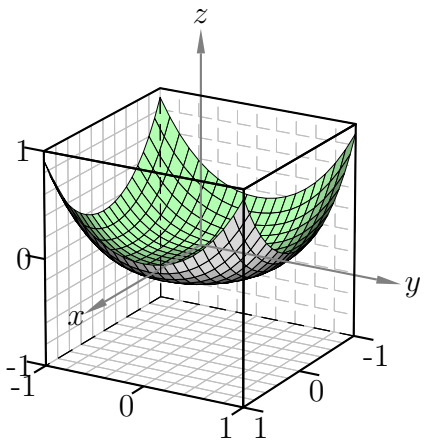

Figure 3.10: TPS RBF with the shape parameter $c = 0.5$.

The value of the shape parameter c is determined by normalizing the distances between the central and the support nodes in the influence domain region. The

distance between two points ${}_{l}r_j$ is scaled in x, y, and z direction, and is calculated as

$$ {}_{l}r_j = \left|\left|\mathbf{p} - {}_{l}\mathbf{p}_j\right|\right| = \sqrt{\left(\frac{x - {}_{l}x_j}{{}_{l}x_{MAX}}\right)^2 + \left(\frac{y - {}_{l}y_j}{{}_{l}y_{MAX}}\right)^2 + \left(\frac{z - {}_{l}z_j}{{}_{l}z_{MAX}}\right)^2}, \tag{3.25} $$

where ${}_{l}x_{MAX}$, ${}_{l}y_{MAX}$ and ${}_{l}z_{MAX}$ are the maximum distances between the central node and the pertained support node in x, y, and z direction, respectively.

3.2.2 Collocation

The expansion coefficients $\boldsymbol{\alpha}$ of the approximation function θ are determined by collocation and depend on the number and shape of the basis functions, values in node positions, and positions of the nodes[1]. The most straightforward way to determine the coefficients is to set the number of the basis functions in such a way, that it equals the number of the domain nodes ($N_{basis} = N_{domain}$). The collocation condition

$$ \theta({}_{l}\mathbf{p}_j) = {}_{l}\theta_j, \tag{3.26} $$

where ${}_{l}\theta_j$ is the corresponding data value and $j = 1, \ldots, N_{domain}$ has to be satisfied for all of the points in the influence domain. By considering the collocation condition, for each of the j calculation nodes in an influence domain l a linear system of N_{domain} equations is obtained

$$ {}_{l}\boldsymbol{\Psi}\, {}_{l}\boldsymbol{\alpha} = {}_{l}\boldsymbol{\theta}, \tag{3.27} $$

or

$$ \begin{bmatrix} \Psi_{11} & \cdots & \Psi_{1N_{domain}} \\ \vdots & \ddots & \vdots \\ \Psi_{N_{domain}1} & \cdots & \Psi_{N_{domain}N_{domain}} \end{bmatrix} \begin{bmatrix} \alpha_1 \\ \vdots \\ \alpha_{N_{domain}} \end{bmatrix} = \begin{bmatrix} \theta_1 \\ \vdots \\ \theta_{N_{domain}} \end{bmatrix}, \tag{3.28} $$

where ${}_{l}\boldsymbol{\Psi}$, ${}_{l}\boldsymbol{\alpha}$, and ${}_{l}\boldsymbol{\theta}$ represent the matrix of the RBFs, the vector of the expansion coefficients, and the vector of corresponding data values respectively. If the basis matrix ${}_{l}\boldsymbol{\Psi}$ is non-singular [Hon and Schaback, 2001], the expansion coefficient of each influence domain can be calculated by multiplying Eq. 3.27 by its inverse ${}_{l}\boldsymbol{\Psi}^{-1}$

$$ {}_{l}\boldsymbol{\alpha} = {}_{l}\boldsymbol{\Psi}^{-1}\, {}_{l}\boldsymbol{\theta}. \tag{3.29} $$

The approximation function of the influence domain can then be rewritten in the following way

$$ {}_{l}\theta(\mathbf{p}) = \sum_{i=1}^{N_{domain}} {}_{l}\psi_i(\mathbf{p}) \sum_{j=1}^{N_{domain}} {}_{l}\psi_{ij}^{-1}(\mathbf{p})\, {}_{l}\theta_j. \tag{3.30} $$

[1] As the number of the influence domain nodes is constant and the same in all of the influence domains, the number of nodes in a influence domain is denoted as N_{domain} instead of ${}_{l}N_{domain}$.

3.3 Solving Partial Differential Equations with Radial Basis Functions

In order to be able to solve the PDEs of the physical model, the first and the second derivatives of the approximation function θ (Eq.3.30) must be calculated in the influence domain. In general, the operator applied on the approximation function is expressed as [Kansa, 1990a,b]

$$\frac{\partial^n}{\partial r_i^n}\,{}_l\theta(\mathbf{p}) = \sum_{j=1}^{N_{domain}} \frac{\partial^n}{\partial r_i^n}\,{}_l\psi_j(\mathbf{p})\,{}_l\alpha_j, \tag{3.31}$$

where the index n represents the order of the derivative. On the boundary, either of the three commonly used BC (Dirichlet, Neuman or Robin BC) can be applied. The implementation of the Dirichlet BC is straightforward as the value of the function on the boundary is prescribed $\theta(\mathbf{p}) = \theta_{BC}$. On the other hand, collocation has to be used in order to satisfy the BC for the Neuman

$$\frac{\partial}{\partial \mathbf{n}}\,{}_l\theta(\mathbf{p}) = \sum_{j=1}^{N_{domain}} \frac{\partial}{\partial \mathbf{n}}\,{}_l\psi_j(\mathbf{p})\,{}_l\alpha_j \tag{3.32}$$

and the Robin

$$a\frac{\partial}{\partial \mathbf{n}}\,{}_l\theta(\mathbf{p}) + b\,{}_l\theta(\mathbf{p}) = \sum_{j=1}^{N_{domain}} \left(a\frac{\partial}{\partial \mathbf{n}}\,{}_l\psi_j(\mathbf{p}) + b\,{}_l\psi_j(\mathbf{p})\right)\,{}_l\alpha_j \tag{3.33}$$

boundaries.

4 Solution Procedure

This chapter describes the solution procedure of the developed numerical method for the incompressible turbulent flow with solidification and under the influence of externally applied magnetic field. In general, the solution procedure consists of three parts: the preprocessing, the main part, and the post-processing as shown in Fig. 4.1. First, the preprocessing that covers the application of numerical tools, such as construction of the computational node arrangement, determination of numerical implementation (RBF or PV coupling type), and time and space discretization, that are required for implementation of the chosen numerical method to the physical model are addressed. The main part of the solution procedure including the solution scheme for the general transport equation is presented next, along with the computational algorithm for the Poisson's equation and the PV coupling. Next, the solution procedure for the full set of governing equations is presented along with the convergence criteria that is needed to determine when the time-marching can be stopped. The last part of the solution procedure, namely the post-processing, is not covered explicitly as the external programs such as Gnuplot [Williams and Kelley, 2010] and ParaView [Henderson, 2007] are standardly used to analyse and process the obtained data. The results of this part of the solution procedure are presented in Sect. 5 and Sect. 6.

4.1 Distribution of Computational Nodes

Each simulation starts with the construction of the discretization nodes. For the purpose of this work, a non-uniform node distribution is built from the uniform node arrangement in the following way. First, a uniform node distribution $y_{uniform}$ is defined between points y_1 and y_2 as [Vertnik, 2010; Mramor et al., 2013b,a]

$$y_{s,uniform} = y_1 + (s-1)\frac{y_2 - y_1}{N-1}, \tag{4.1}$$

where $s = 1, \ldots, N_s$ and N_s is the number of nodes between and points y_1 and y_2. Distance between the edge nodes is then normalized to the interval $[0, 1]$ as

$$y^{norm}_{s,uniform} = \frac{y_{s,uniform} - y_1}{y_2 - y_1}. \tag{4.2}$$

Further, the refined normalized node distribution $y^{norm}_{refined}$ is calculated as

$$y^{norm}_{s,refined} = 1.0 - (1.0 - y^{norm}_{s,uniform})^u, \tag{4.3}$$

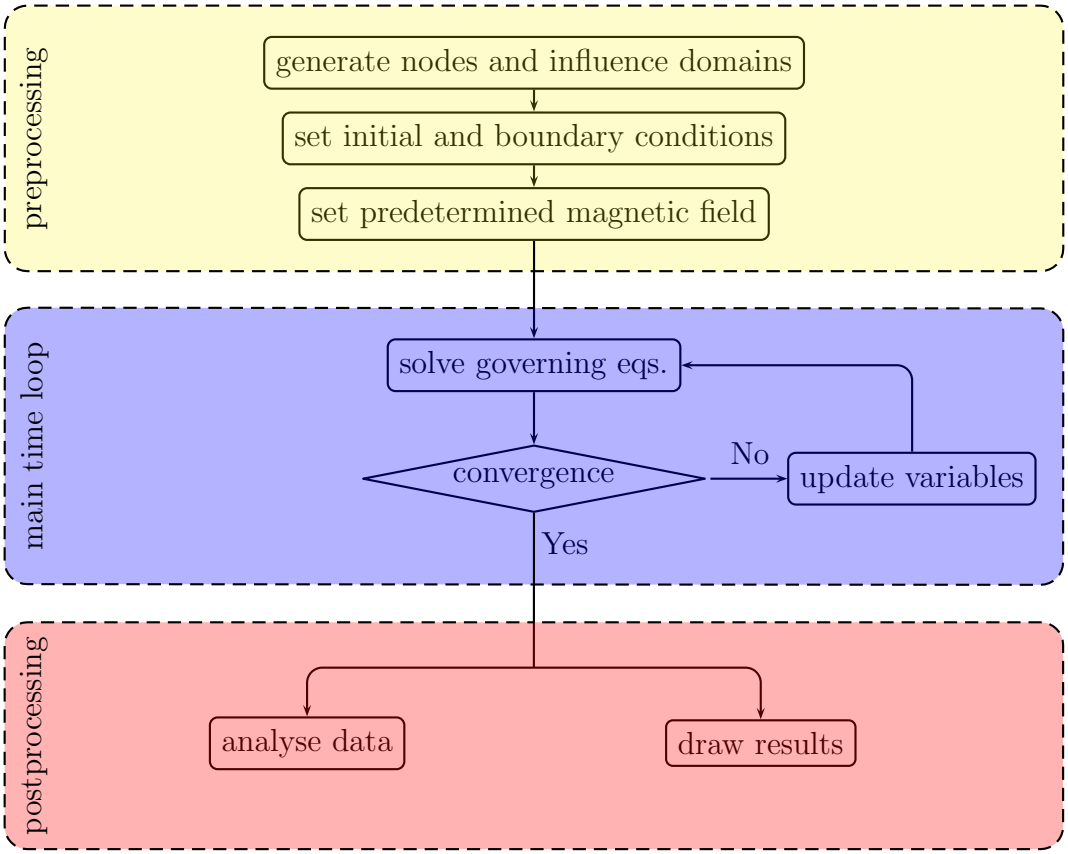

Figure 4.1: Flow chart of solution procedure.

where u stands for the refinement level. Finally, the refinement is rescaled to the original interval $[y_1, y_2]$

$$y_{s,refined} = y_1 + y^{norm}_{s,refined}(y_2 - y_1). \tag{4.4}$$

The procedure is depicted in Fig. 4.2 for the refinement parameter $u = 2$. The same procedure is used to refine the node arrangement in the x direction.

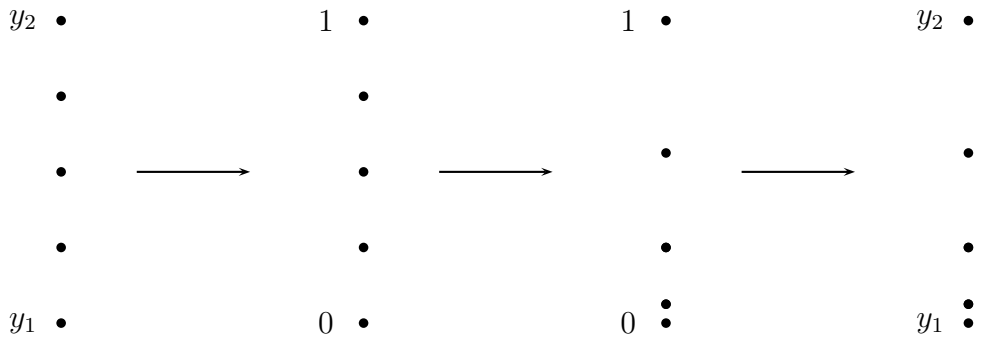

Figure 4.2: Refinement steps of the node refinement process in y direction.

When the geometry of the problem requires a more complex refinement pattern, e.g. refinement in the middle of the interval, such as where the upper node

part of the interval requires the $u = 1.2$ and the lower the $u = 1.6$, the interval is divided into smaller parts. The desired refinement is applied separately on each of the smaller intervals, which are then joined together.The schematics of this process is shown in Fig. 4.3.

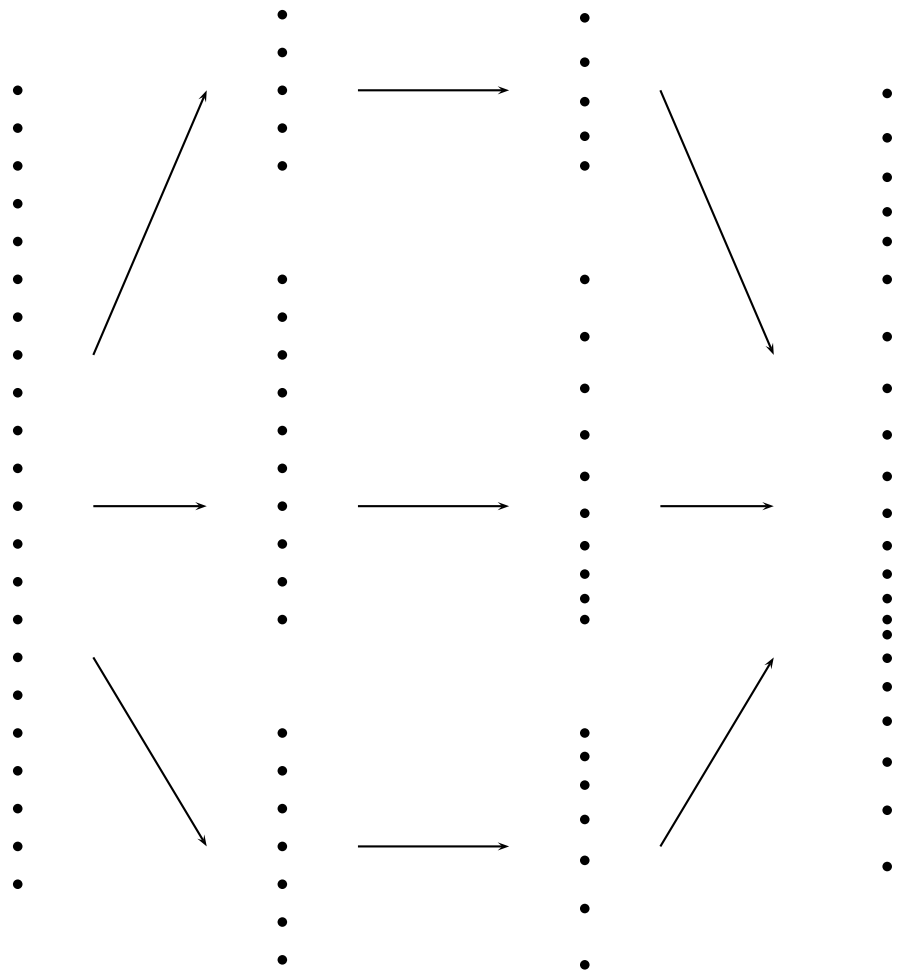

Figure 4.3: A more complex refinement steps of the node refinement process in y direction.

4.2 Time Discretization

The CC process is a transient problem and is as such both space and time dependent and therefore requires both space and time discretization. The objective of the discretization is to replace the derivatives with the difference expressions and thus obtain the algebraic formulation of the equation. The most common time discretization methods are the explicit, implicit, and semi-implicit procedures.

Explicit time discretization

The scheme is explicit when the dependent variables at a future time $t_0 + \Delta t$ can be computed directly from the known variables at current or actual time t_0. In

the obtained algebraic equation, only one unknown variable has to be calculated. As the solution of such algebraic equations is straightforward, it is easy to implement and parallelize, and has low computational cost per time-step. The major drawback of the explicit time discretization scheme is its conditional stability. As the scheme is not necessarily stable, one has to be very careful when choosing the time step, which can quickly become impractically small, especially when solving stiff problems. In general, either the Courant-Friedrichs-Levy [Schär, 2014]

$$\mathrm{Cu} = \frac{v\Delta t}{\Delta x} < 1 \tag{4.5}$$

or the von-Neumann stability [Wright and Fornberg, 2006] criteria

$$\mathrm{G} = \frac{D\Delta t}{\Delta x^2} \leq \frac{1}{2} \tag{4.6}$$

can be implemented to assure, that the explicit time scheme is stable. Here Cu is the Courant number, and the G is diffusion number.

The representative explicit time discretization methods are the forward Euler explicit method, the Leap-frog method and various predictor corrector methods such as the Runge-Kutta or the Adams-Bashforth methods. The explicit time discretization scheme is schematically represented in Fig. 4.5.

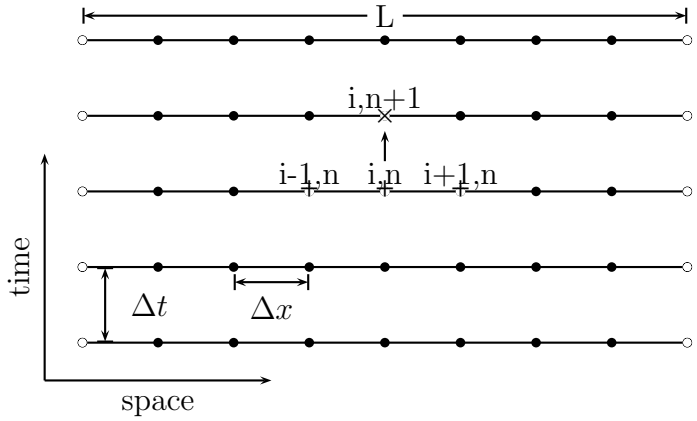

Figure 4.4: Explicit time discretization scheme; ∘ - boundary nodes, + - nodes at time t_0, x - nodes at time $t_0 + \Delta t$.

Implicit Time Disretization

The scheme is implicit when the variables at a future time $t_0 + \Delta t$ cannot be expressed only with the known variables at current time t_0. The algebraic equation, that is thus obtained, consists of several unknown variables. The solution of the implicit scheme therefore requires the solution of a system of linear equations in each time step. The implicit time discretization scheme is more complex and more difficult to implement and parallelize than the explicit time discretization scheme. Consequently, the computational cost per time step is higher. However, the procedure is unconditionally stable, which means that the higher computational cost

can be compensated with the larger time steps. The representative implicit time discretization methods are the backward Euler method and the Adams-Moulton method [Ferziger and Perić, 1996]. The implicit time discretization scheme is schematically represented in Fig. 4.5.

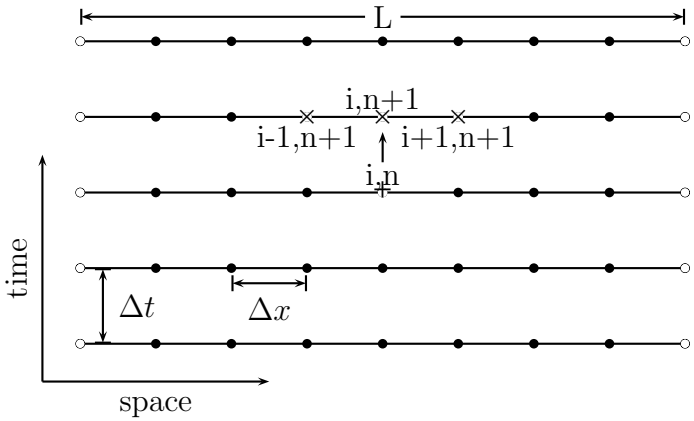

Figure 4.5: Implicit time discretization scheme; ∘ - boundary nodes, + - nodes at time t_0, x - nodes at time $t_0 + \Delta t_0$.

Semi-implicit Time Discretization

The semi-implicit time discretization schemes are a combination of implicit and explicit time discretization schemes, using the former to calculate some of the terms and the later to calculate the rest. The most widely used semi-implicit time discretization methods are the Crank-Nicolson and the Euler-Cromer methods. The semi-implicit time discretization scheme is schematically represented in Fig. 4.6.

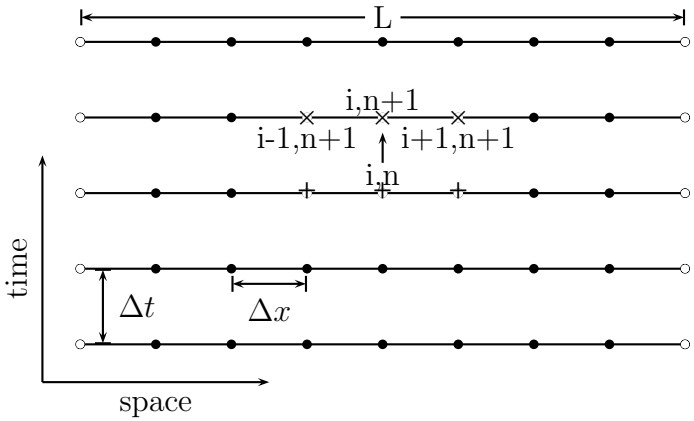

Figure 4.6: Semi-implicit time discretization scheme; ∘ - boundary nodes, + - nodes at time t_0, x - nodes at time $t_0 + \Delta t$.

Among the above described types of time discretization procedures the explicit scheme is used in the present work, due to its simplicity and straightforward numerical implementation. In this instance, another advantage of explicit time

discretization is the option of applying the method locally, as all of the required variable values are known for current time. As opposed to the explicit approach, the implicit and semi-implicit schemes require the solution of a global system for all unknowns at $t_0 + \Delta t$.

4.3 Solution Procedure for the General Transport Equation

The governing equations of the physical model are space and time dependent and are as such described by infinite degrees of freedom. In numerical solution, the continuous equations have to be replaced with a discrete approximation, and hence the continuous functions are matched by formulas with finite degrees of freedom. The problem under consideration is thus reduced to the solution of algebraic equations. In this work, the time discretization is performed with the explicit first-order approximation (explicit Euler) scheme while the space discretization is done with collocation with RBFs.

All of the governing equations follow the conservation principle and can be described with a general transport equation, which consists of four terms: the transient term, the convection term, the diffusion term and the source term

$$\underbrace{\frac{\partial(\rho\Phi)}{\partial t}}_{Transient\ term} + \underbrace{\nabla\cdot(\rho\mathbf{v}\Phi)}_{Convection\ term} = \underbrace{\nabla\cdot(D\nabla\Phi)}_{Diffusion\ term} + \underbrace{S_\Phi,}_{Source\ term} \tag{4.7}$$

where Φ stands for the dependent variable and S_Φ for the source term. The terms of the general transport equations are given in Tab. 4.1.

The explicit Euler time discretization of the general transport equation (Eq. 4.7) at time t_0 is

$$\frac{\rho_0\Big(\Phi(t_0+\Delta t)-\Phi(t_0)\Big)}{\Delta t} = -\nabla\cdot\big(\rho_0\mathbf{v}\Phi(t_0)\big) + \nabla\cdot\big(D\nabla\Phi(t_0)\big) + S_\Phi(t_0), \tag{4.8}$$

where $\Phi(t_0 + \Delta t)$ and $\Phi(t_0)$ represent the value of the sought for variable at time $t_0 + \Delta t_0$ and at time t_0, and ρ_0 represents the value of density at time t_0. Consequently, the value of sought for variable at the new time step $\Phi(t_0 + \Delta t)$ is expressed as

$$\Phi(t_0+\Delta t) = \Phi(t_0) + \frac{\Delta t}{\rho_0}\Big(-\nabla\cdot\big(\rho_0\mathbf{v}\Phi(t_0)\big) + \nabla\cdot\big(D\nabla\Phi(t_0)\big) + S_\Phi(t_0)\Big). \tag{4.9}$$

The individual terms on the right side of the equation are rewritten in an extended form as

$$\nabla\cdot\Big(\rho_0\mathbf{v}\Phi\Big) = \Phi\nabla\cdot\big(\rho_0\mathbf{v}\big) + \rho_0\mathbf{v}\nabla\cdot\Phi \tag{4.10}$$

and

$$\nabla\cdot\Big(D\nabla\Phi\Big) = \nabla D\cdot\nabla\Phi + D\nabla^2\Phi \tag{4.11}$$

Table 4.1: Terms in general transport equation.

	Φ	Diffusion	S_Φ
mass	1	0	0
momentum	$\mathbf{v}$	$-\nabla p - \frac{2}{3}\nabla(\rho k)$ $+\nabla\cdot\Big(\big(\mu_L\frac{\rho}{\rho_L}+\mu_t\big)\big((\nabla\mathbf{v})+(\nabla\mathbf{v})^T\big)\Big)$	$-\mu_L\frac{K_0(1+f_L)^2}{f_{L^3}}\frac{\rho}{\rho_L}\big(\mathbf{v}-\mathbf{v}_S\big)$ $+\rho\mathbf{g}\Big(\beta_T\big(T-T_{ref}\big)+\beta_C\big(C-C_{ref}\big)\Big)+\mathbf{j}\times\mathbf{B}$
energy	h	$\nabla\cdot\big(\lambda\nabla T\big)+\nabla\cdot\Big(f_L\frac{\mu_t}{\sigma_t}\nabla h_L\Big)$ $+\nabla\cdot\Big(\rho f_S\big(h_L-h_S\big)\big(\mathbf{v}-\mathbf{v}_S\big)\Big)$	$\frac{\lvert\mathbf{j}\rvert^2}{\sigma}$
species	C	$\nabla\cdot\Big(\rho f_S D_S\nabla C_S+\rho f_L D_L\nabla C_L\Big)+\nabla\cdot\Big(\frac{f_L\mu_t}{\sigma_C}\nabla C_L\Big)$ $+\nabla\cdot\Big(\rho f_L\big(\mathbf{v}-\mathbf{v}_S\big)\big(C_L-C\big)\Big)$	0
turbulent kinetic energy	k	$\nabla\cdot\Big(\big(\mu_L\frac{\rho}{\rho_L}+\frac{\mu_t}{\sigma_k}\big)\nabla k\Big)$	$P_k+G_k-\rho\varepsilon+\rho D_{k-\varepsilon}+\mu_L\frac{K_0\big(1+f_L\big)^2}{f_L^3}\frac{\rho}{\rho_L}k$
dissipation rate	ε	$\nabla\cdot\Big(\big(\mu_L\frac{\rho}{\rho_L}+\frac{\mu_t}{\sigma_\varepsilon}\big)\nabla\varepsilon\Big)$	$\big(c_{1\varepsilon}f_1(P_k+c_{3\varepsilon}G_k)-c_{2\varepsilon}f_2\rho\varepsilon\big)\frac{\varepsilon}{k}$ $+\rho E_{k-\varepsilon}+\mu_L\frac{K_0(1+f_L)^2}{f_L^3}\frac{\rho}{\rho_L}\varepsilon$

in order to be able to apply the spatial disretization in a more straightforward way. The first term in Eq. 4.10 takes the following form after the implementation of spatial discretization

$$\nabla \cdot \big(\rho_0 \mathbf{v}\big)_l = \sum_{i=1}^{N_{domain}} \frac{\partial}{\partial x_j} {}_l\psi_i \sum_{n=1}^{N_{domain}} {}_l\psi_{in}^{-1}\, {}_l\big(\rho_0 \mathbf{v}\big)_n \tag{4.12}$$

and the second term in Eq. 4.10 is rewritten as

$$\nabla \cdot \Phi_l = \sum_{i=1}^{N_{domain}} \frac{\partial}{\partial x_j} {}_l\psi_i \sum_{n=1}^{N_{domain}} {}_l\psi_{in}^{-1}\, {}_l\Phi_n. \tag{4.13}$$

Similarly, the first term in Eq. 4.11 is rephrased as

$$\nabla D_l \cdot \nabla \Phi_l = \sum_{i=1}^{N_{domain}} \frac{\partial}{\partial x_j} {}_l\psi_i \sum_{n=1}^{N_{domain}} {}_l\psi_{in}^{-1} {}_lD_n \cdot \sum_{i=1}^{N_{domain}} \frac{\partial}{\partial x_j} {}_l\psi_i \sum_{n=1}^{N_{domain}} {}_l\psi_{in}^{-1} {}_l\Phi_n, \tag{4.14}$$

and the second term as

$$D_l \nabla^2 \Phi_l = D_l \sum_{i=1}^{N_{domain}} \frac{\partial^2}{\partial x_j^2} {}_l\psi_i \sum_{n=1}^{N_{domain}} {}_l\psi_{in}^{-1} {}_l\Phi_n. \tag{4.15}$$

By using the above described procedure for time (Sect. 4.2) and space discretization (Sect. 3) Eq. 4.8 becomes

$$\begin{aligned}
\Phi(t_0 + \Delta t)_l &= \Phi(t_0)_l + \frac{\Delta t}{\rho_0}\Big(\Phi_l \sum_{i=1}^{N_{domain}} \frac{\partial}{\partial x_j} {}_l\psi_i \sum_{n=1}^{N_{domain}} {}_l\psi_{in}^{-1}\, {}_l\big(\rho \mathbf{v}\big)_n \\
&- \big(\rho_0\, \mathbf{v}\big)_l \sum_{i=1}^{N_{domain}} \frac{\partial}{\partial x_j}\, {}_l\psi_i \sum_{n=1}^{N_{domain}} {}_l\psi_{in}^{-1}\, {}_l\Phi_n \\
&+ \sum_{i=1}^{N_{domain}} \frac{\partial}{\partial x_j}\, {}_l\psi_i \sum_{n=1}^{N_{domain}} {}_l\psi_{in}^{-1}\, {}_lD_n \cdot \sum_{i=1}^{N_{domain}} \frac{\partial}{\partial x_j}\, {}_l\psi_i \sum_{n=1}^{N_{domain}} {}_l\psi_{in}^{-1}\, {}_l\Phi_n \\
&+ D_l \sum_{i=1}^{N_{domain}} \frac{\partial^2}{\partial x_j^2}\, {}_l\psi_i \sum_{n=1}^{N_{domain}} {}_l\psi_{in}^{-1}\, {}_l\Phi_n + {}_lS_\Phi \Big)_0 .
\end{aligned} \tag{4.16}$$

The solution of the discretized general transport equation by setting the values of the domain and boundary nodes to the initial values and calculating the derivatives at time $t = t_0$. The value of Φ is then calculated from Eq. 4.16. Once the values for all of the interior nodes are calculated from Eq. 4.17, the domain boundary is considered by implementing the BCs. While the application of the Dirichlet BC is straightforward

$$\Phi_{Dirichlet} = \Phi, \tag{4.17}$$

the Neuman and Robin BC are calculated from Eqs. 2.106 as

$$\Phi_{Neuman} = \sum_{i=1}^{N} \frac{\partial}{\partial \mathbf{n}} \psi_i\, \alpha_i \tag{4.18}$$

and

$$\Phi_{Robin} = \sum_{i=1}^{N} \left(w_1 \frac{\partial}{\partial \mathbf{n}} \psi_i + w_2 \psi_i \right) \alpha_i. \tag{4.19}$$

Next, the coefficients α_i are calculated from the system of linear equations (Eq. 3.29) and the procedure is ready for the next step. The time stepping is stopped, when the solution reaches the steady state or when the calculation reaches a predetermined time. The criteria for steady state is described in Sect. 4.7.

In this dissertation, the above described procedure is used for mass, energy, species, turbulent kinetic energy and dissipation rate conservation equations. The solution procedure for momentum equation is slightly different and is described in Sec. 4.4.

4.4 Pressure - Velocity Coupling

Although the solution procedure of all of the transport equations is similar, the momentum equation requires special treatment when the problem under consideration describes the incompressible flow. In the case of compressible flow, the pressure is a function of both density and temperature, and the momentum equation is solved as described above (Sect. 4.3). However, when the flow is incompressible, the pressure is not explicitly linked to density. Hence, additional constraints linking pressure and velocity have to be included into the solution. This problem is referred to as the PV coupling. The most widely used algorithm for solving the pressure velocity coupled problems is the SIMPLE [Ferziger and Perić, 1996; Patankar, 1980] algorithm and its various modifications, like the SIMPLE Consistent (SIMPLEC) [van Doormaal and Raithby, 1984; Latimer and Pollard, 1985], the SIMPLER [van Doormaal and Raithby, 1984], and the Pressure Implicit with Splitting of Operators (PISO) [Jang et al., 1986; Chow and Cheung, 1997]. Another option is to use the the local PV coupling algorithm [Kosec, 2011; Kosec and Šarler, 2009b], that is based on the SIMPLE algorithm, but is calculated on the local instead of on the global domain.

Alternative options are the so called projection methods, in which the Helmholtz-Hodge decomposition [Petronetto et al., 2010] is used to decouple the pressure and the velocity. The projection methods can be split into three groups: the pressure-correction, the velocity correction, and the consistent split methods [Guermond et al., 2006]. In the pressure-correction scheme, two intermediate time sub-steps are performed in each time iteration. In the first sub-step the pressure term is ignored and the velocity is calculated without the pressure term. In the second sub-step the velocity term is corrected by the separately calculated pressure gradient. The most commonly used among the pressure-correction projection methods is the FSM [Chorin, 1967]. Another similar approach is the Artificial Compressibility Method (ACM) [Chorin, 1968] with Characteristic Base Split (CBS) [Zienkiewicz and Codina, 1995; Zienkiewicz et al., 1995]. Analogously to the pressure-correction schemes, in the velocity-correction scheme [Guermond and Shen, 2003b] the viscous term is ignored in the first time sub-step. In the second time sub-step the velocity is corrected by the independently calculated vis-

cous term. The consistent splitting scheme [Guermond and Shen, 2003a] requires the solution of the velocity equation by the explicit treatment of the pressure in the first time sub-step. In the second time sub-step, the velocity is updated by testing the pressure field against the gradients. Unless otherwise stated, the FSM method [Chorin, 1967] is used to solve the pressure velocity coupling in this dissertation.

Fractional Step Method

The FSM [Chorin, 1967] was first developed in 1967. The idea behind this method is to first calculate the intermediate velocity field $\mathbf{v}^\star$ at a new time $t_0+\Delta t$ without the pressure gradient

$$\begin{aligned}\mathbf{v}^\star(t_0+\Delta t) = \mathbf{v}(t_0) + \Bigg(\frac{\Delta t}{\rho}\Big(&- \nabla\cdot(\rho\mathbf{v}\mathbf{v}) - \frac{2}{3}\nabla(\rho k) \\ + \quad &\nabla\cdot\Big(\big(\mu_L\frac{\rho}{\rho_L}+\mu_t\big)\big(\nabla\mathbf{v}+(\nabla\mathbf{v})^T\big)\Big) - \mu_L\frac{K_0(1+f_L)^2}{f_{L^3}}\frac{\rho}{\rho_L}\big(\mathbf{v}-\mathbf{v}_S\big) \\ + \quad &\rho\mathbf{g}\Big(\beta_T\big(T-T_{ref}\big)+\beta_C\big(C-C_{ref}\big)\Big)+\mathbf{j}\times\mathbf{B}\Big)\Bigg)_0 .\end{aligned} \tag{4.20}$$

Next, the pressure Poisson equation

$$\nabla^2 p = \frac{\rho}{\Delta t}\nabla\cdot\mathbf{v}^\star \tag{4.21}$$

is solved in order to calculate the pressure, which is then used to update the velocity

$$\mathbf{v}(t_0+\Delta t) = \mathbf{v}^\star(t_0+\Delta t) - \frac{\Delta t}{\rho}\nabla p. \tag{4.22}$$

The pressure Poisson equation (Eq. 4.21) is solved by using the boundary conditions for pressure specified in Sec. 2.5.2. The flow chart is presented in Fig. 4.7.

Artificial Compressibility Method with Characteristic Base Split

The procedure behind the ACM [Chorin, 1968] is similar to the one behind the FSM. First, the intermediate velocity (Eq. 4.21) is calculated without the pressure gradient. The pressure field is obtained from the following equation

$$p(t_0+\Delta t) = p(t_0) - \beta^2\Delta t\big(\rho\nabla\cdot\mathbf{v}^\star(t_0+\Delta t) - \Delta t\nabla^2 p(t_0)\big), \tag{4.23}$$

where $-\Delta t\nabla^2 p(t_0)$ is CBS stabilization term, and β is the compressibility coefficient. Eq. 4.23 is solved by using the boundary conditions for pressure specified in Sec. 2.5.2 and The initial conditions for pressure specified in Sec. 2.5.3. Next, the pressure is inserted into Eq. 4.22 to calculate the velocity at new time step. The selection of β depends on the problem under consideration. For the CC process β is usually between 0.5 to 1.5. The flowchart is presented in Fig. 4.7.

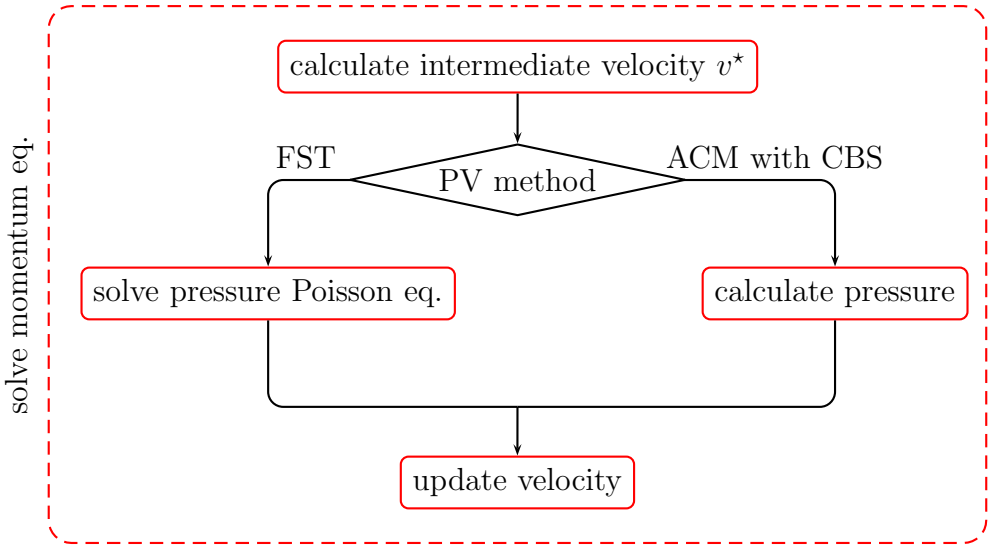

Figure 4.7: Flow chart for solving velocity and pressure.

4.5 Solution of Electromagnetic Field Equations

The electromagnetic field is coupled with the velocity field through the Lorentz force. Due to the $\mathrm{Re}_m \ll 1$, the coupling is done only in one direction. This means that the magnetic field affects the velocity field, but the velocity field does not affect the magnetic field. The procedure starts by solving the Poisson's equation for electric potential (Eq. 2.92). The solution yields $\nabla\phi$, which is inserted into

$$\mathbf{j} = \sigma\big(-\nabla\phi + \mathbf{v}\times\mathbf{B}\big) \tag{4.24}$$

in order to calculate electric current density $\mathbf{j}$. The Lorentz force is then calculated from Eq. 2.93 and inserted into the momentum equation.

Although the CC case does not require the coupling between the temperature and magnetic field, this can be done through the Joule source term, which can be added to the energy equation. The procedure for calculating the Joule source term is analogous to the procedure of calculating the Lorentz force up to the point when the electric current density is calculated. This is then inserted into the Joule source term and if necessary added to the energy equation. The flowchart is presented in Fig. 4.8.

4.6 Description of the Multiphysics Solution Procedure

In this dissertation, the original solution procedure [Vertnik, 2010] that was designed for the incompressible turbulent flow with solidification is upgraded for the application of the externally applied static magnetic field. The magnetic field is modelled by the Maxwell's equations (Eq. 2.77-2.80) through the application

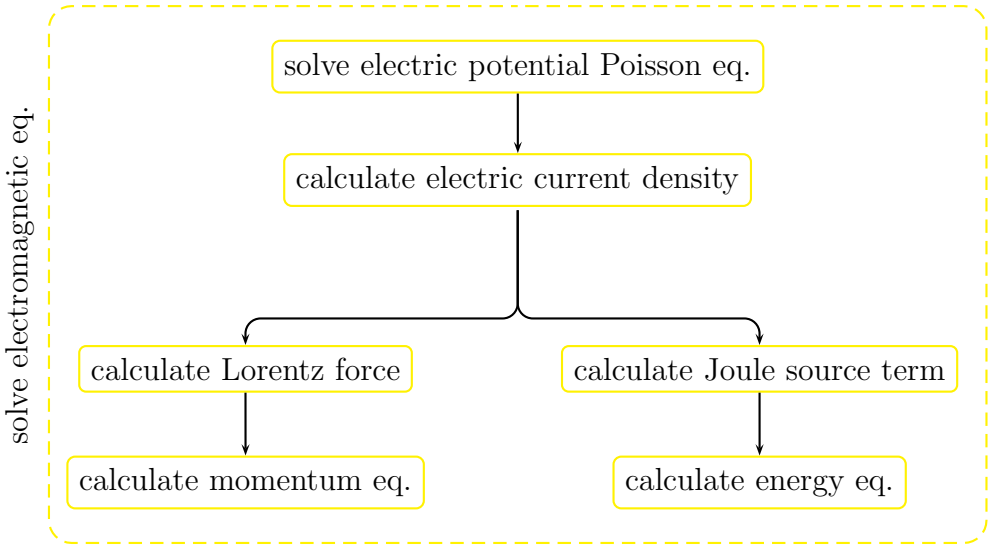

Figure 4.8: Flow chart for solving electromagnetic effects.

of the Lorentz force (Eq. 2.87) in the momentum equation (Eq. 2.101) and if necessary in the Joule source term in the energy equation (Eq. 2.102).

The solution procedure begins at the time $t = t_0$ by implementing the initial values for the velocity $\mathbf{v}_0$, temperature T_0, magnetic field $\mathbf{B}_0$, concentration C_0, turbulent kinetic energy k_0, dissipation rate ε_0, and turbulent viscosity μ_{t0}. Throughout this dissertation $\mathbf{B}_0$ is considered constant. Then, the electric potential equation (Eq. 2.92) has to be solved. The result of this equation is $\nabla\phi$, which is used to compute the electric current density from Eq. 2.85. The $\mathbf{j}$ is inserted in Eq. 2.93 to compute the Lorentz force $\mathbf{f}_{EM}$ and if necessary in Eq. 2.94, to calculate the Joule source term.

The intermediate velocity field is calculated from the momentum equation 2.101 first without the pressure term $-\nabla p$ (Eq. 4.21). Subsequently, the pressure Poisson's equation (Eq. 4.21) is solved. The procedure for solving the pressure Poisson's equation is similar to the procedure of solving the electric potential Poisson's equation and is in detail described in Sect. 4.8.1. The velocity components are then corrected by the pressure gradient as shown in Eq. 4.22. Following is the solution of the energy conservation equation

$$\begin{aligned} h &= h_0 + \frac{\Delta t}{\rho}\Bigg(-\nabla\cdot(\rho\mathbf{v}h) + \nabla\cdot\big(\lambda\nabla T\big) + \nabla\cdot\Big(f_L\frac{\mu_t}{\sigma_t}\nabla h_L\Big) \\ &+ \nabla\cdot\Big(\rho f_S\big(h_L - h_S\big)\big(\mathbf{v}-\mathbf{v}_S\big)\Big) + \frac{|\mathbf{j}|^2}{\sigma}\Bigg)_0 , \end{aligned} \tag{4.25}$$

and the solute concentration equation

$$C = C_0 + \frac{\Delta t}{\rho}\Bigg(- \nabla\cdot(\rho\mathbf{v}C) + \nabla\cdot\Big(\rho f_S D_S \nabla C_S + \rho f_L D_L \nabla C_L\Big) + \nabla\cdot\Big(\frac{f_L\mu_t}{\sigma_C}\nabla C_L\Big) + \nabla\cdot\Big(\rho f_L\big(\mathbf{v}-\mathbf{v}_S\big)\big(C_L - C\big)\Big)\Bigg)_0 . \tag{4.26}$$

Next, the temperature is calculated from the enthalpy with the help of the temperature-enthalpy relations (Eq. 2.56 and Eq. 2.57). Further, the transport equations for k and ε are solved

$$k = k_0 + \frac{\Delta t}{\rho}\Bigg(- \nabla\cdot(\rho\mathbf{v}k) + \nabla\cdot\Big(\big(\mu_L\frac{\rho_L}{\rho} + \frac{\mu_t}{\sigma_k}\big)\nabla k\Big) + P_k + G_k - \rho\varepsilon + \rho D - \mu_L\frac{K_0(1+f_L)^2}{f_L^3}\frac{\rho}{\rho_L}k\Bigg)_0 , \tag{4.27}$$

and

$$\varepsilon = \varepsilon_0 + \frac{\Delta t}{\rho}\Bigg(- \nabla\cdot(\rho\mathbf{v}\varepsilon) + \nabla\cdot\Big(\big(\mu_L\frac{\rho}{\rho_L} + \frac{\mu_t}{\sigma_\varepsilon}\big)\nabla\varepsilon\Big) + \big(c_{1\varepsilon}f_1(P_k + c_{s\varepsilon}G_k) - c_{2\varepsilon}f_2\rho\varepsilon\big)\frac{\varepsilon}{k} + \rho E_{k-\varepsilon} + \mu_L\frac{K_0(1+f_L)^2}{f_L^3}\frac{\rho}{\rho_L}\varepsilon\Bigg)_0 . \tag{4.28}$$

In the next step, the turbulent viscosity μ_t, the liquid fraction f_L, the concentration of solute in liquid phase C_L, the partition ratio k_p and the liquidus temperature T_L are determined from the microsegregation model. Finally, the calculated values are reset to initial values

$$\mathbf{v}_0 = \mathbf{v}, \quad T_0 = T, \quad k_0 = k, \quad \varepsilon_0 = \varepsilon, \quad C_0 = C, \quad p_0 = p \tag{4.29}$$

and the whole procedure is repeated until the system reaches the steady state. The solution in sought for the steady state and the time stepping is only implemented due to the requirements of the method. The criteria for the steady state are discussed in Sect. 4.7.

The procedure of advancing from time t_0 to time $t_0 + \Delta t$ is schematically presented in Fig. 4.9.

4.7 Convergence Criteria

The solution procedure is an iterative process, in which the steps are repeated until the difference between two consecutive variable values is sufficiently small, that the solution can be considered converged. In this dissertation, the steady state is sought for and it is therefore considered that the convergence is reached when steady state is achieved. The time iterations must thus be repeated until

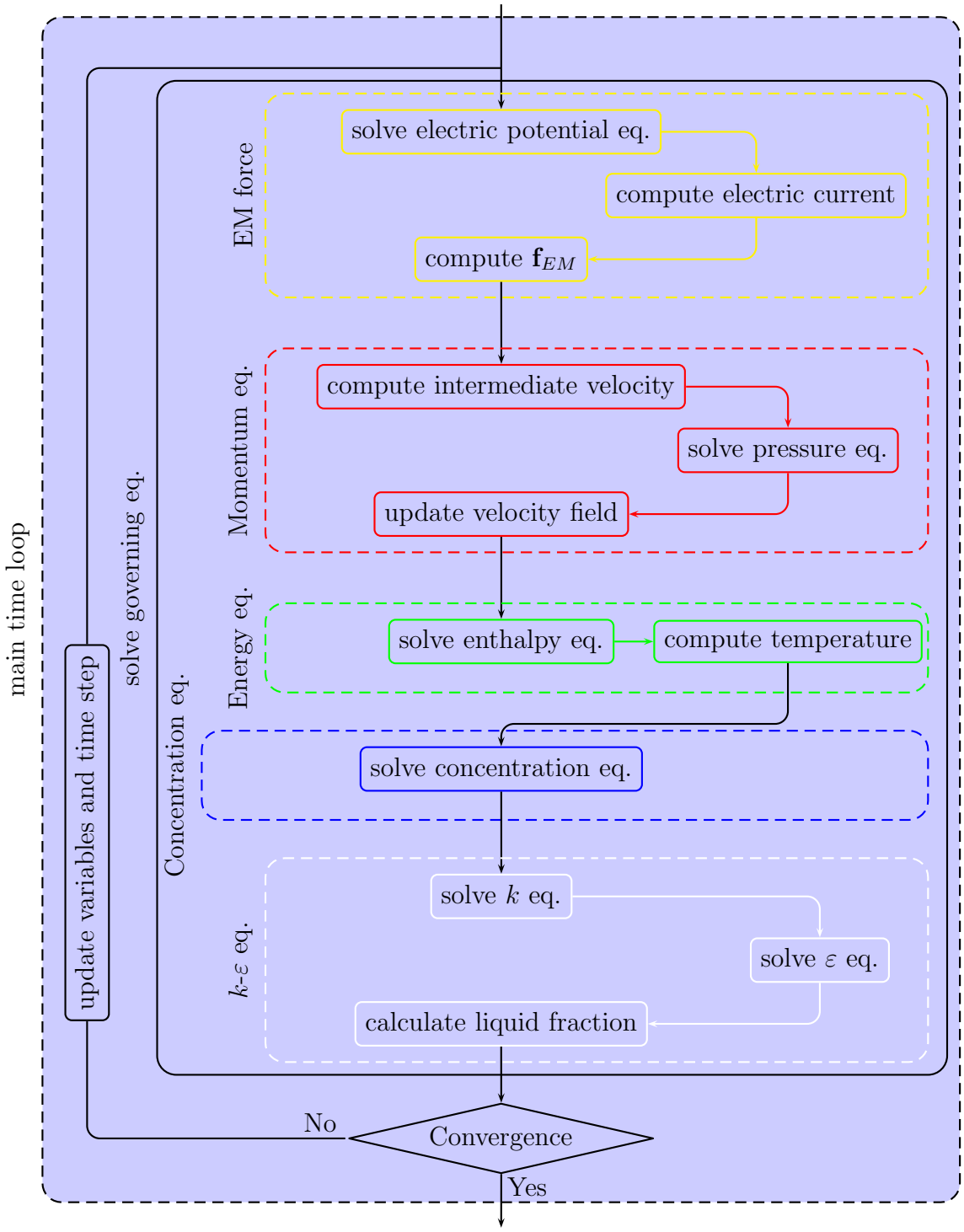

Figure 4.9: Block diagram of the entire solution procedure.

the discrete governing equations for the mass, momentum, species concentration, energy, dissipation rate and turbulent kinetic energy are obeyed in all of the domain nodes in such a way, that the balance is achieved for the mass, momentum, species, energy, dissipation rate and turbulent kinetic energy, and when the solution no longer changes with additional iterations. The iteration process requires convergence criteria, that are used to determine whether the solution has reached

the steady state. The condition for steady state is satisfied, when the following criteria are reached for each of the N computational nodes

$$\begin{aligned} |\mathbf{v} - \mathbf{v}_0| < \varepsilon_v, \quad |T - T_0| < \varepsilon_T, \quad |C - C_0| < \varepsilon_C, \\ |p - p_0| < \varepsilon_p, \quad |k - k_0| < \varepsilon_k, \quad |\varepsilon - \varepsilon_0| < \varepsilon_\varepsilon, \end{aligned} \tag{4.30}$$

where ε_v, ε_T, ε_C, ε_p, ε_k and ε_ε are the iteration criteria for the velocity, temperature, solute concentration, turbulent kinetic energy, dissipation rate and pressure, respectively. The values for iteration criteria are case dependent and are therefore stated for each case separately.

4.8 Numerical Implementation

The numerical implementation of the developed solution procedure is written in the Compaq Visual Fortran (CVF) [Fortran, 2011]. The majority of the solver uses the standard Fortran libraries to solve the mathematical and the system operations. However, when needed, the additional libraries, listed below, are used. The Linear Algebra Package (LAPACK) routines are used to solve the linear systems of equations and the LU decomposition. The sparse matrix is solved with the Parallel Direct Sparse Solver (PARDISO) interface [Schenk and K., 2004] from the Intel Math Kernel Library (MKL). Most of the solver code is parallelized with the Open Multiprocessing (OpenMP) [OpenMP, 2013] library. All line graphs for the velocity, temperature, pressure, and magnetic field are plotted in GNUPLOT 4.4 [Williams and Kelley, 2010]. The streamlines, that are calculated by integrating the velocity field with the 4-th order Runge-Kutta method, are plotted in ParaView [Henderson, 2007] and CVF with PGPLOT Graphics Subroutine Library Pearson [2001]. The contour plots are plotted in ParaView [Henderson, 2007].

The main code is based on the MeshlessLib library developed in [Vertnik, 2010] and upgraded in the course of present dissertation..

The simulations presented in this work were performed on the following computers

- HP EliteBook 8740w Mobile Workstation with two Intel Core i7 2.8 GHz processors,
- HP Z 400 Workstation with two Intel Xeon 3.3 GHz processors,
- Intel S5000VSA with two Xeon 2.83 GHz processors,
- HP ProLiant DL380 G7 with two Xeon 3.47 GHz processors, and
- HP Prodiant DL360p G8 with two Intel Xeon e5-2650 2.0 GHz processors.

4.8.1 Solution of Poisson's Equation

As the same formulation is used to solve the Poisson's equation for the scalar potential (Eq. 2.92) and for the pressure (Eq. 4.21), a formulation for a general

variable Φ is presented here. The global $\mathbf{p}_n$ and the local (influence domain) ${}_l\mathbf{p}_i$ nodes coincide and are connected with the relation $\mathbf{p}_{n(l,i)} = {}_l\mathbf{p}_i$. The Poisson's equation is solved by constructing and solving the sparse matrix [Lee et al., 2003]. The general variable is represented on each of the influence domains as a linear combination of RBFs and their coefficients

$$\Phi(\mathbf{p}) = \sum_{i=1}^{N_{domain}} \psi_{n(l,i)}(\mathbf{p})_l\alpha_. \tag{4.31}$$

The expansion coefficients α_i are determined by a collocation as shown in Eq. 3.29 and the general variable Φ is thus

$$\Phi_{n(l,m)} = \sum_{i=1}^{N_{domain}} {}_l\Psi_{jnl}\alpha_i; \quad j = 1, \ldots, N_{domain}. \tag{4.32}$$

In each of the influence domains, the Φ is determined as

$$\Phi(\mathbf{p}) = \sum_{i=1}^{N_{domain}} \sum_{j=1}^{N_{domain}} {}_l\psi_{n(l,i)}(\mathbf{p})_l\Psi_{ij}^{-1}\Phi_{n,(l,j)}. \tag{4.33}$$

The discretized general Poisson equation s a result of collocation and application of the Laplace operator in global node $\mathbf{p}_k$

$$\sum_{k=1}^{N} \Psi_{kl}\Phi_l = S_k, \tag{4.34}$$

where Ψ_{kl} is the sparse matrix element, and S_k is a function of Φ. For pressure, $S_k = \frac{\rho}{\Delta t}\nabla \cdot \mathbf{v}_k^\star$ and pressure Poisson equation (Eq. 4.21) is discretized to

$$\sum_{k=1}^{N} \Psi_{kl}p_l = \frac{\rho}{\Delta t}\nabla \cdot \mathbf{v}_k^\star. \tag{4.35}$$

For scalar potential, $S_k = \nabla \cdot (\mathbf{v} \times \mathbf{B})_k$ and Eq. 2.92 is discretized to

$$\sum_{k=1}^{N} \Psi_{kl}\phi_l = \nabla \cdot (\mathbf{v} \times \mathbf{B})_k. \tag{4.36}$$

5 Benchmark Test Cases for Fluid Flow and Magnetic Field

The aim of this chapter is to verify the numerical code, to set the free parameters (β, c) and to test the parameter range (ν, α_T) of for liquid metals, especially the molten steel. For this purpose, several benchmark test cases are chosen and the obtained results are assessed against the reference results. When possible, the reference results are obtained by analytical solution or from the already published works of other authors. If the case is too complex to be solved analytically, and there is no previously published reference, the results are compared to the commercial software Fluent [ANSYS, 2013]. It should be noted here that the results obtained with Fluent are not considered entirely exact and that the aim of the author is not to determine the accuracy of the Fluent code, but rather to explore the agreement of the newly developed LRBFCM with the already established and extensively verified FVM approach.

The evaluation begins by first considering the lid driven cavity test case in order to asses the performance of two different RBFs and two different pressure-velocity coupling schemes. In the second test case, the free convection in a rectangular enclosure under the influence of an externally applied magnetic field is investigated. The goal of this test case is to ascertain the accuracy of the addition of the magnetic field equations and the corresponding boundary and initial conditions to the fully coupled momentum and energy equations. The inlet and the outlet boundary conditions are tested in both the Hartmann flow and the free convection over a backward facing step under the influence of the magnetic field. The objective of the former is to test the behaviour of the additional magnetic field components for an in- and out-flow, against the analytical solutions. The aim of the latter test case is to establish the accuracy of the separation and the reattachment positions and is tested both against the published data as well as against the data calculated with Fluent. To describe the turbulent flow and the species conservation, three supplementary equations are required; the turbulent kinetic energy k and the dissipation rate ε equations to describe the turbulence and the species conservation equation to account for the binary alloy species transport. As all of these equations have already been verified [Vertnik, 2010; Šarler et al., 2012, 2013] and no MHD terms are added in this equations, no additional test cases are performed to check the accuracy of the listed three equations.

The results of the benchmark tests have been published in several international journals [Mramor et al., 2013a,b, 2014b] and presented at international

conferences [Mramor et al., 2012].

5.1 Dimensionless Form of Governing Equations

To simplify and generalize the comparisons of present results with the results of other authors and those obtained with the Fluent code, the governing equations have to be written in their dimensionless form. Several dimensionless numbers have to be defined, respectively.

Prandtl Number

Prandtl number (Pr) is a dimensionless number that represents the ratio between the kinematic viscosity and the thermal diffusion

$$\mathrm{Pr} = \frac{\text{viscous diffusion rate}}{\text{thermal diffusion rate}}. \tag{5.1}$$

It is expressed as

$$\mathrm{Pr} = \frac{\nu}{\alpha_T} = \frac{c_p\,\mu}{\lambda}, \tag{5.2}$$

where α_T is thermal diffusivity. Pr is high if the kinematic viscosity is dominant and low if the thermal diffusivity is dominant. A typical value of Pr for steel is 0.14.

Schmidt Number

Schmidt number (Sc) is a dimensionless number that represents ratio between momentum or viscous diffusivity and mass diffusivity

$$\mathrm{Sc} = \frac{\text{viscous diffusion rate}}{\text{mass diffusion rate}}. \tag{5.3}$$

It is expressed as

$$\mathrm{Sc} = \frac{\nu}{D} = \frac{\mu}{\rho\,D}. \tag{5.4}$$

Rayleigh Number

Rayleigh number (Ra) is a dimensionless number defined as

$$\mathrm{Ra} = \frac{|\mathbf{g}\,|\beta_T\,(T_H - T_C)\,\ell^3}{\nu\lambda}, \tag{5.5}$$

where ℓ is the characteristic length that depends on the geometry of the problem, T_C is the cold temperature and T_H is the hot temperature.

Grashof Number

Grashof number (Gr) is a dimensionless number that represents the ratio between the buoyancy and the viscous forces

$$\mathrm{Gr} = \frac{\text{bouyancy force}}{\text{viscous force}}. \tag{5.6}$$

It can be rewritten as a ratio between the Ra and Pr number

$$\mathrm{Gr} = \frac{\mathrm{Ra}}{\mathrm{Pr}}. \tag{5.7}$$

Reynolds Number

Re is a dimensionless number that represents the a ratio of the inertial and the viscous forces

$$\mathrm{Re} = \frac{\text{inertial} \quad \text{forces}}{\text{viscous} \quad \text{forces}} \simeq \frac{|(\mathbf{v}\cdot\nabla)\mathbf{v}|}{|\nu\,\nabla^2\mathbf{v}|}. \tag{5.8}$$

It is defined as

$$\mathrm{Re} = \frac{v_c\,\ell}{\nu}, \tag{5.9}$$

where v_c is the characteristic velocity.

Interaction Parameter or Stuart Number

Interaction parameter ($\mathcal{N}$), also called Stuart number (St), is a dimensionless number, which is defined as the ratio between the Lorentz force and the inertial forces of the fluid

$$\mathrm{St} \equiv \mathcal{N} = \frac{\text{electromagnetic} \quad \text{forces}}{\text{inertial} \quad \text{forces}} \simeq \frac{|\mathbf{j}\times\mathbf{B}|}{\rho\,|(\mathbf{v}\cdot\nabla)\mathbf{v}|}. \tag{5.10}$$

It can be written as

$$\mathrm{St} \equiv \mathcal{N} = \frac{\sigma\,\ell\,B_0^2}{\rho v_c} = \frac{\mathrm{Ha}^2}{\mathrm{Re}}. \tag{5.11}$$

Hartmann Number

Hartmann number (Ha) is a dimensionless number that is defined as the ration between the electromagnetic and the viscous forces

$$\mathrm{Ha}^2 = \frac{\text{electromagnetic} \quad \text{force}}{\text{viscous} \quad \text{force}} \simeq \frac{|\mathbf{j}\times\mathbf{B}|}{|\nu\nabla^2\mathbf{v}|} \tag{5.12}$$

or in the mathematical notation

$$\mathrm{Ha} = \ell B_0\sqrt{\frac{\sigma}{\rho\nu}} = \sqrt{\mathcal{N}\mathrm{Re}}. \tag{5.13}$$

Magnetic Reynolds Number

Magnetic Reynolds number (Re_M) is a dimensionless number that represents the ratio of the magnetic advection and the magnetic diffusion

$$\mathrm{Re_M} = \frac{\text{advection of magnetic field}}{\text{diffusion of magnetic field}} \simeq \frac{|(\mathbf{v}\cdot\nabla)\mathbf{B}|}{|\chi\,\nabla^2\mathbf{B}|}. \tag{5.14}$$

It can be written as

$$\mathrm{Re_M} = \mu_0\,\sigma\,v_c\,\ell = \frac{v_c\,\ell}{\chi}. \tag{5.15}$$

Batchlor Number or Magnetic Prandtl number

Batchlor number (Bt), also called the magnetic Prandtl number (Pr_M), represents the ratio of the viscous diffusivity and the electromagnetic diffusivity

$$\mathrm{Bt} = \mathrm{Pr}_M = \frac{\text{viscous diffusion}}{\text{electromagnetic diffusion}} = \mu\sigma\nu. \tag{5.16}$$

The effect of the external magnetic field is stabilizing for small Pr_M.

Turbulent Prandtl Number

Pr_t represents the ratio between viscous eddy diffusivity and thermal eddy diffusivity

$$\mathrm{Pr}_t = \frac{\text{viscous eddy diffusivity}}{\text{thermal eddy diffusivity}} \tag{5.17}$$

or equivalently

$$\mathrm{Pr}_t = \frac{\nu_t}{\alpha_{Tt}}, \tag{5.18}$$

where α_{Tt} is thermal eddy diffusivity.

Local Turbulent Reynolds Number

Local turbulent Reynolds number (Re_t) represents the ratio between the turbulent fluctuation and the turbulent length scale

$$\mathrm{Re}_t = \frac{\text{turbulent fluctuation}}{\text{turbulent length scale}} \tag{5.19}$$

or equivalently

$$\mathrm{Re}_t = \frac{k^2}{\nu\varepsilon}. \tag{5.20}$$

5.2 Lid Driven Cavity Problem

5.2.1 Problem Description

A two-dimensional lid driven cavity flow problem describes the motion of a laminar incompressible Newtonian flow in a square cavity with a moving top wall and fixed side and bottom walls. The moving upper wall sets the fluid in the cavity into motion and when moving in the left to the right direction, the clockwise rotating vortex is formed. The primary eddy develops at approximately the geometric center of the cavity. The higher order eddies, which develop when Re is increased, are positioned at the bottom left and right corners of the cavity. This eddies are smaller in size and rotate in the opposite direction of the primary vortex.

Literature Review for Lid Driven Cavity Problem

The lid-driven cavity problem was first proposed in 1982 [Ghia et al., 1982] and has since become one of the standard benchmark test cases used to asses the performance of a chosen numerical method used to calculate the fluid flow. A wide variety of different numerical methods that have so far been applied to this problem include the FDM [Bruneau and Jouron, 1990; Bruneau and Saad, 2006], the FEM [Barragy and Carey, 1997], different variations of BEM [Liao, 1992; Liao and Zhu, 1996; Grigoriev and Dargush, 1999; Aydin and Fenner, 2001], the Chebyshev Collocation Method (CCM) [Botella and Peyret, 1998], the Multi Grid Method (MGM) [Ghia et al., 1982], the Lattice Boltzman Method (LBM) [Hou et al., 1995], and many others. Among the meshless methods, the MLPG [Lin and Atluri, 2000], the MFS [Young et al., 2006], the MPCM [Kim et al., 2007] and the LRBFCM [Divo and Kassab, 2007].

The purpose of this test case is to asses the performance of two different PV coupling schemes (FSM and ACM with CBS term), of two different RBFs (MQ and IMQ) and to extend the work of [Divo and Kassab, 2007] to intermediate Re numbers range. The results of this test case have already been published in [Mramor et al., 2013a].

5.2.2 Governing Equations and Numerical Parameters

The Newtonian incompressible flow is described in a fixed domain $\Omega = (0,1) \times (0,1)$ with boundary $\Gamma = ([0,1]\times[0,1]) \cap ((0,1)\times(0,1))$ by the following equations

$$\nabla \cdot \mathbf{v} = 0, \tag{5.21}$$

and

$$\rho\left(\frac{\partial \mathbf{v}}{\partial t} + \nabla \cdot \left(\mathbf{v}\mathbf{v}\right)\right) = -\nabla p + \mu \nabla^2 \mathbf{v}. \tag{5.22}$$

The dimensionless equivalents of these equations are

$$\nabla \cdot \mathbf{v}' = 0, \tag{5.23}$$

and

$$\frac{\partial \mathbf{v}'}{\partial t'} + \nabla \cdot (\mathbf{v}'\mathbf{v}') = -\nabla p' + \frac{1}{\mathrm{Re}}\nabla^2 \mathbf{v}', \tag{5.24}$$

where the variables denoted by the prime stand for the dimensionless variables. The derivation of the dimensionless equation along with the definition of the pertained dimensionless variables is elaborated in Appx. B.1.

Initial Conditions

The solution is sought at the following initial conditions

$$\mathbf{v}' = 0, \quad \text{and} \quad p' = 0. \tag{5.25}$$

Boundary Conditions

Dirichlet BC are used on all boundaries Γ. On the top part of Γ the dimensionless velocities have the following values

$$v_x' = 1, \quad v_y' = 0, \tag{5.26}$$

and on the rest of the Γ the velocity values are

$$v_x' = 0, \quad v_y' = 0. \tag{5.27}$$

A scheme of the computational domain is depicted in Fig. 5.1.

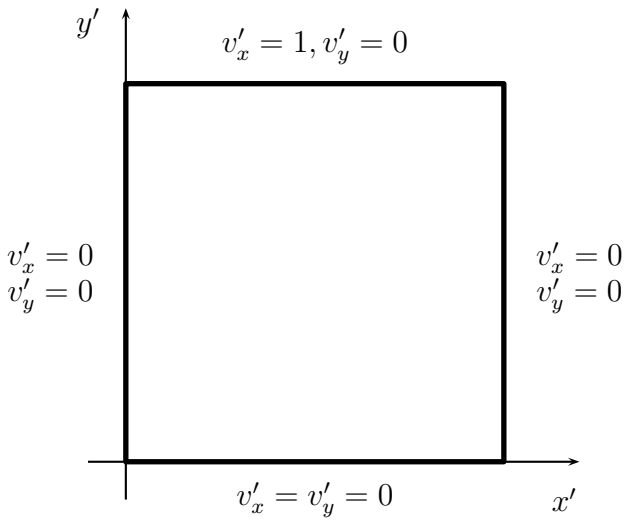

Figure 5.1: Computational scheme of a 2D cavity with boundary conditions.

5.2.3 Results and Discussions

The refinement parameter $u = 1.2$ is used to improve the node arrangement along the walls. A scheme of the node arrangement for a computational domain of a 2D cavity is depicted in Fig. 5.2. All of the calculations are done for a shape parameter $c = 32$ with the time step $\Delta t' = 10^{-3}$ and the following convergence

criteria for pressure $\varepsilon_p = 10^{-5}$ and for velocity $\varepsilon_v = 10^{-5}$. Unless otherwise stated, the calculations are done with the MQ RBFs and the FSM PV coupling scheme.

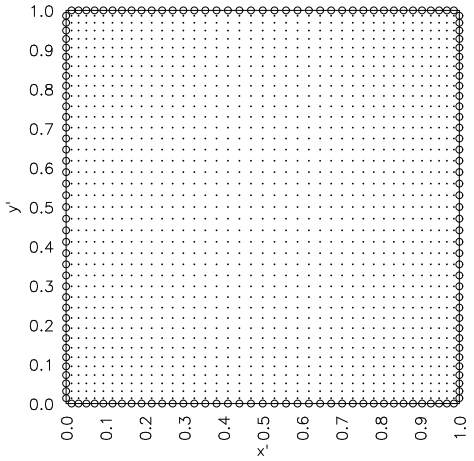

Figure 5.2: Scheme of the node arrangement (41x41, $u = 1.2$) for the computational domain of a 2D cavity. Circles represent the boundary nodes whereas dots represent the domain nodes.

The numerical examples are organized as follows. First, the convergence of the method is tested on several different node arrangements. The results are then compared with the reference results of other authors. Further, the behaviour of different RBF forms, namely MQ and IMQ RBFs, is investigated, and lastly, the comparison between two different types of PV couplings, namely the FSM and ACM with CBS term, is performed. The dimensionless velocities in x and y direction are assessed for a horizontal and a vertical line through the center of the cavity as depicted in Fig. 5.3.

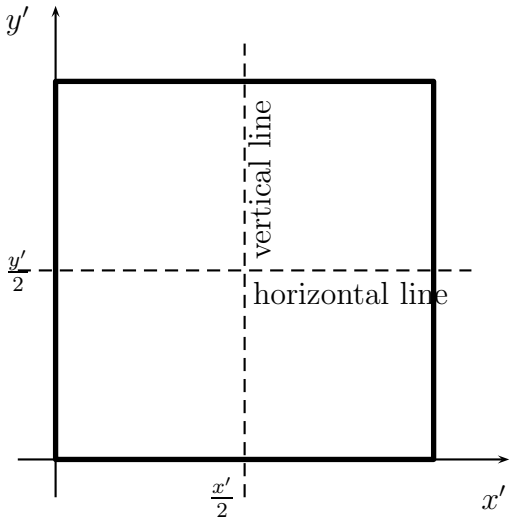

Figure 5.3: Positions of vertical and horizontal lines through the geometric center of a square cavity.

Convergence of the Method

The convergence of the method is investigated for four different node arrangements, with the number of nodes varying from 1677 nodes (41x41 without 4 corner nodes)[1] to 16637 (129x129) nodes. The dimensionless velocities (v'_x and v'_y) are compared for Re=1000, on horizontal and vertical lines through the geometric center of the cavity as depicted on Fig. 5.3. The comparison is presented in Fig. 5.4 and confirms the assumption that the poorest agreement appears for the smallest number of the nodes. The velocity profiles of the denser node arrangements are in accordance with the expected results and do not exhibit noticeable differences with respect to minimal node arrangement. The smallest of the node arrangements with 81x81 nodes, that appears to be reasonably node independent is chosen for further calculations unless otherwise stated.

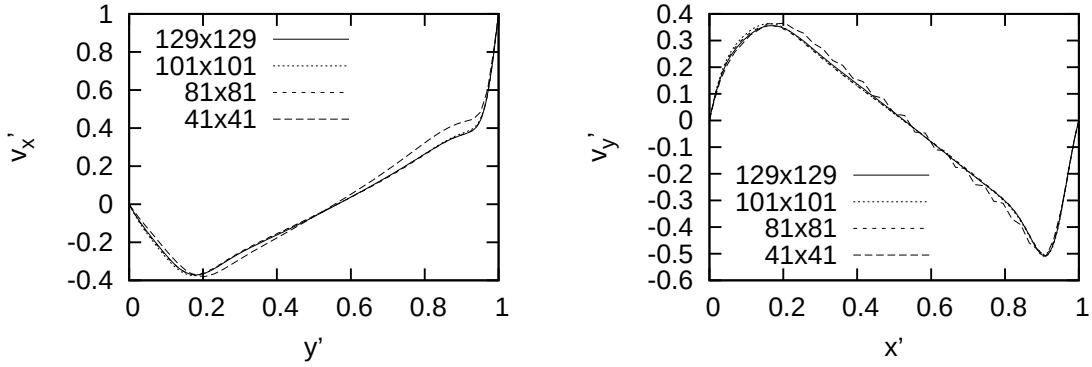

Figure 5.4: Comparison of dimensionless velocities at different node densities for the Re=1000. Left: the v'_x component of velocity along the horizontal line through the center of the cavity. Right: the v'_y component of the velocity along the vertical line through the center of the cavity.

Comparison with Reference Results

The flow in the lid driven cavity is calculated for the low and the intermediate Re, ranging from 100 to 3200 on a 81x81 node arrangement as shown in Figs. 5.5-5.8. The results are compared to a wide spectra of reference results, given by [Ghia et al., 1982; Bruneau and Saad, 2006; Erturk, 2009; Botella and Peyret, 1998; Erturk et al., 2005; Erturk and Gökçöl, 2006]. As predicted, the best agreement between the velocity profiles of the calculated and the previously published results is achieved for the small Re such as 100 and 400 (Figs. 5.5 and 5.6). A comparison between the data and the calculations exhibits a slightly poorer correlation for the intermediate Re such as 1000 and 3200 (Figs. 5.7 and 5.8). An odd data point in the right graph in Fig. 5.6 is probably a wrongly entered data point in the reference table [Ghia et al., 1982]. Additionally, for Re=400, the velocity profiles

[1]In none of the calculations with LRBFCM in this dissertation, the node arrangements have corner nodes. The notation of the node arrangement will from now on be denoted as a x b instead of a x b without 4 corner nodes. In practice this means, that the node arrangement denoted as 41x41 has 41x41-4 nodes, that is 1677 instead of 1681.

are compared to Fluent. The results from Fluent are calculated on 129x129 mesh.

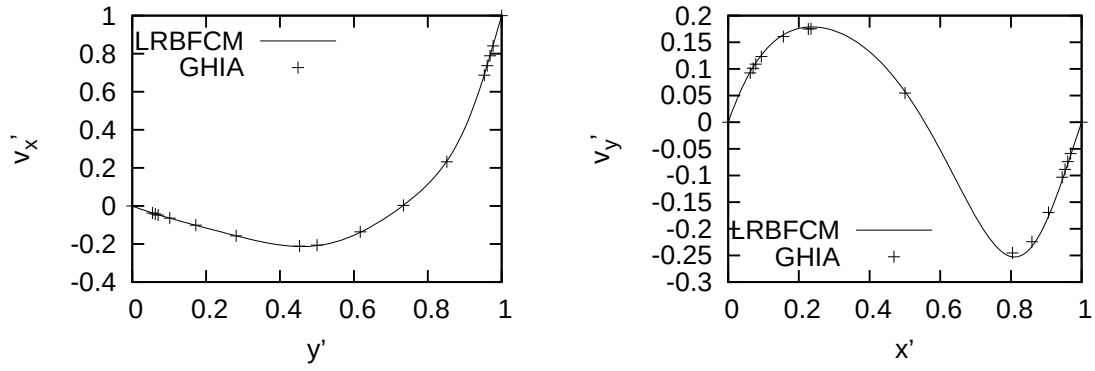

Figure 5.5: Comparison of dimensionless velocities for Re=100, calculated with LRBFCM with the results of [Ghia et al., 1982]. Left: v'_x component of the velocity along the horizontal line through the center of the cavity. Right: v'_y component of the velocity along the vertical line through the center of the cavity.

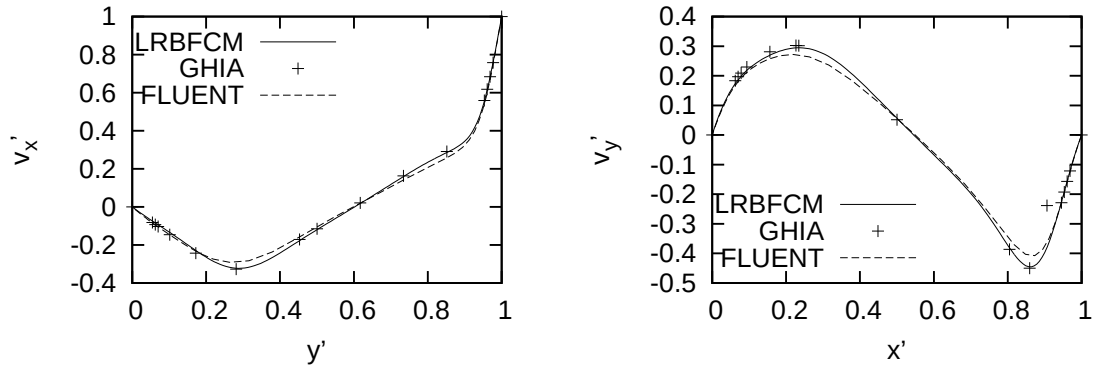

Figure 5.6: Comparison of dimensionless velocities for Re=400, calculated with LRBFCM and Fluent, and the results of [Ghia et al., 1982]. Left: v'_x component of velocity along the horizontal line through the center of the cavity. Right: v'_y component of the velocity along the vertical line through the center of the cavity.

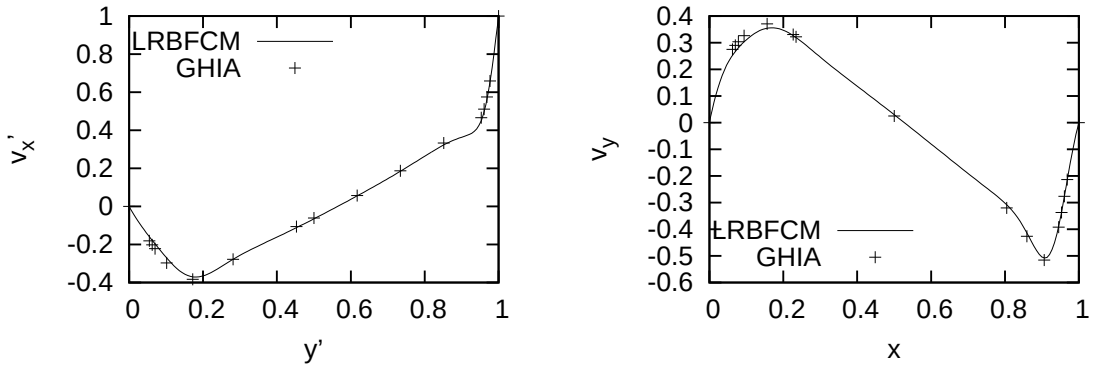

Figure 5.7: Comparison of dimensionless velocities for Re=1000, calculated with LRBFCM and the results of [Ghia et al., 1982]. Left: v'_x component of the velocity along the horizontal line through the center of the cavity. Right: v'_y component of the velocity along the vertical line through the center of the cavity.

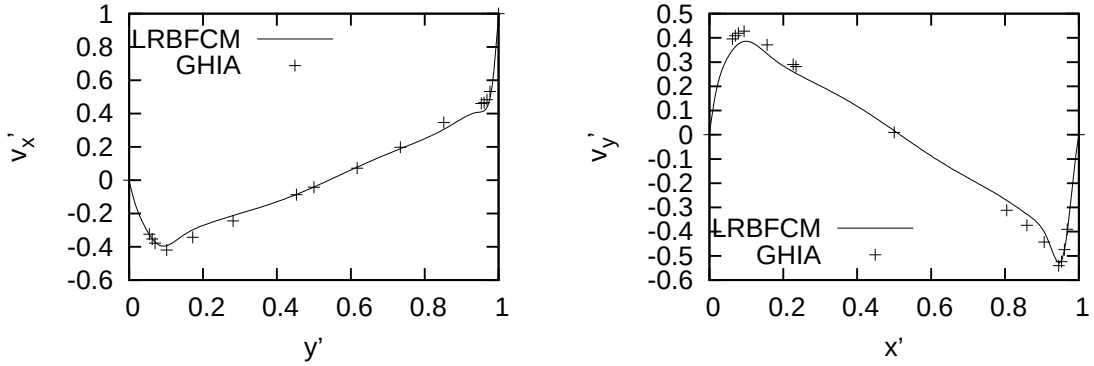

Figure 5.8: Comparison of dimensionless velocities for Re=3200, calculated with LRBFCM and the results of Ghia et al. [1982]. Left: v'_x component of the velocity along the horizontal line through the center of the cavity. Right: v'_y component of the velocity along the vertical line through the center of the cavity.

The minimum (for v'_x and v'_y) and the maximum (for v'_y) values of the velocities along the horizontal and the vertical lines that pass through the geometric center of the cavity are given in Tab. 5.1 for 129x129 node arrangement for a variety of different Re.

Comparison of Different RBF Types

Next, results with MQ and IMQ trial functions are compared for Re=1000 and 129x129 nodes. The results for both types of the RBF forms are almost the same: the minimum velocities in the x direction are - 0.3713 in the case of the MQ RBFs and -0.3674 in the case of the IMQ RBFs, whereas the minimum velocities in the y direction are -0.5082 in the case of MQ RBFs and -0.5035 in the case of the IMQ RBFs. The difference in the case of minimum velocities is 1.0%, whereas the difference in the case of maximum velocities is 0.9%. In both cases the number of iterations required to achieve the steady state is 20900. The results are depicted

Table 5.1: Minimum and maximum velocities along the horizontal line (y'=0.5) and the vertical line (x'=0.5) that pass through the geometric center of the cavity. 1: present, 2: [Ghia et al., 1982], 3: [Erturk et al., 2005], 4: [Botella and Peyret, 1998], 5: [Sahin and Owens, 2003a,b], 6: [Bruneau and Jouron, 1990].

Re	$v'_x(min)$	y'	$v'_y(min)$	x'	$v'_y(max)$	x'	Ref.
100	-0.21325	0.4542	-0.25296	0.8102	0.17884	0.2379	1
	-0.21090	0.4531	-0.24533	0.8047	0.17527	0.2344	2
	-0.21392	0.4598	-0.25660	0.8127	0.18089	0.2354	5
	-0.2106	0.4531	-0.2521	0.8125	0.1786	0.2344	6
400	-0.32276	0.2876	-0.44523	0.86374	0.29453	0.2379	1
	-0.32726	0.2813	-0.44993	0.8594	0.30203	0.2266	2
	-0.32838	0.2815	-0.45632	0.8621	0.30445	0.2253	5
1000	-0.37126	0.1820	-0.50821	0.90701	0.35603	0.1665	1
	-0.38289	0.1719	-0.51550	0.9063	0.37095	0.1563	2
	-0.3869	0.180	-0.5263	0.910	0.3756	0.150	3
	-0.38866	0.1719	-0.52644	0.9063	0.37692	0.1563	4
	-0.38810	0.1727	-0.52845	0.9087	0.37691	0.1573	5
	-0.3764	0.1602	-0.5208	0.9102	0.3665	0.1523	6
3200	-0.39664	0.0930	-0.52900	0.94710	0.38611	0.1000	1
	-0.41933	0.1016	-0.54053	0.9453	0.42768	0.0938	2
	-0.43540	0.0921	-0.56915	0.9491	0.43245	0.0972	5

in Fig. 5.9.

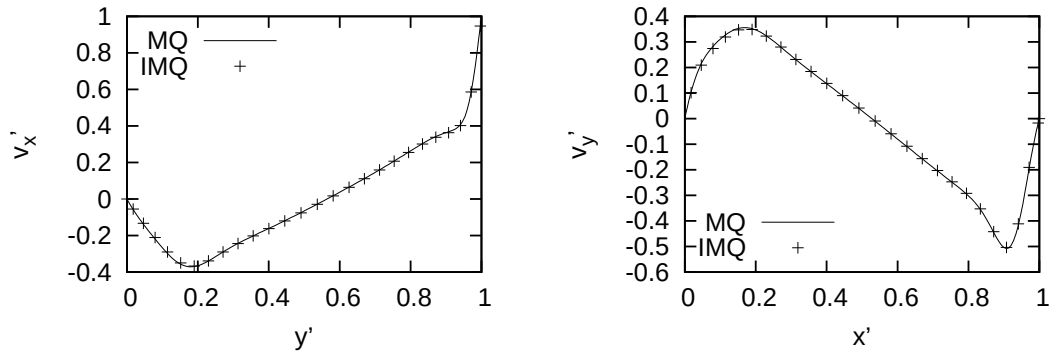

Figure 5.9: Comparison of the results with two different RBF types (MQ and IMQ). Left: v'_x velocity along the horizontal line through the center of the cavity. Right: v'_y velocity along the vertical line through the center of the cavity.

Comparison of Different Pressure Velocity Coupling Schemes

Two different PV coupling schemes are compared for 129x129 node arrangement and Re=1000. The first method is FSM [Chorin, 1968] and the second method is ACM [Chorin, 1967] with CBS term [Zienkiewicz and Codina, 1995; Zienkiewicz et al., 1995, 1999]. The selection of the compressibility coefficient β in the ACM method is not trivial, as it is a free parameter. A reasonable range of β for lid-driven cavity problem is from 0.5 to 1.5. For the purposes of this study β is fixed and set to 1. The pressure in the ACM method with the CBS term is calculated directly in each of the domain nodes. On the other hand, the FSM method, requires calculation of a sparse matrix obtained from pressure Poisson's equation. Although, the calculation of sparse matrix is a more complex operation than the point wise calculation of pressure, it turns out that the FSM method is faster and needs less iterations than the ACM method with the CBS term to reach the steady state, especially in case of larger node arrangements. In our case, both of the methods give similar results, as is evident from Fig. 5.10. The number of iterations required to reach the steady state is 20900 with the FSM method and 31400 with the ACM with the CBS term. The minimum values of the velocities in the x direction are - 0.3713 when employing of the FSM method and -0.3780 when employing of the ACM with the CBS, whereas the minimum velocity values in the y direction are -0.5082 for the FSM and -0.5080 for the ACM with the CBS. The difference in minimum velocities is 1.8% and the difference in maximum velocities is 0.02%.

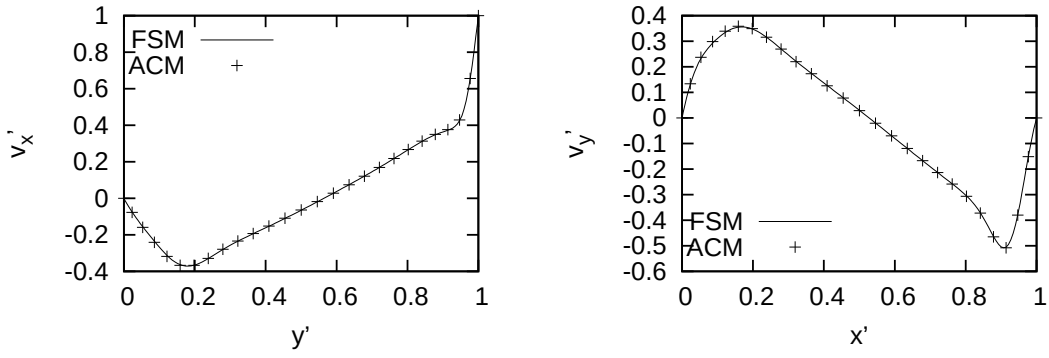

Figure 5.10: Comparison of dimensionless velocities for different PV coupling schemes. Left: v'_x velocity along the horizontal line through the center of the cavity. Right: v'_y component of velocity along the vertical line through the center of the cavity.

Additionally, a sensitivity to β is tested for three different values: 0.5, 1.0, and 1.5. The results of comparison are presented in Fig. 5.11, where the velocities for different parameter values appear almost the same. The number of iterations required to reach the steady state is the smallest for the largest parameter value and the largest for the smallest parameter value. The corresponding minimum velocities are listed along with the iteration time in Tab. 5.2.

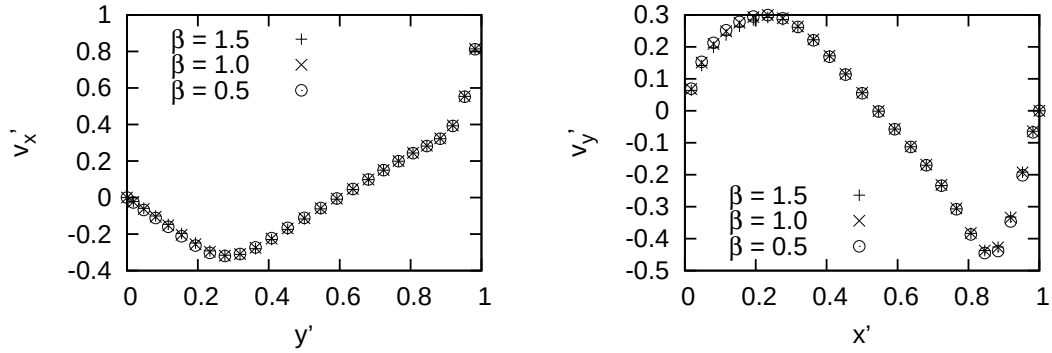

Figure 5.11: Comparison of dimensionless velocities for different β. Left: v'_x component of velocity along the horizontal line through the center of the cavity. Right: v'_y component of velocity along the vertical line through the center of the cavity.

Table 5.2: Iteration times with the values of minimum velocities in the x and y direction for different values of β.

β	iterations	$v'_x(min)$	$v'_y(min)$
0.5	72700	-0.3809	-0.5116
1.0	31400	-0.3780	-0.5080
1.5	26400	-0.3702	-0.5019

5.2.4 Summary and Conclusions

The results, calculated with LRBFCM, are in a good agreement with reference results. Both of the RBF trial functions give similar results. The difference between the velocity values of the extremes is 1.0% or smaller. The results obtained with IMQ RBFs differ from reference slightly more than the results calculated with MQ RBFs. respectively, MQ RBFs are chosen for subsequent calculations. Sinilarly, both PV coupling methods give comparable results. The FSM method, however, is more efficient as it requires a lower number of iterations and was therefore chosen for the following calculations. On the other hand FSM method is more complex from the coding point of view since it requires solution of a sparse matrix.

5.3 Natural Convection in a Rectangular Enclosure with Magnetic Field

5.3.1 Problem Description

A laminar natural convection flow under the influence of a transversal magnetic field is considered in a square cavity, with fixed domain $\Omega = (0,1) \times (0,1)$ and a boundary $\Gamma = ([0,1] \times [0,1]) \cap ((0,1) \times (0,1))$. The top and bottom walls of the cavity are adiabatic, whereas the left and right walls are kept at constant, albeit

different, temperatures. The influence of magnetic field is incorporated through a body force $\mathbf{f}_b$, which in present case points in x direction.

Literature Review of Natural Convection in a Rectangular Enclosure with a Magnetic Field

The natural convection in a rectangular cavity test with and without the presence of a magnetic field is one of the most widely used test cases. The problem without the presence of magnetic field was first proposed by [de Vahl Davis, 1983], and has since been used to verify a number of different numerical methods, such as FVM [Hortmann et al., 1990], FDM [de Vahl Davis, 1983], GRBFCM [Šarler, 2005], LRBFCM [Kosec and Šarler, 2008c] and several others. The standard de Vahl Davis test case and its variations have lately been extended for the application of the magnetic field. Among the various numerical methods, that have already been used to solve the problem are the FEM [Salah et al., 2001; Sathiyamoorthy and Chamkha, 2010, 2012], the FDM [Rudraiah et al., 1995], the FVM [Di Piazza and Ciofalo, 2002a,b; Sarris et al., 2005], the MLPGM [Arefmanesh et al., 2010], the GRBFCM [Colaço et al., 2009], and MDAM [Sadat and Couturier, 2000].

The purpose of this test case is to asses the performance of the method for the application of magnetic field. The results have already been published in [Mramor et al., 2013b].

5.3.2 Governing Equations

The governing equation of mass has the same form as in the case of the lid driven cavity test problem (Eq. 5.21)

$$\nabla \cdot \mathbf{v} = 0. \tag{5.28}$$

In the momentum equation (Eq. 5.22), an additional body force term $\mathbf{f}_b$, is added

$$\rho\left(\frac{\partial \mathbf{v}}{\partial t} + \nabla \cdot \left(\mathbf{v}\mathbf{v}\right)\right) = -\nabla p + \mu \nabla^2 \mathbf{v} + \mathbf{f_b}. \tag{5.29}$$

The body force term $\mathbf{f}_b = \mathbf{f}_{tbu} + \mathbf{f}_{EM}$ in this particular case consists of the thermal buoyancy force $\mathbf{f}_{tbu} = \mathbf{g}\rho\beta_T(T - T_{ref})$ and the Lorentz force (Eq. 2.93) $\mathbf{f}_{EM} = \mathbf{j} \times \mathbf{B}$. Energy equation is needed to account for the temperature gradient

$$\frac{\partial T}{\partial t} + \nabla \cdot \left(\mathbf{v}T\right) = \alpha_T \nabla^2 T. \tag{5.30}$$

The dimensionless equivalents of mass conservation equation for this problem is the same as in the case of lid-driven cavity (Eq. 5.23)

$$\nabla \cdot \mathbf{v}' = 0. \tag{5.31}$$

The momentum equation in its dimensionless form is rewritten as

$$\frac{\partial \mathbf{v}'}{\partial t'} + \nabla \cdot (\mathbf{v}'\mathbf{v}') = -\nabla p' + \frac{1}{\mathrm{Re}}\nabla^2 \mathbf{v}' + \frac{\mathrm{Ha}^2}{\mathrm{Re}}\mathbf{v}' - \mathbf{g}'\,\beta_T'\,\Theta, \tag{5.32}$$

where $\frac{\mathrm{Ha}^2}{\mathrm{Re}}\mathbf{v}'$ represents dimensionless $\mathbf{f}_{EM}$ and $\mathbf{g}'\,\beta_T'\,\Theta$ represents the dimensionless $\mathbf{f}_{tbu}$. The energy conservation equation is rewritten as

$$\frac{\partial \Theta}{\partial t'} + \nabla \cdot (\mathbf{v}'\Theta) = \frac{\mathrm{Pr}}{\mathrm{Re}}\nabla^2\Theta. \tag{5.33}$$

The derivation of dimensionless equations along with the definition of the pertained dimensionless variables is given in Appx. B.2.

Initial Conditions

The initial conditions for velocity and pressure are

$$\mathbf{v} = 0, \quad p = 0. \tag{5.34}$$

The values for the temperature and the predefined magnetic field are given as

$$T_{ref} = \frac{T_H + T_C}{2}, \tag{5.35}$$

and

$$B_x = 1T, \quad B_y = 0. \tag{5.36}$$

Boundary Conditions

The velocity BC on all the walls are non-permeable and non-slip

$$v_x = 0, \qquad v_y = 0. \tag{5.37}$$

The temperature BC on the top and bottom walls are of the Neuman insulation type

$$\frac{\partial T}{\partial \mathbf{n}} = 0, \tag{5.38}$$

as the walls are adiabatic. The temperature on the left wall is T_H and is considered higher than the temperature on the right wall T_C. The BC for the electric potential is obtained from Eq. 2.109 for an insulating boundary. The electric potential BC is

$$\frac{\partial \phi}{\partial \mathbf{n}} = 0, \tag{5.39}$$

as all the walls are electrically insulated and the velocities are 0 on the boundary. The Dirichlet BC are set for magnetic field and are $B_x = 1$ T and $B_y = 0$ on all boundaries. The BC for pressure is obtained from Eq. 2.108. The $\mathbf{v}_w = 0$ and the $\mathbf{v}^*$ is calculated as

$$\mathbf{v}^* = \mathbf{v} + \frac{\Delta t}{\rho}\big(- \rho\nabla \cdot (\mathbf{v}\mathbf{v}) + \mu\nabla^2\mathbf{v} + \mathbf{f}_b\big). \tag{5.40}$$

The scheme of the computational domain with the initial and boundary conditions is depicted in Fig. 5.12.

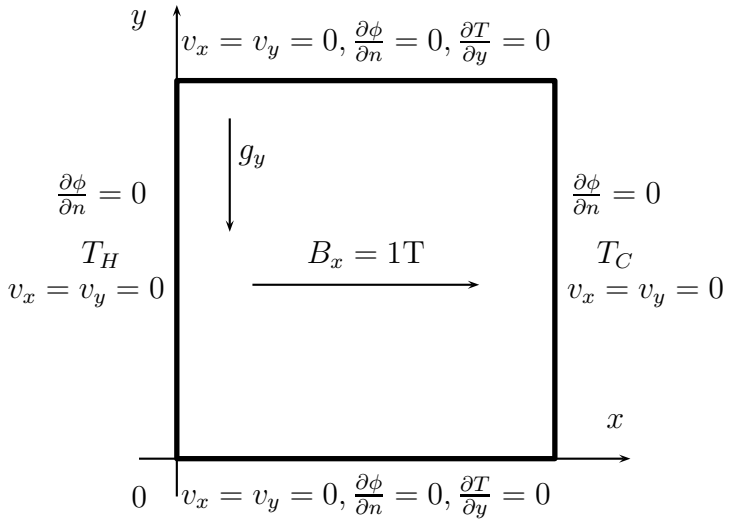

Figure 5.12: Scheme of a 2D differentially heated cavity with initial and boundary conditions.

5.3.3 Results and Discussions

Three different tests are performed to validate the numerical method. The first test case (Case 1) describes the standard de Vahl Davis natural convection benchmark test [de Vahl Davis, 1983] without the presence of the magnetic field. The second test case (Case 2) describes a stable, laminar fluid flow in a square cavity under the influence of the magnetic field. The most common reference papers for the defined problem, use Pr=0.71 [Colaço et al., 2009; Rudraiah et al., 1995; Salah et al., 2001; Sathiyamoorthy and Chamkha, 2010, 2012], which is a Prandtl number typical for air. In the third test case (Case 3) the MHD flow with Pr=0.14, (typical for steel), is used. Each of the three cases is compared to the results obtained from the Fluent code or the results obtained from reference papers [de Vahl Davis, 1983; Kosec and Šarler, 2008c; Šarler, 2005; Colaço et al., 2009].

The node arrangement is refined near the walls. A non-uniform node arrangement with a refinement parameter $u = 1.2$ is used in all of the cases. A scheme of a non-uniform node arrangement with 1677 nodes is depicted in Fig. 5.2. All of the examples are calculated with MQ RBFs, with shape parameter $c = 32$ and a FSM PV scheme. The time step $\Delta t' = 10^{-4}$ is used and a following convergence criteria is applied: $\varepsilon_p = 10^{-6}$, $\varepsilon_v = 10^{-6}$ and $\varepsilon_T = 10^{-6}$.

All of the results are presented in their dimensionless form. The MHD flow in a square cavity of dimension L is characterized by Ra (Eq. 5.9), Pr (Eq. 5.2), Ha (Eq. 5.13), Gr (Eq. 5.7), and Re_m (Eq. 5.15) dimensionless parameters, where the characteristic length ℓ is equal to the dimension L of the cavity. The derivation of the dimensionless equation is presented in Appx. B.2. The Nusselt number (Nu), defined as

$$\mathrm{Nu} = \int_0^L \left. \frac{\partial T}{\partial x} \right|_{x=0} dy, \tag{5.41}$$

is used to compare the results obtained with the developed LRBFCM, the pub-

lished reference results [Colaço et al., 2009] and the results calculated with Fluent. The stream function Ψ is calculated by integrating the velocity

$$\Psi(x,y) = \int_0^y v_x(x,\tilde{y})d\tilde{y}. \tag{5.42}$$

Case 1

Case 1 is the well known de Vahl Davis benchmark test [de Vahl Davis, 1983], which is presented here only as a basic test of the accuracy of the method, since the purpose of this test is to investigate the behaviour of the MHD flow characterised by small Pr numbers. The results are calculated for a node arrangement with 101x101 nodes and are compared to the reference results [de Vahl Davis, 1983; Kosec and Šarler, 2008c; Šarler, 2005] presented in Tab. 5.3. Values of Nu in the present application of the LRBFCM method are slightly larger than those obtained with the LRBFCM and the local pressure correction [Kosec and Šarler, 2008c], and slightly smaller than those obtained with the FVM [de Vahl Davis, 1983]. The difference between the present results and the results obtained by [Kosec and Šarler, 2008c] might arise due to a different approach in node arrangement; in the present case the nodes are refined near the wall, whereas in [Kosec and Šarler, 2008c], a uniform node arrangement is used. The results are also compared to the results obtained with the global RBFCM [Šarler, 2005], where 30x30 nodes were employed. A slight difference in Nu between the present results and those obtained with the global method is mainly due to the difference in the node density. It should be noted that it is impossible to apply the 101x101 node arrangement in the global method due to the ill conditioning of the collocation matrix.

Table 5.3: Case 1. Comparison of LRBFCM predictions with previous solutions for Pr=0.71 and various Ra numbers. 1: [de Vahl Davis, 1983], 2: [Kosec and Šarler, 2008c], 3: [Šarler, 2005].

Ra	Nu (present case)	Nu [1]	Nu [2]	Nu [3]
10^3	1.108	1.116	1.089	1.114
10^4	2.223	2.234	2.258	2.246
10^5	4.497	4.510	4.511	4.523
10^6	8.779	8.798	8.970	8.834

Case 2

Case 2 deals with a laminar fluid flow in a square cavity, characterized by a relatively high Pr=0.71, which is typical for air. The results in this case are compared to the reference results obtained in [Colaço et al., 2009] as well as those calculated with Fluent. Ha number that characterises the flows in the presence of the magnetic field is varied between 0 and 100 (Ha=0, 10, 50, 100) whereas

the behaviour of the flow is investigated for Gr variations that range from 10^4 to 10^6.

A summary of the results is presented in Tab. 5.4, where it is clearly shown that Nu decreases with increasing Ha. The values of Nu obtained with the present method are slightly lower than those obtained with the FVM and slightly higher than those obtained with the RBF method used in [Colaço et al., 2009].

Table 5.4: Case 2. Comparison of present predictions with previous works in terms of Nu for Pr=0.71 and various Ha and Gr numbers. 1: [Colaço et al., 2009], 2: Fluent.

Ha	Nu (present method)	Nu [1]	Nu [2]
$Gr = 10^4$			
0	2.03	2.02	2.06
10	1.71	1.70	1.84
50	1.01	0.97	1.06
$Gr = 10^6$			
0	8.15	9.21	7.98
10	7.99	9.04	7.88
100	3.33	3.54	4.27

Next, Nu is compared for an increasingly dense node arrangements; with 41x41, 61x61, 81x81 and 101x101 nodes respectively. As can be seen in Fig. 5.13, Nu is slightly higher for the coarsest node arrangement (41x41). For 61x61, 81x81 and 101x101, the value of Nu is approximately the same. The calculations are considered reasonably independent, since Nu does not change significantly for node arrangements with larger number of nodes. All the subsequent calculations are therefore done on the 81x81 node arrangement. For comparison, the 15x15 and 25x25 node arrangement is used in [Colaço et al., 2009].

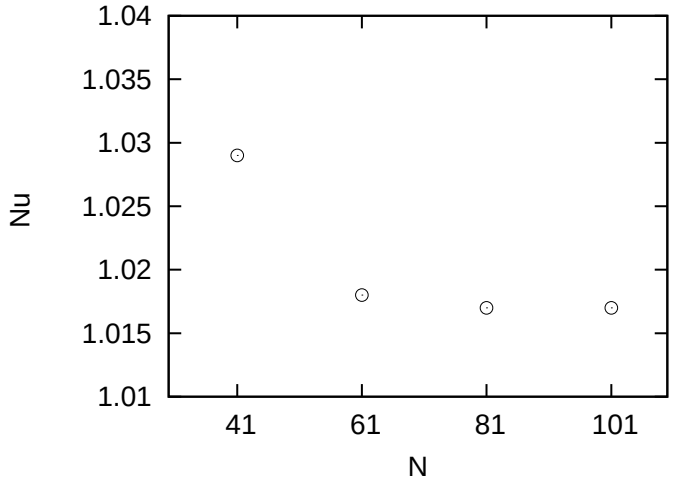

Figure 5.13: Case 2. Nu as function of four different node arrangements (41x41, 61x61, 81x81 and 101x101) at Gr = 10^4 and Pr=0.71.

Finally, the dimensionless velocity and temperature profiles are drawn along the horizontal and vertical lines through the center of the cavity as presented in

Fig. 5.3. A comparison is made between the results from [Colaço et al., 2009], Fluent and those calculated with the LRBFCM, which are all calculated on a near-the-wall refined node arrangement with $u = 1.2$. As can be seen in Figs. 5.14 and 5.15 the results are in good agreement. In the work of [Colaço et al., 2009], the non-dimensional velocity is calculated as

$$\mathbf{v}' = \frac{\mathbf{v}}{\sqrt{\mathbf{g}\beta_T(T_H - T_C)L}}, \tag{5.43}$$

whereas in this dissertation the dimensionless velocity for the square cavity is calculated as

$$\mathbf{v}' = \frac{\mathbf{v}}{v_c}. \tag{5.44}$$

The difference in definition does not reflect in the results.

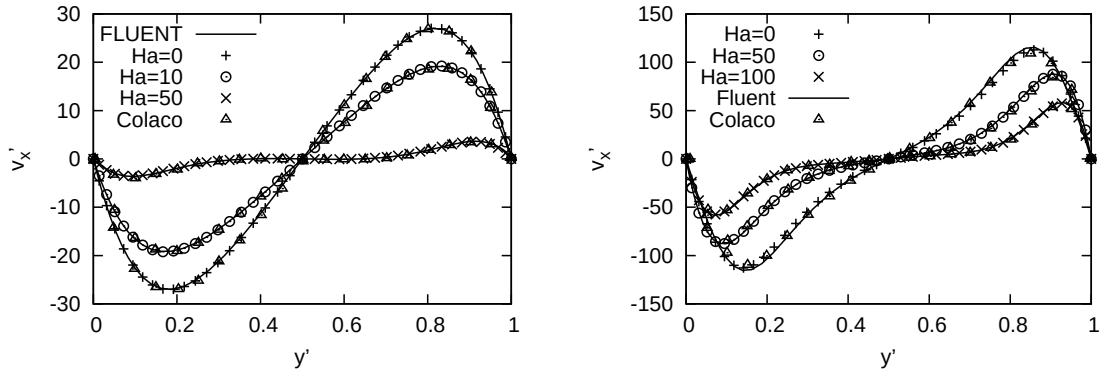

Figure 5.14: Case 2. Comparison of dimensionless velocities v'_x for $\mathrm{Gr} = 10^4$ (left) and $\mathrm{Gr} = 10^6$ (right) along the horizontal line through the center of the cavity.

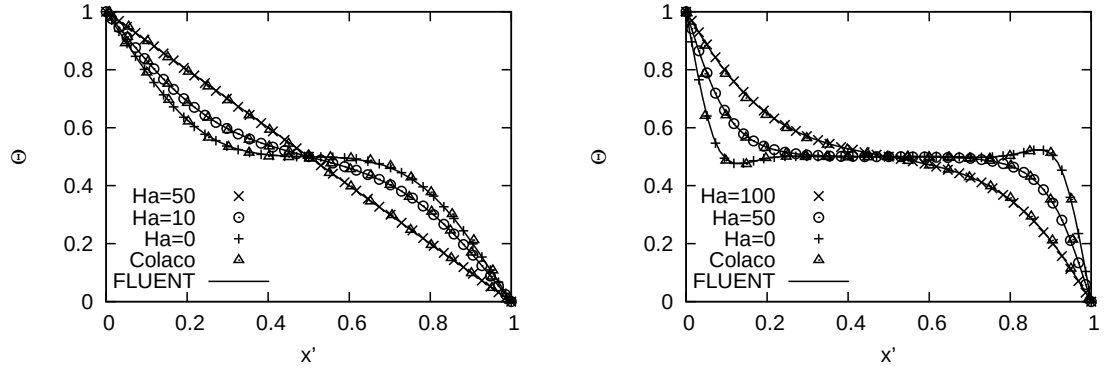

Figure 5.15: Case 2. Comparison of dimensionless temperatures Θ for $\mathrm{Gr} = 10^4$ (left) and $\mathrm{Gr} = 10^6$ (right) along the horizontal line through the center of the cavity.

Case 3

Case 3 tackles a MHD flow test case with a stable, laminar flow with low Pr number Pr=0.14, typical for steel. Due to the lack of relevant published data,

this test case is compared only to the results obtained with the FVM. The results are calculated for a variety of Ha numbers, ranging from 0 to 200 (0, 10, 50, 100, 200) and Gr values ranging from $\mathrm{Gr} = 10^4$ and $\mathrm{Gr} = 10^6$ ($\mathrm{Gr} = 10^4$, $\mathrm{Gr} = 10^5$, $\mathrm{Gr} = 10^6$). The results calculated with the in-house LRBFCM method are in a very good agreement with the results calculated with Fluent, as is shown in Figs. 5.16 - 5.20.

The dimensionless temperature profiles along the horizontal line through the center of the cavity, depicted in Figs. 5.16 and 5.17, show that the temperature profiles change with the increasing Gr number. The temperature gradients at both sides of the cavity increase, while the temperature gradient at the middle of the cavity decreases, thus causing a thicker boundary layer. In other words, the increase in Ha number causes the convection to quench. As a result the isotherms are straightened and parallel with the vertical wall.

The dimensionless velocities v'_x and v'_y along the horizontal and along the vertical lines through the center of the cavity are depicted in Figs. 5.18, 5.19, and 5.20. The quench due to the externally applied magnetic field is evident in both of the velocity components. By increasing the Gr number, the external magnetic field has to be amplified in order to annihilate the fluid flow. The values for the dimensionless velocities v'_x and v'_y are for a representative example with Ha=0 and Ha=50, and $\mathrm{Gr} = 10^6$ given in Tab. 5.5.

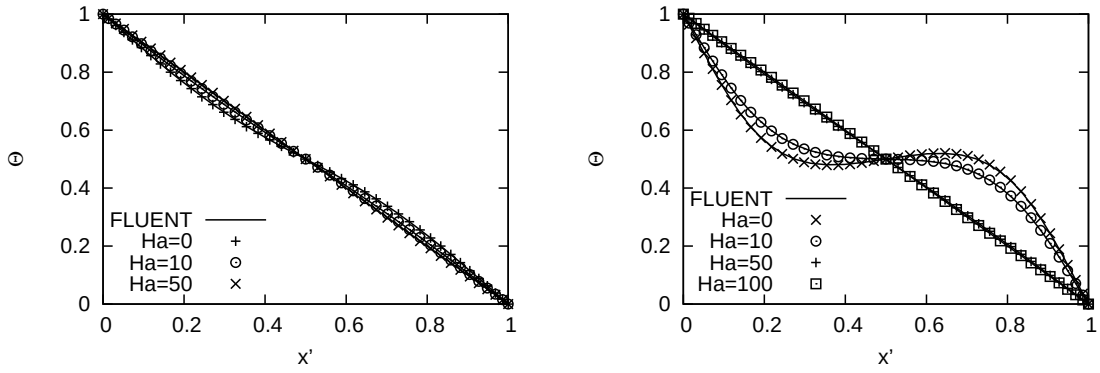

Figure 5.16: Case 3. Comparison of dimensionless temperatures Θ for $\mathrm{Gr} = 10^4$ (left) and $\mathrm{Gr} = 10^5$ (right) along the horizontal line through the center of the cavity.

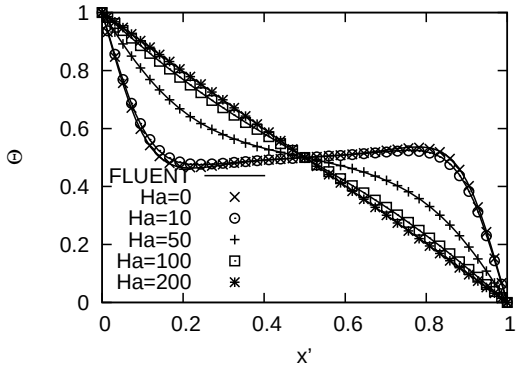

Figure 5.17: Case 3. Comparison of dimensionless temperatures Θ for $\mathrm{Gr} = 10^6$ along the horizontal line through the center of the cavity.

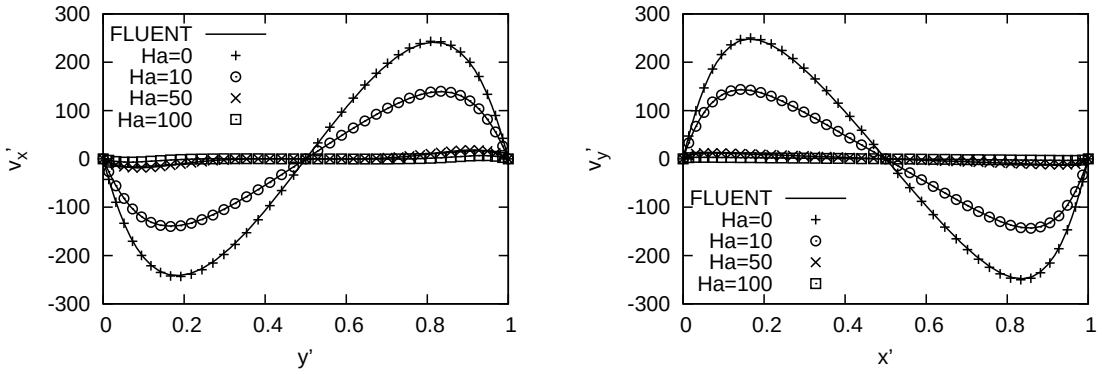

Figure 5.18: Case 3. Comparison of v'_x along the horizontal (left) and v'_y along the vertical (right) lines through the center of the cavity for $\mathrm{Gr} = 10^4$ as a function of different Ha.

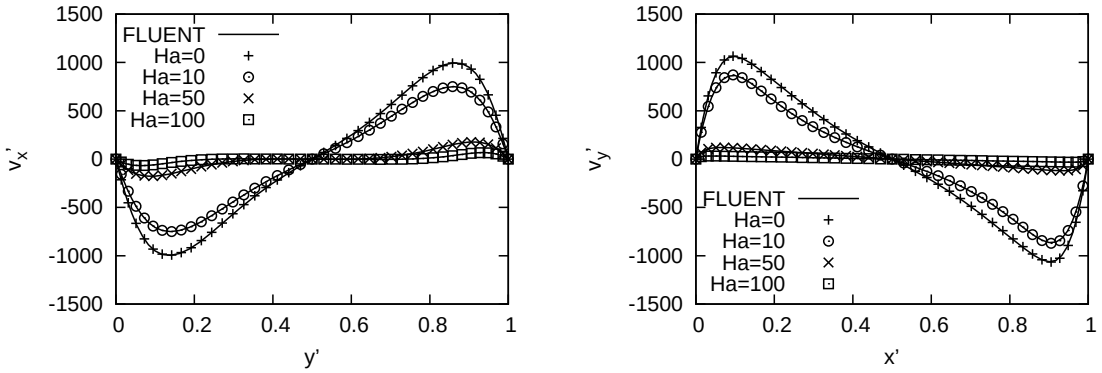

Figure 5.19: Case 3. Comparison of v'_x along the horizontal (left) and v'_y along the vertical (right) lines through the center of the cavity for $\mathrm{Gr} = 10^5$ as a function of different Ha.

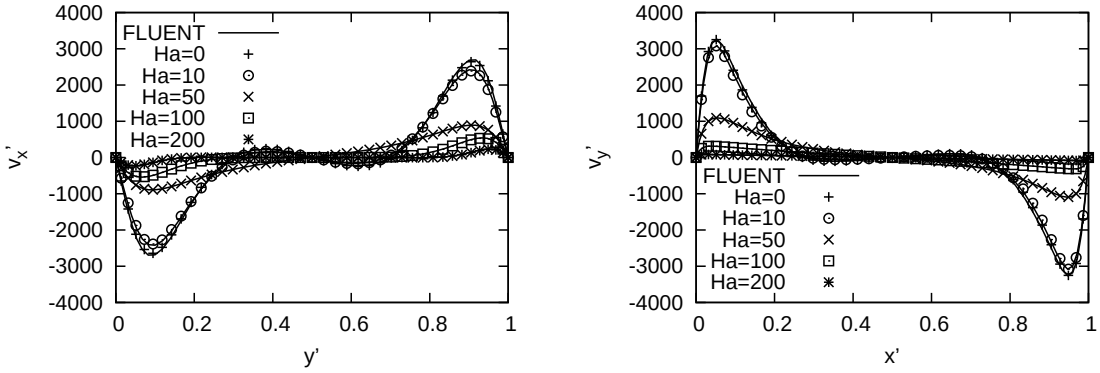

Figure 5.20: Case 3. Comparison of v'_x along the horizontal (left) and v'_y along the vertical (right) lines through the center of the cavity for Gr = 10^6 as a function of different Ha.

Table 5.5: Case 3. Tabulated dimensionless velocities for Gr = 10^6, Ha = 0 and 50, obtained with LRBFCM.

x (in actual nodal points)	v'_x, Ha=0	v'_y, Ha=0	v'_x, Ha=50	v'_y, Ha=50
0.0000	0.0000	0.0000	0.0000	0.0000
0.0513	-2118.4	3230.0	-762.79	1092.6
0.1179	-2480.2	1865.8	-861.00	841.29
0.1665	-1695.4	957.14	-717.00	615.38
0.2176	-821.50	332.76	-548.51	430.96
0.2708	-194.71	20.478	-397.38	291.58
0.3259	144.73	-102.16	-271.57	188.84
0.3825	244.16	-93.843	-168.14	112.34
0.4406	168.41	-50.000	-80.286	52.309
0.5000	-0.1860	0.0128	0.1889	0.1202

The streamlines and isotherms are depicted in Figs. 5.21 - 5.24 for Ha = 0, 10, 50, 100 and 200, and Gr = 10^4, 10^5 and 10^6. The profile of streamlines in the presence of a weak magnetic field is similar to the profile of streamlines with no magnetic field. As the strength of the magnetic field is increased, the profile of streamlines changes and becomes tilted and elongated in y direction. In the presence of a strong magnetic field, the convection is completely quenched, due to the suppressing effect of the Lorentz force. The isotherms (Fig. 5.23 and Fig. 5.24) act in a similar way; in the presence of the weak magnetic field the profiles are similar to the ones without the magnetic field, whereas in the presence of the strong magnetic fields the convection is suppressed and the isotherms become parallel to the vertical wall.

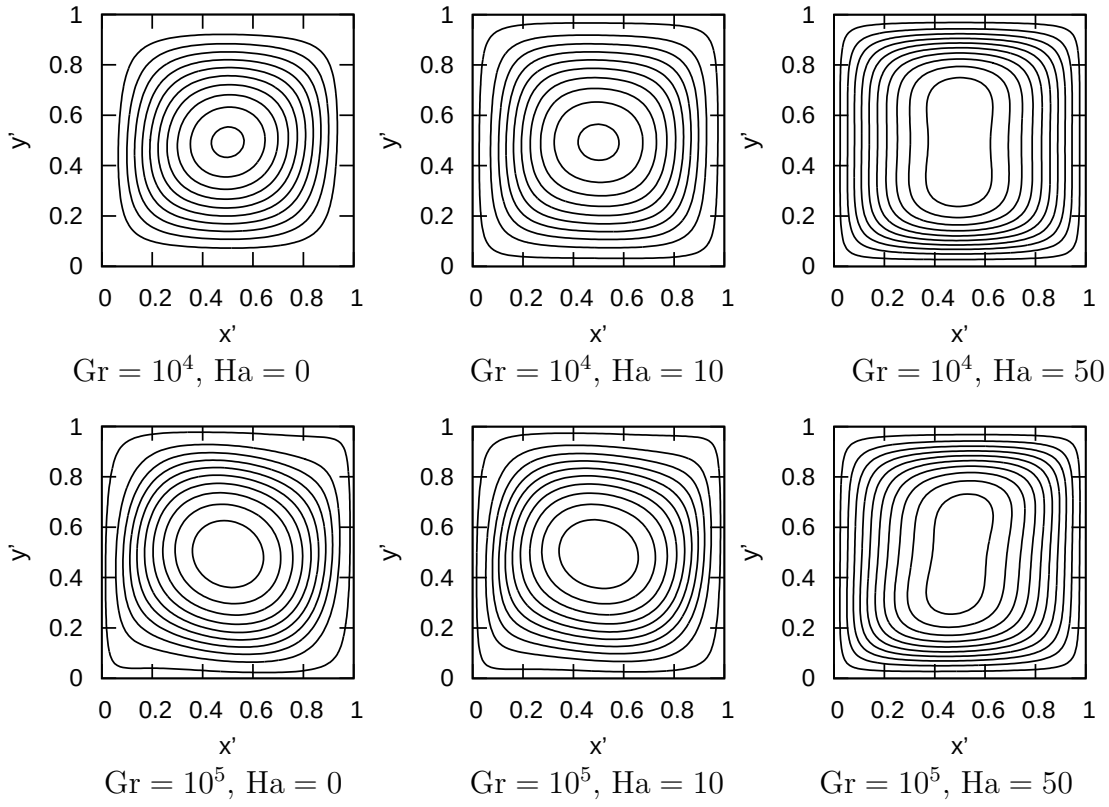

Figure 5.21: Case 3. Comparison of streamlines at various Gr ($Gr = 10^4$,$Gr = 10^5$) and Ha (0, 10, 50). The streamlines are equidistantly spaced.

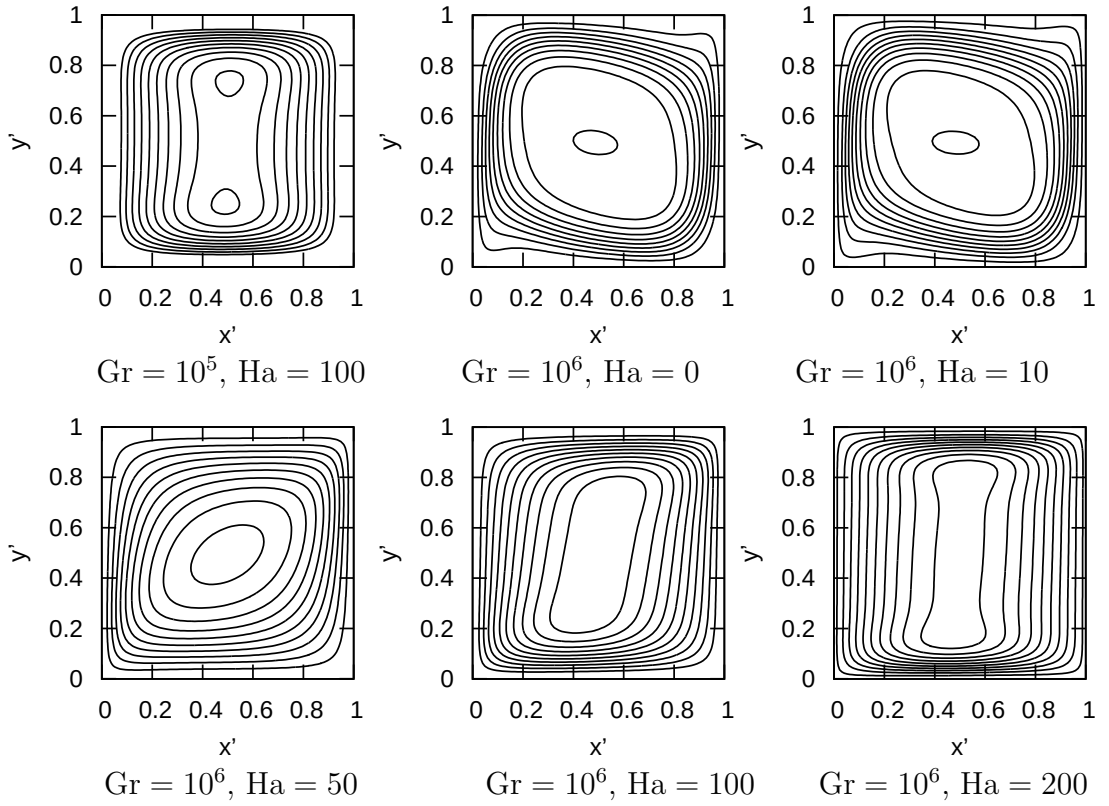

Figure 5.22: Case 3. Comparison of streamlines at various Gr ($Gr = 10^5$, $Gr = 10^6$) and Ha (0, 10, 50, 100, 200). The streamlines are equidistantly spaced.

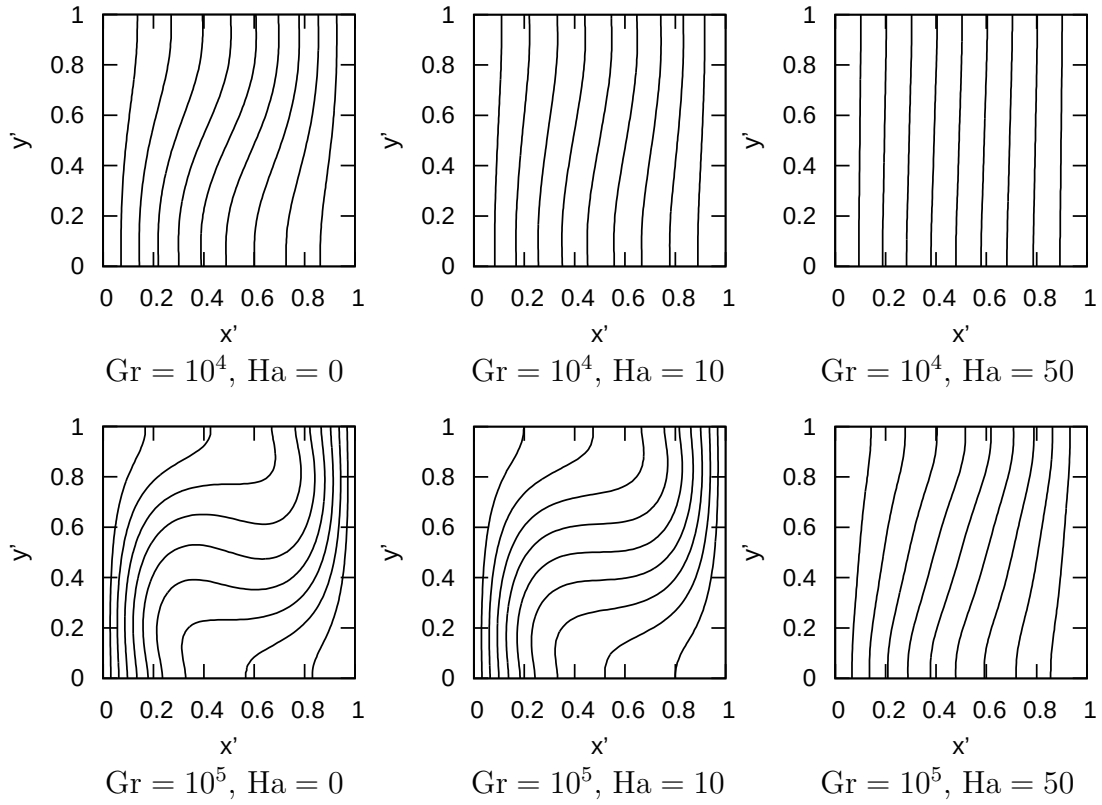

Figure 5.23: Isotherms at various Gr (Gr = 10^4, Gr = 10^5) and Ha (0, 10, 50) at Pr=0.14. The isotherms are equidistantly spaced, the minimum is at T_C (right boundary) and the maximum is at T_H (left boundary).

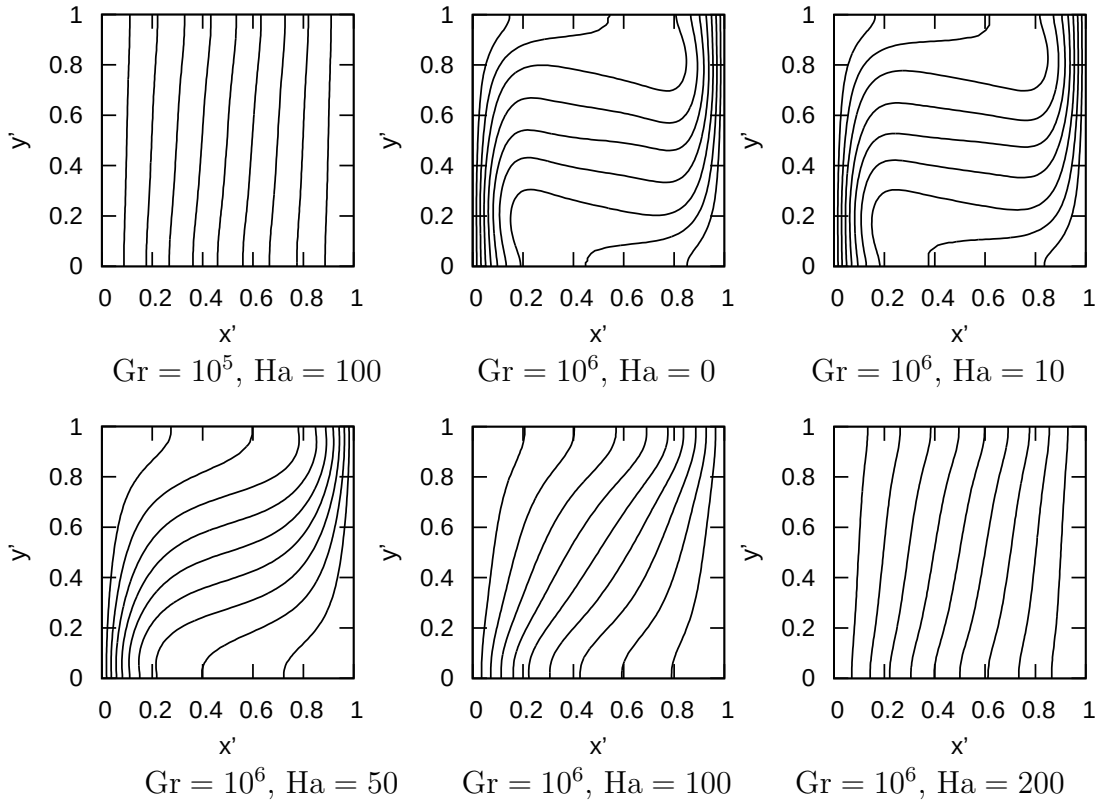

Figure 5.24: Isotherms at various Gr (Gr = 10^5, Gr = 10^6) and Ha (0, 10, 50, 100, 200) at Pr=0.14. The isotherms are equidistantly spaced, the minimum is at T_C (right boundary) and the maximum is at T_H (left boundary).

5.3.4 Summary and Conclusions

The aim of this test case is to asses the behaviour of the LRBFCM method on a natural convection in the presence of magnetic field for a Pr number that is consistent with Pr for steel. The results in all of the cases match the previously published reference results [de Vahl Davis, 1983; Kosec and Šarler, 2008c; Šarler, 2005; Colaço et al., 2009] as well as those calculated with Fluent. It is shown, that the method produces accurate results both in the case with and without the presence of magnetic field as well as for the low Pr typical for steel.

5.4 Hartmann Flow

5.4.1 Problem Description

A laminar, conducting fluid, confined between two parallel plates with insulating walls is investigated. The magnetic field orientation is perpendicular to the direction of the flow, that is driven by the constant pressure gradient. This magnetic Poisseuille flow was first investigated by Hartmann in 1937 [Hartmann and Lazarus, 1937] and is thus called Hartmann flow. In this instance, the Hartmann

flow is important as an analytical reference against which the numerical calculation of the flow in the presence of a magnetic field can be verified. The laminar, incompressible flow is considered in a rectangular domain.

The purpose of this test case is to asses the LRBFCM against analytical results.

5.4.2 Governing Equations

The Hartmann flow is described by the mass (Eq. 5.21)

$$\nabla \cdot \mathbf{v} = 0 \tag{5.45}$$

and momentum equations (Eq. 5.29)

$$\rho\left(\frac{\partial \mathbf{v}}{\partial t} + \nabla \cdot \left(\mathbf{v}\mathbf{v}\right)\right) = -\nabla p + \mu \nabla^2 \mathbf{v} + \mathbf{j} \times \mathbf{B}. \tag{5.46}$$

As the plates are parallel, the velocities in y direction are equal to 0. The velocities are time invariant, and thus the velocity profile does not change in the x direction. By applying these assumption to Eq. 5.29 it is simplified into

$$0 = -\nabla p + \mu \nabla^2 \mathbf{v} + \mathbf{j} \times \mathbf{B}. \tag{5.47}$$

The dimensionless forms of the mass equation (Eq. 5.23) is

$$\nabla \cdot \mathbf{v}' = 0 \tag{5.48}$$

and the dimensionless form of momentum equation is

$$0 = -\nabla p' + \nabla^2 \mathbf{v}' + \mathrm{Ha}^2 \mathbf{v}'. \tag{5.49}$$

The derivation of dimensionless equation is together with the definition of dimensionless variables elaborated in Appx. B.3.

Initial Conditions

The solution is sought for the following initial conditions for velocity

$$\mathbf{v} = 0, \tag{5.50}$$

magnetic field

$$B_x = 0, \quad B_y = 1T, \tag{5.51}$$

and pressure

$$p = 0. \tag{5.52}$$

Boundary Conditions

The BC for velocity, electric potential and pressure on the top and bottom walls are

$$v_x = 0, \quad v_y = 0, \quad \frac{\partial \phi}{\partial \mathbf{n}} = 0, \quad \frac{\partial p}{\partial \mathbf{n}} = 0. \tag{5.53}$$

The prescribed BC on the inlet are

$$v_x = 1\text{m/s}, \quad v_y = 0, \quad \frac{\partial \phi}{\partial \mathbf{n}} = 0, \quad p = 0, \tag{5.54}$$

and at the outlet

$$v_x, \quad v_y, \quad \frac{\partial \phi}{\partial \mathbf{n}} = 0, \quad p = 0. \tag{5.55}$$

A scheme of the computational domain with the initial and boundary conditions is shown in Fig. 5.25.

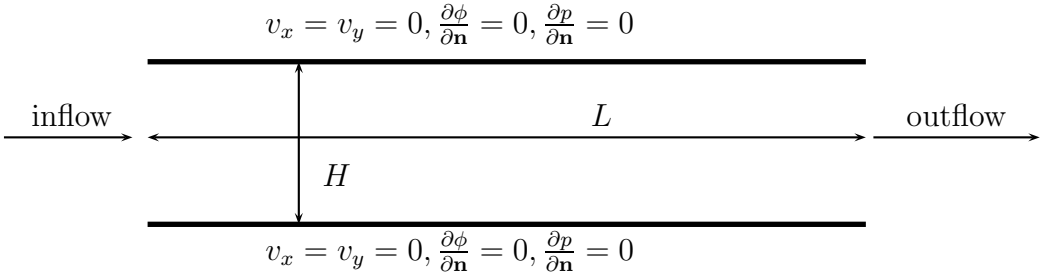

Figure 5.25: Scheme with initial and boundary conditions.

5.4.3 Results and Discussions

The result are calculated first for the classical channel flow and then for the flow of a conducting liquid through the channel in the presence of an externally applied magnetic field. The analytical solution for the Hartmann flow [Hartmann and Lazarus, 1937] is stated as

$$\frac{v(x)}{v_{x(MAX)}} = \frac{\text{Ha}}{\text{Ha} - \tanh(\text{Ha})}\Big(1 - \frac{\cosh(L\text{Ha})}{\cosh(\text{Ha})}\Big), \tag{5.56}$$

where $v_{x(MAX)}$ is the center-line velocity. If Ha= 0, the flow is reduced to the standard flow in the channel. The analytical solution for the channel flow is written as

$$v(x) = \frac{3}{2} v_{x(MAX)} \left(1 - \left(\frac{2x}{L}\right)^2\right). \tag{5.57}$$

The results are drawn at the outlet of the channel that has 39x99 node arrangement. The node arrangement is refined only in the x direction, with the

refinement parameter $u = 1.2$ as shown in Fig. 5.26. The shape parameter is $c = 32$. The calculations were done for Pr = 0.71 and Re = 100 for various Ha (0, 1, 5, 10, 20, 50, 100, 200, 500, 1000) numbers. The time step used for this particular case is $\Delta t = 10^{-4}$ s and the calculations were stopped when the convergence criteria for the velocity $\varepsilon_v = 10^{-8}$ is reached.

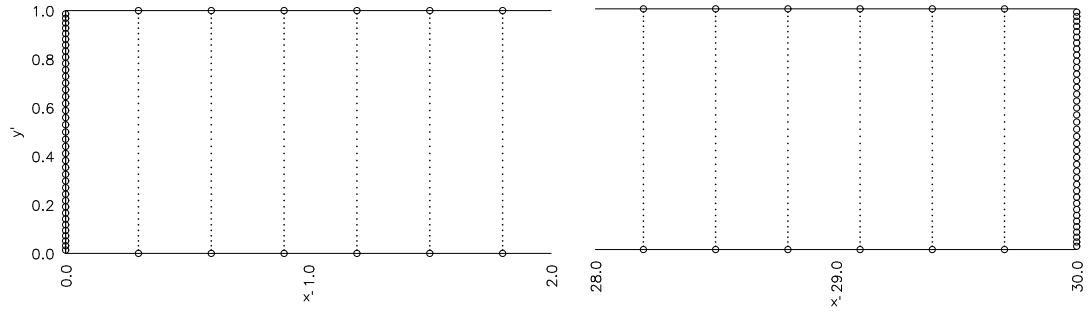

Figure 5.26: Node arrangement with 39x99 nodes. The H/L ratio is 30. Left: beginning of the channel. Right: end of the channel.

First, the dimensionless center-line velocity is compared for several different Ha numbers ranging from 0 to 1000 (0, 5, 10, 20, 50, 100, 200, 500, 1000). By increasing the Ha number the velocity is decreased, as can be seen in the left graph in Fig. 5.27. The graph presents both the logarithmic scale, which is depicted with blue markings, and the regular scale which is denoted with red markings. The right graph in Fig. 5.27 shows the dependence of the Lorentz force on the Ha number. The Lorentz force is depicted for Ha values 5, 10, and 20. By increasing the Ha, the magnitude of the Lorentz force increases and consequently the velocity profiles become more and more flattened.

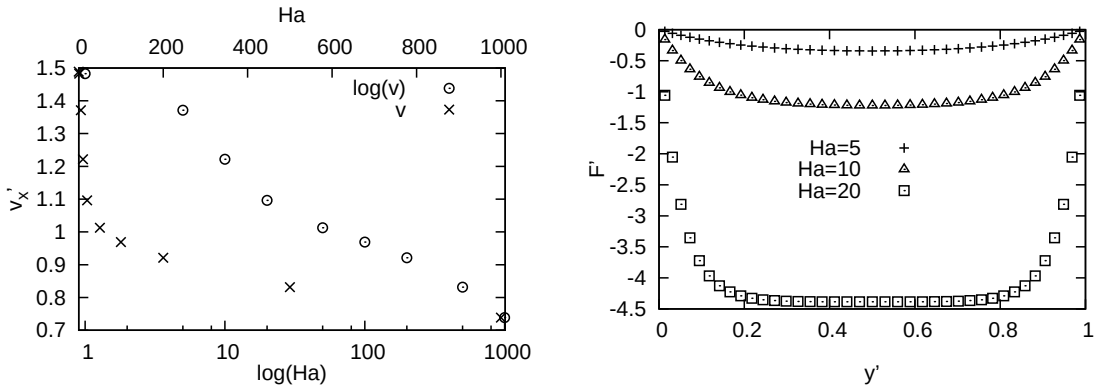

Figure 5.27: Comparison of dimensionless velocities for different node arrangements for Re = 800. Left: v'_x along the vertical line at the end of the channel. Right: Lorentz force (dimensionless) along the vertical line at the end of the channel.

The effect of Ha number on the velocity profile is shown in Fig. 5.28. The left graph depicts the normalized velocity for various Ha numbers (0, 5, 10, 20 and 100). The dimensionless velocity profiles are shown in the right graph. It is apparent from both graphs that the larger the Ha is, the more the velocity

profile is flattened. This phenomenon is called the Hartmann effect and the area in which the velocity changes from 0 to $v_{x(MAX)}$ is called the Hartmann layer.

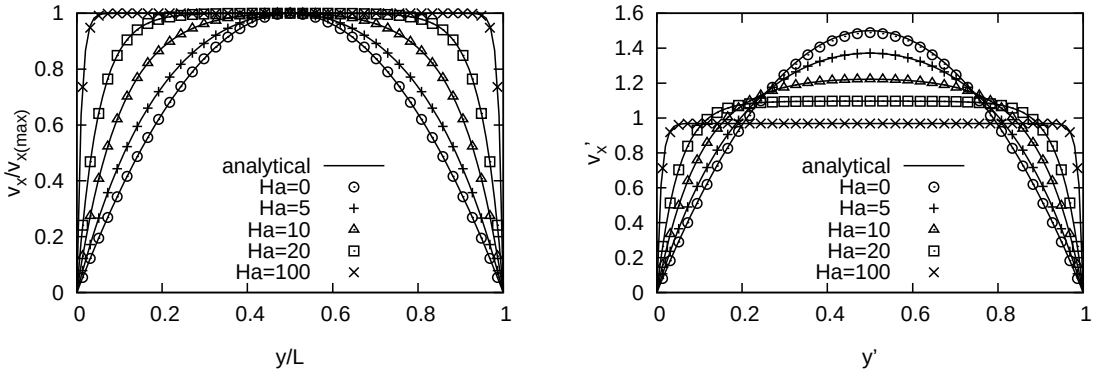

Figure 5.28: Comparison of velocity profiles for different Ha. Left: normalized velocity ($v_x/v_{x(MAX)}$) along the vertical line at the end of the channel. Right: dimensionless velocity (v'_x) along the vertical line at the end of the channel.

5.4.4 Summary and Conclusions

The analysis is performed for the laminar fluid flow under the influence of transverse magnetic field. It is shown that the Lorentz force increases (in opposite direction of the flow) with increasing Ha. The drop in the velocity is approximately logarithmic. The results calculated with LRBFCM match the analytical results for a wide range of Ha numbers (0, 5, 10, 20, 100).

5.5 Forced Convection in a Backward Facing Step Channel with Magnetic Field

5.5.1 Problem Description

The backward facing step problem represents one of the standard benchmark test cases in fluid dynamics. A Newtonian, incompressible fluid flow in the presence of a static magnetic field is considered in a domain Ω with a boundary Γ. The behaviour of the flow over the backward facing step depends on Re number, especially when the magnetic field is not present. Without the presence of the magnetic field, typically two re-circulation zones are formed downstream. By increasing Re number, the recirculation zones become more pronounced. The opposite is true when the magnetic field is applied; by increasing Ha number, the recirculation zones are diminished. The governing equations and the precise boundary conditions used to solve these equations are described in the following chapters.

Literature Review of Numerical Modelling of Backward Facing Step Channel with Magnetic Field

As a standard benchmark test case, the backward facing step problem has already been used to asses several different numerical methods, such as FEM [Gartling, 1990; Ravindran, 2000; Kozel et al., 2004], FVM [Kozel et al., 2004], DRBEM [Bozkaya and Tezer-Sezgin, 2011], MLPGM [Wu et al., 2010], LRBFCM [Vertnik and Šarler, 2009b], finite point method based on incremental calculus [Oñate et al., 2000], local boundary integral method [Sellountos and Sequeira, 2008], local RBF method [Sanyasiraju and Chandhini, 2008], RBFCM [Chinchapatnam et al., 2007], LBM [Yang et al., 2013], and several others. Lately, various configurations of magnetic field were applied to the backward facing problem and solved with a number of different numerical methods, such as FEM [Codina and Hernández-Silva, 2006], generalized integral transform technique [Lima and Rêgo, 2013][2], FDM [Hsu et al., 2010], modified version of control volume FEM [Abbassi and Ben Nassrallah, 2007], and many others.

In this dissertation, the backward facing test is used to asses the accuracy of the method, when calculating the separation and the reattachment positions of the flow. The results of this test case have already been published in [Mramor et al., 2014b].

5.5.2 Governing Equations

The governing equations that describe the problem are the mass conservation equation (Eg. 5.21)

$$\nabla \cdot \mathbf{v} = 0 \tag{5.58}$$

and the momentum equations (Eq. 5.46)

$$\rho\left(\frac{\partial \mathbf{v}}{\partial t} + \nabla \cdot \left(\mathbf{v}\mathbf{v}\right)\right) = -\nabla p + \mu \nabla^2 \mathbf{v} + \mathbf{j} \times \mathbf{B}. \tag{5.59}$$

The dimensionless form of the mass conservation equation (Eq. 5.23) is

$$\nabla \cdot \mathbf{v}' = 0 \tag{5.60}$$

and the dimensionless form of the momentum conservation equation is

$$\frac{\partial \mathbf{v}'}{\partial t'} + \nabla(\mathbf{v}'\mathbf{v}') = -\nabla p' + \frac{1}{Re}\nabla^2 \mathbf{v}' + \frac{Ha^2}{Re}\mathbf{v}'. \tag{5.61}$$

The dimensionless variables along with the derivation of dimensionless equation is elaborated in Appx. B.4.

Initial Conditions

The initial conditions are predetermined and are given as

$$v_x = 0, \quad v_y = 0, \tag{5.62}$$

[2]Generalized integral transform technique is a hybrid numerical/analytical method.

for the velocity, as

$$B_x = 0, \quad B_y = B_{y0}, \tag{5.63}$$

for the magnetic field, and as

$$p = 0 \tag{5.64}$$

for the pressure.

Boundary Conditions

The velocity BC on all the walls are non-slip and non-permeable (Dirichlet)

$$v_x = 0, \quad v_y = 0. \tag{5.65}$$

The Neuman BC are applied for the pressure and the electric potential on the solid walls as well as on the left boundary with the inlet flow and are written as

$$\frac{\partial p}{\partial \mathbf{n}} = 0, \quad \frac{\partial \phi}{\partial \mathbf{n}} = 0. \tag{5.66}$$

The velocities on the left boundary with the inlet flow are prescribed with the Gartling velocity profile for a fully developed flow and are 0 on the wall bellow. The velocity in x direction is on the left side of the computational domain prescribed as

$$v_x = \begin{cases} 0 & \text{if } 0 \leq x \leq 0.5 \\ v_x = 12(x-1)(1-2x) & \text{if } 0.5 \leq x \leq 1 \end{cases}$$

The velocity in y direction is on the left side of the computational domain given with the Dirichlet BC as

$$v_y = 0. \tag{5.67}$$

At the right boundary with the outlet flow, the Neuman BC are used for the velocities and the electric potential

$$\frac{\partial v_x}{\partial x} = 0, \quad \frac{\partial v_y}{\partial y} = 0, \quad \frac{\partial \phi}{\partial n} = 0, \tag{5.68}$$

and the Dirichlet BC is used for the pressure

$$p = 0. \tag{5.69}$$

The geometry of the backward facing step problem is presented in Fig. 5.29 and the computational domain with the initial and boundary conditions are presented in Fig. 5.30.

5.5.3 Results and Discussions

To validate the method, two different tests are considered. The first test case (Case 1) features a standard backward facing step problem [Gartling, 1990], whereas the second test case (Case 2) presents a fluid flow over a backward facing step under the influence of an externally applied magnetic field. The results of

Figure 5.29: Geometry of the backward facing step problem. The H/L ratio is 15.

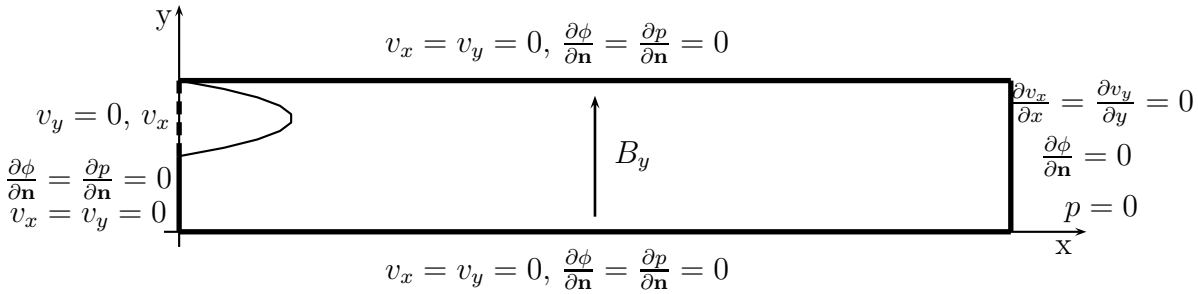

Figure 5.30: Scheme of the backward facing step problem with initial and boundary conditions.

each test case are compared either to the results from the pertained reference papers or to those calculated with Fluent. The MQ trial functions and FSM PV coupling method are used in calculations. The convergence criteria ε_v and ε_p are set to 10^{-6}.

The test cases are validated on a non-uniform node arrangement as shown in Fig. 5.31. The refinement is calculated as stated in Sect. 4.1 with the refinement parameter $u = 1.4$. A scheme of the node arrangement can be seen in Fig. 5.31.

Case 1

Case 1 features the standard backward facing step benchmark problem without the magnetic field [Gartling, 1990]. The grid independency is tested on the non-uniform 201x51, 301x101, 401x151, and 501x201 node arrangements for Re = 800 and Ha = 0 and the results are presented in Fig. 5.32. The 301x101 node arrangement is adopted for all the subsequent calculations as the difference between the results for 301x101, 401x151, and 501x201 node arrangements is insignificant. A comparison of extreme values of the v'_x and the v'_y at the outlet are given in Tab. 5.6 for different node arrangements.

The results calculated with LRBFCM were first compared with the results from [Gartling, 1990] that were calculated with the FEM at two different horizontal positions ($x' = 7$ and $x' = 15$). The results of the comparison are shown in Fig. 5.33, where only a slight difference between the reference results [Gartling, 1990] and present results in the vertical profile for $x' = 7$ is evident. The results differ less then 0.02%, except for $v'_y(x' = 7)$, where the difference is 3.5 %.

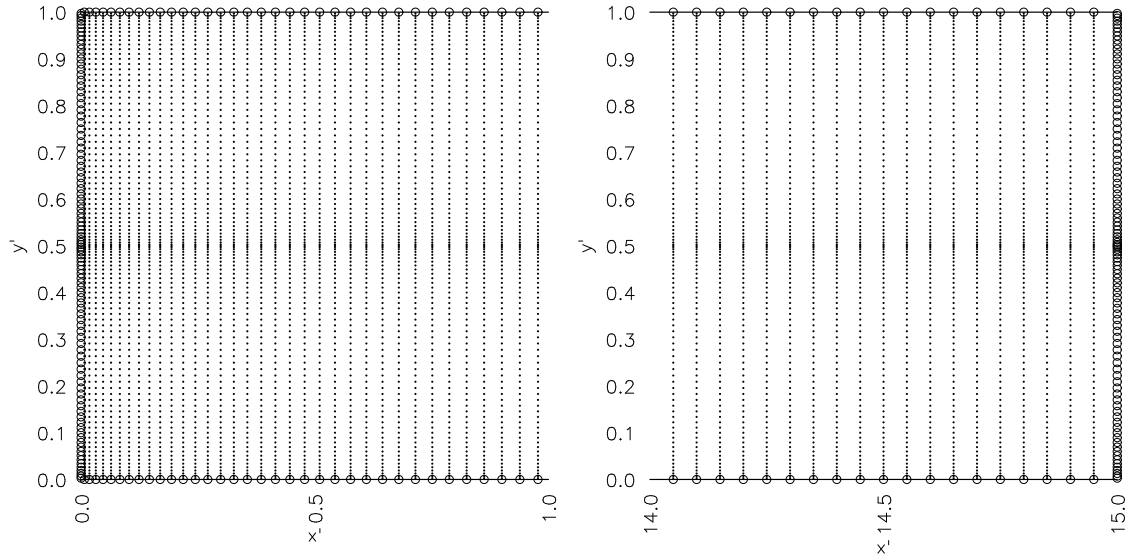

Figure 5.31: Scheme of 301x101 node arrangement. Due to the size of the domain only a section of the flow inlet (left) and flow outlet (right) parts of the channel are presented. The circles represent the boundary nodes and the dots represent the domain nodes.

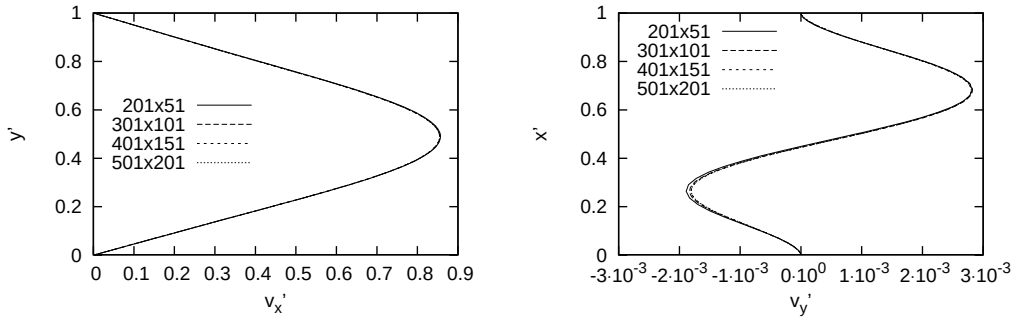

Figure 5.32: Comparison of dimensionless outlet velocities for different node arrangements for Re = 800 and Ha = 0. Left: x component of the velocity (v'_x) along the vertical line at the end of the channel. Right: y component of the velocity (v'_y) along the vertical line at the end of the channel.

Table 5.6: Comparison of extreme velocity values at the outlet for Re = 800 and Ha = 0 for 201x51, 301x101, 401x151, and 501x201 node arrangements.

nodes	$v'_x(max)$	$v'_y(min)(y')$	$v'_y(max)(y')$
201x51	0.85689	-0.0018882(0.26389)	0.0028217(0.68292)
301x101	0.85501	-0.0018313(0.26389)	0.0028237(0.68292)
401x151	0.85467	-0.0018057(0.26389)	0.0028043(0.68292)
501x201	0.85467	-0.0018057(0.26389)	0.0028043(0.68292)

Next, the dimensionless velocity profiles v'_x and v'_y were examined for various Re numbers ranging from 300 to 800 (300, 400, 500, 600, 700 and 800). As ex-

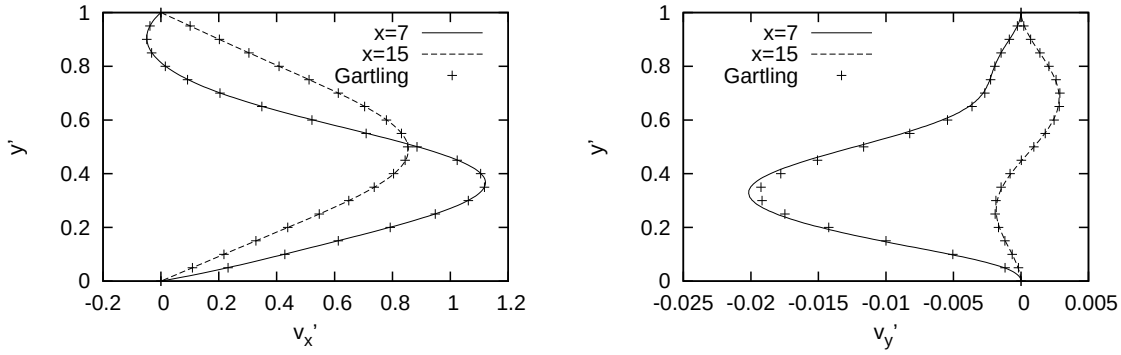

Figure 5.33: Comparison of v'_x (left) and v'_y (right) at two different positions ($x' = 7$ and $x' = 15$) for Re = 800 and Ha = 0, and 301x101 node arrangement.

pected, the velocity profiles demonstrate (Fig. 5.34) the increase in the extremes in both directions as Re is increased. The extreme values of velocities v'_x and v'_y are given in Tab. 5.7.

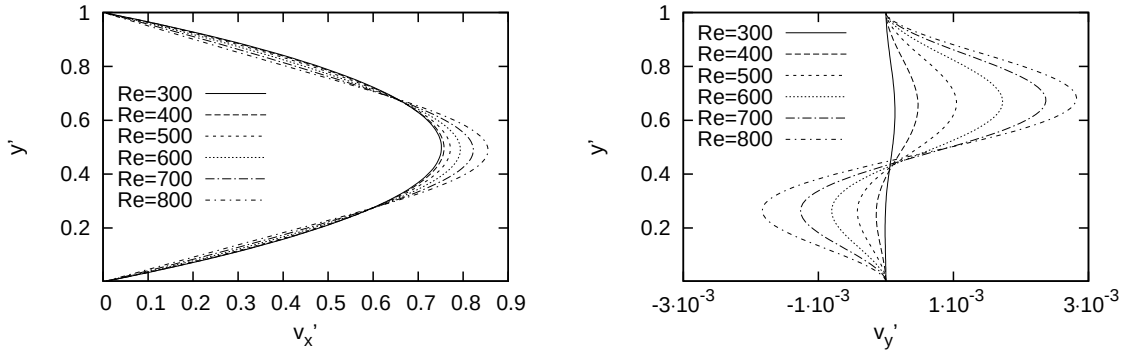

Figure 5.34: Comparison of outlet velocities for Re = 300, 400, 500, 600, 700, and 800 and Ha = 0 for 301x101 node arrangement.

Table 5.7: Extreme velocity values for the outlet velocity profiles for Re 300 to 800 (step 100) and Ha = 0.

Re	$v'_x(max)$	$v'_y(min)(y')$	$v'_y(max)(y')$
300	0.75167	$-1.1861\cdot10^{-5}(0.19585)$	$1.3445\cdot10^{-4}(0.63384)$
400	0.75751	$-1.4333\cdot10^{-4}(0.25000)$	$4.7601\cdot10^{-4}(0.65784)$
500	0.77141	$-4.2275\cdot10^{-4}(0.26389)$	$1.0443\cdot10^{-3}(0.65784)$
600	0.79370	$-8.0308\cdot10^{-4}(0.26389)$	$1.7292\cdot10^{-3}(0.67025)$
700	0.82242	$-1.2644\cdot10^{-3}(0.26389)$	$2.3681\cdot10^{-3}(0.67025)$
800	0.85501	$-1.8313\cdot10^{-3}(0.26389)$	$2.8237\cdot10^{-3}(0.68292)$

The wall shear stress τ_w, defined as

$$\tau_w = \mu \frac{\partial v_x}{\partial y}, \tag{5.70}$$

is calculated for Re ranging from 300 to 800 (step 100) on both the upper and the lower channel walls. The LRBFCM results are compared to the reference results [Gartling, 1990] for Re = 800 and Ha = 0. A comparison presented in Fig. 5.35 shows an excellent agreement with the reference results. The wall shear stresses are compared for different Re numbers (300 to 800 with step 100) for the upper and the lower walls of a backward facing configuration. The results are depicted in Fig. 5.36 and confirm that the recirculation zones are more pronounced for larger Re.

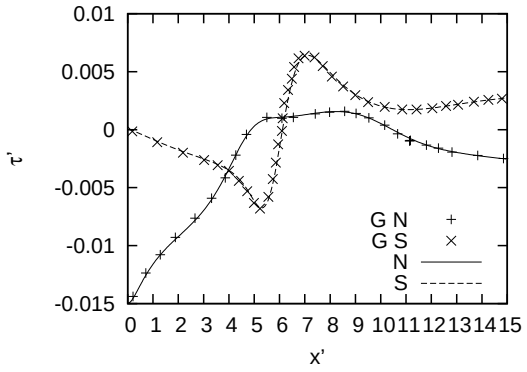

Figure 5.35: Comparison of wall shear stresses for the upper (N) and the lower (S) walls with reference results (G N) and (G S) [Gartling, 1990]) at Re = 800.

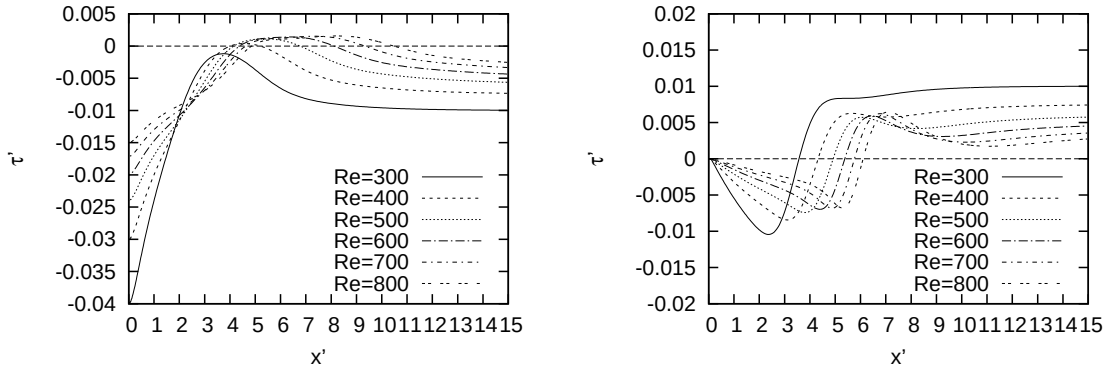

Figure 5.36: Comparison of wall shear stresses and reattachment positions for 301x101 node arrangement, Ha = 0 and Re ranging from 300 to 800 (step 100). Left: the wall shear stress profile at the upper wall. Right: the wall shear stress profile at the lower wall.

Finally, a comparison between the reattachment positions is made in Tab. 5.8. The results calculated with present method are compared to the reference results [Gartling, 1990; Gresho et al., 1993; Chiang et al., 1999; Keskar and Lyn, 1999; Barton, 1995; Barton and Kirby, 2000] and are in good agreement.

Case 2

Case 2 presents a backward facing step in the presence of an externally applied magnetic field in the vertical direction. The result calculated with LRBFCM

Table 5.8: Reattachment positions for Ha = 0 and various Re numbers.

Re	method	$x'(y'=0)$	$x'(y'=1)$	$x'(y'=1)$
300	[Barton, 1995]	3.55	/	/
	present	3.57	/	/
400	[Barton, 1995]	4.30	4.10	5.15
	present	4.33	4.00	5.20
500	[Barton, 1995]	4.95	4.22	6.68
	present	4.92	4.15	6.78
600	[Barton, 1995]	5.36	4.36	8.12
	present	5.38	4.39	8.11
700	[Barton, 1995]	/	/	/
	present	5.76	4.62	9.32
800	[Barton, 1995]	6.08	4.81	11.03
	[Gartling, 1990]	6.10	4.85	10.48
	[Gresho et al., 1993]	6.10	4.86	10.48
	[Chiang et al., 1999]	6.16	4.82	10.63
	[Keskar and Lyn, 1999]	6.09	4.85	10.48
	[Barton and Kirby, 2000]	6.01	5.02	9.90
	present	6.10	4.87	10.48

are compared with the results calculated with Fluent. The calculations are done for Re ranging from 300 to 800 (step 100) and Ha varied from 0 to 100 (0, 5, 10, 50, and 100). The node arrangement is the same as in the Case 1 and is compared to the 301x101 mesh in Fluent. First, a comparison of streamlines for Re (300, 600 and 800) and Ha (0, 5, 10, 50, and 100) is made. The streamlines are drawn by implementing the 4-th order Runge-Kutta integration method. The representative initial points, from which the streamlines are drawn, are chosen in such a way that the motion of the fluid in the vicinity of the step and the vortices is presented as clearly as possible.

As already proven in the previous section (Sect. 5.3), the application of a magnetic field dampens the fluid flow, which can initially be seen as the decrease in the lower recirculation zone. By further increasing the magnetic field strength, the recirculation zone is further damped, until it totally diminishes (at Ha = 50 and Ha = 100). As can be seen in Fig. 5.37 top picture, at Re = 300 only the lower recirculation zone exists. By applying the magnetic field, this zone is decreased (Fig. 5.37).

For higher Re numbers (Re>400) another recirculation zone appears at the upper wall. By increasing Re both the upper and the lower recirculation zones grow. This can be seen in Fig. 5.38 and in Fig. 5.39 for Re = 600 and Re = 800. Similarly, as in the case for Re = 300, the recirculation zones, both the upper and the lower, are damped and vanish by increasing the Ha number.

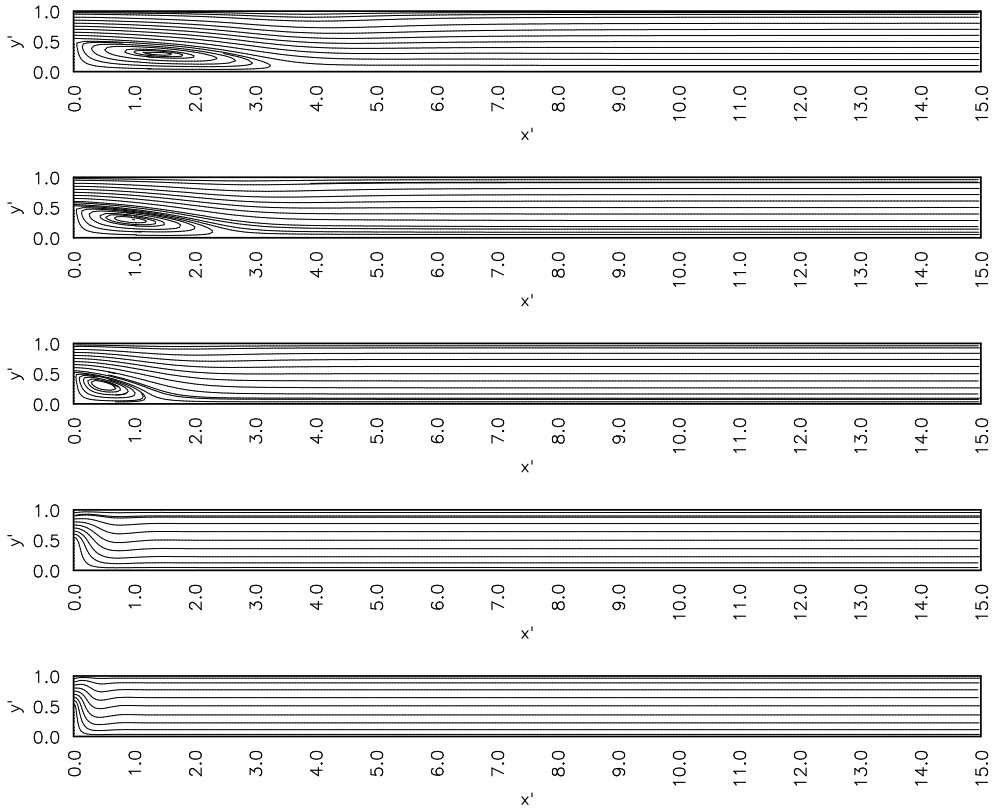

Figure 5.37: Streamlines for Re = 300 and Ha = 0, 5, 10, 50, and 100 (from the top to the bottom) for 301x101 node arrangement. The recirculation zones are dampened as a consequence of the application of the magnetic field.

A comparison of v'_x and v'_y for different vertical cross sections is made in Fig. 5.40. The values at the outlet ($x' = 15$) and at the intermediate cross section ($x' = 7$) have the same value at higher Ha. To ensure that the method is sufficiently accurate for the whole length of the backward facing channel, additional cross section is added at $x' = 2$. Fig. 5.40 shows excellent agreement between the results computed with LRBFCM and those computed with Fluent.

Dimensionless velocities v'_x and v'_y are represented in Figs. 5.41-5.43 for Re = 300, 600 and 800, and Ha = 0, 5, 10, 50 and 100. The velocity at the outlet is in all of the cases decreasing with increasing Ha. The values of the extremes for the final velocities at the outlet are given in Tabs. 5.9-5.11.

Table 5.9: Extreme values of v'_x and v'_y for 301x101 node arrangement, Re = 300, and Ha = 0, 5, 10, 50, and 100.

Ha	$v'_x(max)$	$v'_y(min)(y')$	$v'_y(max)(y')$
0	0.75167	$-1.1861\cdot10^{-5}(0.19585)$	$1.3445\cdot10^{-4}(0.63384)$
5	0.69183	/	$6.9623\cdot10^{-5}(0.54207)$
10	0.61695	$-6.2651\cdot10^{-8}(0.17025)$	$7.8349\cdot10^{-8}(0.80415)$
50	0.52127	$-4.2862\cdot10^{-7}(0.05981)$	$4.3003\cdot10^{-7}(0.94019)$
100	0.51132	$-7.6154\cdot10^{-7}(0.04207)$	$7.6478\cdot10^{-7}(0.95793)$

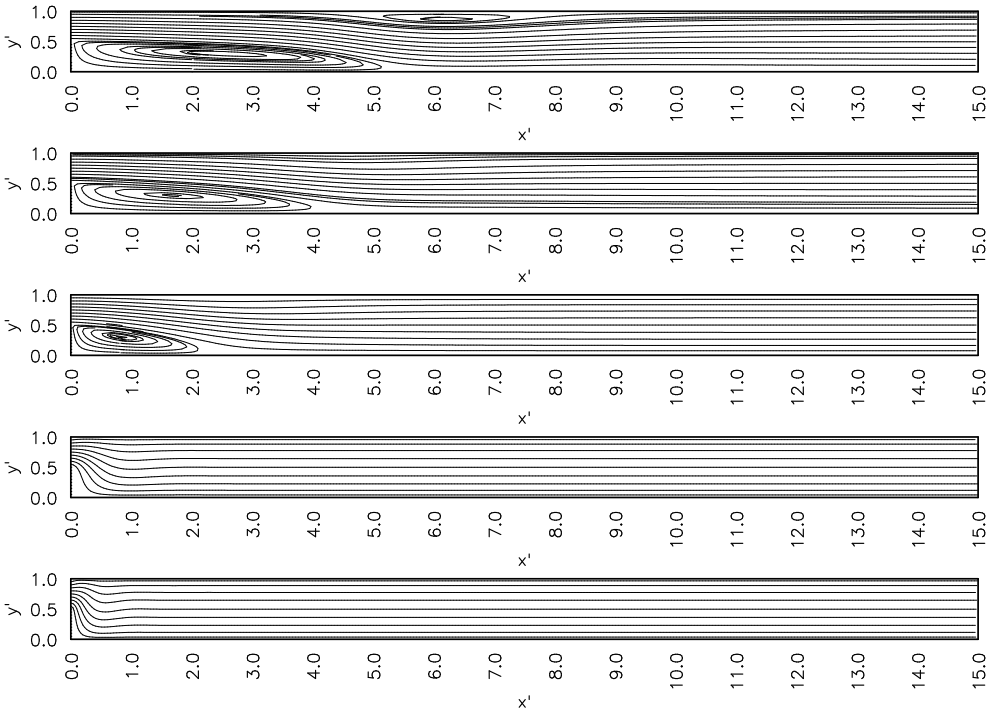

Figure 5.38: Streamlines for Re = 600 and Ha = 0, 5, 10, 50, and 100 (from the top to the bottom) for 301x101 node arrangement. The recirculation zones are dampened as a consequence of the application of the magnetic field.

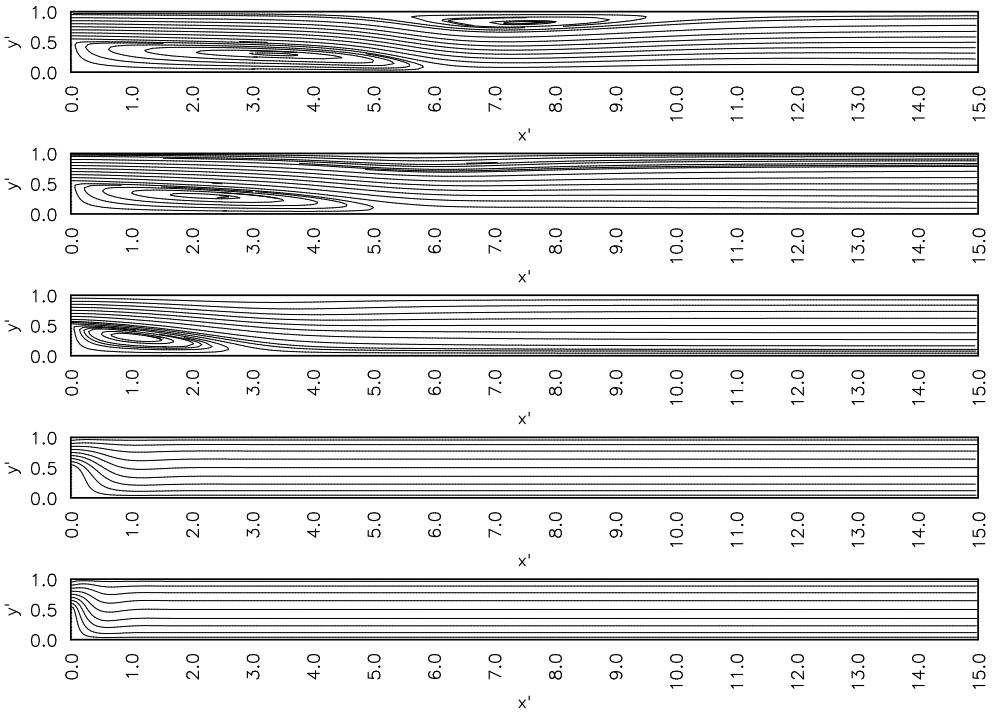

Figure 5.39: Streamlines for Re = 800 and Ha = 0, 5, 10, 50, and 100 (from the top to the bottom) for 301x101 node arrangement. The recirculation zones are dampened as a consequence of the application of the magnetic field.

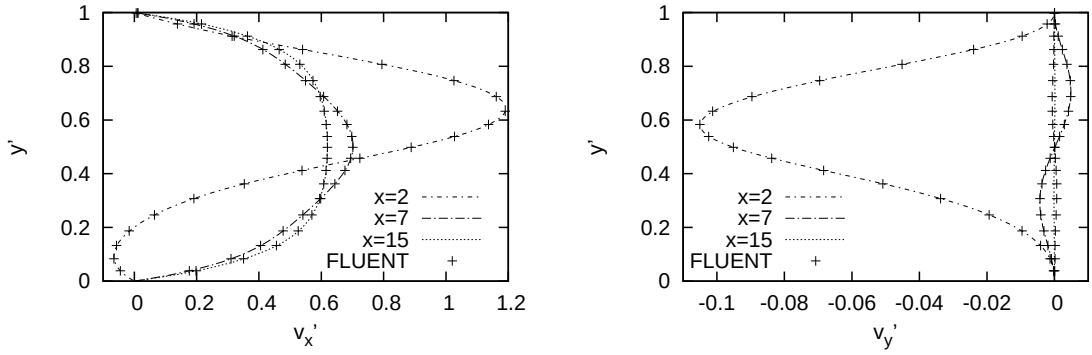

Figure 5.40: Comparison of the vertical cross sections for v'_x (left) and v'_y (right) for Re = 800 and Ha = 10. The cross sections are placed at the channel outlet ($x' = 15$), and two intermediate positions ($x' = 7$ and $x' = 2$).

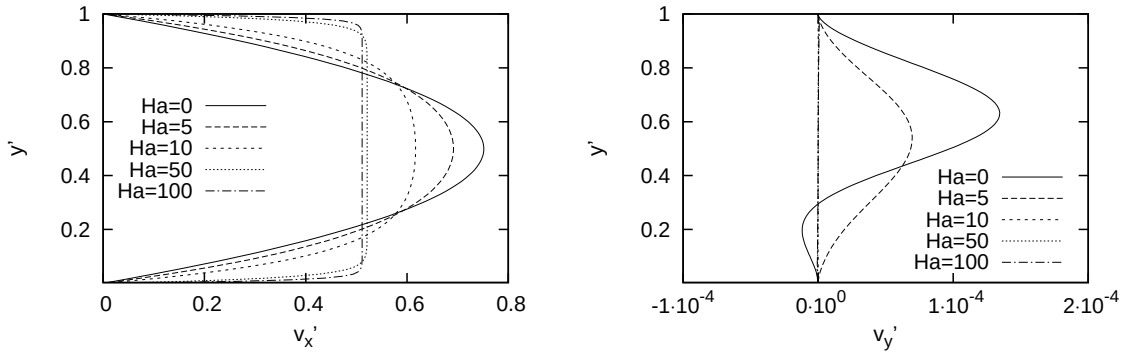

Figure 5.41: Comparison of the final velocities at the outlet for Re = 300, and Ha = 0, 5, 10, 50, and 100. The recirculation zones are dampened as a consequence of the application of the magnetic field.

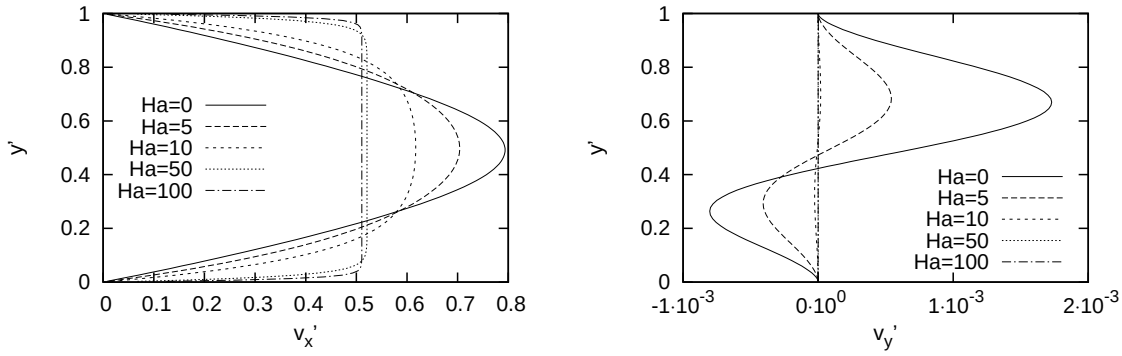

Figure 5.42: Comparison of the final velocities at the outlet for Re = 600, and Ha = 0, 5, 10, 50, and 100. The recirculation zones are dampened as a consequence of the application of the magnetic field.

Table 5.10: Extreme values of v'_x and v'_y for 301x101 node arrangement, Re = 600, and Ha = 0, 5, 10, 50, and 100.

Ha	$v'_x(max)$	$v'_y(min)(y')$	$v'_y(max)(y')$
0	0.79370	-8.0308·10^{-4}(0.26389)	1.7292·10^{-3}(0.67025)
5	0.70406	-4.0713·10^{-4}(0.29097)	5.4234·10^{-4}(0.68292)
10	0.61728	-2.6220·10^{-5}(0.32975)	1.8808·10^{-5}(0.69585)
50	0.52113	-3.5885·10^{-7}(0.050717)	3.5974·10^{-7}(0.94928)
100	0.51079	-7.1038·10^{-7}(0.042069)	7.1170·10^{-7}(0.96610)

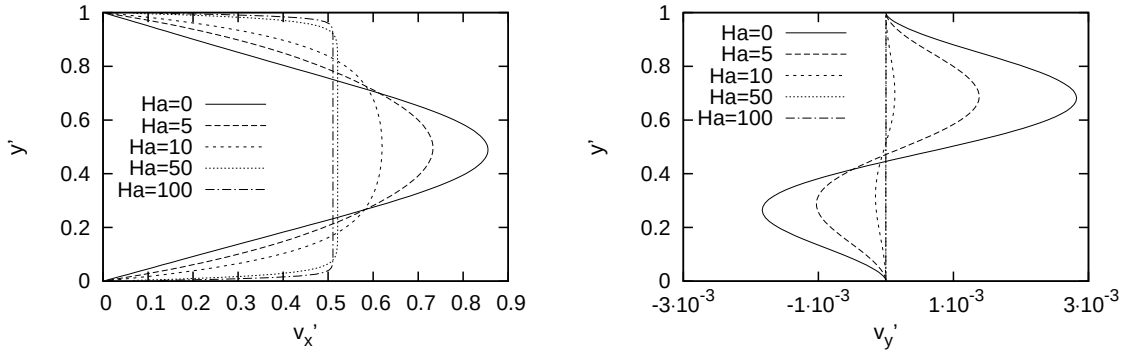

Figure 5.43: Comparison of the final velocities at the outlet for Re = 800, and Ha = 0, 5, 10, 50, and 100. The recirculation zones are dampened as a consequence of the application of the magnetic field.

Table 5.11: Extreme values of v'_x and v'_y for 301x101 node arrangement, Re = 800, and Ha = 0, 5, 10, 50, and 100.

Ha	$v'_x(max)$	$v'_y(min)(y')$	$v'_y(max)(y')$
0	0.85501	-0.0018313(0.26389)	0.0028237(0.68292)
5	0.73286	-1.0295·10^{-3}(0.29097)	1.3810·10^{-3}(0.68292)
10	0.61980	-1.5415·10^{-4}(0.31708)	1.3274·10^{-4}(0.69585)
50	0.52110	-3.2575·10^{-7}(0.050717)	3.2825·10^{-7}(0.94928)
100	0.51065	-6.7597·10^{-7}(0.033903)	6.8086·10^{-7}(0.96610)

The maximum outlet velocities in the vertical direction are presented in Fig. 5.44 for various Ha and Re numbers. The effect of Re number is for large Ha almost negligible.

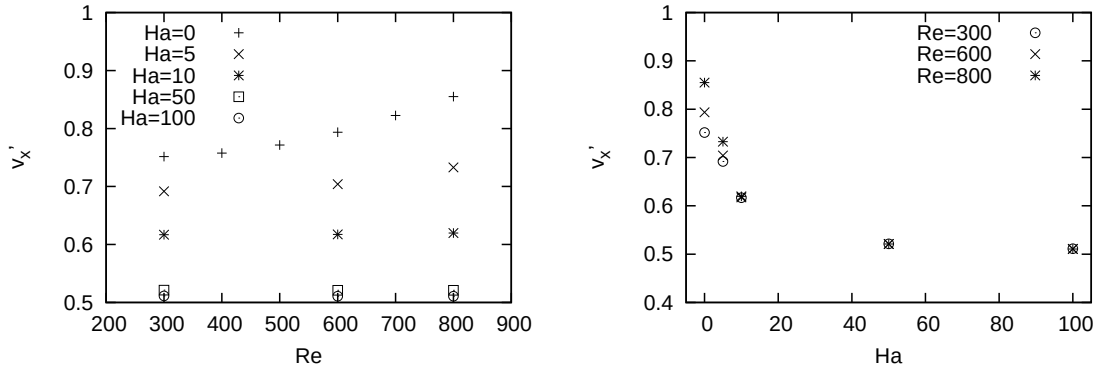

Figure 5.44: Comparison of the maximum outlet velocities at the outlet for different Re and Ha.

Finally, the wall shear stresses are examined. The accuracy of the method is first tested against the reference results calculated with Fluent for Re = 800 and Ha = 10. The results are presented in Fig. 5.45 and are in good agreement.

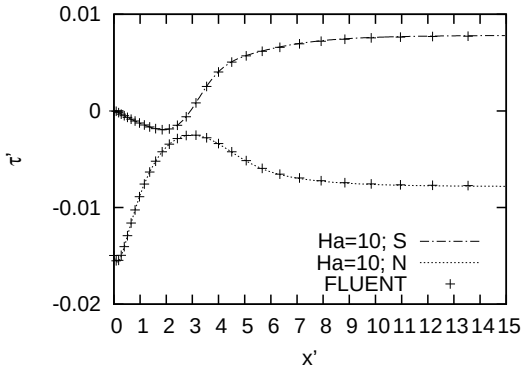

Figure 5.45: Comparison of the wall shear stresses calculated with the LRBFCM and reference results calculated with Fluent for Re = 800 and Ha = 10 for the upper (N) and the lower (S) walls.

Next, the wall shear stresses are compared for Re = 300, 600 and 800, and Ha = 0, 5, 10, 50 and 100. The results are presented in Figs. 5.46-5.48, where the disappearance of the recirculation zones for higher Ha is confirmed. The reattachment positions are given in Tab. 5.12.

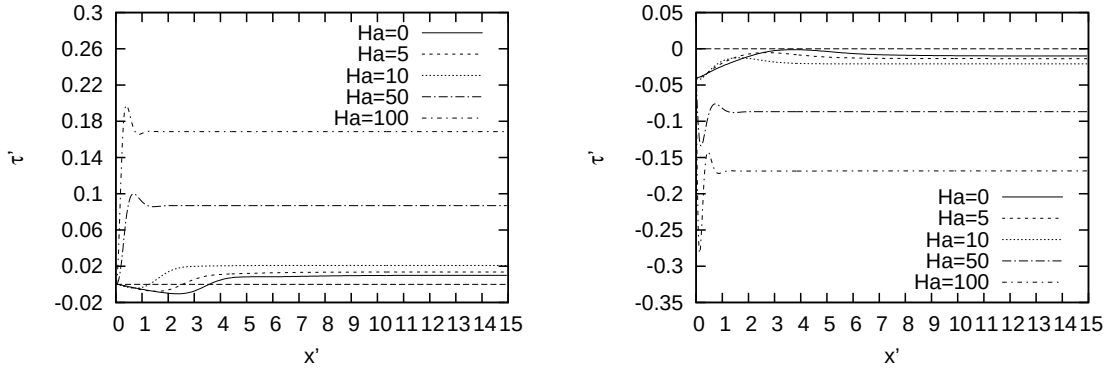

Figure 5.46: Wall shear stress for Re = 300 and Ha = 0, 5, 10, 50 and 100. Left: lower wall. Right: upper wall.

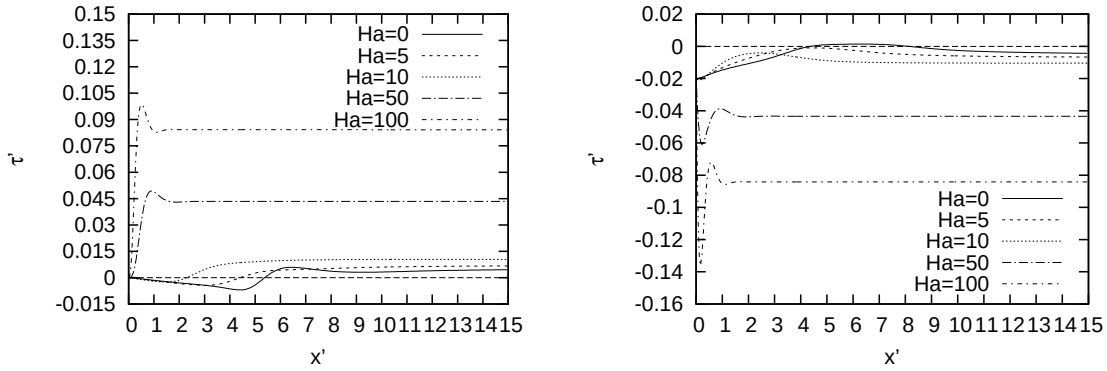

Figure 5.47: Wall shear stress for Re = 600 and Ha = 0, 5, 10, 50 and 100. Left: lower wall. Right: upper wall.

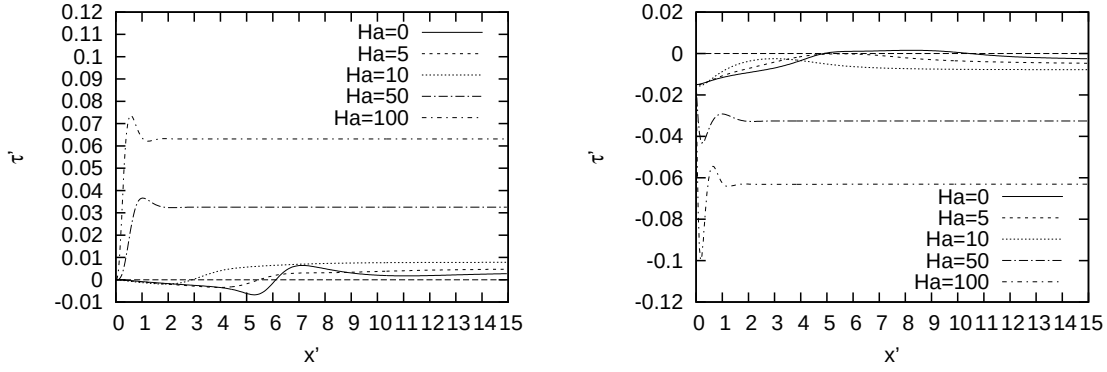

Figure 5.48: Wall shear stress for Re = 800 and Ha = 0, 5, 10, 50 and 100. Left: lower wall. Right: upper wall.

5.5.4 Summary and Conclusions

The results calculated with LRBFCM are first compared for a classical backward facing benchmark case without the presence of magnetic field. The results are

Table 5.12: Reattachment positions for various Re and Ha numbers.

Re	Ha	$x'(y'=0)$
300	0	3.57
	5	2.55
	10	1.28
	50	0.02
	100	0.01
600	0	5.38
	5	4.41
	10	2.29
	50	0.04
	100	0.01
800	0	6.10
	5	5.48
	10	2.93
	50	0.07
	100	0.01

compared to the reference FEM solutions [Gartling, 1990; Gresho et al., 1993; Chiang et al., 1999; Keskar and Lyn, 1999] and FDM [Barton and Kirby, 2000; Barton, 1995]. Afterwards, the externally applied magnetic field is added in vertical direction. The results of these calculations are compared to the results calculated with Fluent. The results differ less then 2.5%.

6 Continuous Casting of Steel

In this chapter, the model assumptions and characteristics for a simplified continuous casting model are presented. The model has been defined in [Šarler et al., 2012]. The geometry of the casting machine is introduced and adjusted to fit the simplified numerical model. Next, assumptions of a simplified numerical model are implemented for the magnetic field source. The magnetic field is calculated for different configurations, among which the most appropriate with respect to the real caster conditions is then chosen. Although the parameter values are taken from the Štore Steel [Štore Steel, d. o. o., 2013] casting machine, the magnetic field of the current model does not represent the magnetic field of the real caster. The magnetic field in the current model is designed for EMBR system and thus requires a DC current, whereas the EMS system working on the AC current is employed in the real caster. However, the current model is a first step towards the model for EMS.

The influence of the temperature field is taken into account and the magnetic field strength is adjusted accordingly. Further, the boundary and the initial conditions for velocity, temperature, concentration, magnetic field, turbulent viscosity, turbulent kinetic energy and dissipation rate are specified for the given model assumptions. The node arrangement is then presented for the simplified model and the chosen magnetic field specifications. Next, the model is verified and validated with Fluent, which is based on the FVM. Finally, the effects of the process and geometry parameters are investigated.

6.1 Model Assumptions

The model in the present dissertation represents a simplified 2D model of a CC machine. Some of the assumptions for the present model are taken from [Vertnik, 2010]. In present dissertation, the following assumptions are adopted in the formulation of the computational model.

- Although the CC process is a transient process, we seek the solution of a steady state problem.
- The molten steel is considered as an incompressible Newtonian fluid.
- The curvature of the strand is not taken into account. An assumption of a straight vertical strand is considered as a computational domain.

- A simplified 2D geometry of the casting machine is considered. Although the simplification is not a realistic approximation of a 3D curved casting machine, it serves a sufficiently good layout for checking the accuracy of the numerical model.

- The assumption of small Re_m ($\mathrm{Re}_m \ll 1$) is adopted. Such approximation is suitable for liquid metal flows and means that the induced magnetic field is negligible in comparison with the imposed magnetic field. Furthermore, the Joule heating effect is sufficiently small to be neglected.

- Thermophysical properties, such as density, dynamic viscosity, specific heat, liquid fraction, thermal conductivity and thermal expansion coefficient, are considered to be constant and independent of temperature. The values of this thermophysical quantities, except viscosity, are taken from the JMatPro database at the value of solidus temperature of steel (51CrV4). Density, dynamic viscosity, specific heat, thermal conductivity, thermal expansion coefficient, and enthalpy, are equal for both phases.

- The heat release as a result of the solid-solid transformation is not considered.

- The solidification of the slurry region of the mushy zone is not considered and the assumption is made that no equiaxed dendrites float in the molten steel. Instead, it is assumed, that the mushy zone consists only of a porous medium composed of columnar dendrites and interdendritic liquid. The velocity of the solid phase is constant and equal to the casting speed.

- Local thermodynamic equilibrium is assumed during solidification.

- The model is based on the mixture continuum model that is used to describe the macrosegregation. The model assumes the thermodynamic equilibrium of the liquid and the solid phases in the mushy zone, with the assumption that each location in this zone is simultaneously occupied by both phases and all components.

- The microsegregation is modelled either with the linear distribution of latent heat or with the Lever rule.

- The boundary and initial conditions for velocity, temperature and pressure fields are taken from the benchmark test case for CC [Šarler et al., 2012].

- The low-Re k-ε turbulence model is applied to account for the turbulence effects. The AKN model is used [Abe et al., 1994] to define the closure relations.

- Magnetic field is modelled as a consequence of two solenoids, each placed on one side of the strand. The solenoids are turned in the same direction and thus form the magnetic field in a transverse direction. This magnetic field is not a realistic representation of a 3D magnetic field in a real casting machine that is generated by four perpendicular solenoids. As the main objective of

such placement of solenoids is to achieve a homogeneous field in the middle of the strand, the above described simplification is appropriate.

- The chosen placement of the two solenoids is consistent with ruler EMBR.
- The winding of the coils is assumed to be smooth and even.

6.2 Geometry

A simplified 2D model is used to represent the CC machine. A billet with a square cross-section is considered. The geometry of the simplified model is shown in Fig. 6.1. Due to the mirror symmetry, only right half of the simplified model domain is chosen as a computational domain. The layout of the computational domain is shown in Fig. 6.2. The values of the computational domain dimensions are listed in Tab. 6.1. The variables a_b, d_2, l_m, l_{EM}, and l, stand for the diameter of SEN, billet width, mould height, electromagnet height and domain height, respectively. In general, the source of the magnetic field is placed at l_{mEM}. However, in the basic case, the end of the mould coincides with the placement of the EM field source and thus $l_m = l_{mEM}$. The values of all of the geometry parameters can be varies at the model. The coordinate system origins x and y are set at the top left corner of the model, transverse to and along the direction of the flow, respectively.

Table 6.1: Geometry parameters of the simplified CC process.

parameter	description	unit	value
billet width	d_2	[m]	0.14
diameter of SEN	a_b	[m]	0.07
mould height	l_m	[m]	0.8
EM height	l_{mEM}	[m]	0.8
domain height	l	[m]	1.8
EM width	l_{EM}	[m]	0.1

6.3 Magnetic Field

The magnetic field in the industrial mould is 3D and is produced by four square coils perpendicularly facing each other as is shown in Fig. 6.3. The objective of this dissertation is to form a 2D model of electromagnetic breaking. 2D geometry of simplified model is obtained from 3D geometry of a realistic coil arrangement by first removing the coils facing the x-y plane from each direction. The remaining two coils (6.3 right) are then used to assure the uniformity of the magnetic field. The 2D model is then obtained from the 3D model of two coils by assuming that one of the coordinates (z in this instance) is infinite. This is done by assuming that the z sides of the coils are much larger than the coils' dimensions in either x or y direction. The x-y plane cross-section of the magnetic field around the coil

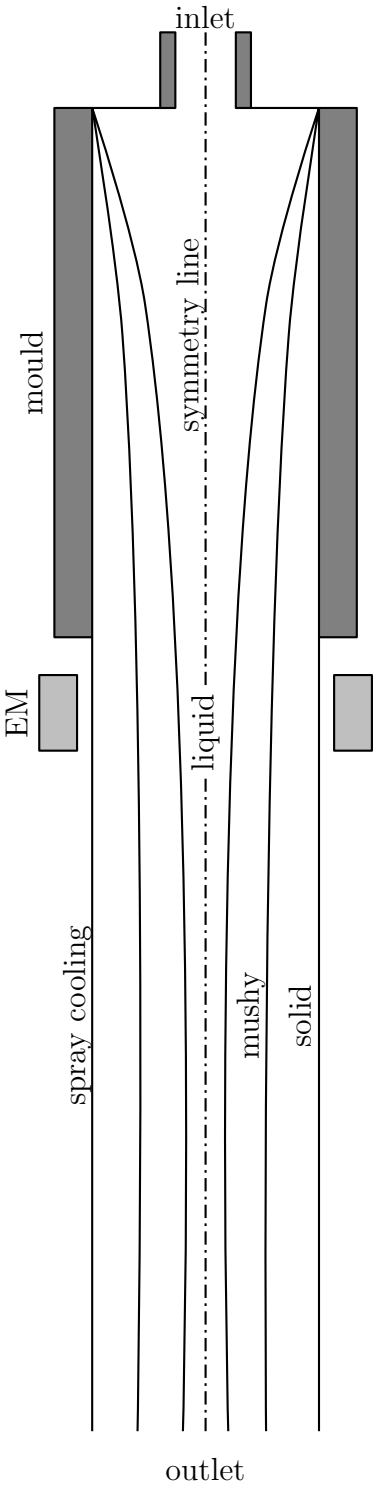

Figure 6.1: Scheme of a simplified model for CC of steel.

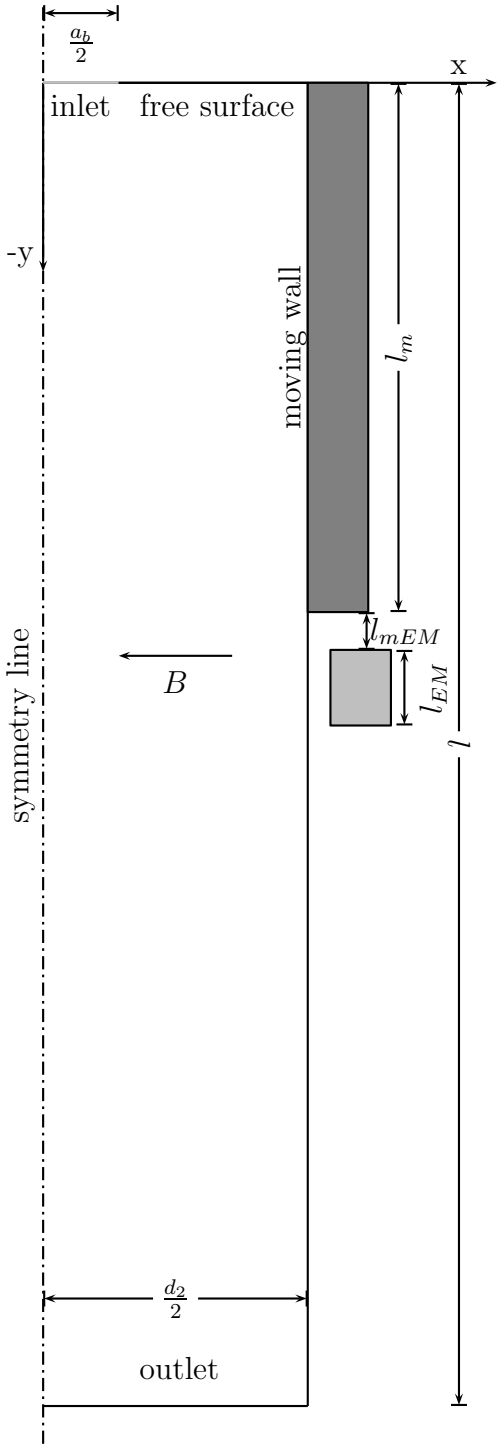

Figure 6.2: Scheme of a simplified computational domain model of CC of steel.

wires is thus approximately the same as the magnetic field around an equivalent arrangement of infinite wires (Fig. 6.4). However, in the realistic configuration, the coils encircle the iron core and consequently, the magnetic field is enhanced. As the iron core electromagnets are a common occurrence in the physics of the

EM field, further simplification into the wire arrangement is not adopted here. The magnetic field is calculated with Biot-Savart law for all the configurations and additional equations are used to account for the magnetisation effect of the iron core.

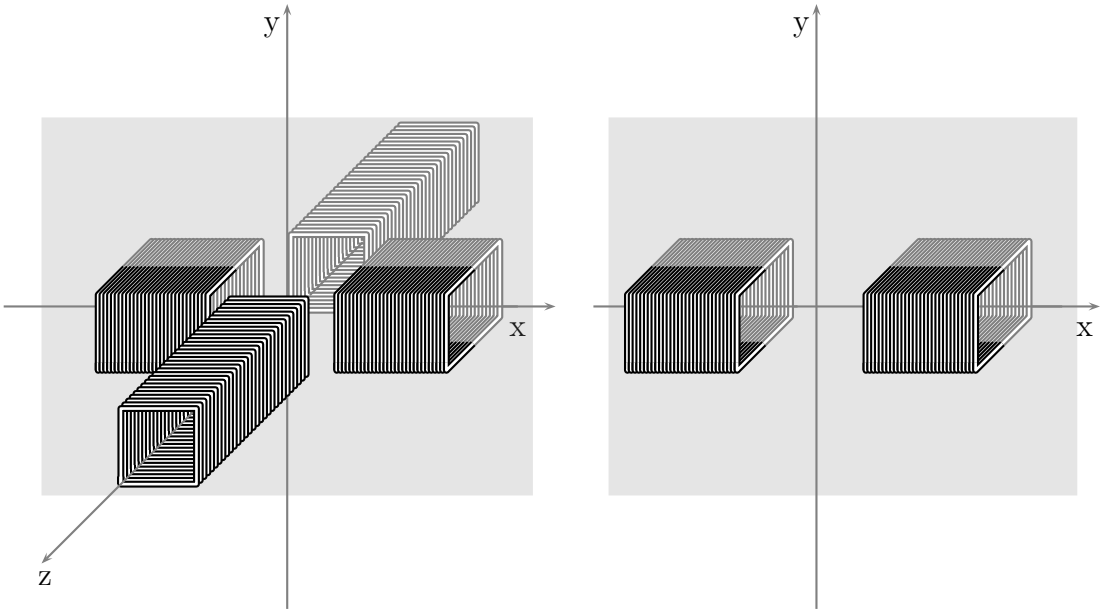

Figure 6.3: Square coils layout. Left: realistic 3D layout. Right: simplified 2D layout used in computation.

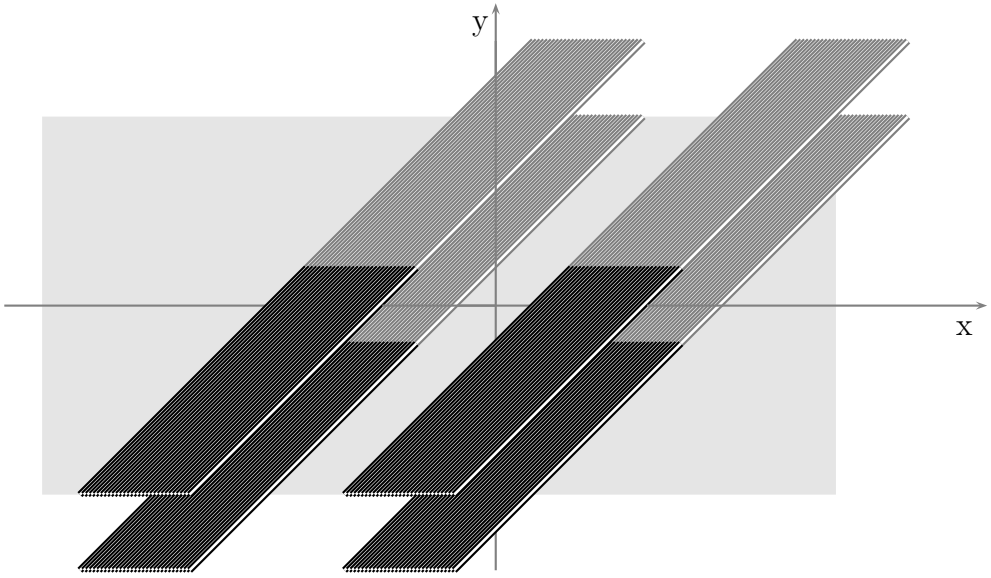

Figure 6.4: A 2D approximation of the wire arrangement for a simplified model of CC process.

6.3.1 Magnetic Field due to Rectangular Coils

In the present dissertation, it is assumed that the magnetic field inside the casting machine is produced by two rectangular solenoid coils. Each of the solenoids is made out of $N_N \times N_M$ windings or loops, where N_N and N_M stand for the number of coils in x and y directions, respectively. In order to be able to calculate the magnetic field produced by the rectangular solenoid coil, first the magnetic field of a single rectangular loop is calculated. As each of the windings is made of four finite straight wires, the magnetic field can be calculated as the sum of the magnetic fields of each of these wires. The procedure of how the magnetic field of the finite rectangular solenoid arrangement is calculated, is elaborated below.

Magnetic Field due to a Finite Straight Wire

The current (**I**) carrying finite straight wire of length b is considered. The wire is positioned along the z axis as shown in Fig. 6.5.

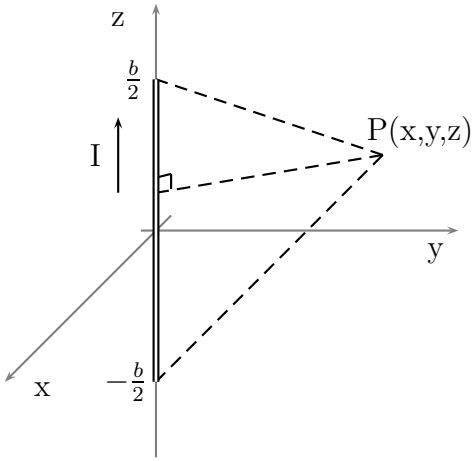

Figure 6.5: Finite, straight, current carrying wire with length b.

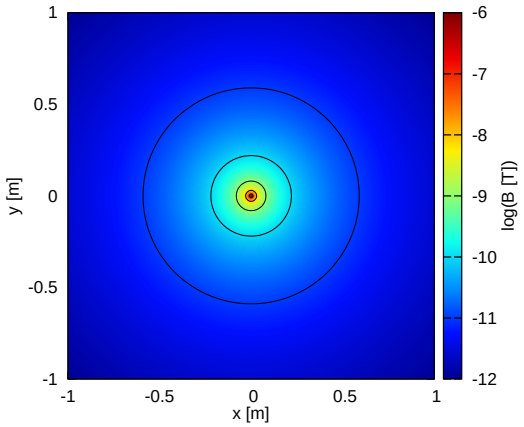

Figure 6.6: Magnetic field (ln(B)) of a finite straight wire with length b.

To begin with, the value of the magnetic field at a field point P is examined. According to the Biot-Savart law

$$d\mathbf{B} = \frac{\mu_0 \mathrm{I}}{4\pi} \frac{d\mathbf{s} \times \hat{\mathbf{r}}}{r^2} = \frac{\mu_0 \mathrm{I}}{4\pi} \frac{d\mathbf{s} \times \mathbf{r}}{r^3}; \quad \hat{\mathbf{r}} = \frac{\mathbf{r}}{r}, \tag{6.1}$$

each of the infinitesimally small segments of wire $d\mathbf{s}$ contributes a small part to the magnetic field. By adding up all of the contributions $d\mathbf{B}$, the strength of the magnetic field due to the current in the wire can be calculated

$$\mathbf{B} = \int d\mathbf{B} = \frac{\mu_0 I}{4\pi} \int_{-\frac{b}{2}}^{\frac{b}{2}} \frac{(x\mathbf{i}_y - y\mathbf{i}_x)d\tilde{z}}{\left(\sqrt{x^2 + y^2 + (z - \tilde{z})^2}\right)^3}. \tag{6.2}$$

The solution of the integral in Eq. 6.2 yields

$$B_x = \frac{\mu_0 I}{4\pi} \Big(\frac{y\big(z - \frac{b}{2}\big)}{(x^2 + y^2)\sqrt{x^2 + y^2 + \big(z - \frac{b}{2}\big)^2}} - \frac{y\big(z + \frac{b}{2}\big)}{(x^2 + y^2)\sqrt{x^2 + y^2 + \big(z + \frac{b}{2}\big)^2}} \Big), \tag{6.3}$$

$$B_y = \frac{\mu_0 I}{4\pi}\Big(\frac{x\big(z+\frac{b}{2}\big)}{(x^2+y^2)\sqrt{x^2+y^2+\big(z+\frac{b}{2}\big)^2}} - \frac{x\big(z-\frac{b}{2}\big)}{(x^2+y^2)\sqrt{x^2+y^2+\big(z-\frac{b}{2}\big)^2}}\Big) \tag{6.4}$$

and

$$B_z = 0. \tag{6.5}$$

The strength of magnetic field $B = \sqrt{B_x^2 + B_y^2 + B_z^2}$ is depicted in Fig. 6.6.

Magnetic Field of a Rectangular Loop

As already mentioned, the magnetic field of a rectangular loop with sides a and b [1], shown in Fig. 6.8, is obtained by adding up the field contributions of each of its sides. The present derivation of the magnetic field in a square loop is based on the previously published works of [Li, 2004; Herceg et al., 2009; Misakian, 2000]. The magnetic field of a single side is equal to the magnetic field of a finite straight wire (Fig. 6.6). In order to get the magnetic fields of each of the sides, the coordinate system is shifted in the y direction first for $-\frac{a}{2}$ (B_{0x}, B_{0y}, B_{0z})

$$\begin{aligned} x &\rightarrow x \\ y &\rightarrow y - \frac{a}{2} \\ z &\rightarrow z. \end{aligned} \tag{6.6}$$

The original coordinate system is than rotated for 180° around the y axis and shifted for $+\frac{a}{2}$ (B_{180x}, B_{180y}, B_{180z})

$$\begin{aligned} x &\rightarrow -x \\ y &\rightarrow y + \frac{a}{2} \\ z &\rightarrow -z. \end{aligned} \tag{6.7}$$

The original coordinate system is than rotated for 90° around the x axis, so that the wire is parallel to the y axis, and shifted for $\frac{b}{2}$ along z axis (B_{90x}, B_{90y}, B_{90z})

$$\begin{aligned} x &\rightarrow x \\ y &\rightarrow z \\ z &\rightarrow y + \frac{b}{2}. \end{aligned} \tag{6.8}$$

Finally, the original coordinate system is rotated for 270° around the x and then shifted for $-\frac{b}{2}$ (B_{270x}, B_{270y}, B_{270z})

$$\begin{aligned} x &\rightarrow x \\ y &\rightarrow -z \\ z &\rightarrow y - \frac{b}{2}. \end{aligned} \tag{6.9}$$

[1] The actual loop considered is square, i.e. $a = b$. However, to be more general and to be able to separate the shifts of coordinate systems in the y and z direction, a rectangle is considered and its dimensions are in y direction denoted as a and in z direction as b.

The schematics of coordinate rotations are depicted in Fig. 6.7. The corresponding rotations and shifts (Eqs. 6.7, 6.8, 6.9, and 6.10) are inserted into Eq. 6.2 to obtain the magnetic field of each individual wire segment.

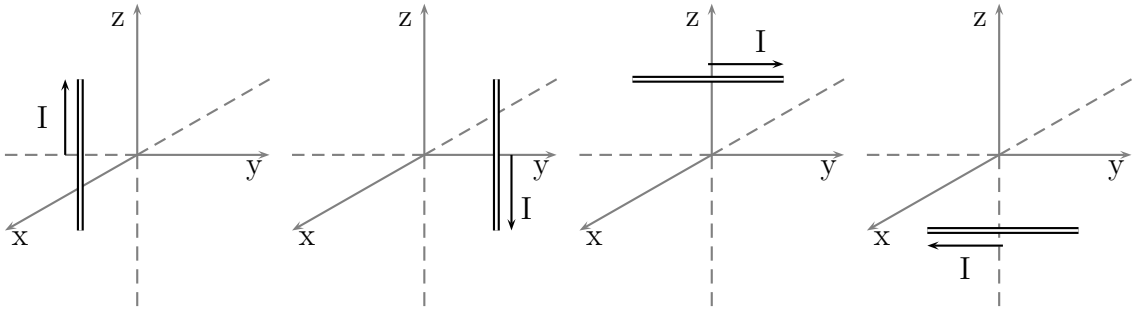

Figure 6.7: Finite, straight, current carrying wire with length b. Rotations from the left to the right: 0°, 180°, 90° and 270°.

The magnetic field components of a rectangular coil are calculated by adding the magnetic field components of finite wire segments

$$\begin{aligned} B_x &= B_{0x} + B_{90x} + B_{180x} + B_{270x}, \\ B_y &= B_{0y} + B_{90y} + B_{180y} + B_{270y}, \\ B_z &= B_{0z} + B_{90z} + B_{180z} + B_{270z}. \end{aligned} \tag{6.10}$$

The equations for each of the components B_{0x}, B_{90x}, ..., B_{180z}, B_{270z} are presented in Appx. C. The components of the magnetic flux density of a rectangular coil are therefore

$$B_x = \frac{\mu_0 I}{4\pi} \sum_{i=1}^{4} \Big(\frac{(-1)^i z_i}{r_i (r_i + (-1)^{i+1} y_i)} - \frac{y_i}{r_i (r_i + z_i)} \Big), \tag{6.11}$$

$$B_y = \frac{\mu_0 I}{4\pi} \sum_{i=1}^{4} \Big(\frac{(-1)^{i+1} x}{r_i (r_i + z_i)} \Big), \tag{6.12}$$

and

$$B_z = \frac{\mu_0 I}{4\pi} \sum_{i=1}^{4} \Big(\frac{(-1)^{i+1} x}{r_i (r_i + (-1)^{i+1} y_i)} \Big), \tag{6.13}$$

where

$$\begin{aligned} z_1 &= z + \frac{b}{2}, \quad y_1 = y + \frac{a}{2}, \quad r_1 = \sqrt{x^2 + y_1^2 + z_1^2} \\ z_2 &= z + \frac{b}{2}, \quad y_2 = y - \frac{a}{2}, \quad r_2 = \sqrt{x^2 + y_2^2 + z_2^2} \\ z_3 &= z - \frac{b}{2}, \quad y_3 = y + \frac{a}{2}, \quad r_3 = \sqrt{x^2 + y_3^2 + z_3^2} \\ z_4 &= z - \frac{b}{2}, \quad y_4 = y - \frac{a}{2}, \quad r_4 = \sqrt{x^2 + y_4^2 + z_4^2} \end{aligned} \tag{6.14}$$

The resulting magnetic field is shown in Fig. 6.9.

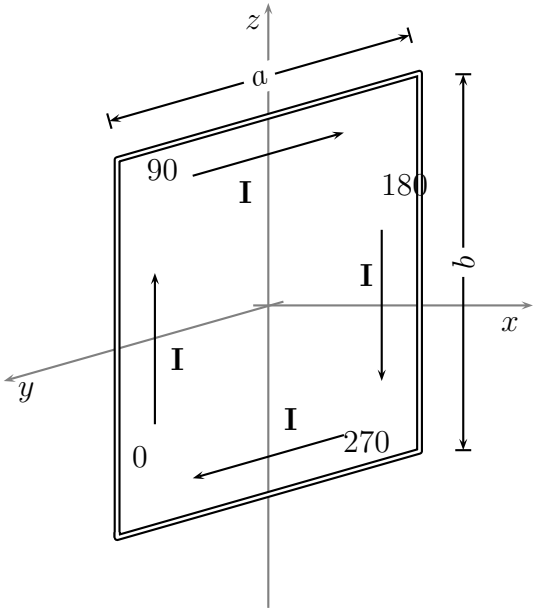

Figure 6.8: Square loop with sides $a = b$.

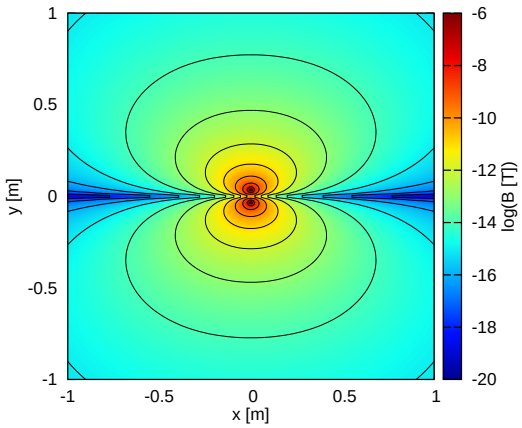

Figure 6.9: Magnetic field of a square loop.

Parallel Square Loops

If the loops in a square solenoid are tightly-wound, it can be assumed that the square solenoid is made out of several parallel square loops (Fig. 6.10). The loops are placed tightly next to each other in the x direction, with the assumption that the distance between two neighbouring loops is equal to the diameter of the wire. Substituting

$$x \to x + n \cdot \phi_w, \tag{6.15}$$

where $n = 1, \ldots, N_N$ and ϕ_w is the diameter of the wire in equations 6.11, 6.12, 6.13, and 6.15, provides the magnetic field $\mathbf{B}_n$ of an individual loop at position $n \cdot \phi_w$. Again, the total magnetic field of a square solenoid is the sum of all the singular field contributions and can be written as

$$\mathbf{B} = \mathbf{B}_1 + \cdots + \mathbf{B}_{N_N} = \sum_{n}^{N_N} \mathbf{B}_n. \tag{6.16}$$

The magnetic field of square solenoid with N_N loops is shown in Fig. 6.11.

A similar procedure is repeated for wires winded around each other in y and z directions by enforcing the following substitutions

$$y \to y + m \cdot \phi_w, \tag{6.17}$$

and

$$z \to (z + m \cdot \phi_w), \tag{6.18}$$

where $m = 1, \ldots, N_M$. A schematic representation of the loop arrangement is shown in Fig. 6.12. The total magnetic field is the sum of all the partial field

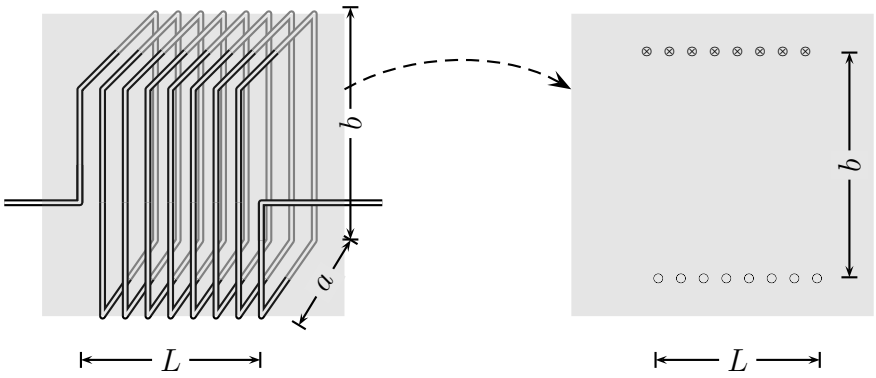

Figure 6.10: Schematic picture of parallel square loops. Left: scheme. Right: side view.

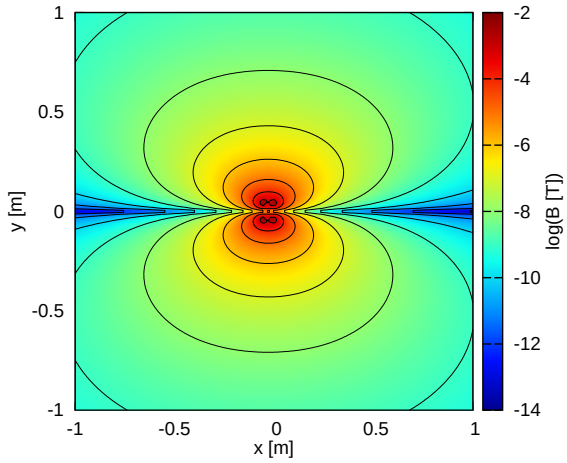

Figure 6.11: Magnetic field of N_N square parallel loops.

contributions

$$\mathbf{B} = \mathbf{B}_1 + \cdots + \mathbf{B}_{N_M} = \sum_{m}^{N_M} \mathbf{B}_m. \tag{6.19}$$

Two Square Solenoids

Next, two such arrangements are placed along the x direction at a distance $\frac{d}{2}$ from the axis as shown in Fig. 6.13. It should be noted here, that the direction of the electric current is very important as it affects the orientation of the magnetic field. In the realistic 3D coil arrangement, the coils are placed perpendicular to each other and the magnetic field of each coil points towards the center of the strand. The configuration of the realistic coil arrangement and the corresponding magnetic field strength are depicted in Fig. 6.14.

In the case of two coils, each placed on the same axis at one side of the strand, the magnetic field strength vectors can either point in the same direction or in the

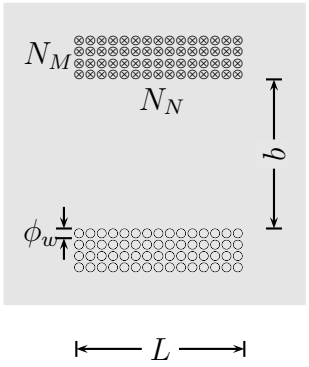

Figure 6.12: Parallel square loops arrangement.

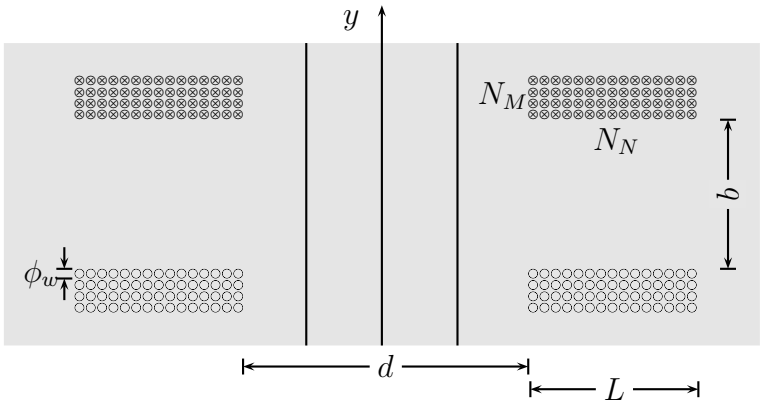

Figure 6.13: Square solenoid 2D model arrangement.

opposite directions. The described coil configuration is schematically presented in Fig. 6.15. The magnetic fields for both coil configurations are presented in Fig. 6.16. As the objective of the chosen coil configuration is to obtain the homogeneous field in the center of the strand, the parallel configuration is chosen for the purposes of this dissertation. The coil parameters inclusive the orientation of the coil can be varied.

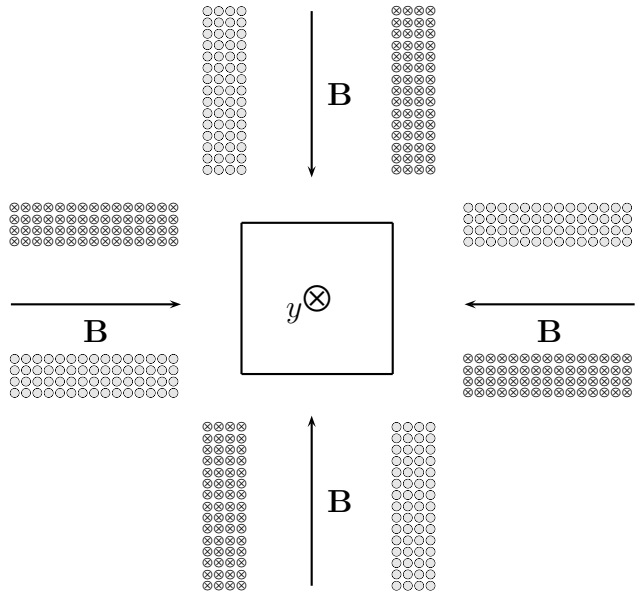

Figure 6.14: Orientation of magnetic field in a realistic coil arrangement with four coils.

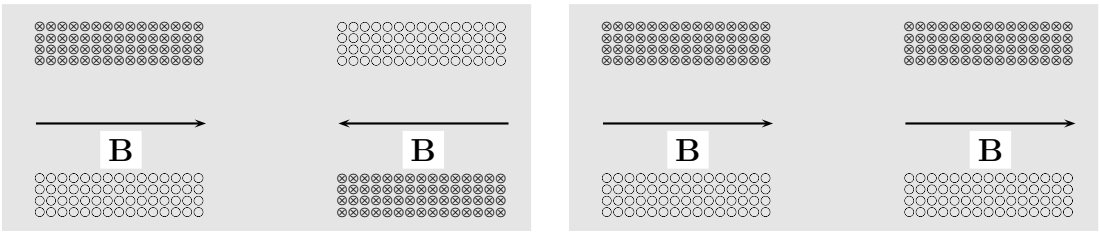

Figure 6.15: Orientation of magnetic field in two coil arrangement. Left: opposite coil configuration. Right: parallel coil configuration.

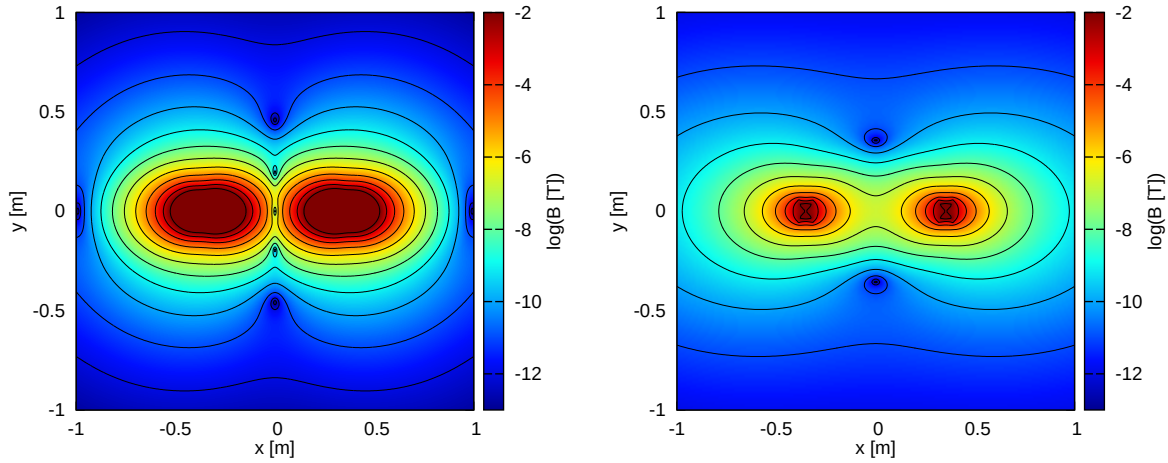

Figure 6.16: Magnetic field of $N_N \times N_M$ square loops placed at a distance d. Left: opposite coil configuration. Right: parallel coil configuration.

As already mentioned, the parallel coil configuration shown in Fig. 6.13 is chosen in this dissertation. Similarly to the previous transformations, the x co-

ordinate is substituted by

$$x \to x + \frac{d}{2}, \tag{6.20}$$

to obtain the magnetic field of the left coil and by

$$x \to x - \frac{d}{2}, \tag{6.21}$$

to obtain the magnetic field of the right coil. The transformations (Eq. 6.20 and Eq. 6.21) are inserted into Eq. 6.19. Both of the magnetic field components are then added

$$\mathbf{B} = \mathbf{B}_{-\frac{d}{2}} + \mathbf{B}_{\frac{d}{2}} \tag{6.22}$$

to obtain the total magnetic field. The result is shown on the right in Fig. 6.16.

Magnetic Field in 2D

As the computational model is 2D the 3D magnetic field of two coils has to be reduced to 2D. This is achieved by

$$z \to \infty. \tag{6.23}$$

The magnetic field of the 2D approximation is shown in Fig. 6.17.

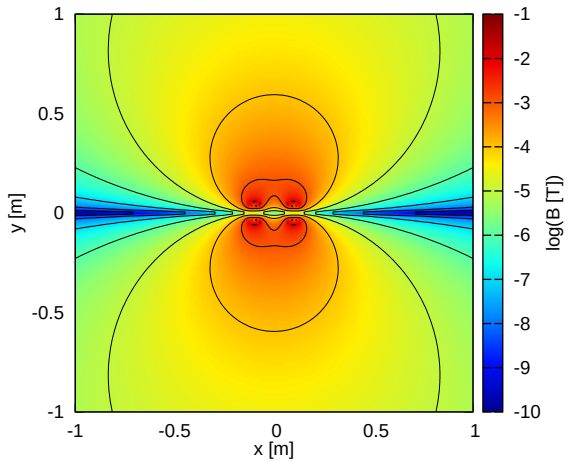

Figure 6.17: Magnetic field of $N_M \times N_N$ infinite square coils.

The above stated descriptions and equations are valid for paramagnetic material and do not take into account neither the iron core of realistic solenoids nor the molten steel flow in the strand. First the influence of external magnetic field on the magnetization of the molten steel flow is investigated and further, the magnetization due to the iron core inserted into the coils is considered and calculated in subsequent chapters.

6.3.2 Influence of Temperature on Magnetic Behaviour of Molten Steel

Steel is an iron alloy and is thus ferromagnetic, which means that it exhibits strong magnetic effects [Vollhardt et al., 2001; Moffatt, 1978]. The atomic spin in ferromagnetic materials have permanent magnetic moments and due to the ferromagnetic coupling between them, tend to align with adjacent neighbours. This regions of mutual spin alignment are called domains. The magnetic fields of the domains are in an absence of an external magnetic field aligned randomly. However, when exposed to an externally applied magnetic field, even a small one, the domains realign in the direction of the applied magnetic field, which is consequently strongly amplified. The material tends to stay magnetized even when the external magnetic field is removed. The magnetic field inside the material is

$$\mathbf{B} = \mathbf{B}_0 + \mu_0\mathbf{M} = \mu_0(\mathbf{H} + \mathbf{M}) = \mu_0\mu_r\mathbf{H}. \tag{6.24}$$

Magnetization is proportional to the magnetic field strength

$$\mathbf{M} = \chi\mathbf{H} = (\mu_r - 1)\mathbf{H} = \left(\frac{\mu_{steel}}{\mu_0} - 1\right)\mathbf{H}, \tag{6.25}$$

where χ indicates the degree to which the applied magnetic field has magnetized the material. μ_{steel} is the magnetic permeability of steel.

Temperature influences the magnetic behaviour of the ferromagnetic materials. By increasing the temperature, the thermal motion of the atoms becomes large enough to neutralize the coupling forces between the magnetic dipole moments. This results in random orientation of the magnetic moments, and the material therefore becomes paramagnetic. This phenomena happens, when the temperature exceeds Curie temperature (T_{Currie}), the temperature at which the magnetization $\mathbf{M}$ drops to zero.

Fig. 6.18 shows the temperature dependence of permeability of steel for four different cooling rates (0.1 K/s, 1 K/s, 10 K/s and 100 K/s). T_{Currie} slightly depends on the cooling rate. However, in all of the cases, permeability of steel drops to μ_0 as the temperature exceeds T_{Currie}. As the temperature in our model never falls below T_{Currie}, magnetic permeability is constant throughout the calculation. The value of μ_{steel} is calculated with the JMatPro and is μ_0 for $T \gg T_{Currie}$. According to Eq. 6.25 the magnetization above T_{Currie} is $\mathbf{M} = 0$, which means that the magnetisation can be neglected and $\mathbf{B} = \mathbf{B}_0$.

6.3.3 Magnetization due to the Iron Core in Solenoids

In the real solenoid arrangement, the core, made of soft iron, is inserted inside each of the solenoids. The susceptibility of the material inside the solenoid is therefore no longer μ_0 but μ_{iron} and consequently the magnetic field is

$$\mathbf{B} = \mu_{iron}\mathbf{H} \tag{6.26}$$

instead of

$$\mathbf{B}_0 = \mu_0\mathbf{H}. \tag{6.27}$$

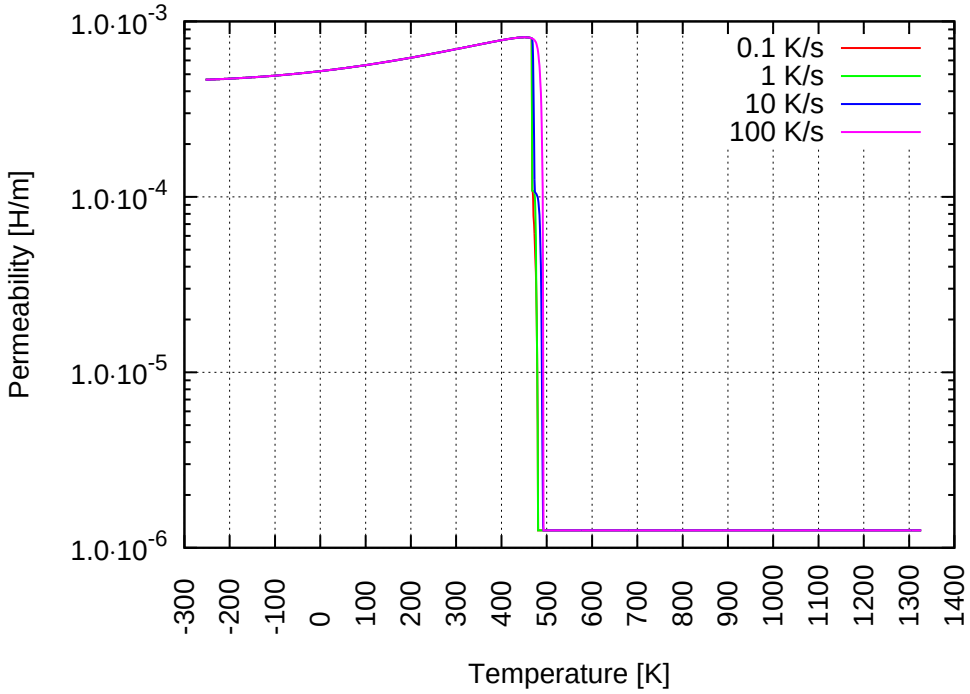

Figure 6.18: Temperature dependence of permeability of 51CrV4 steel for four different cooling rates taken from JMatPro database.

The material outside of the solenoid still has the permeability μ_0 but is influenced by the magnetized material inside the solenoid. The magnetic field outside of the solenoids is hence corrected to account for the additional magnetization of the iron core and is

$$\mathbf{B} = \mathbf{B}_0 + \mathbf{B}_{corr}, \tag{6.28}$$

where $\mathbf{B}_{corr}$ is the magnetic flux correction. In order to be able to calculate the latter, the material inside the solenoid is considered first. The soft iron core is ferromagnetic, which means that by inserting the material into the solenoid, the magnetic field inside the solenoid is strongly enhanced. This is due to the realignment of the magnetic dipole moments in the direction of the externally applied magnetic field. The magnetization is proportional to the net magnetic dipole moments $\mathbf{m}$ per volume V

$$\mathbf{M} = \frac{d\mathbf{m}}{dV}. \tag{6.29}$$

The total magnetic dipole momentum inside the solenoid can be obtained by integrating over the volume of the solenoid. The correction factor is obtained by calculating the magnetic field of the magnetic dipoles

$$\mathbf{B}_{corr} = \int_V d\mathbf{B}_{corr} = \int_V \frac{\mu_0}{4\pi} \left(\frac{3\mathbf{r}(\mathbf{M}\cdot\mathbf{r})}{r^5} - \frac{\mathbf{M}}{r^3} \right) dV, \tag{6.30}$$

where $\mathbf{M}$ is obtained from Eq. 6.25. The influence of the iron core is depicted in Fig. 6.19.

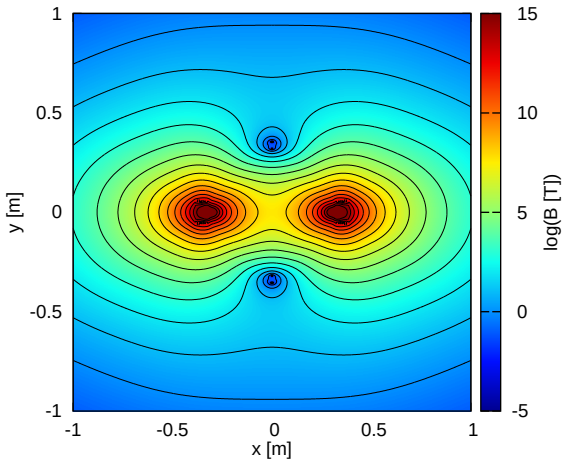

Figure 6.19: Magnetic field of two parallel iron core solenoids, each with $N_N \times N_M$ infinite square coils.

6.4 Magnetic Field in the Continuous Casting Problem

In terms of the magnetic field two different cases are considered in this dissertation. In the first case the constant magnetic field with a predefined value $\mathbf{B}_0$ is considered. The value is set either to 3.5 mT or 2.6 mT. The first value is obtained from literature, whereas the second value has been measured in Štore Steel.

The calculations for the former test case are performed at different vertical positions and influence ranges of the magnetic field sources. A detailed description of the pertained positions and ranges is given in Sect. 6.7.1. In the second case, the magnetic field is calculated according to the above described procedure. The values stated below are consistent with the realistic dimensions of the coil arrangement. The parameters are stated in Tab. 6.2.

Table 6.2: Parameters for magnetic field.

Parameter	Description	Unit	Value
current	$\|\mathbf{I}\|$	[A]	50
number of windings in x direction	N_N		25
number of windings y direction	N_M		11
span	a_d	[m]	0.1
coil dimension in y direction	a	[m]	0.035
coil dimension in z direction	b	[m]	0.045
wire diameter	ϕ_w	[m]	0.00275

The parameters in Tab. 6.2 are valid for the 3D problem and concur with the measured value of the magnetic field in the real caster. However, in this instance, the problem is 2D and as the objective of the problem is to have a realistic value for the magnetic field (260 G), one of the parameters has to be adjusted, in order

to obtain the desired value for the magnetic field. The parameters, needed for calculation, are therefore set in such a way, that the value of the magnetic field density in the middle of the strand is 260 G. In the basic case, the adjusted parameters are the span between the strand and the electromagnets a_d, and the dimension of the coil in z direction (b), which is set to ∞ in order to reduce the problem to 2D. The rest of the parameters in the basic case are kept at the values stated in Tab. 6.2. In the following chapters (Sect. 6.7.2), the parameter analysis is made in order to check the influence of each of the parameters on the magnetic field strength. All of the parameters can be adjusted to the desired values.

6.5 Node Arrangement

The computational domain is divided into four parts: the SEN part (bellow the SEN), the mould part (the mould region not including the SEN part) the inner spray region (the spray region below the SEN part) and the outer spray region (the spray region below the mould part) as shown in Fig. 6.20. The parts differ by levels of node refinement. Figs. 6.21, 6.22, and 6.23 depict the details of the node arrangement for a simplified computational domain scheme with 20200 nodes.

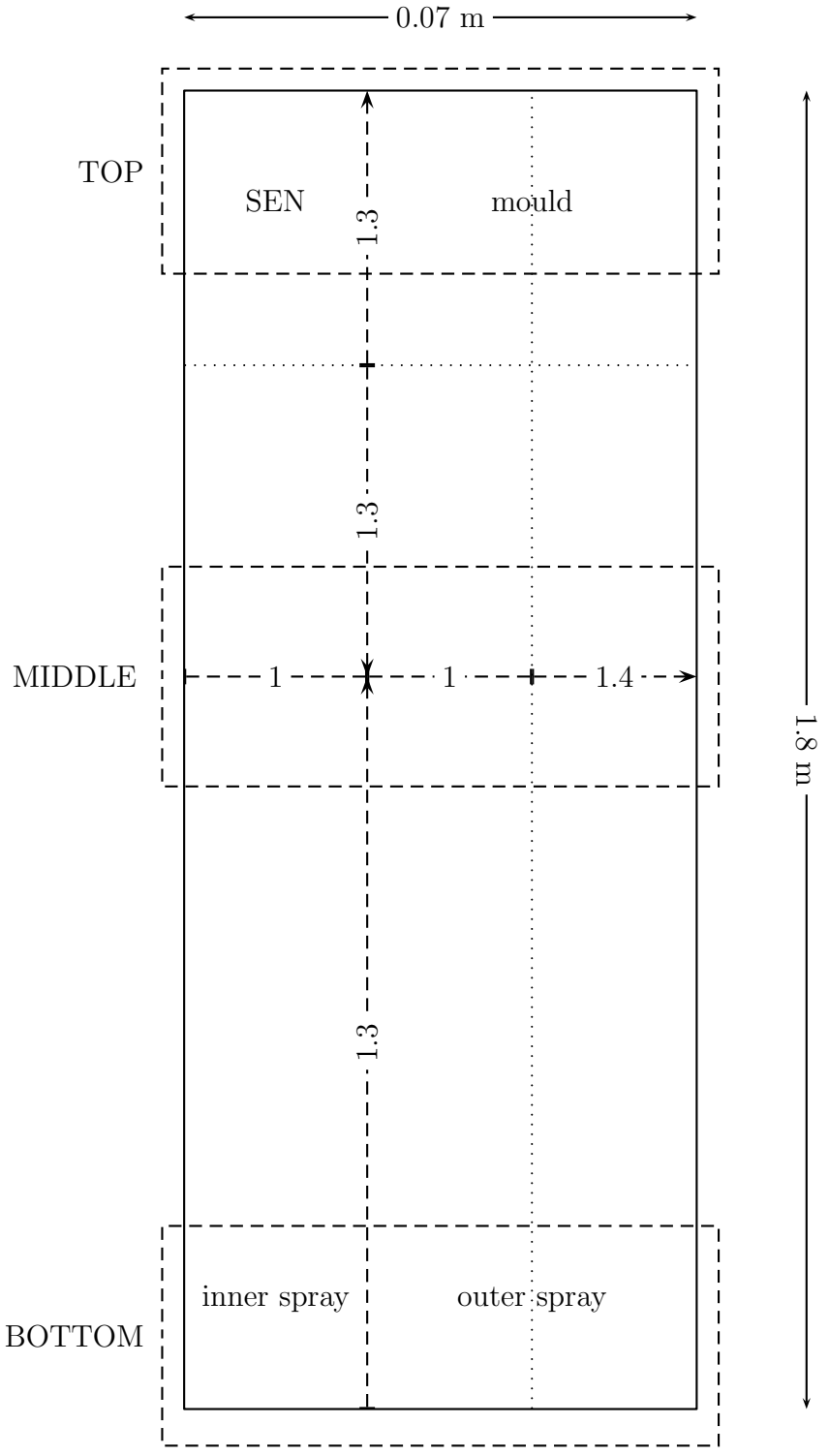

Figure 6.20: Levels of the refinement in the computational domain.

6.6 Initial and Boundary Conditions

The initial and boundary conditions for the simplified CC model are described in the following subsections. The Dirichlet, Neuman and Robin BC are used to

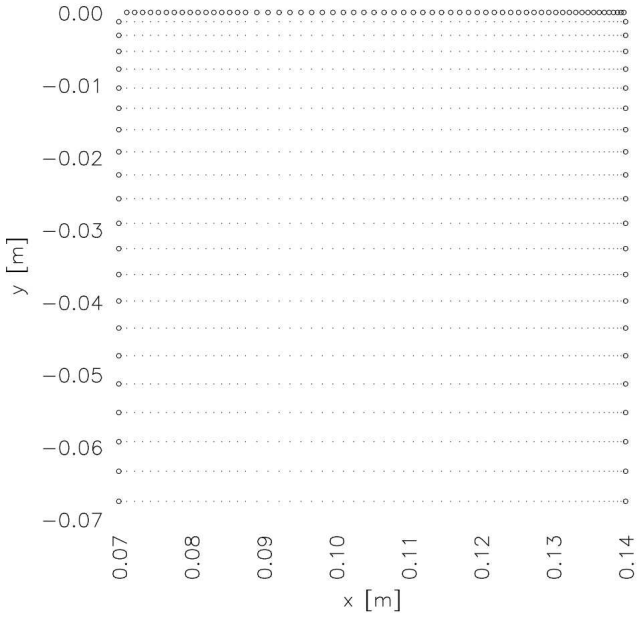

Figure 6.21: Node arrangement at the top of the computational domain. See TOP section in Fig. 6.20.

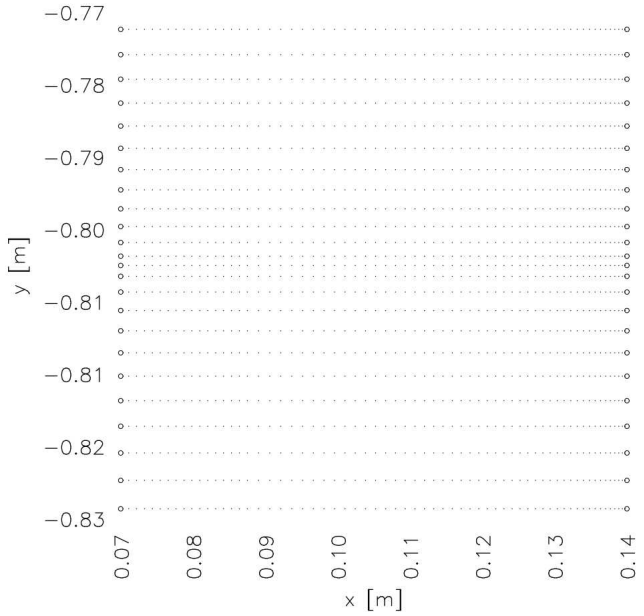

Figure 6.22: Node arrangement detail at the end of the mould. See MIDDLE section in Fig. 6.20.

define the model.

6.6.1 Initial Conditions

The values of velocity, temperature, pressure, magnetic field and species concentration at $t = t_0$ are prescribed by initial conditions described below.

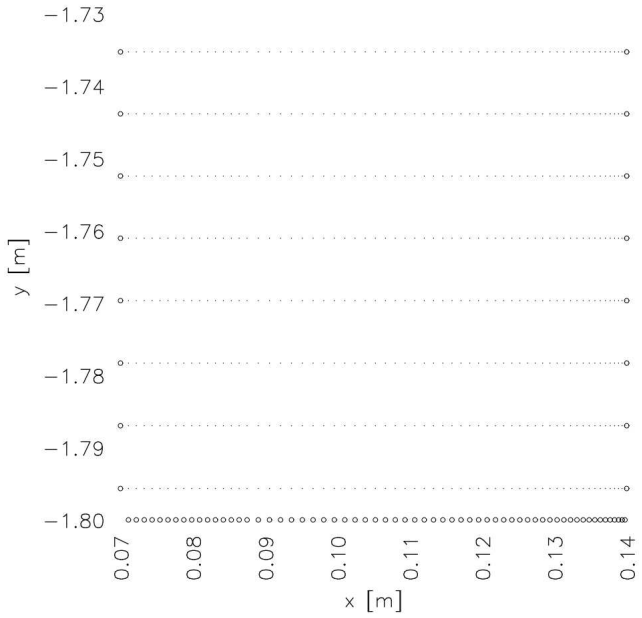

Figure 6.23: Node arrangement at the bottom of the computational domain. See BOTTOM section in Fig. 6.20.

Velocity

The initial value for velocity is calculated by solving the potential field equation as shown in Sect. 2.5.3, Eq. 2.110.

Temperature

The initial value for temperature is set to a constant value and is equal to the casting temperature ($T_0 = T_{cast}$).

Pressure

The initial value for pressure is constant and set to zero, i.e. $p_0 = 0$.

k and ε

The initial values for the turbulent kinetic energy k and the dissipation rate ε are set to constant values $k_0 = 10^{-3}$ m^2/s^2 and $\varepsilon_0 = 10^{-3}$ m^2/s^3.

Magnetic Field

The initial value for the magnetic field is either set to a predefined value $\mathbf{B}_0 = \mathbf{B}$ or calculated as shown in Sect. 6.3.

Species Concentration

The initial value of solute concentration is set to a predefined constant value ($C = C_0$).

6.6.2 Boundary Conditions

BC have to be set on five different surfaces: inlet, free surface, moving wall, outlet and symmetry line as shown in Fig. 6.2.

Velocity

- Dirichlet BC are adopted for the velocity at the inlet. The value of the velocity in x direction is set to $v_x = 0$, whereas the value of the velocity in y direction is calculated from the casting velocity as

$$v_y = \frac{a_b v_{cast}}{d_2}. \tag{6.31}$$

- Neuman BC are used at the outlet, where an assumption of fully developed flow is made. The velocity gradient is set to zero ($\frac{\partial \mathbf{v}}{\partial \mathbf{n}} = 0$).

- On the free surface, the velocity in y direction is set zero $v_y = 0$, whereas the Neuman BC is used to define the velocity in x direction $\frac{\partial v_x}{\partial \mathbf{n}} = 0$.

- No-slip BC is used for the velocity at the moving walls. The walls move in the direction of casting with the velocity $v = v_{cast}$.

- Neuman BC are used on the symmetry line, i.e. $\frac{\partial v_x}{\partial \mathbf{n}} = \frac{\partial v_y}{\partial \mathbf{n}} = 0$.

Temperature

- Dirichlet BC is used to describe the temperature at the inlet. The value is constant and set to T_{cast}.

- Neuman BC are set to describe the temperature at the outlet, free surface and symmetry line ($\frac{\partial T}{\partial \mathbf{n}} = 0$).

- The temperature at the moving walls is prescribed with the Robin BC by considering the heat fluxes. The moving walls are divided into two parts; the mould region and the spray cooling region. In the mould region, the heat transfer coefficient h_{mc} is 2000 W/(m^{2}K), whereas in the spray cooling region the heat transfer coefficient h_{sc} is 800 W/(m^{2}K). In the mould region, heat flux is calculated as

$$q_{mould} = h_{mc}(T - T_{sc}), \tag{6.32}$$

  where T_{sc} is the temperature of the cooling water, set to 293 K. The heat flux in spray cooling region is obtained from

$$q_{sc} = h_{sc}(T - T_{sc}). \tag{6.33}$$

Pressure

- Neuman boundary condition is used to calculate the pressure at the inlet, free surface, moving walls and symmetry line.
- Dirichlet boundary condition is prescribed for pressure at the outlet. The pressure is constant and set to gauge pressure, i.e. $p = 0$ for ambient pressure.

k **and** ε

- Dirichlet boundary conditions are prescribed for k and ε at the inlet.
- Neuman boundary conditions are used at the outlet, free surface, symmetry line and moving walls. As the flow is assumed to be fully developed, the $\frac{\partial k}{\partial \mathbf{n}} = 0$ and $\frac{\partial \varepsilon}{\partial \mathbf{n}} = 0$.

Magnetic Field

- Neuman boundary condition is prescribed at the input, free surface, outlet and symmetry line, $\frac{\partial \mathbf{j}}{\partial \mathbf{n}} = 0$.
- Dirichlet boundary condition is prescribed for magnetic field at the moving walls, i.e. $\mathbf{j} = 0$. The "wall" is insulated, so that the $\sigma_w = 0$ and consequently, the $\frac{\partial \phi}{\partial \mathbf{n}} = 0$.

Species Concentration

- Dirichlet boundary conditions are prescribed for species concentration at the inlet. The value is set to a constant, predetermined value $C = C_0$.
- Neuman boundary conditions are used at the outlet, free surface, symmetry line and moving walls, i.e. $\frac{\partial C}{\partial \mathbf{n}} = 0$.

6.7 Numerical Examples

Three different numerical examples are considered: a simple, predetermined magnetic field (A), a magnetic field calculated from the coil model (B) and a magnetic field calculated from the coil model with consideration of species transfer (C). As can be deduced from the example titles, the first example describes the classical, simplified CC process with a predefined magnetic field. The results of the developed numerical model are verified by comparison with the results acquired with FVM. In the second case, the magnetic field is calculated as described in Sec. 6.3. In the third case, species transfer is added to the example B.

The thermophysical properties are given in Tab. 6.3. If the specific numerical parameter is required in any of the three numerical examples, it is stated separately at the corresponding section.

Table 6.3: Thermophysical properties of steel used in the computation.

Parameter	**Description**	**Unit**	**Value**
Density	ρ	[kg/m^3]	7200
Dynamic viscosity of liquid	μ_L	[kg/(ms^2)]	0.006
Thermal conductivity	λ	[W/(mK)]	30
Specific heat	c_p	[J/(kg K)]	700
Heat transfer coefficient in the mould	h_{mc}	[W/(m^{2}K)]	2000
Heat transfer coefficient in the spray cooling region	h_{sc}	[W/(m^{2}K)]	800
Melting enthalpy	h_m	[J/kg]	250000
Diffusion coefficient of solid	D_S	[m^2/s]	$1.6 \cdot 10^{-11}$
Diffusion coefficient of liquid	D_L	[m^2/s]	$1.0 \cdot 10^{-8}$
Solidus temperature	T_S	[K]	1680
Liquids temperature	T_L	[K]	1760
Casting temperature	T_{cast}	[K]	1800
Melting temperature	T_m	[K]	1812
Eutectic temperature	T_E	[K]	1420
Spray cooling temperature	T_{sc}	[K]	293
Casting velocity	v_{cast}	[m/s]	0.0292
Permeability constant	K_0	[m^{-1}]	$6.25 \cdot 10^{-9}$
Gravitational acceleration	g_y	[m/s^2]	9.81
Electric conductivity	σ	[(Ω m)$^{-1}$]	$0.59 \cdot 10^6$
Permeability of free space	μ_0	[H/m]	$4\pi \cdot 10^{-7}$
Permeability of soft iron	μ_{iron}	[H/m]	$6.28 \cdot 10^{-3}$
Permittivity of free space	ε_0	[F/m]	$8.85 \cdot 10^{-12}$
Thermal expansion coefficient	β_T	[K^{-1}]	$1 \cdot 10^{-4}$
Solute expansion coefficient	β_C	[/]	$4 \cdot 10^{-3}$
Partition coefficient	k_p	[/]	0.48
Reference concentration	C_{ref}	[/]	0.008
Eutectic concentration of solid	C_{ES}	[/]	2.06
Eutectic concentration of liquid	C_{EL}	[/]	4.3

The results are compared for several different cross-sections; two of which are in the vertical direction (one at the center of the billet or symmetry line, the other at the surface of the billet) and three at different positions in the horizontal direction (one at the outlet, and two before and after the application of magnetic field). A scheme of the plotting cross-section positions is shown in Figs. 6.24 and 6.25. The positions of the horizontal (Fig. 6.25) plotting cross-sections are adjusted in such a way, that they correspond to the area of interest. Unless otherwise stated, the vertical positions are placed at 0.07 m (vI) and 0.14 m (vII) and the horizontal positions are placed at -0.8 m (hI), -0.9 m (hII) and -1.8 m (hIII).

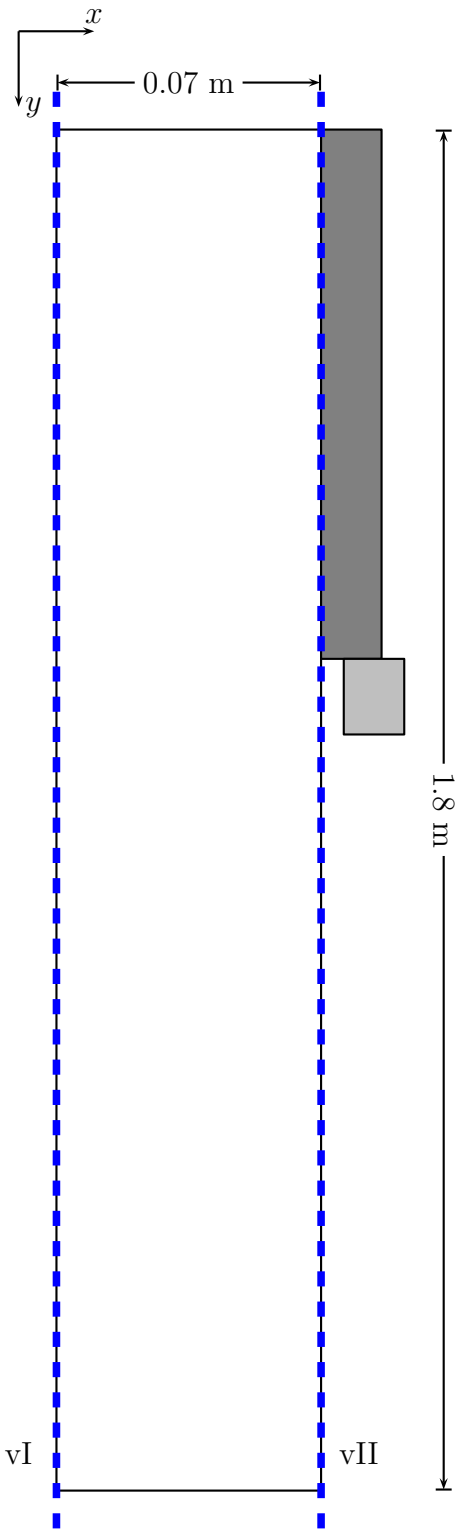

Figure 6.24: Positions of plotting cross-sections. The dashed line represents plotting cross-section along y axis.

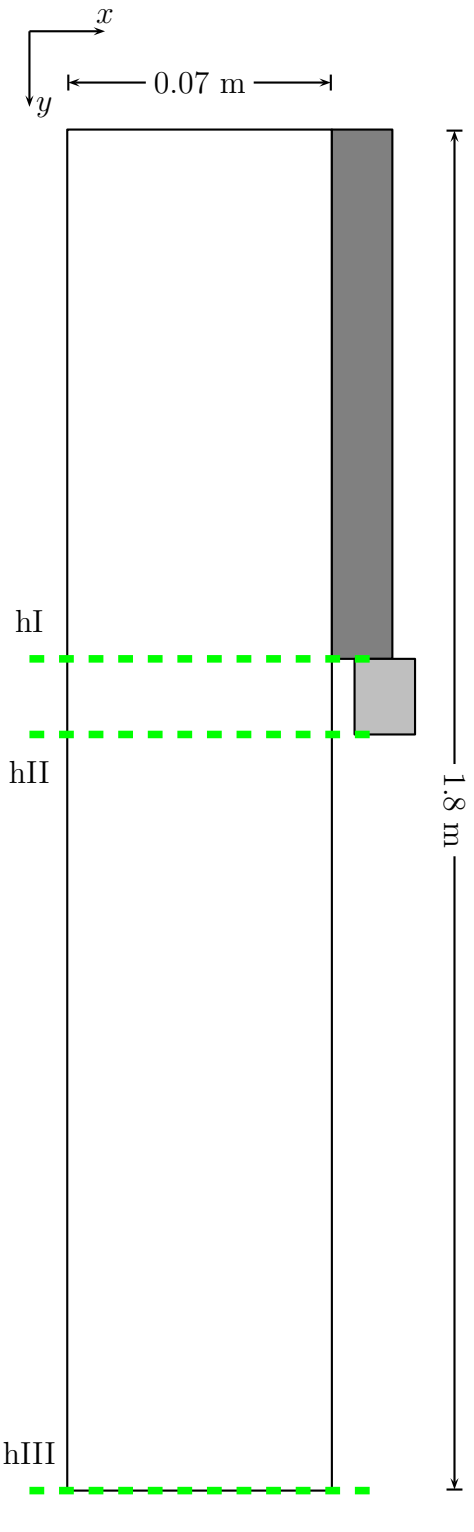

Figure 6.25: Positions of plotting cross-sections. The dashed line represents plotting cross-sections along x axis.

6.7.1 A: Simple Predetermined Magnetic Field

The numerical example A with a simple predetermined magnetic field describes a case with completely homogeneous magnetic field with magnitude $\mathbf{B} = \mathbf{B}_0$ inside the interval $[-l_m, -l_m - l_{EM}]$ and $\mathbf{B} = 0$ T for $y < -l_m - l_{EM}$ and $y > -l_m$. The cross-section of such magnetic field is depicted in Fig. 6.26 at $x = 0.07$ m. The default magnetic field is placed at $l_{mEM} = -0.8$ m, has the range of 0.1 m ($l_{EM} = 0.1$ m), is oriented in x direction and has either magnitude $B = 0.026$ T or $B = 0.035$ T.

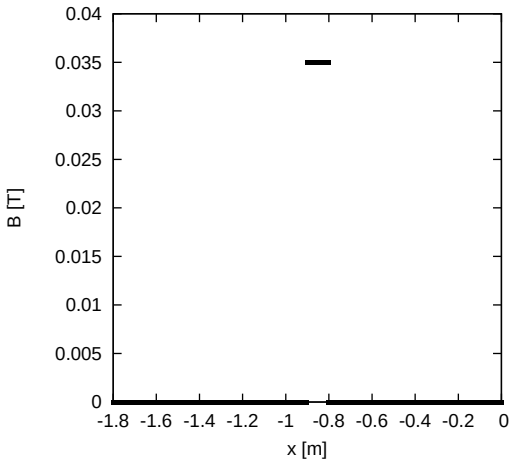

Figure 6.26: An example of a simple magnetic field with $l_m = -0.8$ m and $l_{EM} = 0.1$ m.

First, the results calculated with the developed numerical model are compared for several different node arrangements in order to determine the node independent solution which is then compared with Fluent. The objective of the comparison is to show that the results obtained with the in-house developed code are in good agreement with reference results and not to comment on which of the compared codes is authentic.

Next, a sensitivity study is performed for several different parameters, namely the magnitude of the magnetic field B, the position of the magnetic field l_{mEM}, and the effective interval range l_{EM}.

Mesh Convergence and Comparison with Reference Results

The node independence is tested on a non-uniform node arrangements with 20220, 50951, 73940, 100089, 131452 and 165426 nodes. In FVM, mesh with 169169 quadrilateral cells generated in the Gambit software [ANSYS, 2013], is used for the calculations. The mesh refinement near the walls is similar to the one used in LRBFCM code. Based on the comparison with the Fluent and the following results, a node arrangement with 73940 nodes is chosen. The study was made for the temperature and velocity fields at the following cross-sections: $x = 0.07$ m (symmetry line) and $x = 0.14$ m (surface) in the horizontal direction and $y = -1.8$ m (outlet), $y = -0.9$ m and $y = -0.8$ m in the vertical direction for

the magnetic field $B_x = 3.5 \cdot 10^{-2}$ T placed at the end of the mold $l_m = 0.8$ m. The width of the magnetic field interval is $l_{EM} = 0.1$ m.

Temperature is shown in Figs. 6.27, 6.27, and 6.27. All of the comparisons, both at vertical and at horizontal cross-sections, are in a very good agreement, even for node arrangements with the smallest number of nodes. The values obtained with FVM are in a very good agreement with the in-house developed method.

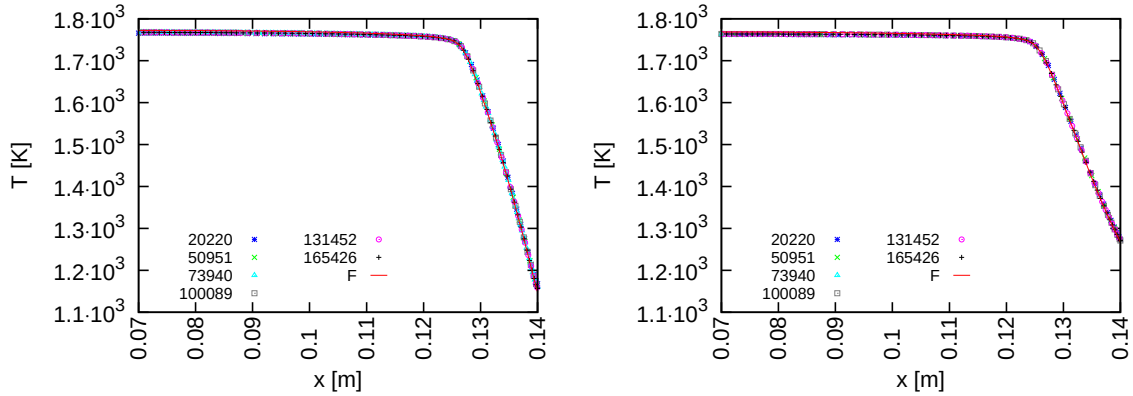

Figure 6.27: Temperature at simplified magnetic field. Left: −0.8 m. Right: −0.9 m.

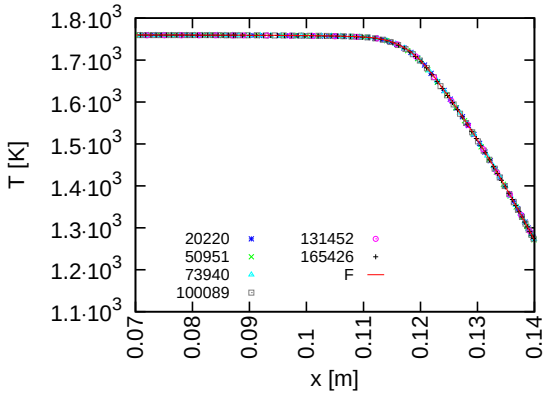

Figure 6.28: Temperature at simplified magnetic field at cross-section −1.8 m.

The absolute velocity magnitude is shown in Figs. 6.30, 6.31, and 6.32. The velocity magnitudes for horizontal cross-sections (Figs. 6.30 and 6.31) in the examples with 20220 and 50951 nodes have slightly lower values in the extremes, compared to the examples with 73940, 100089, 131452 and 165426. In the cases with denser node arrangements, the difference is negligible and cannot be visually perceived. The FVM results give slightly larger values at the extremes, especially at the cross-sections at the higher part of the strand (−0.8 m and −0.9 m in Fig. 6.30). In all of the calculations, the range to which the material has solidified appears to be the same. Like-wise could be said for the velocity at which the solidified material is moving. The agreement between the results for velocity magnitude calculated with LRBFCM and with FVM is much better

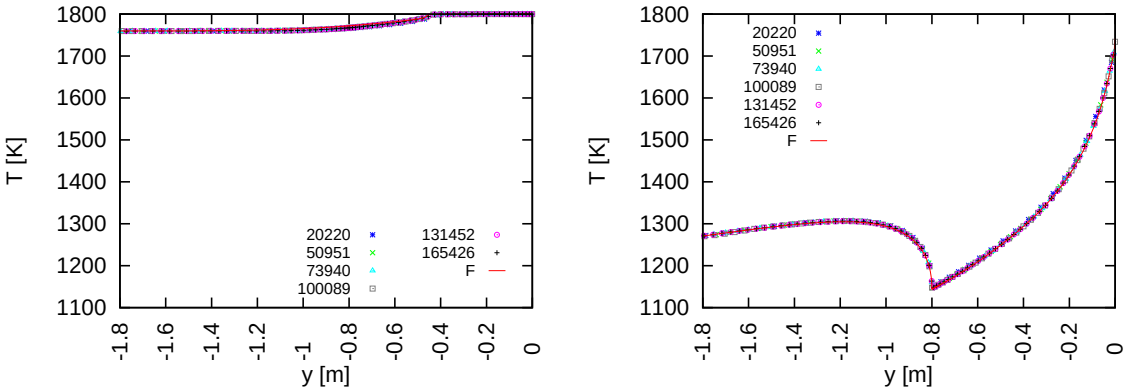

Figure 6.29: Temperature at simplified magnetic field. Left: cross-section at 0.07 m. Right: cross-section at 0.14 m.

for the cross-section at the end of the calculation domain (at −1.8 m as shown in Fig. 6.32) where the observed difference is very small. A comparison of the velocity magnitudes for different node arrangements for the vertical cross-section at the horizontal positions of 0.07 m (the center of the strand) and of 0.14 m (the outer edge of the strand) gives a very good agreement between all of the examples, no matter how dense the node arrangement is. A comparison with the FVM presents a very good agreement at the outer edge, where the velocity of the solidified material equals the casting velocity. In the center of the strand, the velocity magnitude calculated with the FVM gives slightly different values, especially at the part of the strand where the change in the velocity magnitude is the fastest.

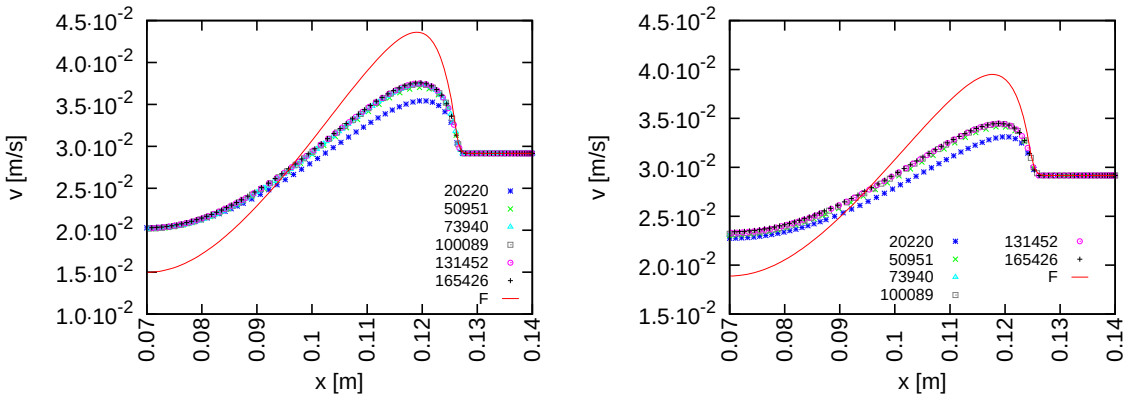

Figure 6.30: Absolute velocity field at simplified magnetic field. Left: cross-section at −0.8 m. Right: cross-section at −0.9 m.

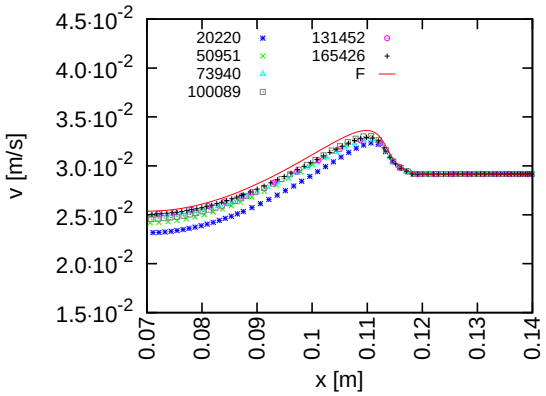

Figure 6.31: Absolute velocity at simplified magnetic field at cross-section −1.8 m.

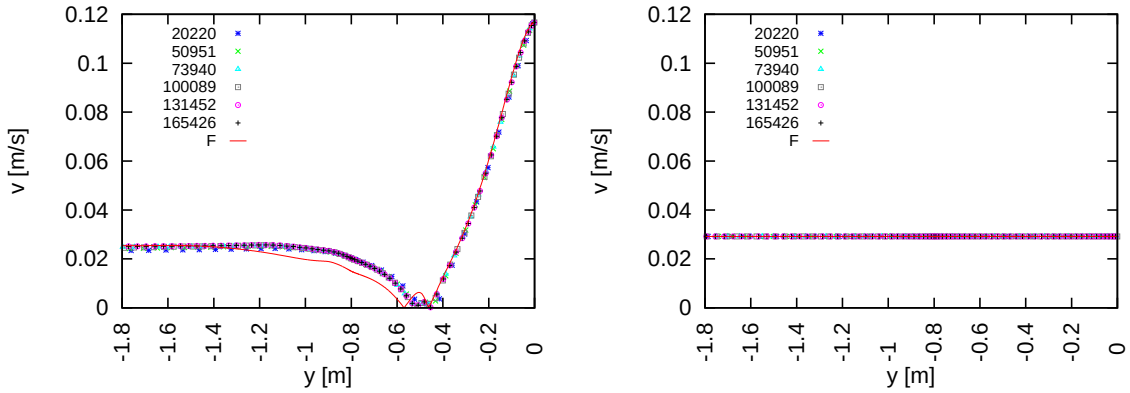

Figure 6.32: Absolute velocity at simplified magnetic field. Left: 0.07 m. Right: 0.14 m.

As the velocity magnitudes for different node arrangement calculated with LRBFCM, exhibit a slight discrepancy with the results from Fluent, another comparison was made. In this case, the agreement between the results calculated with LRBFCM on the 73940 node arrangement with and without the presence of magnetic field is compared to the results obtained with the FVM both with and without the presence of the magnetic field. This test is performed to check if the difference between the results calculated with the LRBFCM and FVM is the same if there is no magnetic field. The comparison is done only for the velocities, as the discrepancy of the results appears only for the velocity magnitudes. The comparison of velocity magnitudes for the magnetic field and without the magnetic field is presented in Figs. 6.33, 6.35 and 6.34. In this case the magnetic field with a magnitude of 350 G is used. As can be seen in Figs. 6.33, 6.35 and 6.34 the difference between the cases with and without the magnetic field is comparable. The figures also show, that the weak magnetic field of 350 G only slightly influences the velocity field.

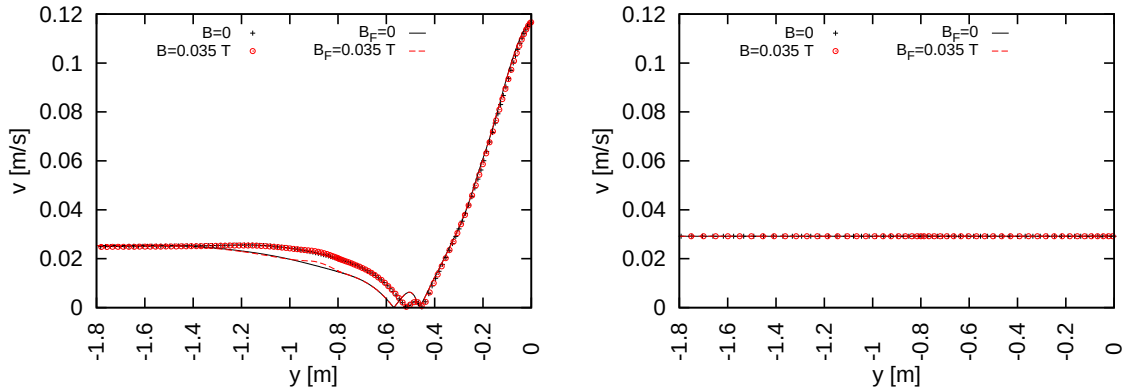

Figure 6.33: Comparison of absolute velocity magnitudes for the cases with and without magnetic field. Left: cross-section at 0.07 m. Right: cross-section at 0.14 m.

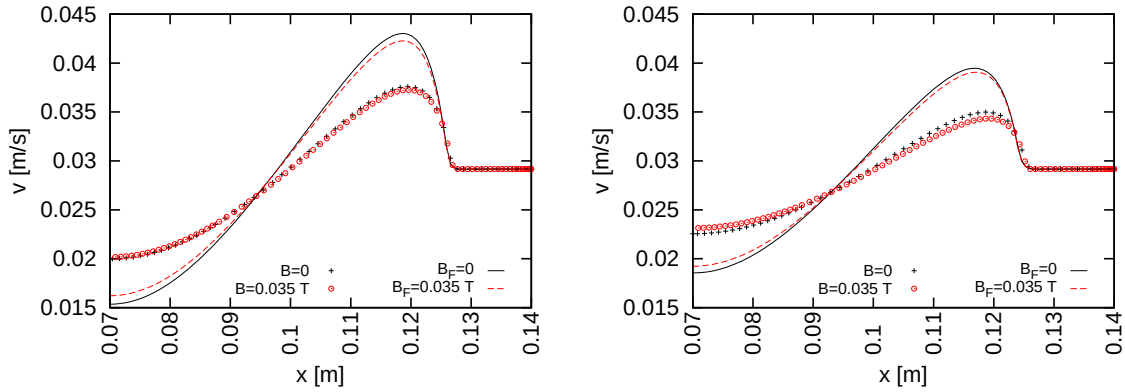

Figure 6.34: Comparison of absolute velocity magnitudes for the cases with and without magnetic field. Left: cross-section at −0.8 m. Right: cross-section at −0.9 m.

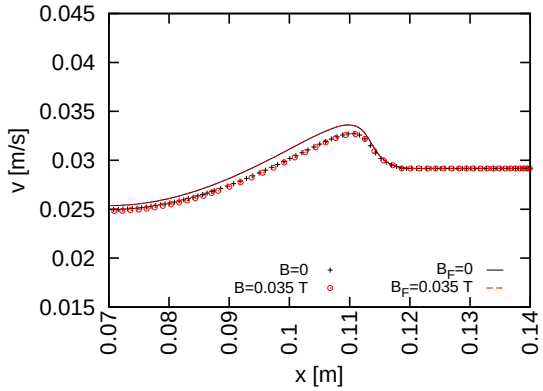

Figure 6.35: Comparison of absolute velocity magnitudes for the cases with and without magnetic field at cross-section −1.8 m.

The comparison of streamlines and contour plots for T and $\mathbf{v}$ fields for the cases with and without the magnetic field is given in Figs. 6.36, 6.37 and 6.38.

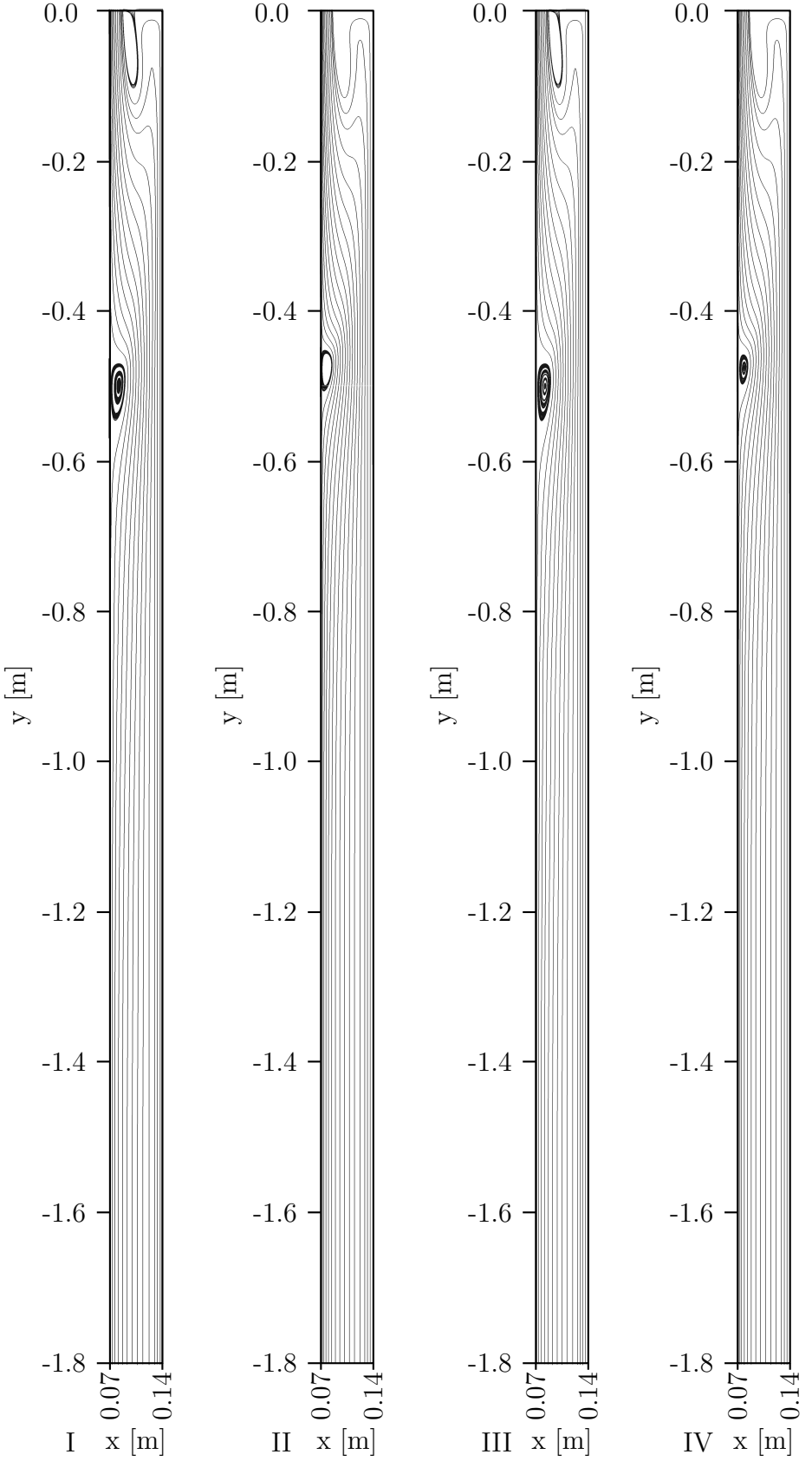

Figure 6.36: Comparison of streamlines between FVM and LRBFCM simulations with and without magnetic field. I: Fluent $B_x = 0$ T. II: $B_x = 0$ T. III: Fluent $B_x = 3.5 \cdot 10^{-2}$ T. IV: $B_x = 3.5 \cdot 10^{-2}$ T.

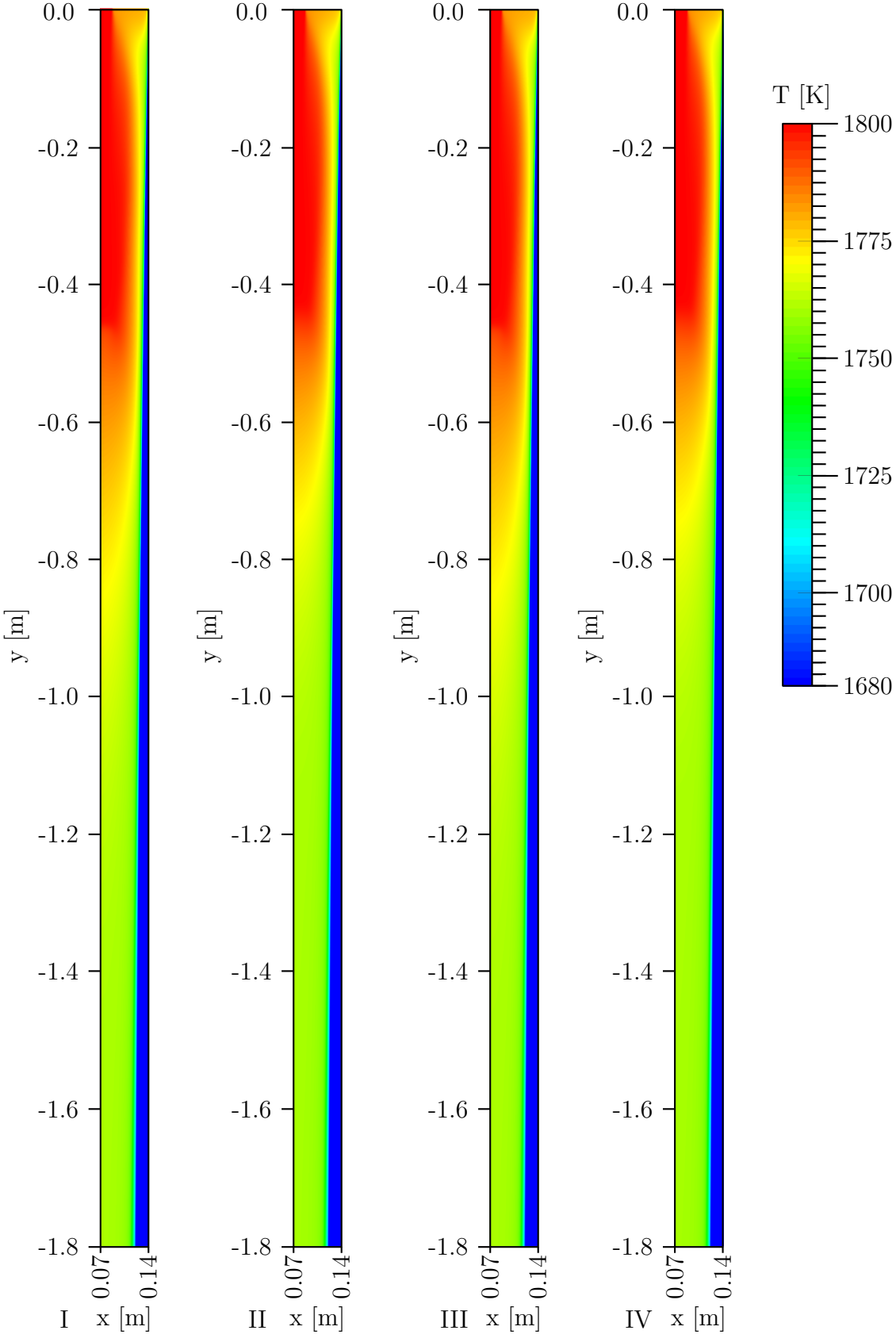

Figure 6.37: Comparison of temperature field between FVM and LRBFCM simulations with and without magnetic field. I: Fluent $B_x = 0$ T. II: $B_x = 0$ T. III: Fluent $B_x = 3.5 \cdot 10^{-2}$ T. IV: $B_x = 3.5 \cdot 10^{-2}$ T.

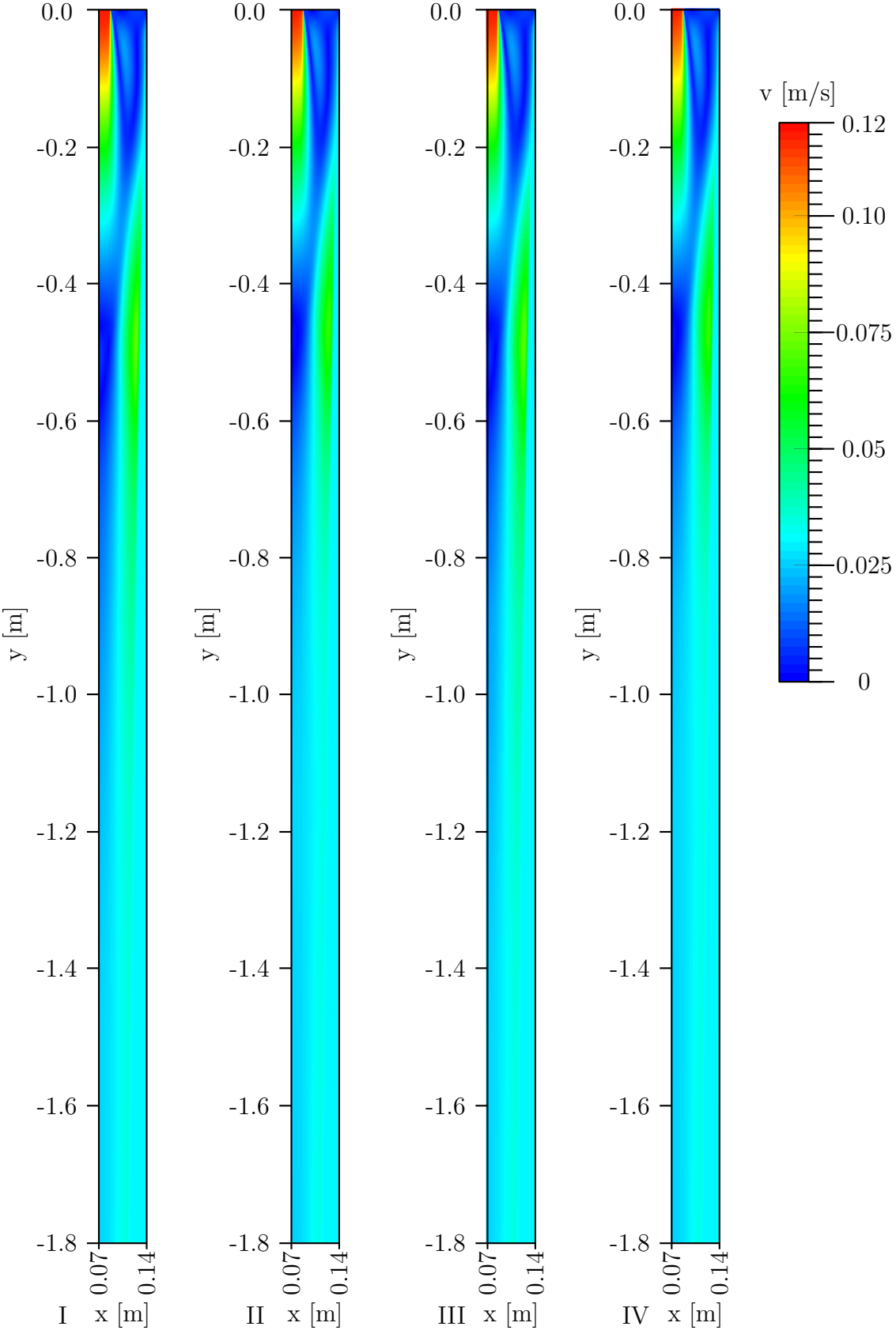

Figure 6.38: Comparison of velocity field between FVM and LRBFCM simulations with and without magnetic field. I: Fluent $B_x = 0$ T. II: $B_x = 0$ T. III: Fluent $B_x = 3.5 \cdot 10^{-2}$ T. IV: $B_x = 3.5 \cdot 10^{-2}$ T.

The Strand Length Sensitivity Study

The study of the influence of the strand length is made for strand lengths $l = 1.8$ m and $l = 2.6$ m. The objective of this test is to ascertain, that the length of the computational domain does not affect the velocity and temperature profiles in upper parts of the strand. As the length of the computational domain is most likely to affect the velocity and the temperature profiles at the end of the computational domain, Fig. 6.39 shows the vertical cross-section at the horizontal position of 0.14 m and the horizontal cross-section at the end of the shorter computational domain, that is at -1.8 m. As can be seen in the Fig. 6.39 the velocity and temperature profiles on both graphs are visually identical.

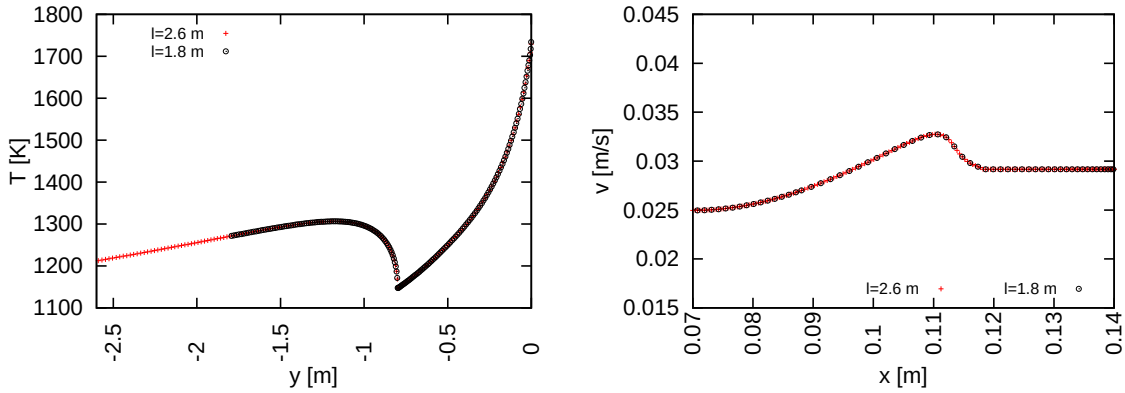

Figure 6.39: Comparison of profiles for strand length of $l = 1.8$ m and $l = 2.6$ m. Left: temperature profile at 0.14 m. Right: velocity profile at -1.8 m.

Graphs in Fig. 6.40 show contour plots for velocity and temperature fields for shorter and longer configuration of the computational domain. The contour plots confirm that the 1.8 m long computational domain is long enough. Extending the computational domain to 2.6 m does not affect neither the velocity field nor the temperature field. The metallurgical length, at which the entire cross-section of the billet is solidified, is at approximately 10 m.

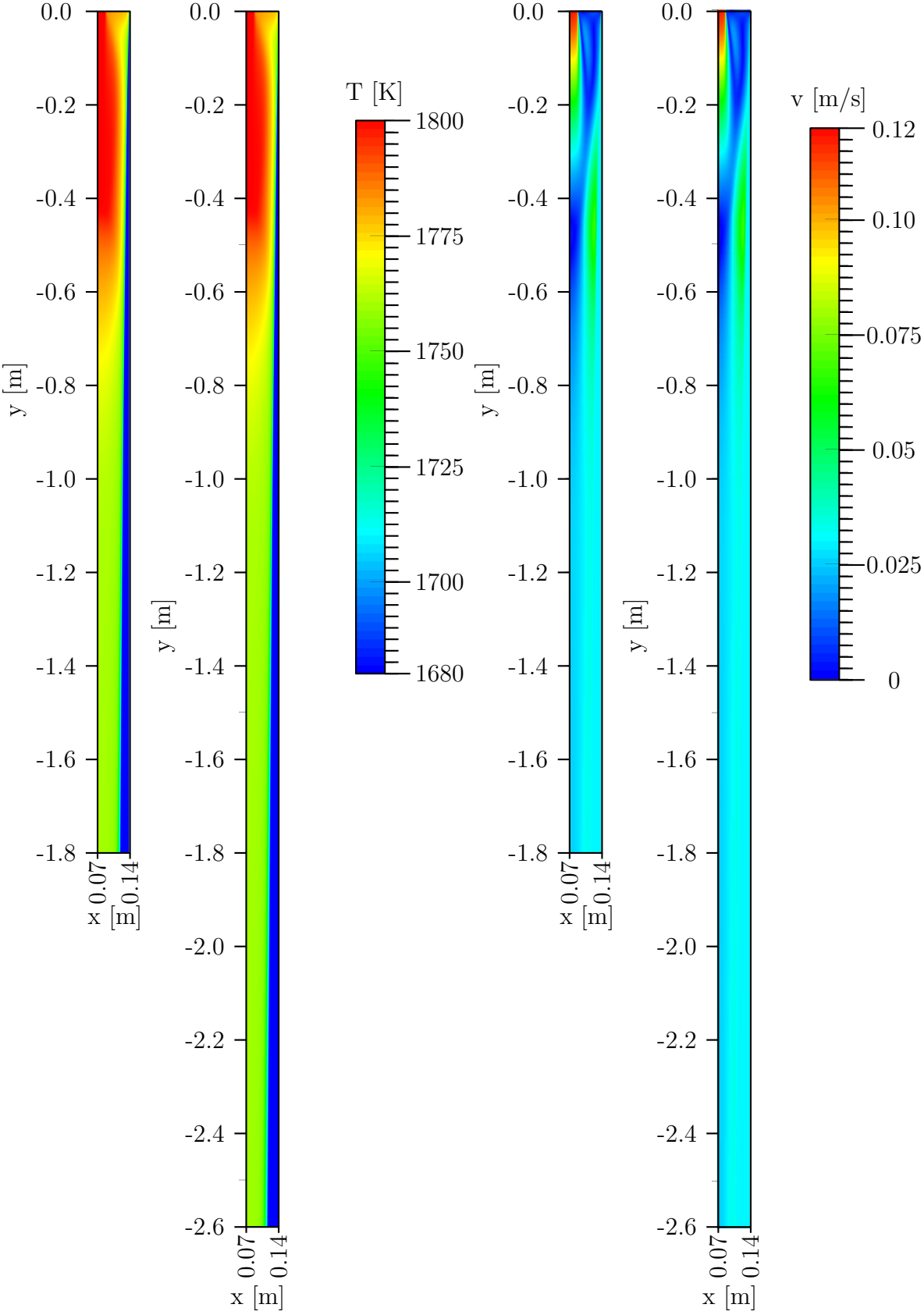

Figure 6.40: Comparison of temperature and velocity fields as a function of computational domain length. Left: temperature field. Right: velocity field.

Influence of the Magnetic Field Magnitude

The influence of the magnetic field magnitude is tested for several magnetic field magnitudes, ranging from 0.0 T to 2.6 T. The changes in the temperature profiles due to the changes in the magnetic field magnitude are negligible as can be seen in Figs. 6.41 and 6.42.

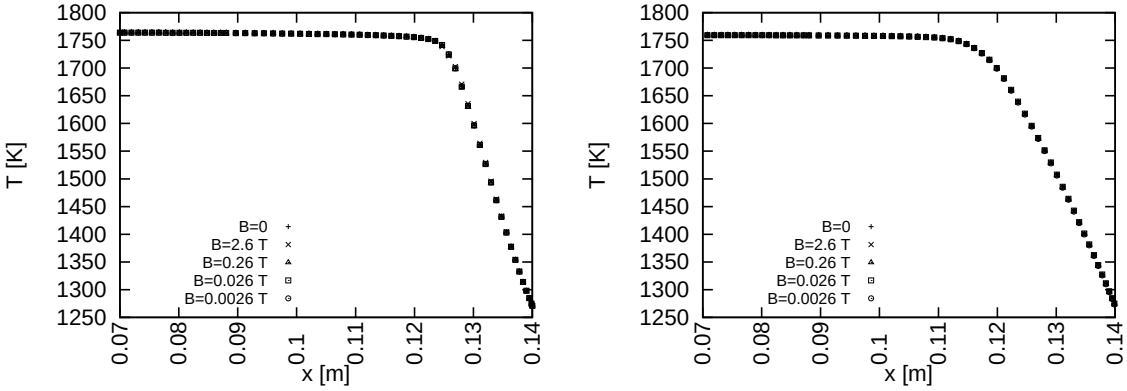

Figure 6.41: Comparison of temperature profiles along x direction. Left: -0.9 m. Right: -1.8 m.

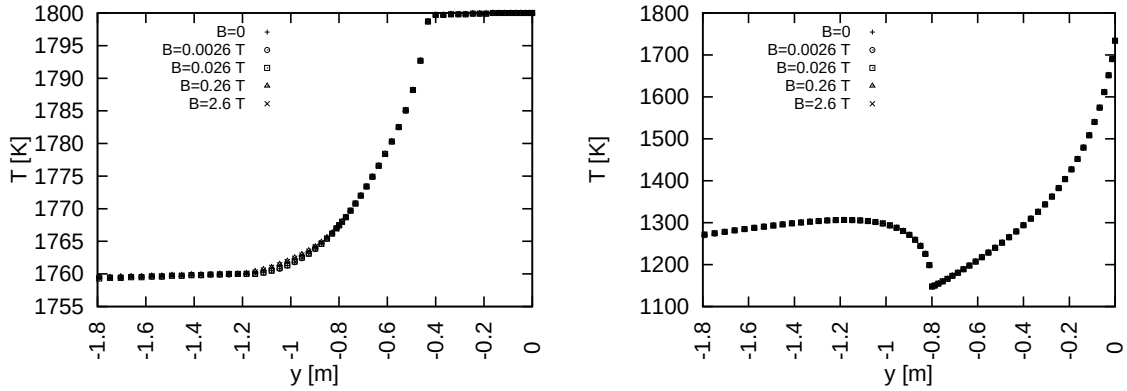

Figure 6.42: Comparison of temperature profiles along y direction. Left: 0.07 m. Right: 0.14 m.

The contour plots of the temperature field for different magnetic field magnitudes are nearly identical and are presented in Appx. D. Since the influence of magnetic field on temperature is very small, related plots are arranged in such a way that the difference between the the case with magnetic field and reference case without magnetic field is shown ($T(\mathbf{B}) - T(\mathbf{B} = 0)$). As expected, the temperature does not change significantly, especially in the cases with small magnetic fields ($B_x = 2.6 \cdot 10^{-3}$ T and $B_x = 2.6 \cdot 10^{-2}$ T), where the temperature difference is smaller than one degree. The change in temperature is more pronounced in cases with stronger magnetic fields ($B_x = 0.26$ T and $B_x = 2.6$ T), especially at the solidified shell.

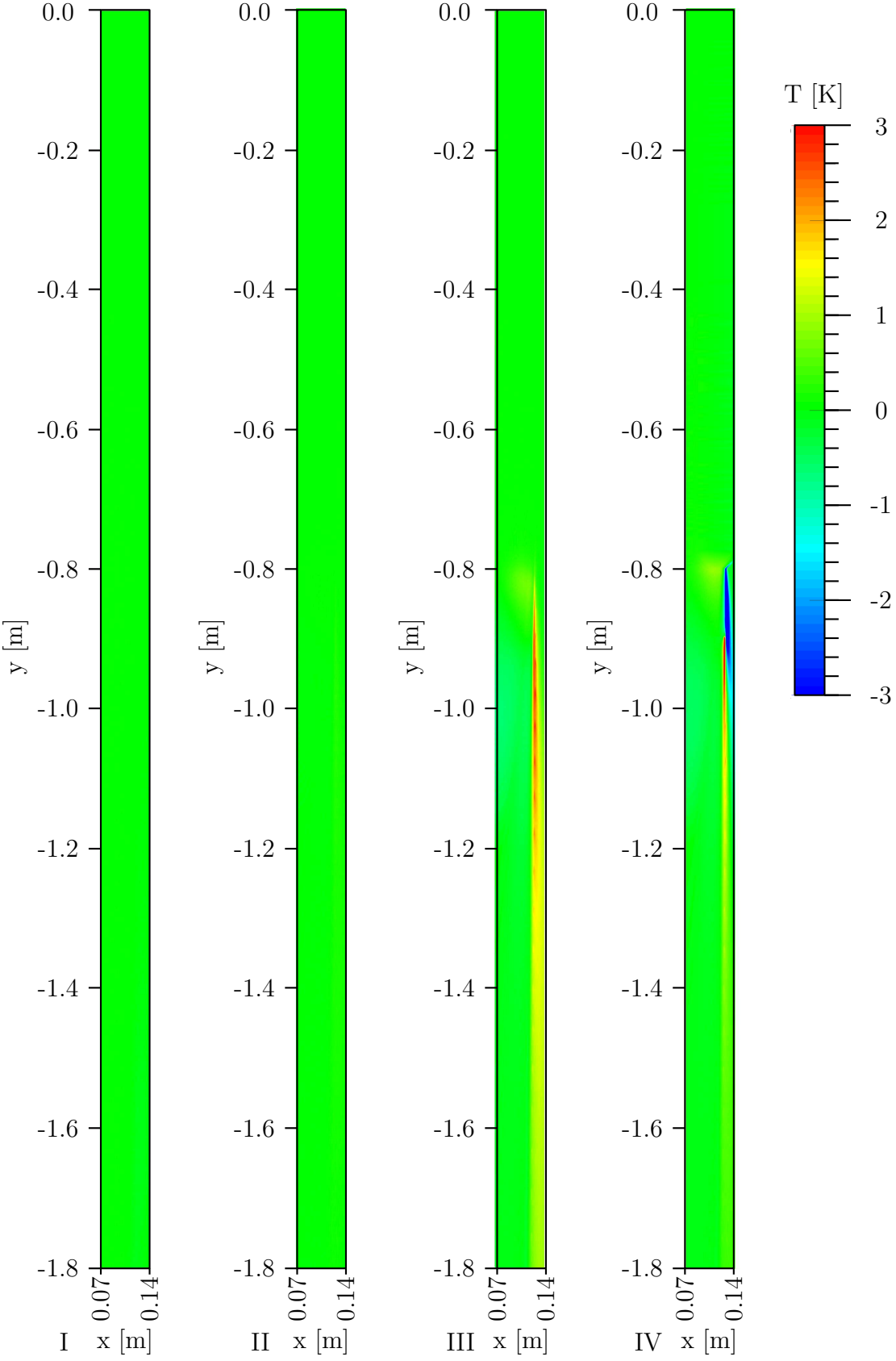

Figure 6.43: Temperature field $(T(\mathbf{B}) - T(\mathbf{B} = 0))$ as a function of magnetic field magnitude. I: $B_x = 2.6 \cdot 10^{-3}$ T. II: $B_x = 2.6 \cdot 10^{-2}$ T. III: $B_x = 2.6 \cdot 10^{-1}$ T. IV: $B_x = 2.6$ T.

Next, the velocity profiles are examined for three different horizontal cross-sections at vertical positions −0.8 m, −0.9 m and −1.8 m. The influence of the magnetic field magnitude is the most apparent for the strongest magnetic fields (0.26 T and 2.6 T). As expected, the increase in the magnetic field causes the decrease in the velocity magnitude, as can be seen in Figs. 6.44 and 6.45. Whereas, the trends in the velocity magnitudes are similar for small and intermediate magnitudes of the magnetic fields, the velocity trend of the strongest calculated example is different at the place of application of magnetic field. The difference in the velocity magnitude is the most apparent at position −0.9 m (Fig. 6.44 right), where the velocity magnitude of the strongest magnetic field changes direction. Although such behaviour could be expected for the strong magnetic fields, the results might not be completely correct because the current numerical model is not adapted to include the strong magnetic fields, as one of its major approximations was that the $\mathrm{Re}_m \ll 1$. As the objective of this dissertation was to research the influence of the magnetic field in the industrial example of continuous casting of steel, the behaviour of molten steel at the very high magnetic fields that are currently out of reach to be applied industrially, is not considered. The cross-section of the velocity magnitudes at −1.8 m again shows only a slight difference between the velocity profiles influenced by magnetic fields with different magnitudes, even in the case of a very strong magnetic field. This is to be expected, as the range of the applied simple magnetic fields does not reach this low in the casting direction.

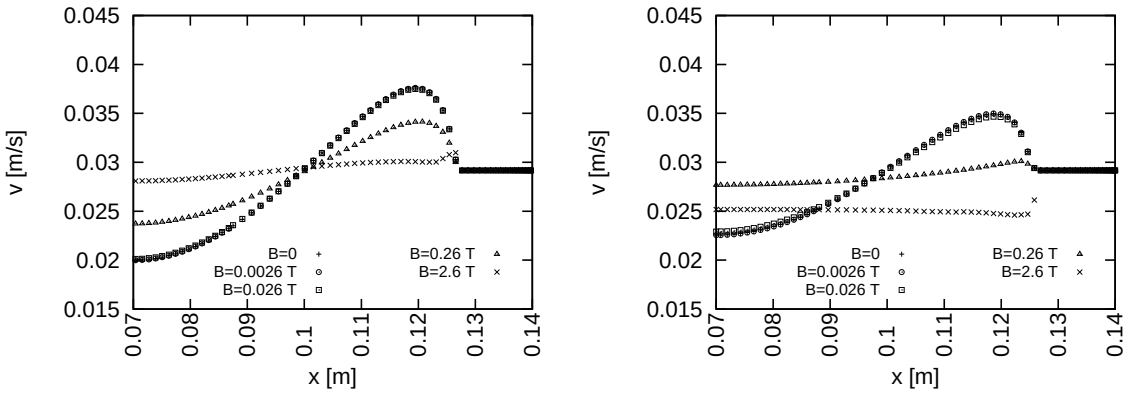

Figure 6.44: Comparison of velocity profiles along x direction. Left: −0.8 m. Right: −0.9 m.

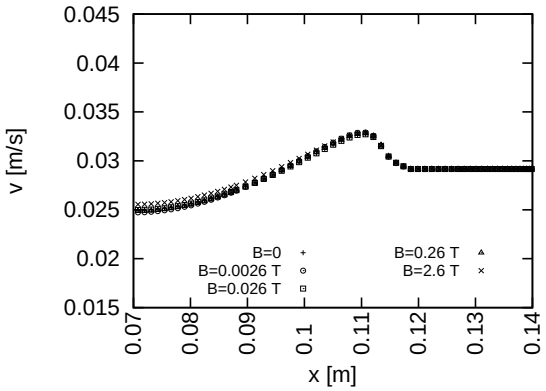

Figure 6.45: Comparison of velocity profiles along x direction at cross-section -1.8 m.

Fig. 6.46 presents the contour plots of the velocity field. Since the influence of magnetic field on the velocity is very small, related plots are arranged in such a way that the difference between the cases with magnetic field and reference case without magnetic field is shown ($\mathbf{v}(\mathbf{B}) - \mathbf{v}(\mathbf{B} = 0)$). The change in velocity is the most pronounced at the place of application of magnetic field, that is between -0.8 m and -0.9 m.

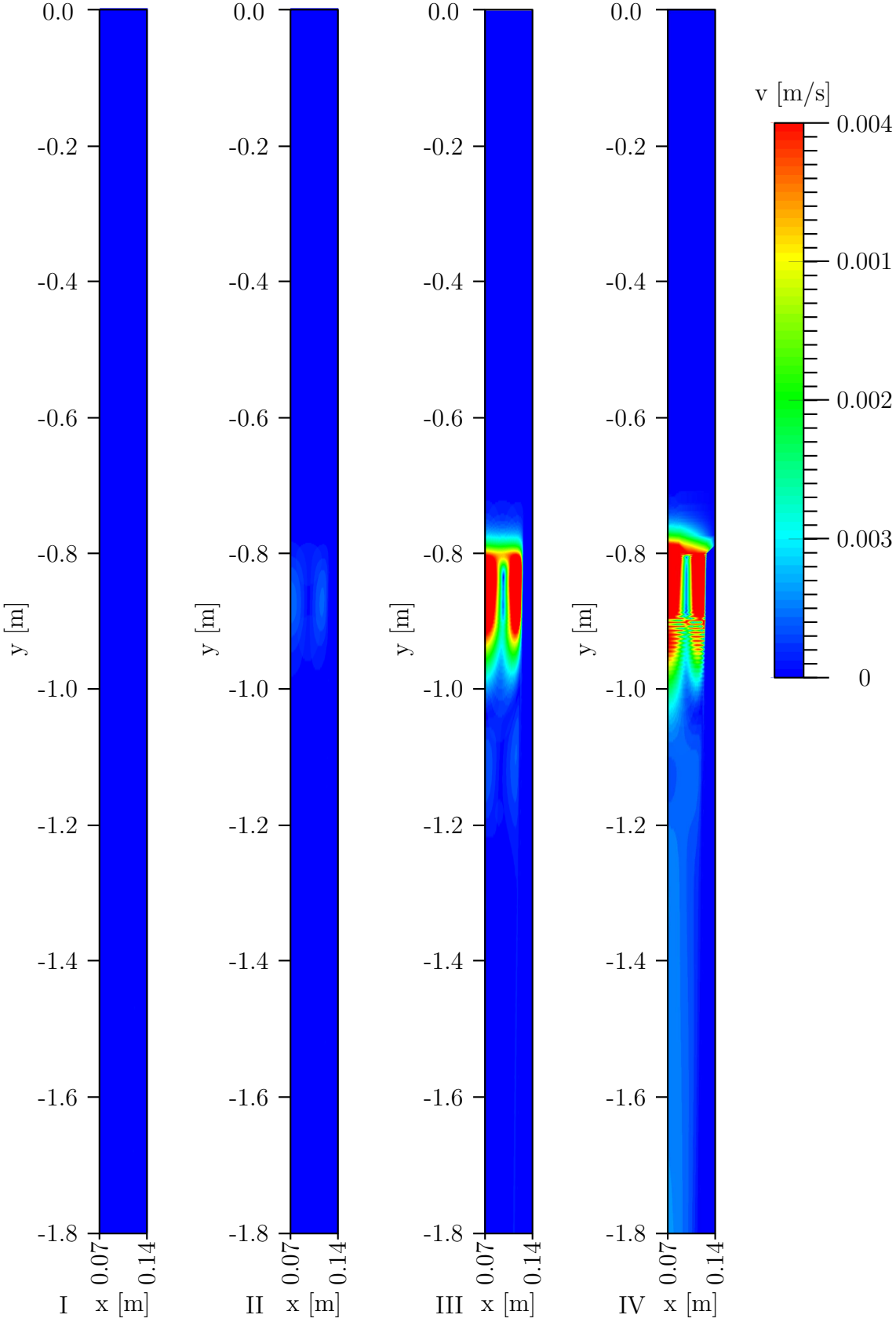

Figure 6.46: Velocity field ($\mathbf{v}(\mathbf{B}) - \mathbf{v}(\mathbf{B} = 0)$) as a function of EM magnitudes. I: $B_x = 2.6 \cdot 10^{-3}$ T. II: $B_x = 2.6 \cdot 10^{-2}$ T. III: $B_x = 2.6 \cdot 10^{-1}$ T. IV: $B_x = 2.6$ T.

The Influence of the Magnetic Field Position

Regarding the position of the magnetic field, the vertical positioning l_{mEM} of the magnetic field is varied between -0.6 m and -0.9 m. First, temperature field and then the velocity field are examined and compared for the default magnetic field $\mathbf{B}_0$ of 0.026 T. The influence of the magnetic field position on the temperature field is presented in Fig. 6.47 for the horizontal cross-sections at the vertical positions 0.07 m and 0.14 m. The magnetic field is to weak too cause significant observable change.

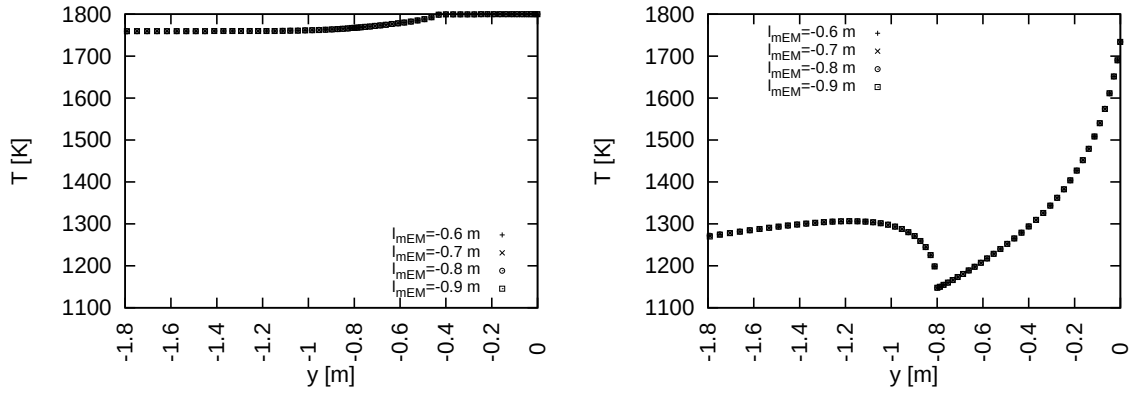

Figure 6.47: Comparison of temperature profiles along x direction. Left: 0.07 m. Right: 0.14 m.

The velocity field for different positions of the magnetic field is depicted in Figs. 6.48 and 6.49. Similarly as in the case of the temperature field, the difference in the velocity is very small. Shifting of the position of the magnetic field influences the extreme values of the velocity as seen in Figs. 6.48 and 6.49. The reason for this might be a more turbulent behaviour of the flow in the higher regions of the strand.

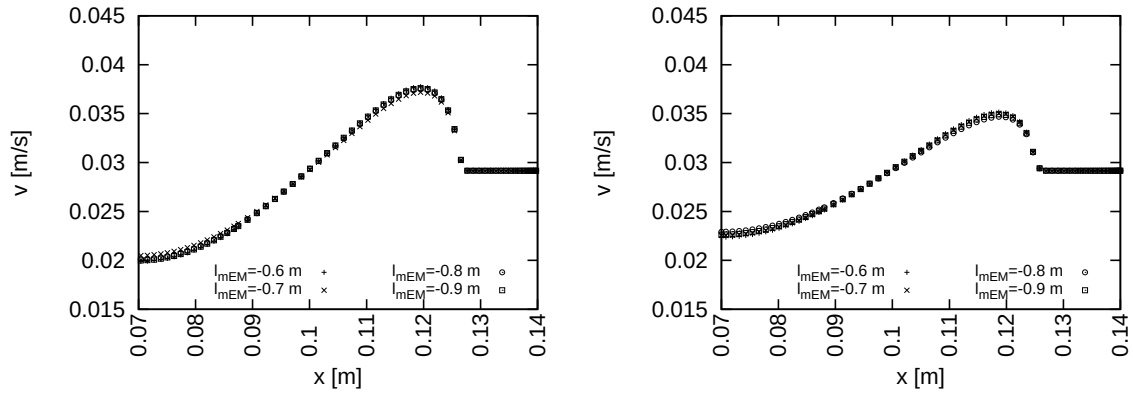

Figure 6.48: Comparison of velocity profiles along y direction. Left: -0.8 m. Right: -0.9 m.

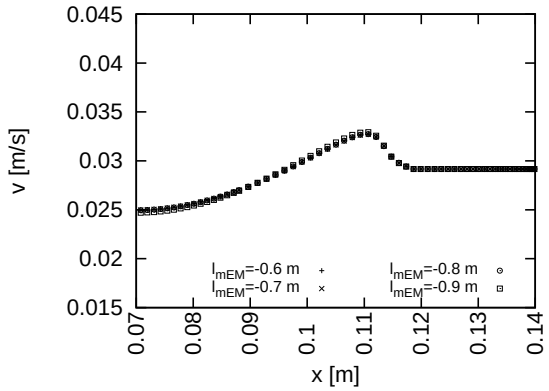

Figure 6.49: Comparison of velocity profiles along y direction at -1.8 m.

Analogously to the temperature cross-sections, the contour plots of the temperature fields are very similar, and not able to be observed visually. Therefore, each of the graphs in Fig. 6.50 presents the difference between the default magnetic field configuration and the configuration of the related case $(T(\mathbf{B}) - T(\mathbf{B}_0))$.

The contour plots of the velocity field are very similar, thus the differences cannot be visually observed. Therefore, each of the graphs presented in Fig. 6.51 shows the difference between the example with the default magnetic field configuration and the related case $(\mathbf{v}(\mathbf{B}) - \mathbf{v}(\mathbf{B}_0))$.

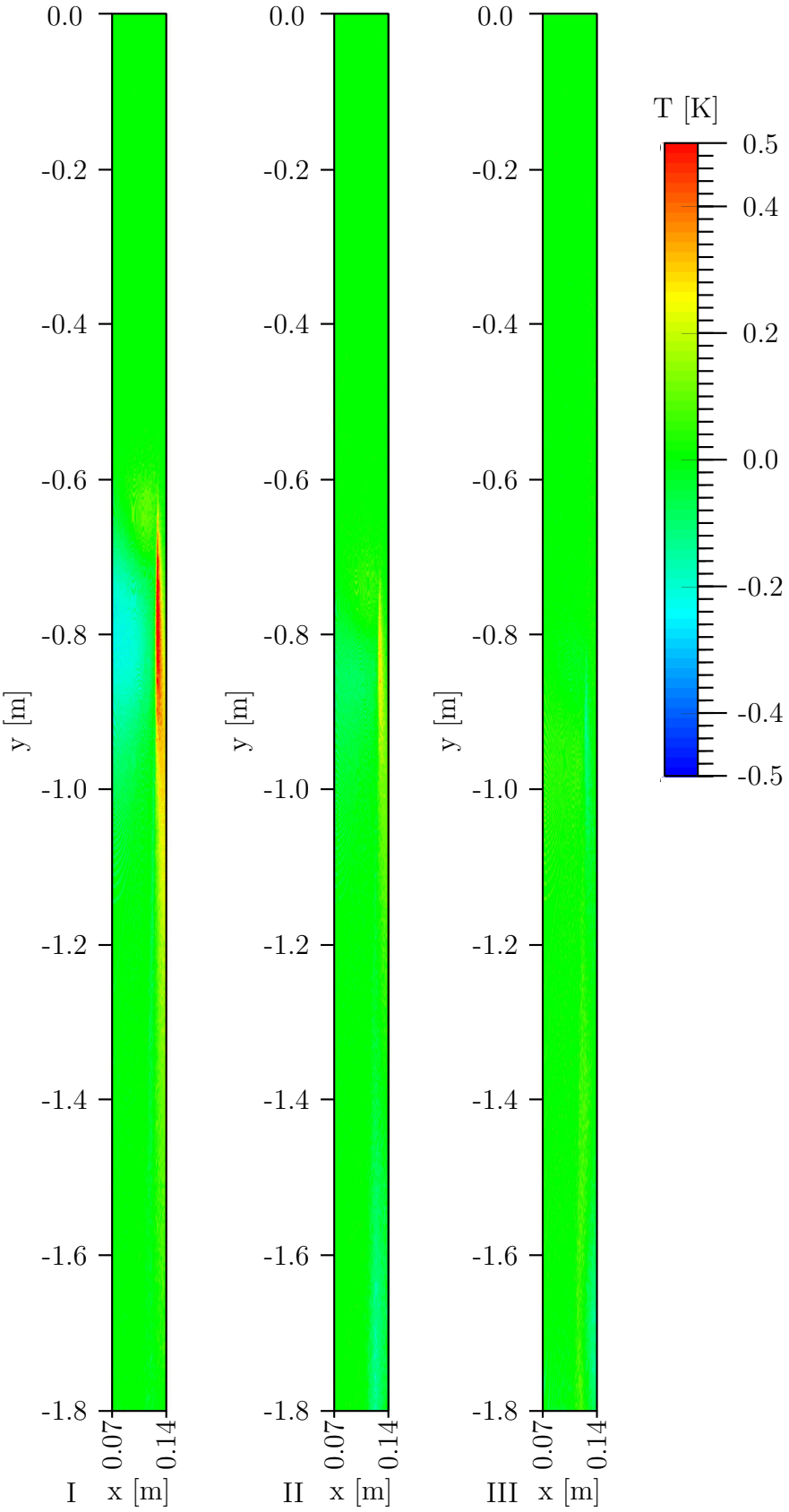

Figure 6.50: Temperature field $(T(\mathbf{B}) - T(\mathbf{B}_0))$ as a function of magnetic field position. I: $l_{mEM} = -0.6$ m. II: $l_{mEM} = -0.7$ m. III: $l_{mEM} = -0.9$ m.

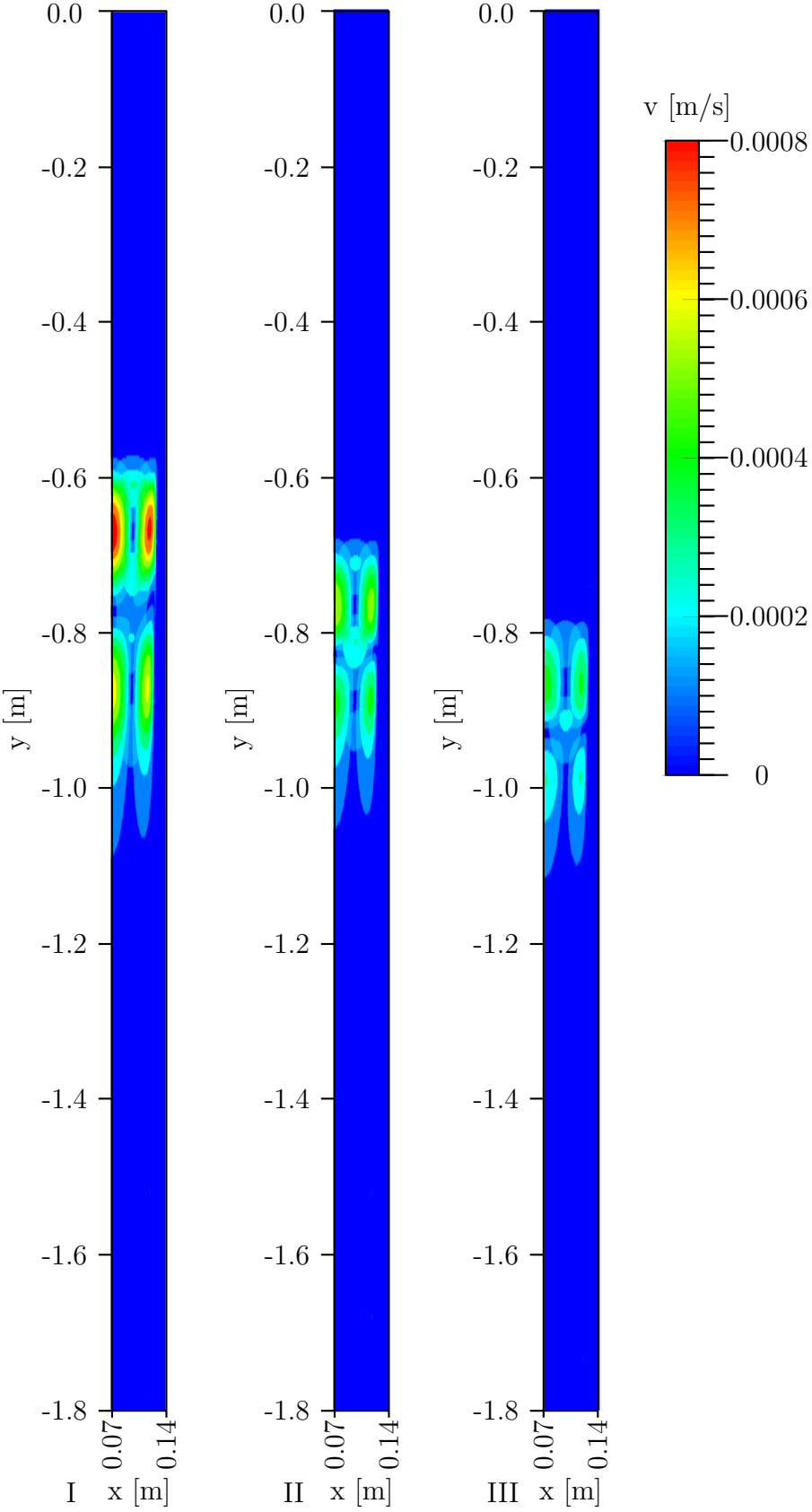

Figure 6.51: Velocity field $(\mathbf{v}(\mathbf{B}) - \mathbf{v}(\mathbf{B}_0))$ as a function of EM positions. I: $l_{mEM} = -0.6$ m. II: $l_{mEM} = -0.7$ m. III: $l_{mEM} = -0.9$ m.

The Influence of the Magnetic Field Height

The influence of the magnetic field range is examined for four different heights: $l_{EM} = 0.05$ m, $l_{EM} = 0.1$ m, $l_{EM} = 0.15$ and $l_{EM} = 0.2$ m. In all of the cases, the magnetic field is placed at the end of the strand, that is at -0.8 m. The temperature profiles for different heights of the magnetic field are presented in Fig. 6.52. There are no significant observable differences.

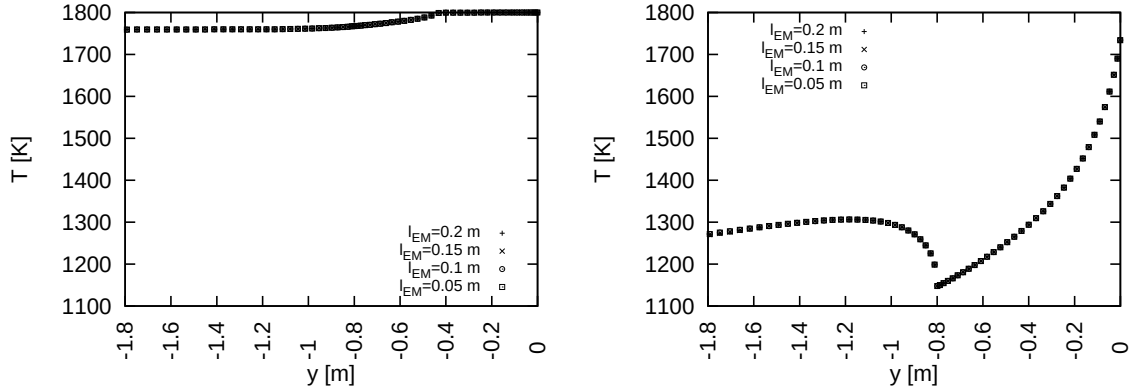

Figure 6.52: Comparison of temperature profiles along x direction. Left: 0.07 m. Right: 0.14 m.

The velocity fields for different magnetic field heights are presented in Figs. 6.53 and 6.54 and are very similar.

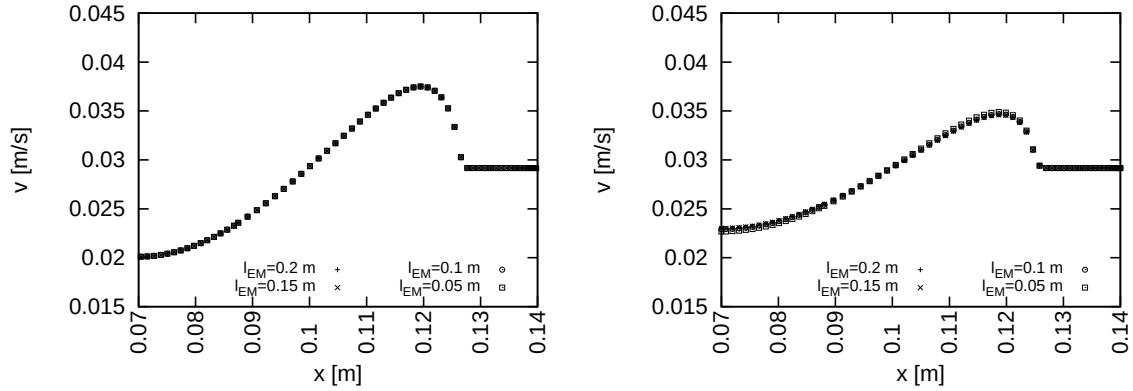

Figure 6.53: Comparison of velocity profiles along y direction. Left: -0.8 m. Right: -0.9 m.

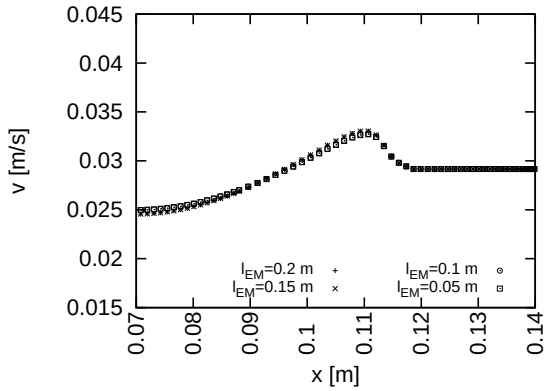

Figure 6.54: Comparison of velocity profiles along y direction at -1.8 m.

The contour plots for temperature fields are very similar and differences cannot be observed visually. Instead, the contour plot of the difference between the temperature of the default arrangement and the temperature of the related example ($T(\mathbf{B}) - T(\mathbf{B}_0)$) are displayed in Fig. 6.55. The differences in the contour plots of the velocity fields cannot be observed visually. Therefore, the difference of the velocity field of the default example and the velocity field of the related examples ($\mathbf{v}(\mathbf{B}) - \mathbf{v}(\mathbf{B}_0)$) are shown in Fig. 6.56.

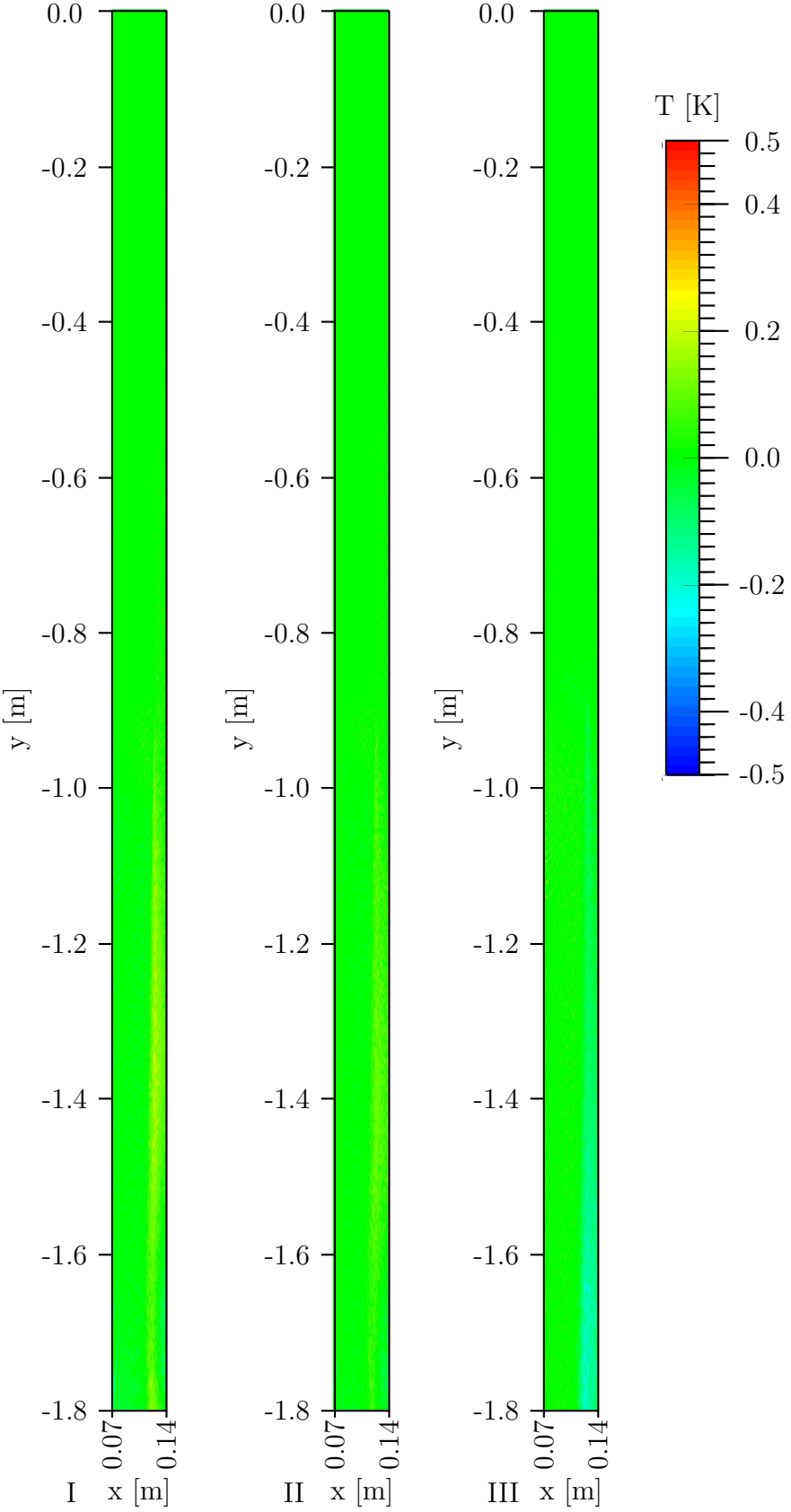

Figure 6.55: Temperature field $(T(\mathbf{B}) - T(\mathbf{B}_0))$ as a function of magnetic field position. I: -0.8 m $< l_{EM} < -1.0$ m. II: -0.8 m $< l_{EM} < -0.95$ m. III: -0.8 m $< l_{mEM} < -0.85$ m.

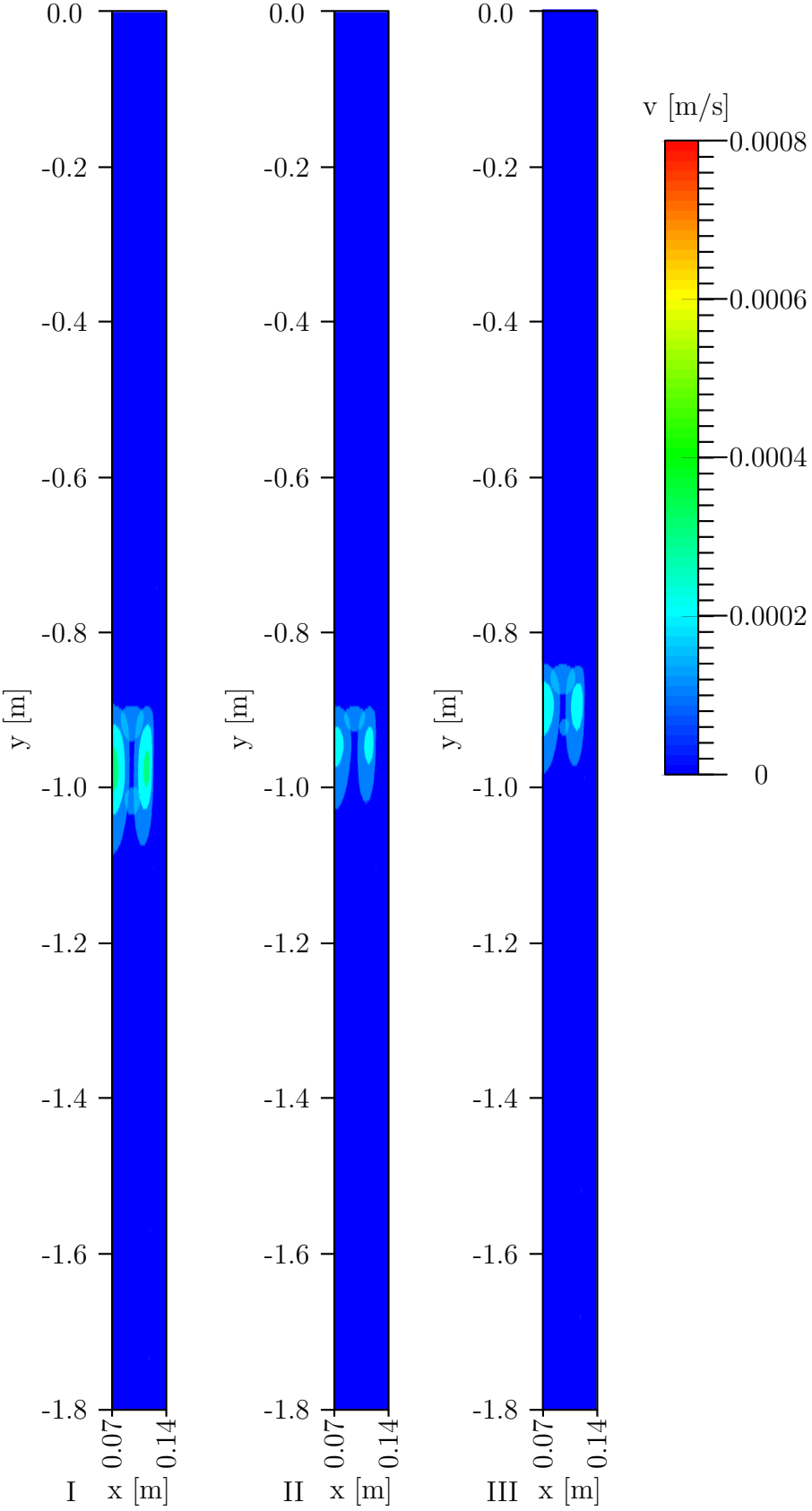

Figure 6.56: Velocity field $(\mathbf{v}(\mathbf{B}) - \mathbf{v}(\mathbf{B}_0))$ as a function of magnetic field range. I: -0.8 m $< l_{EM} < -1.0$ m. II: -0.8 m $< l_{EM} < -0.95$ m. III: -0.8 m $< l_{mEM} < -0.85$ m.

6.7.2 B: Coil Magnetic Field - Temperature, Velocity

The second numerical example B tackles a magnetic field that is calculated from the coil model described in the previous section (Sect. 6.4) by using the parameters described in Tab. 6.2.

First, a comparison between the case without the magnetic field and the default magnetic field configuration ($I = 50$ A, $N_N = 25$, $N_M = 11$ and $a_d = 0.05$ m) is made. Next, the parametric study is performed for the following parameters: the electric current, the span, and the number of windings in x and y direction. The results are presented on vertical and horizontal cross-sections. The position of certain cross-section is chosen in such a way that it represents the profile that is the most interesting.

Comparison between Configuration with and without Magnetic Field

To better understand the influence of the magnetic field on the velocity and temperature fields in the continuous casting process of steel the vertical and horizontal cross-sections and the contour plot of the realistic magnetic field of the default coil configuration are presented in Figs. 6.57 and 6.58.

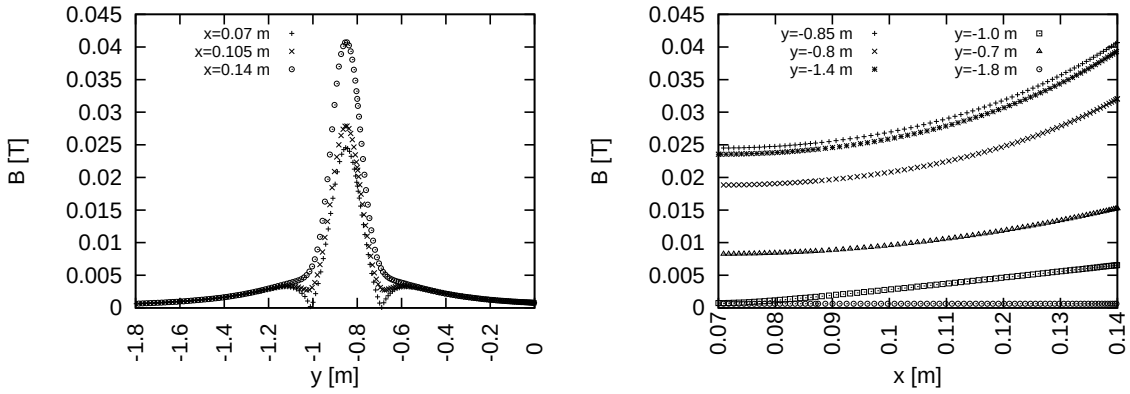

Figure 6.57: Left: the vertical cross-sections of the coil magnetic field. Right: the horizontal cross-sections of the coil magnetic field.

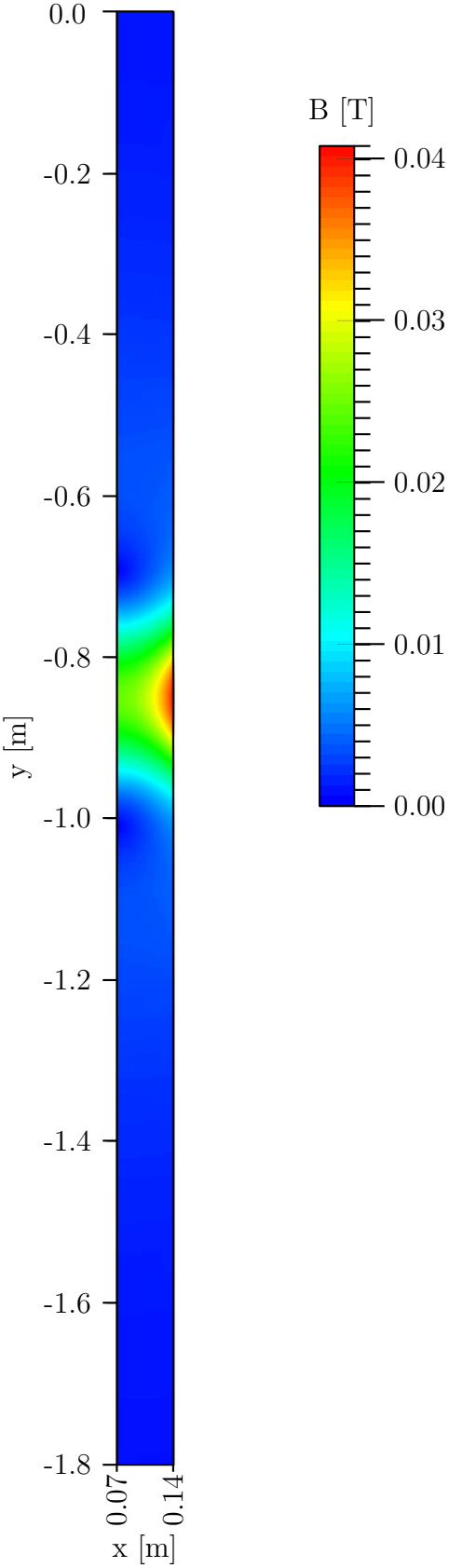

Figure 6.58: Magnetic field of the default coil configuration.

Temperature profile at the vertical and horizontal cross-sections is depicted in Fig. 6.59. The temperature profiles are depicted at the vertical cross-sections 0.07 m, 0.125 m and 0.14 m and at the horizontal cross-sections −0.8 m, −0.9 m and −1.8 m with and without the presence of the magnetic field. The trend of the temperature profiles is similar for both examples, however, the temperature magnitudes are slightly lower in the example with the magnetic field.

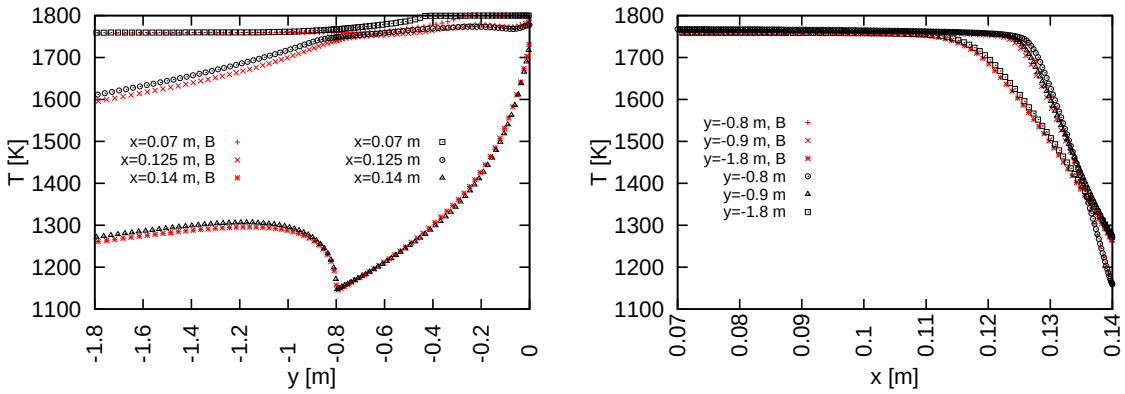

Figure 6.59: Temperature fields. Left: vertical cross-sections. Right: horizontal cross-sections.

The velocity magnitude profiles are presented for several vertical (0.07 m, 0.125 m and 0.14 m) and horizontal (−0.8 m, −0.9 m and −1.8 m) cross-sections. The comparisons can be seen in Fig. 6.60. The results confirm that the velocity magnitude is diminished in the presence of the magnetic field. The segregation width is approximately the same in both cases.

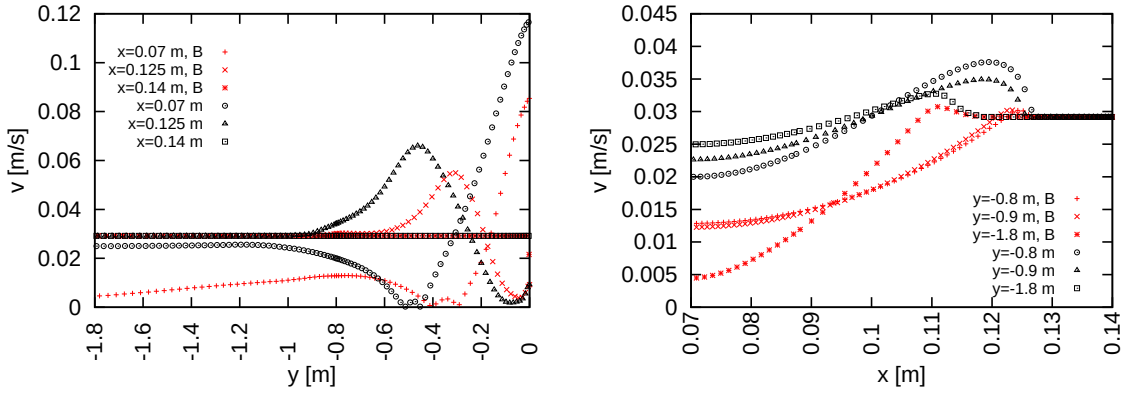

Figure 6.60: Velocity fields. Left: vertical cross-sections. Right: horizontal cross-sections.

The liquid fraction for the horizontal and vertical cross-sections is depicted in Fig. 6.61. It confirms the assumption that the magnetic field influences solidification.

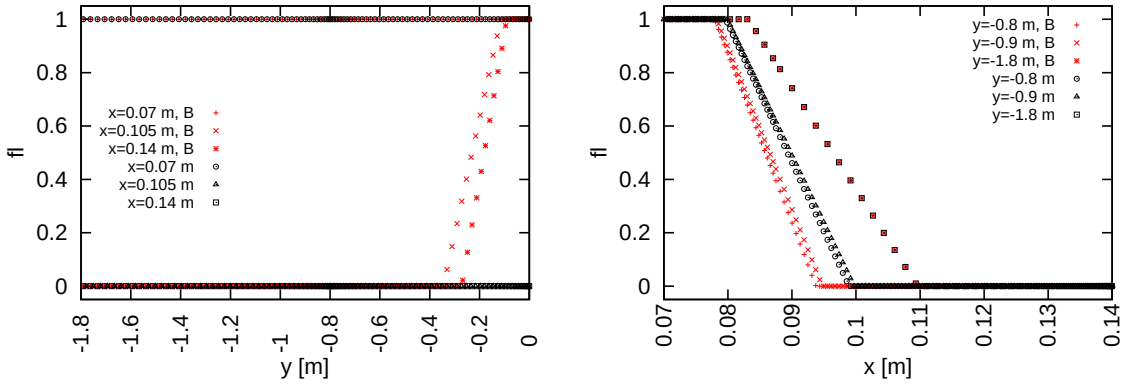

Figure 6.61: Liquid fraction. Left: horizontal cross-sections. Right: vertical cross-sections.

A comparison of the temperature and the velocity fields contour plots for examples with and without magnetic field is shown in Figs. 6.62 and 6.63.

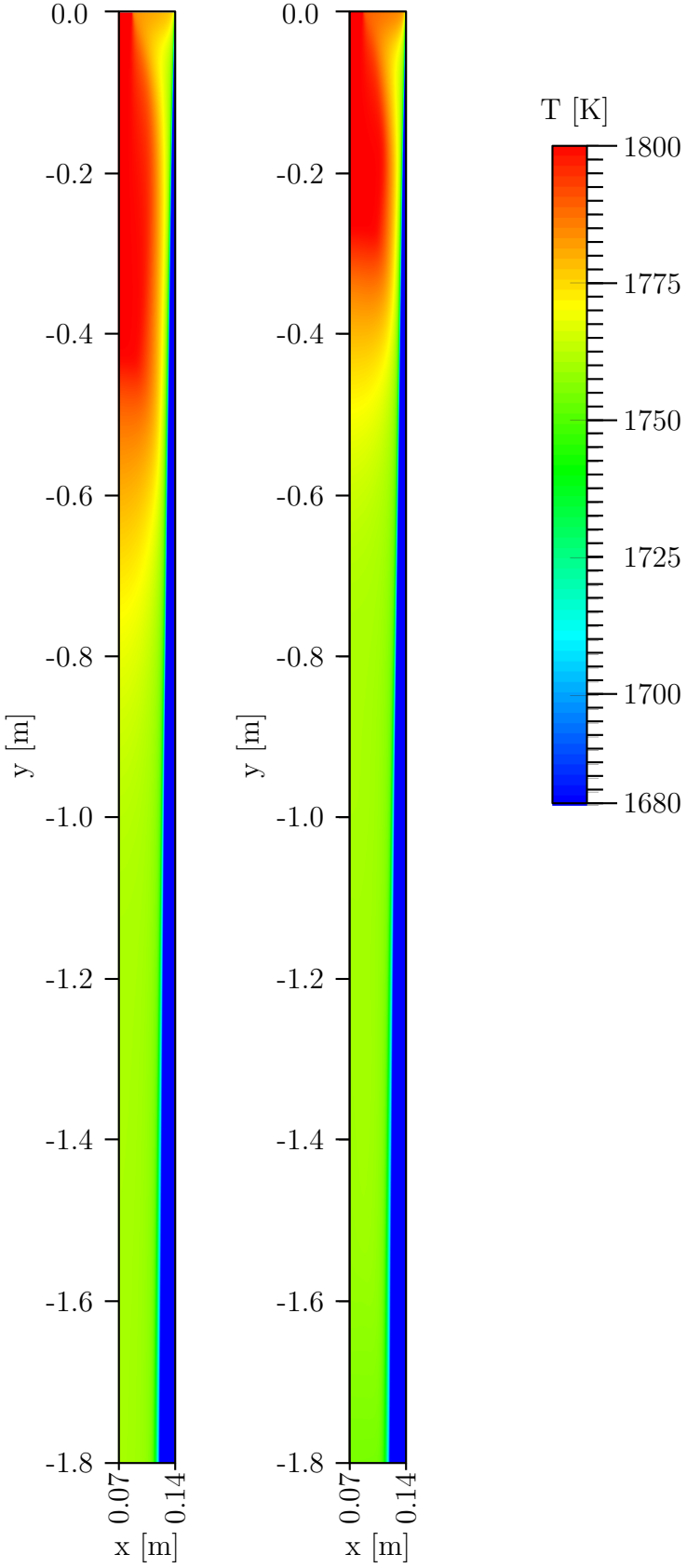

Figure 6.62: Temperature fields. Left: without magnetic field. Right: with magnetic field.

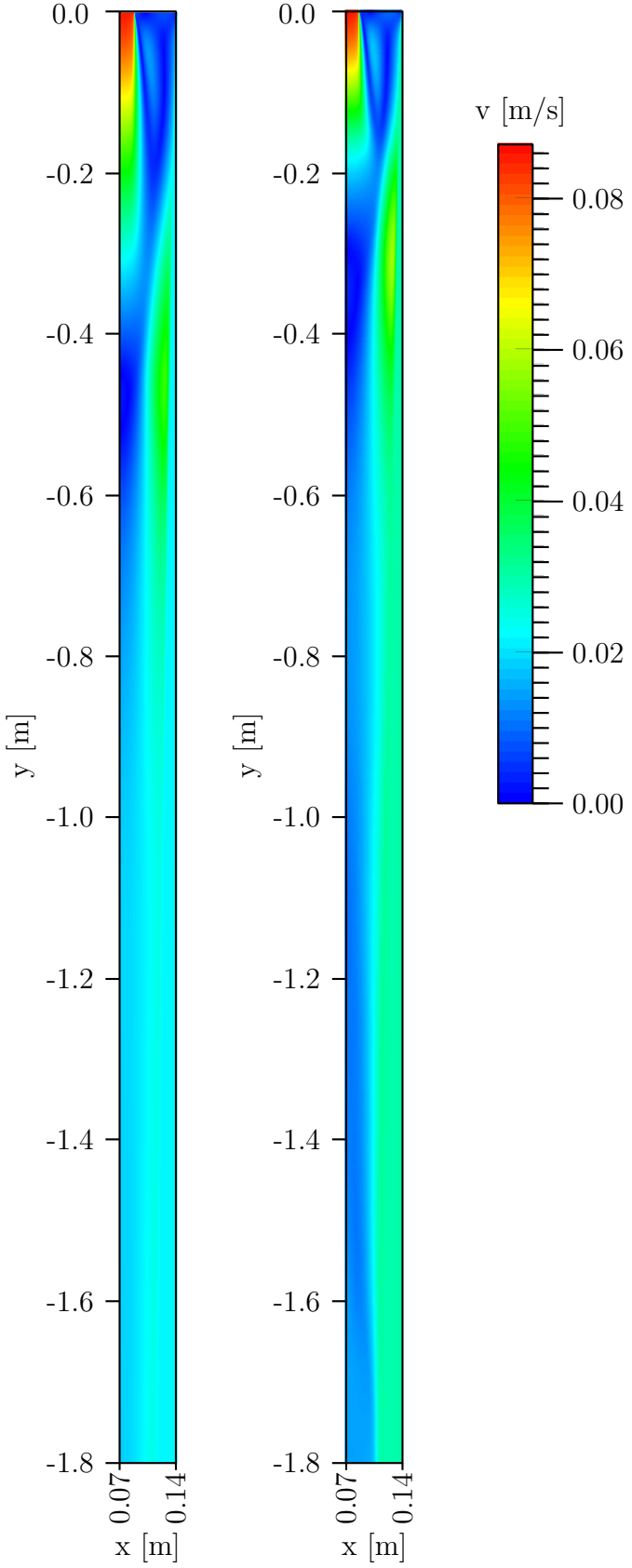

Figure 6.63: Velocity fields. Left: without magnetic field. Right: with magnetic field.

The Influence of a_d

The magnitude of the magnetic field in the strand depends on the distance between the coils and the edge of the strand a_d. To investigate how the span affects the velocity and the temperature fields, the fields were calculated for three different span distances: 0.0 m, 0.05 m and 0.075 m. First, the magnetic field for all three examples is calculated. As expected, the magnetic field in the strand is the strongest for the shortest span distance and the weakest for the longest span distance. The change in the magnetic field magnitude due to the change in the span distance is shown in Fig. 6.64.

Next, the temperature profiles are compared for different vertical and horizontal cross-sections. Due to their similarity, the horizontal cross-sections for temperature field were taken only at -0.9 m and -1.8 m. As can be seen in Fig. 6.65, the effect of the span change is not significant. The vertical cross-section of the temperature fields are shown in Fig. 6.66. The effect of the span distance on the temperature magnitude at the edge of the strand is negligible (Fig. 6.66 right). On the other hand, by reducing the span, the temperature magnitude in the center of the strand changes. As apparent from the results depicted at the left side in Fig. 6.66, the temperature falls at higher vertical positions for shorter spans. As the magnetic field in the strand is stronger when the coils are placed closer to the strand, the effect of the magnetic field is also stronger thus causing the temperature to fall at higher vertical positions. This effect is clearly apparent in the contour plots depicted in Fig. 6.67, where the zone with the highest temperature is diminished for the increased span distance.

The velocity magnitude profiles are depicted for four vertical cross-sections: -0.4 m, -0.8 m, -0.9 m and -1.8 m. As apparent in Fig. 6.68, the decrease in the span distance decreases the velocity in all of the examples. This is to be expected, because the shorter span distance produces the strongest magnetic field, which in turn causes the highest decrease of the velocity magnitude. The velocity profiles in the horizontal cross-section at 0.07 m (Fig. 6.69 left) are shifted to slightly lower vertical positions as the span is increased. Again, this is the expected behaviour due to the effect of the magnetic field magnitude. The velocity profiles at the cross-section at 0.14 m (Fig. 6.69 right) coincide. The linear velocity profile in all of the cases confirms, that the velocity of the solidified steel moves in the vertical direction with the speed of casting. The overall velocity magnitude profile is presented in the contour plot in Fig. 6.70 and confirms the above mentioned observations.

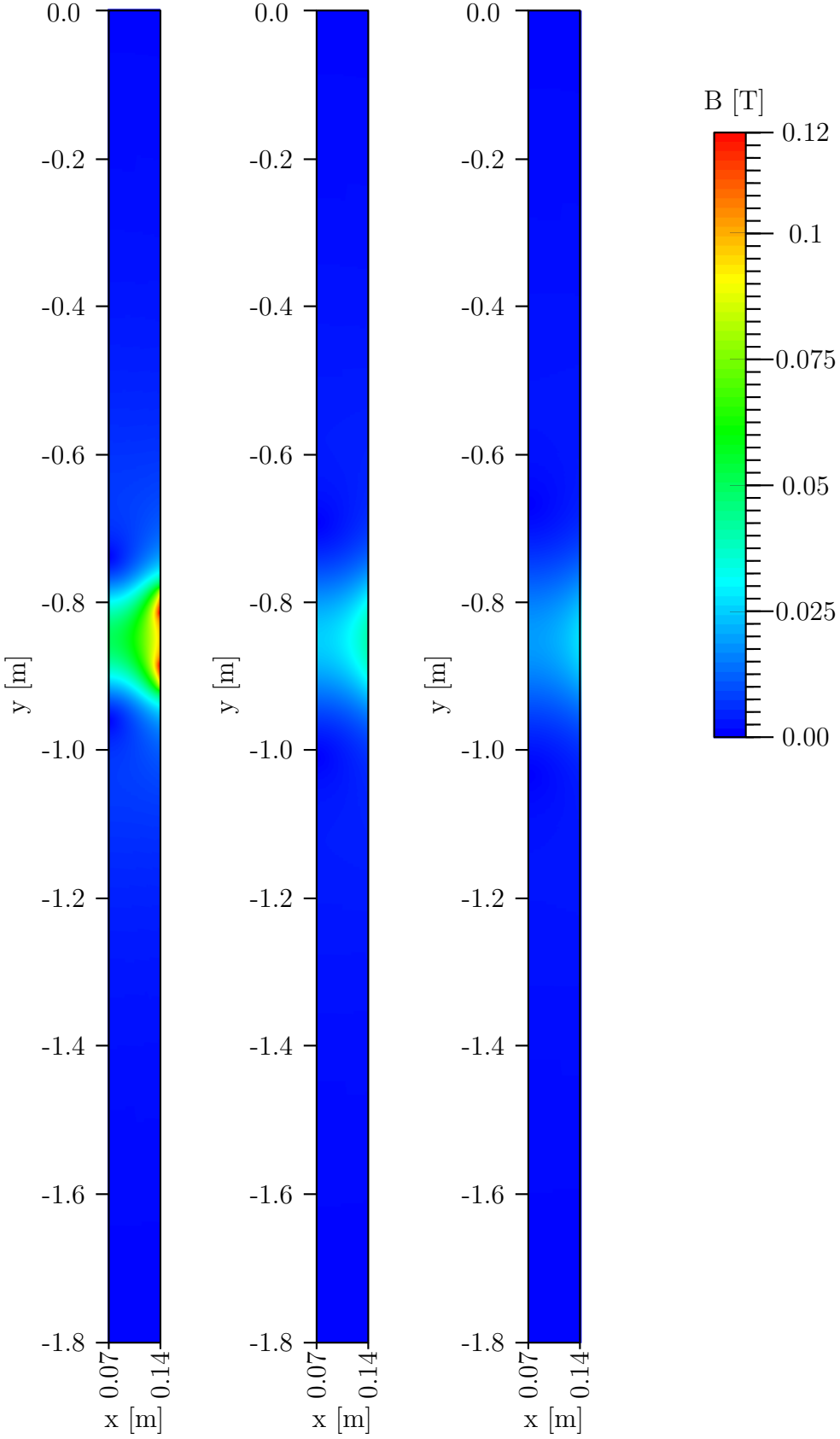

Figure 6.64: Magnetic field as a function of the span distance a_d. Left: $a_d = 0.00$ m. Middle: $a_d = 0.05$ m. Right: $a_d = 0.075$ m.

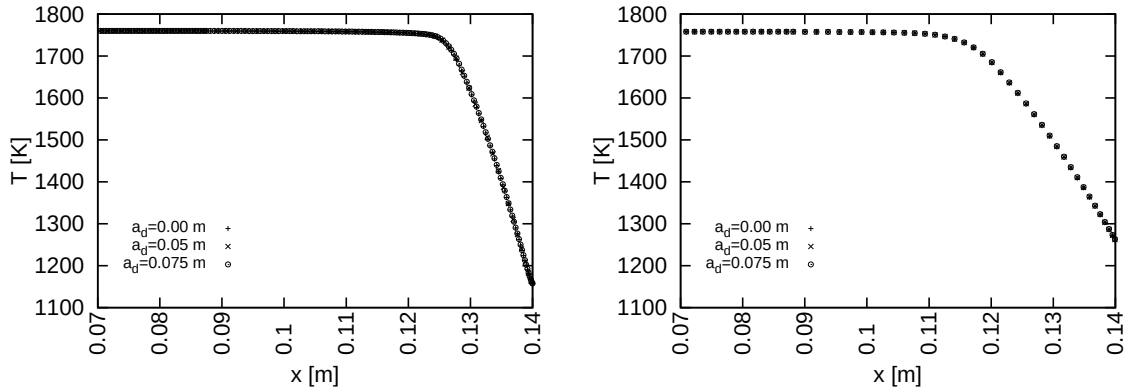

Figure 6.65: Temperature profiles. Left: -0.8. Right: -1.8 m.

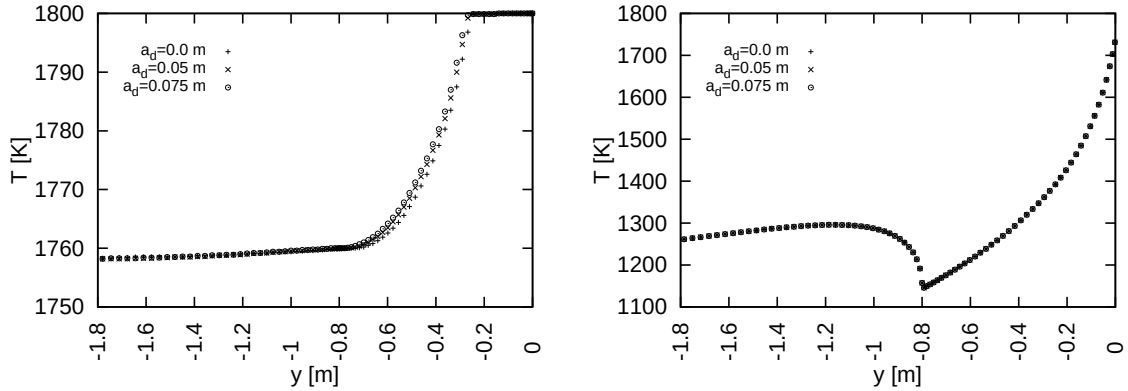

Figure 6.66: Temperature profiles. Left: $x = 0.07$ m. Right: $x = 0.14$ m.

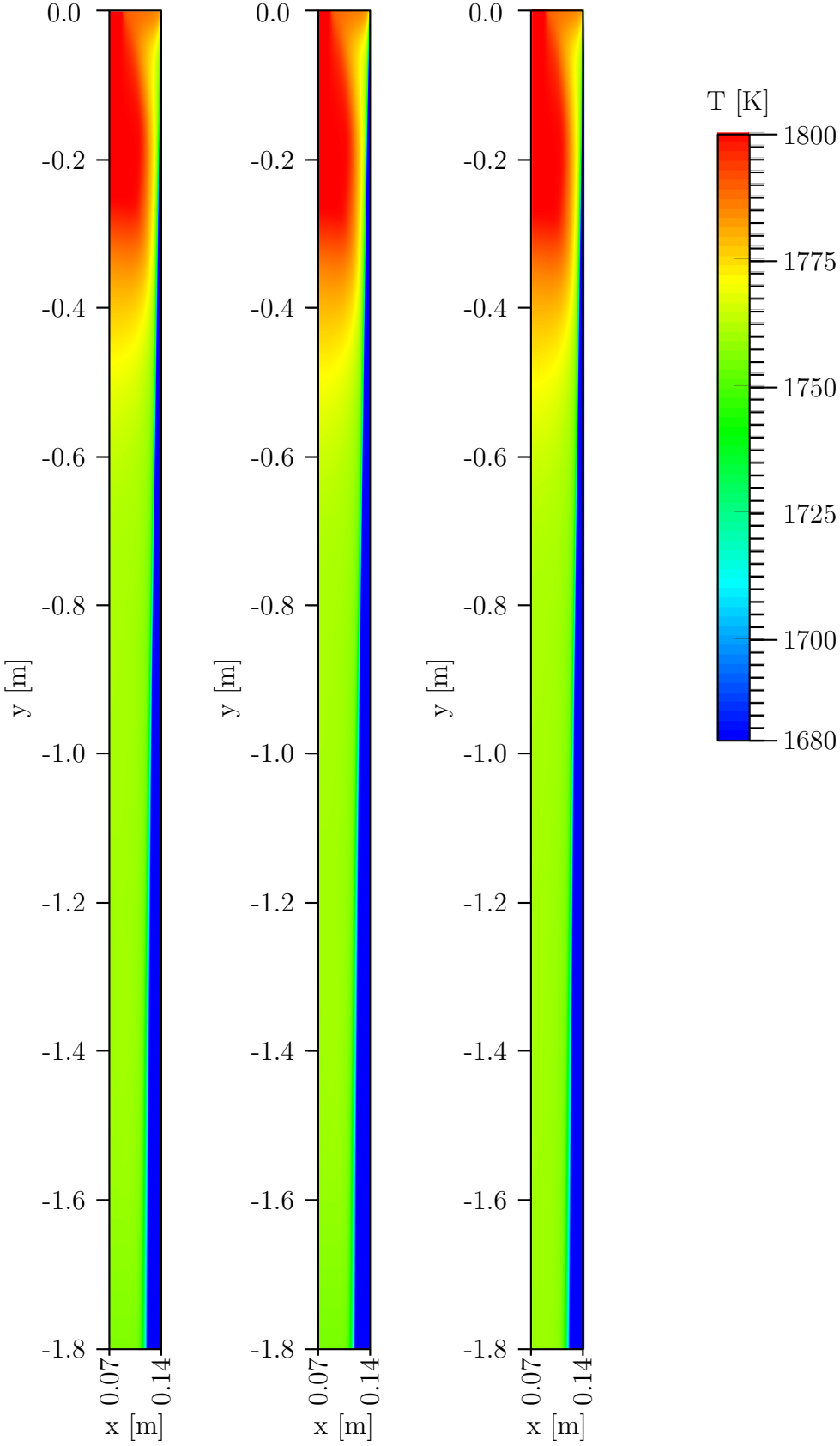

Figure 6.67: Temperature field as a function of a_d. Left: $a_d = 0.00$ m. Middle: $a_d = 0.05$ m. Right: $a_d = 0.075$ m.

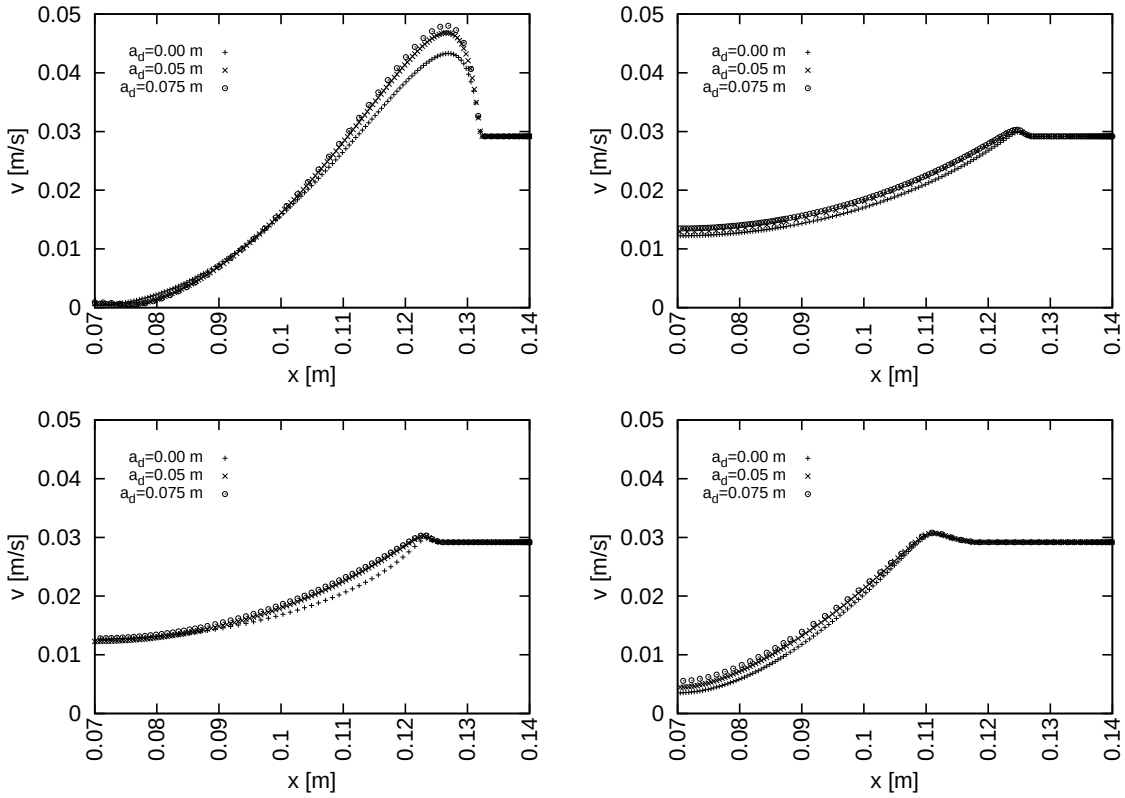

Figure 6.68: Velocity profiles at $y = -0.4$ m, -0.8 m, -0.9 m, and -1.8 m.

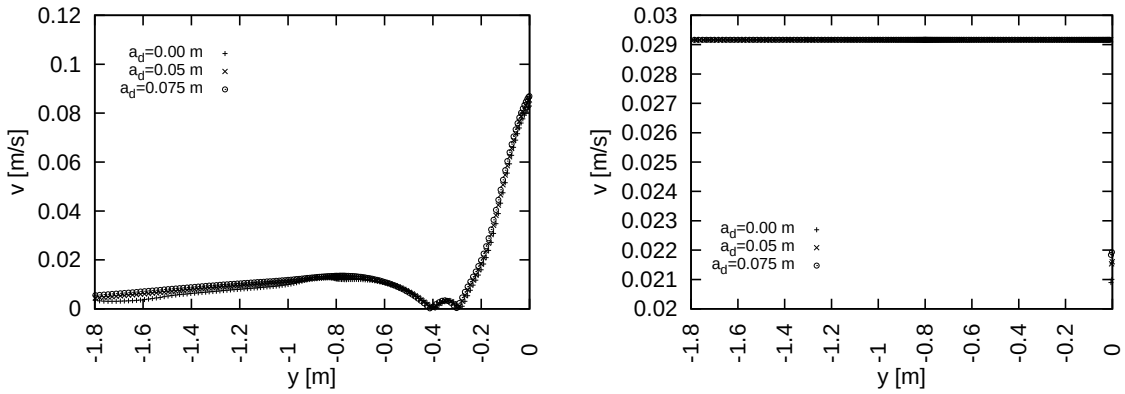

Figure 6.69: Velocity profiles at $x = 0.07$ m and 0.14 m.

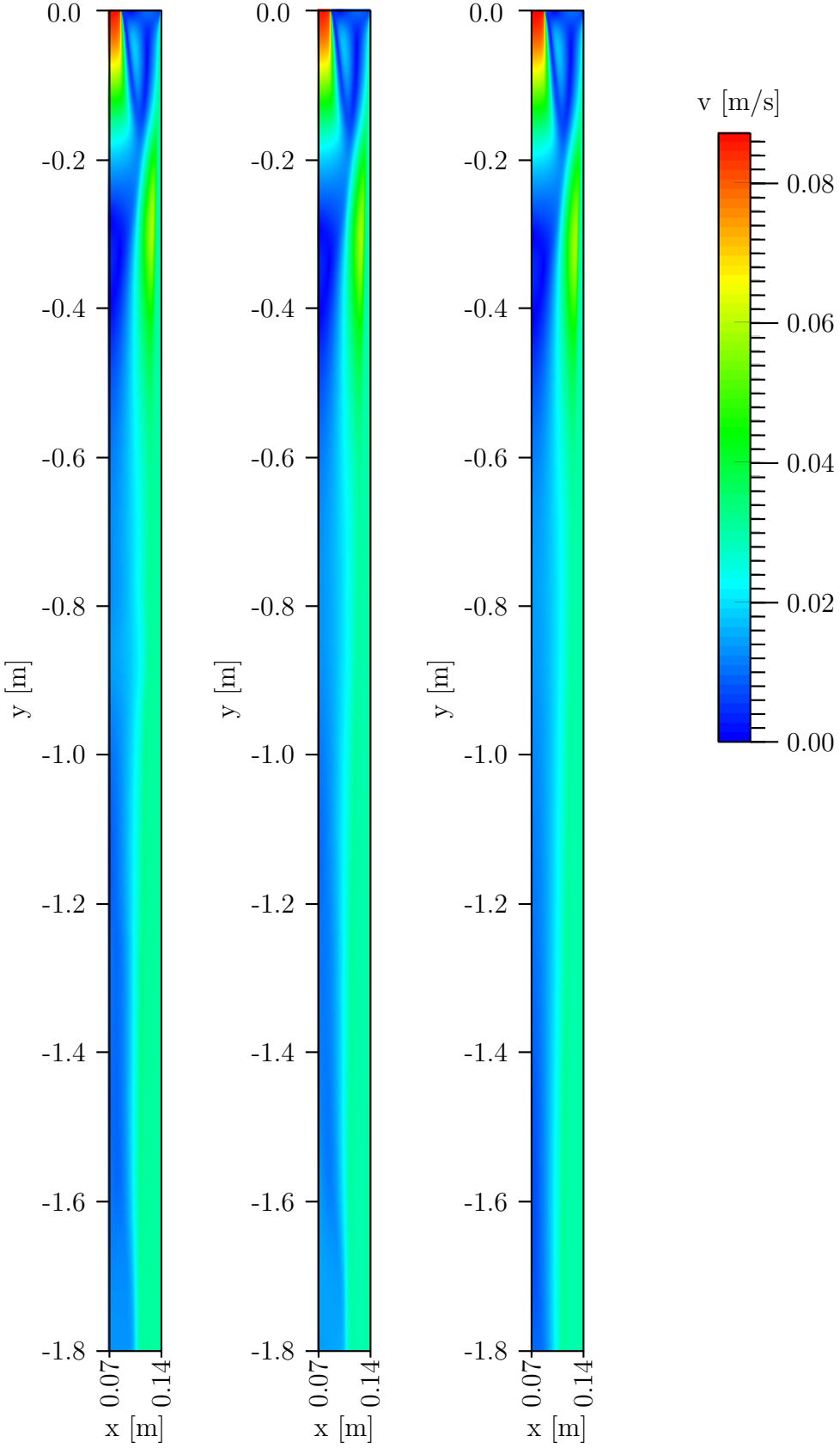

Figure 6.70: Velocity field as a function of a_d. Left: $a_d = 0.00$ m. Middle: $a_d = 0.05$ m. Right: $a_d = 0.075$ m.

The Influence of the Electric Current

The behaviour of temperature and velocity fields is investigated for several different electric current magnitudes. The range of the electric current varies from 12.5 A to 50 A. First, the magnetic field is presented as a function of the electric current. The related contour plots are depicted in Fig. 6.71. The magnetic field is directly proportional to the electric current. This means that by increasing the electric current, the magnitude of the magnetic field is increased. The contour plots depicted in Fig. 6.71 reflect this behaviour.

The temperature field profiles at vertical cross-sections at position −0.4 m, −0.8 m, −0.9 m and −1.8 m have similar profiles. The temperature magnitude is slightly lower for the example with the highest electric current (50 A). The difference, however, is very small. The vertical cross-sections are depicted in Fig. 6.72. The horizontal cross-sections were taken at the center of the strand (0.07 m) and at its edge (0.14 m). The effect of the electrical current, and consequently the changes in the magnetic field, are clearly visible at the left side in Fig. 6.73. It is again observed that the temperature drops at higher vertical positions if the magnetic field is stronger. As already explained in the case of the span distance, the higher vertical positions of the temperature drop are due to the stronger magnetic field, the range of which is much broader then the range of the weaker magnetic fields. In the right graph in Fig. 6.76 the temperature profiles are nearly the same. However, at closer inspection it can be seen, that the temperature magnitude is sightly smaller for the largest electric current. The contour plots in Fig. 6.74 confirm these observations.

Next, the velocity profiles are examined for vertical and horizontal cross-sections. The vertical velocity profile cross-sections are drawn at −0.4 m, −0.8 m, −0.9 m and −1.8 m and are presented in Fig. 6.75. Comparable to the example with different span distances, the velocity profiles for different values of the electrical current are diminished as the magnetic field increases. The same is apparent at the left side in Fig. 6.76, where the horizontal cross-sections at 0.07 m are drawn. The velocity profiles at the horizontal cross-section at 0.14 m (Fig. 6.76 right) are linear and have the same value, which is due to the fact, that the solidified material moves with the casting velocity. The contour plots of the velocity profiles as a function of electrical current are depicted in Fig. 6.77.

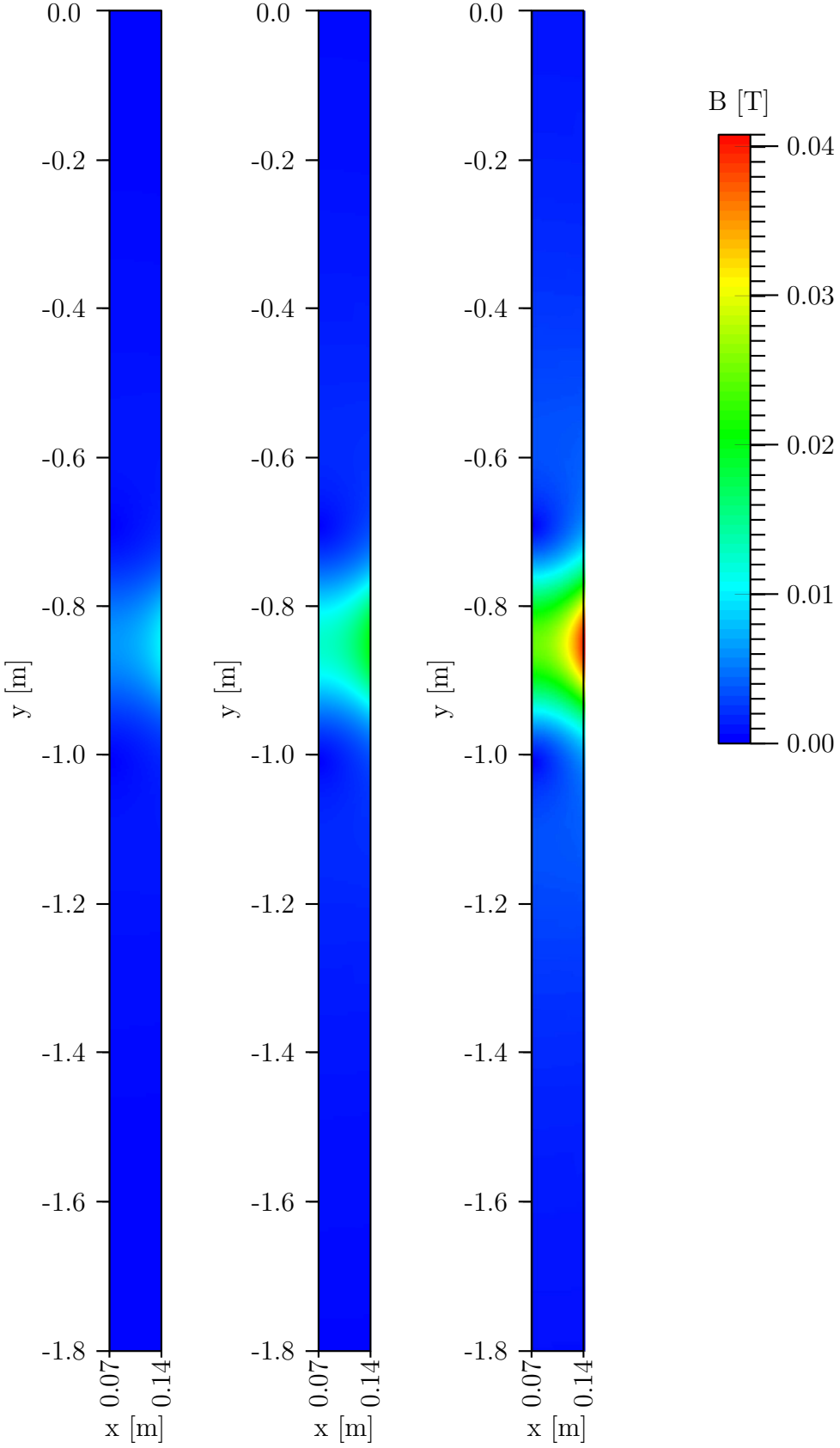

Figure 6.71: Magnetic field as a function of electric current. Left: $I = 12.5$ A. Middle: $I = 25.0$ A. Right: $I = 50.0$ A.

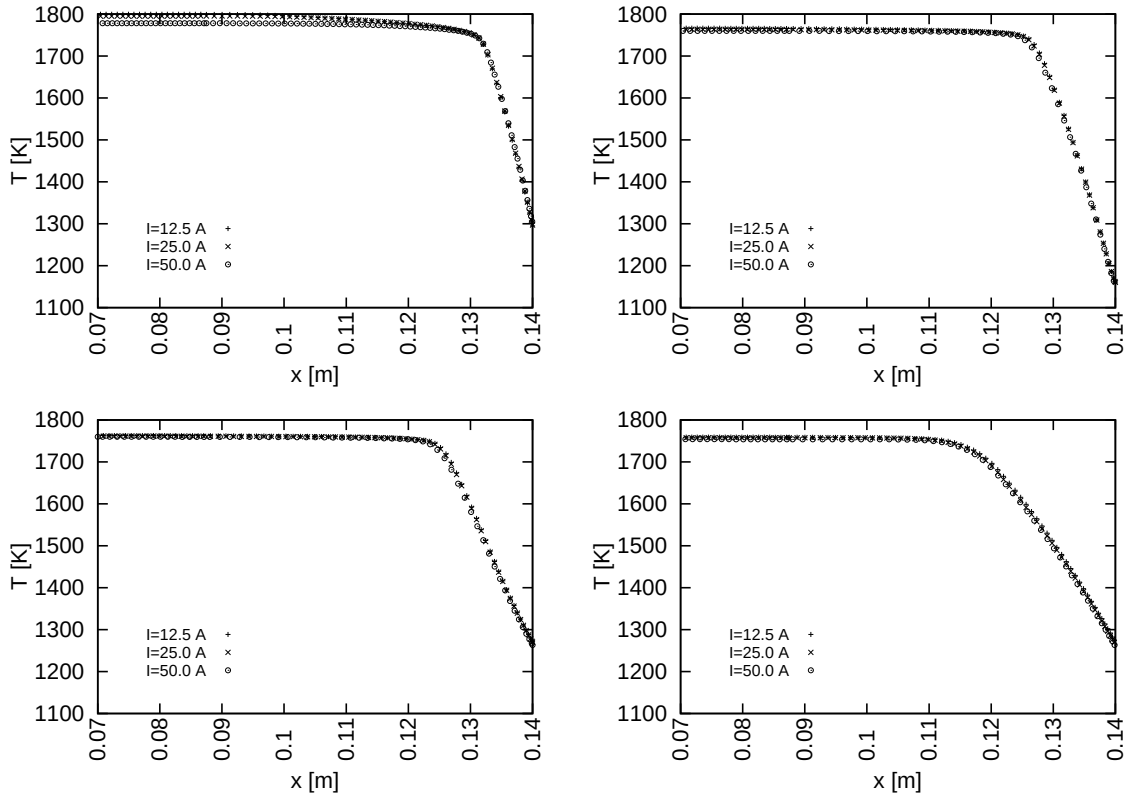

Figure 6.72: Temperature profiles. Top left: -0.4 m. Top right: -0.8 m. Bottom left: -0.9 m. Bottom right: -1.8 m.

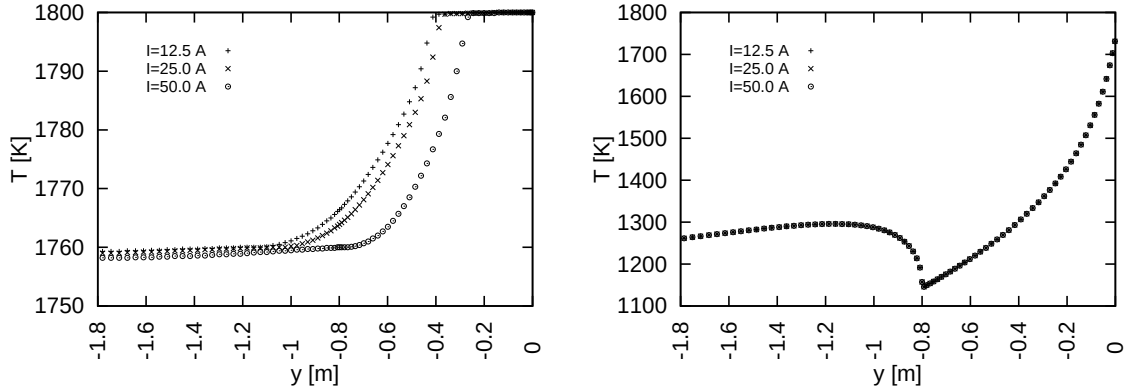

Figure 6.73: Temperature profiles. Left: $x = 0.07$ m. Right: $x = 0.14$ m.

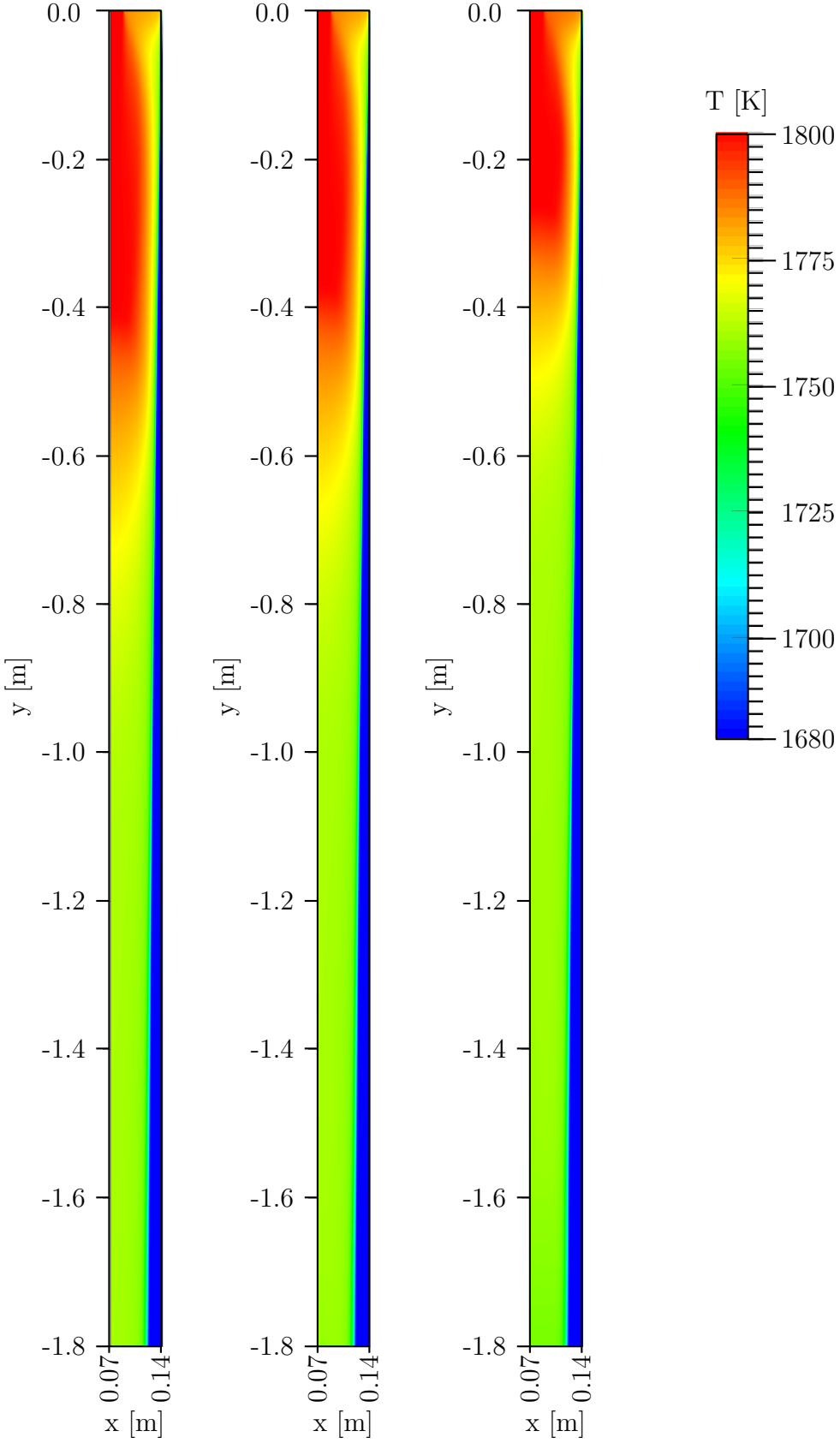

Figure 6.74: Temperature field electric current. Left: $I = 12.5$ A. Middle: $I = 25.0$ A. Right: $I = 50.0$ A.

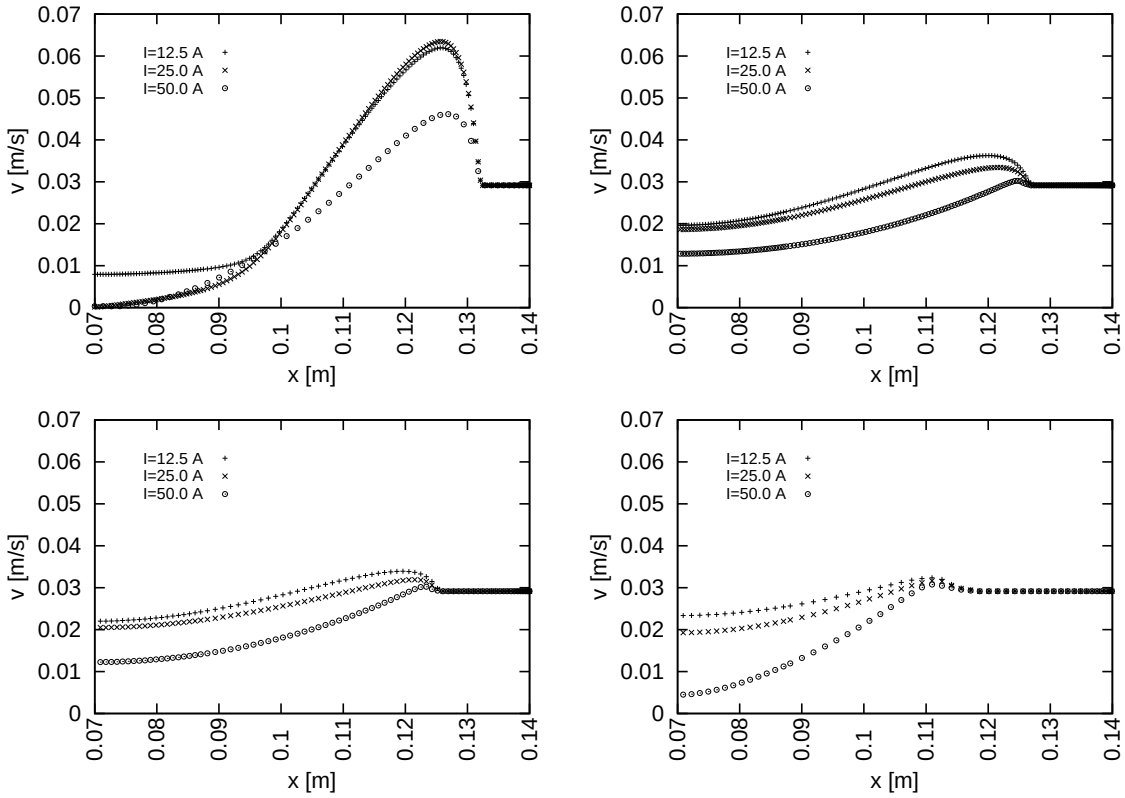

Figure 6.75: Velocity profiles. Top left: −0.4 m. Top right: −0.8 m. Bottom left: −0.9 m. Bottom right: −1.8 m.

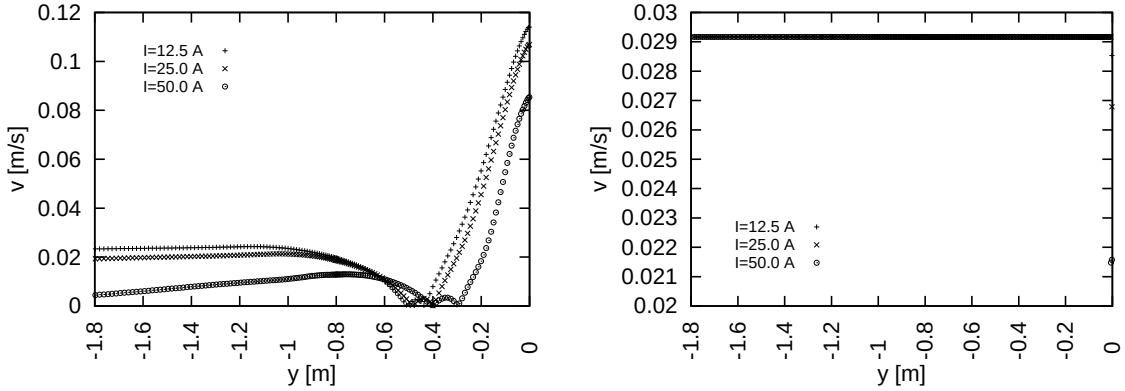

Figure 6.76: Velocity profiles. Left: $x = 0.07$ m. Right: $x = 0.14$ m.

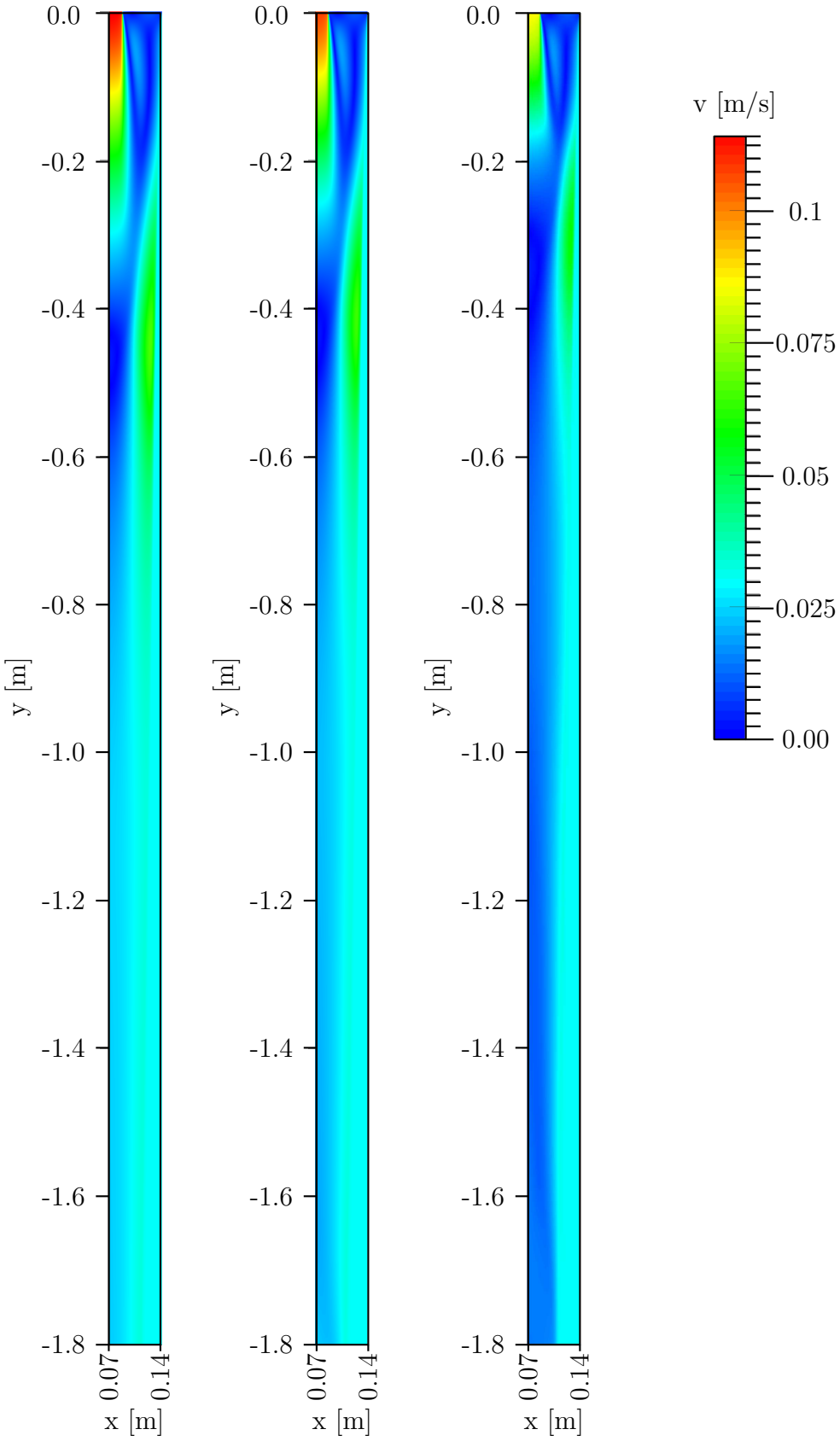

Figure 6.77: Velocity field as a function of electric current. Left: $I = 12.5$ A. Middle: $I = 25.0$ A. Right: $I = 50.0$ A.

The Influence of N_N

Apart from the electrical current and span distance, the magnetic field also depends on the number of windings. The number of the windings can change in x (N_N) as well as in y (N_M) direction. In this subsection, the influence of the number of windings in x direction is explored. For this purpose, three different examples with 20, 25 and 30 windings are considered.

By considering Eq. 6.16 for the magnetic field, it is clear that by increasing the number of windings, the magnetic field is increased. This is confirmed in the contour plots of the magnetic fields as functions of the number of windings, which are presented in Fig.6.78. An example with the largest number of windings (30) has the strongest magnetic field.

The temperature profiles are depicted in the horizontal and vertical direction. The temperature profiles in horizontal direction do not change much when the number of windings is increased. The temperature difference in the vertical cross-sections (-0.4 m, -0.8 m, -0.9 m and -1.8 m) shown in Fig. 6.79 are not very discernible. The vertical cross-sections (Fig. 6.80 left) of temperature fields show that the temperature of the liquid drops sooner when the magnetic field is stronger, which is when the coils have more windings. As is apparent from Fig. 6.80 the temperature of the solid shell is approximately the same for all three winding arrangements. In Fig. 6.81, the contour plots of temperature fields that are affected by the magnetic fields generated by coils that consist of 20, 25 and 30 windings in x direction are presented. The coil arrangement with 30 windings has the smallest area of high temperature (Fig. 6.81 left) and the coil arrangement with 20 windings has the largest area of high temperature (Fig. 6.80 right). The strongest magnetic field has the highest range and consequently causes the temperature drop at higher vertical positions. Considering this, the above described behaviour is to be expected.

The velocity profiles in Figs. 6.82 and 6.83 confirm that the velocity magnitude is reduced by the strengthening the magnetic field. At the lower vertical profiles (-0.8 m, -0.9 m and -1.8 m) that can be seen in top right, bottom left and bottom right graphs in Fig. 6.82, the profile changes in such a way that the maximum velocity value is notably diminished, the minimum value, however, stays approximately the same and the turning point is moved towards the edge of the strand. This can be explained by taking a closer look at the magnetic field magnitude (Fig. 6.78). A realistic coil configuration produces a magnetic field that is the strongest at its edge. Therefore, the effect of the opposing Lorentz force is much more pronounced at the outer layers of the flow than at its center. The contour plots presented in Fig. 6.84 confirm, that the stronger magnetic field with the larger number of windings slows down the fluid flow.

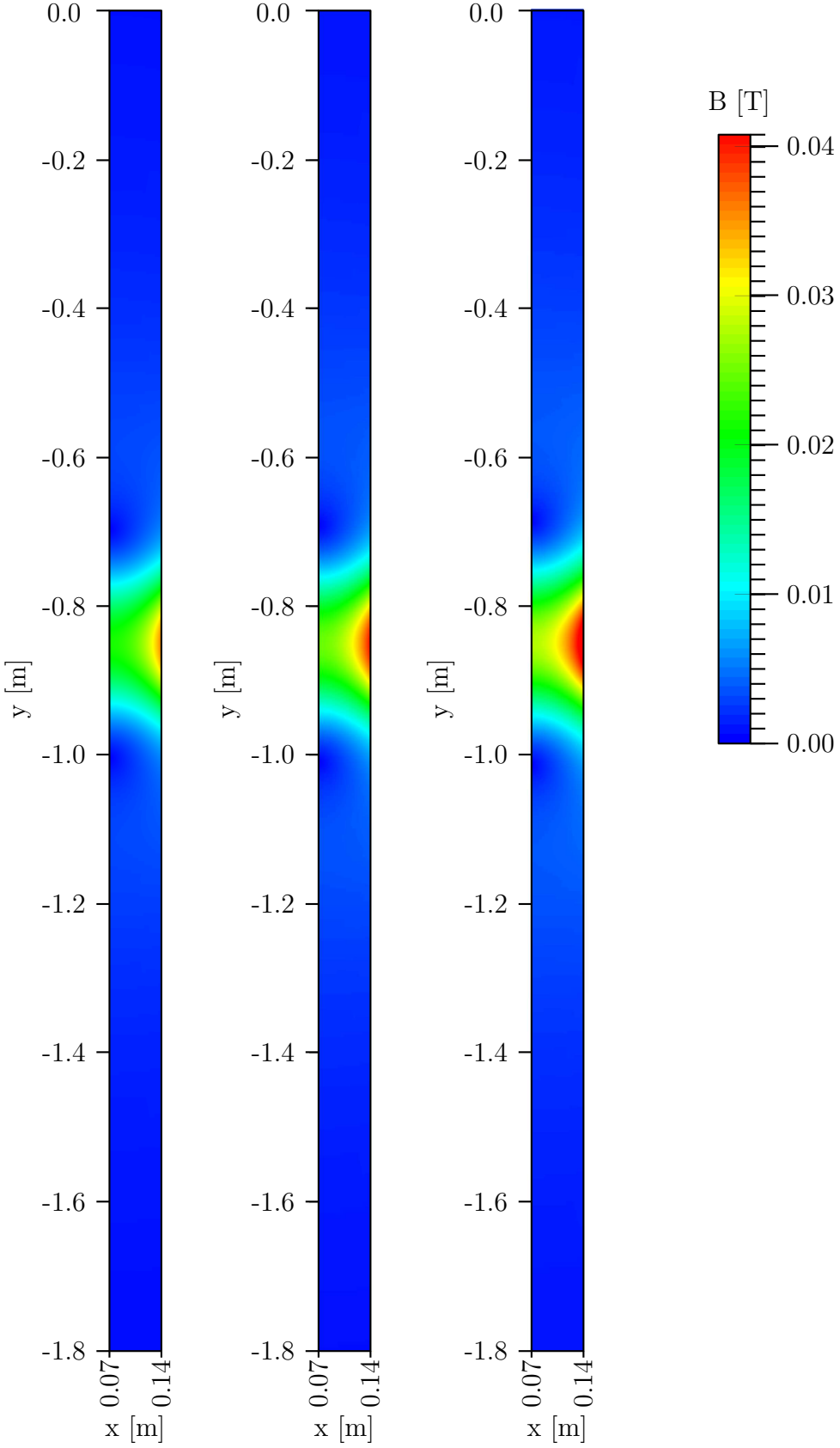

Figure 6.78: Magnetic field as a function of N_N. Left: $N_N = 20$. Middle: $N_N = 25$. Right: $N_N = 30$.

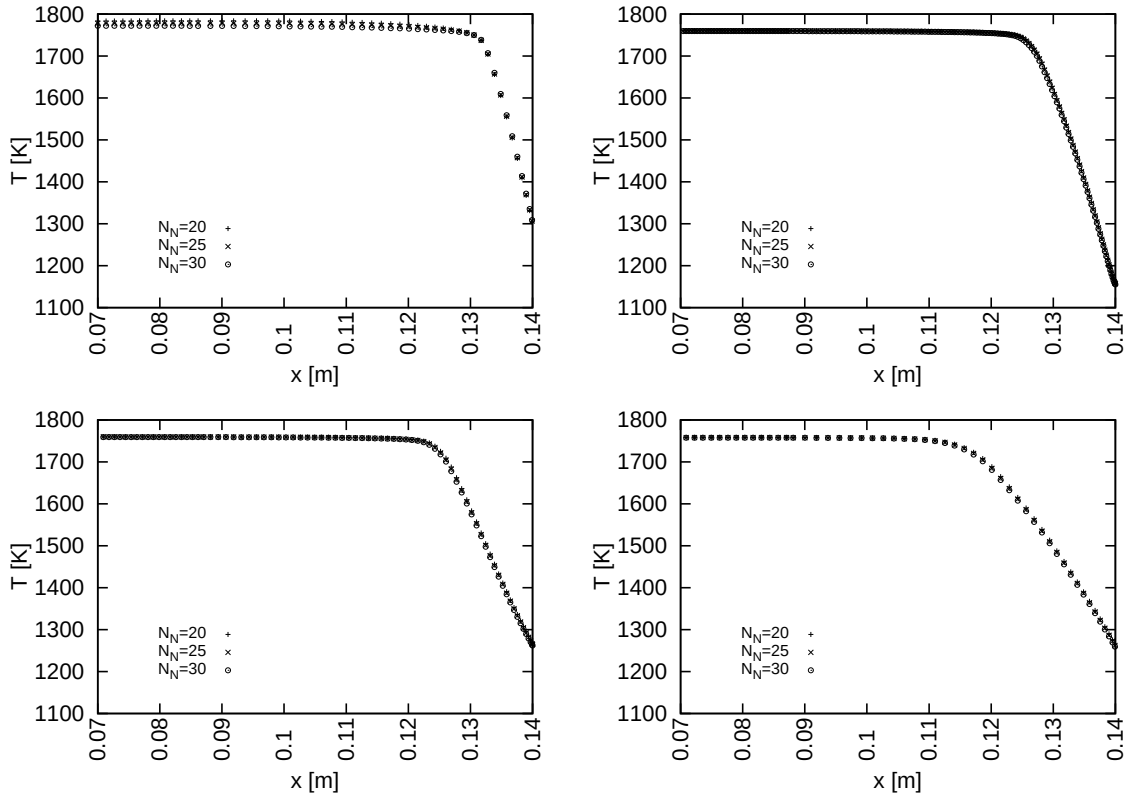

Figure 6.79: Temperature profiles. Top left: -0.4 m. Top right: -0.8 m. Bottom left: -0.9 m. Bottom right: -1.8 m.

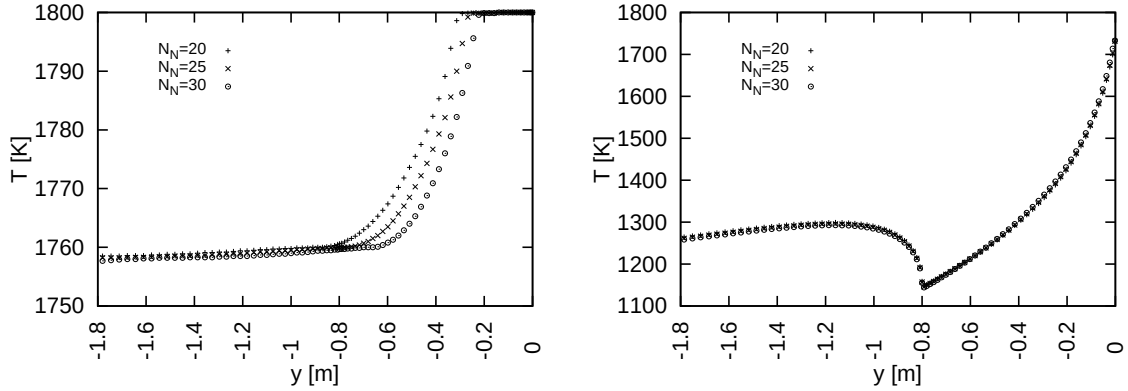

Figure 6.80: Temperature profiles. Left: $x = 0.07$ m. Right: $x = 0.14$ m.

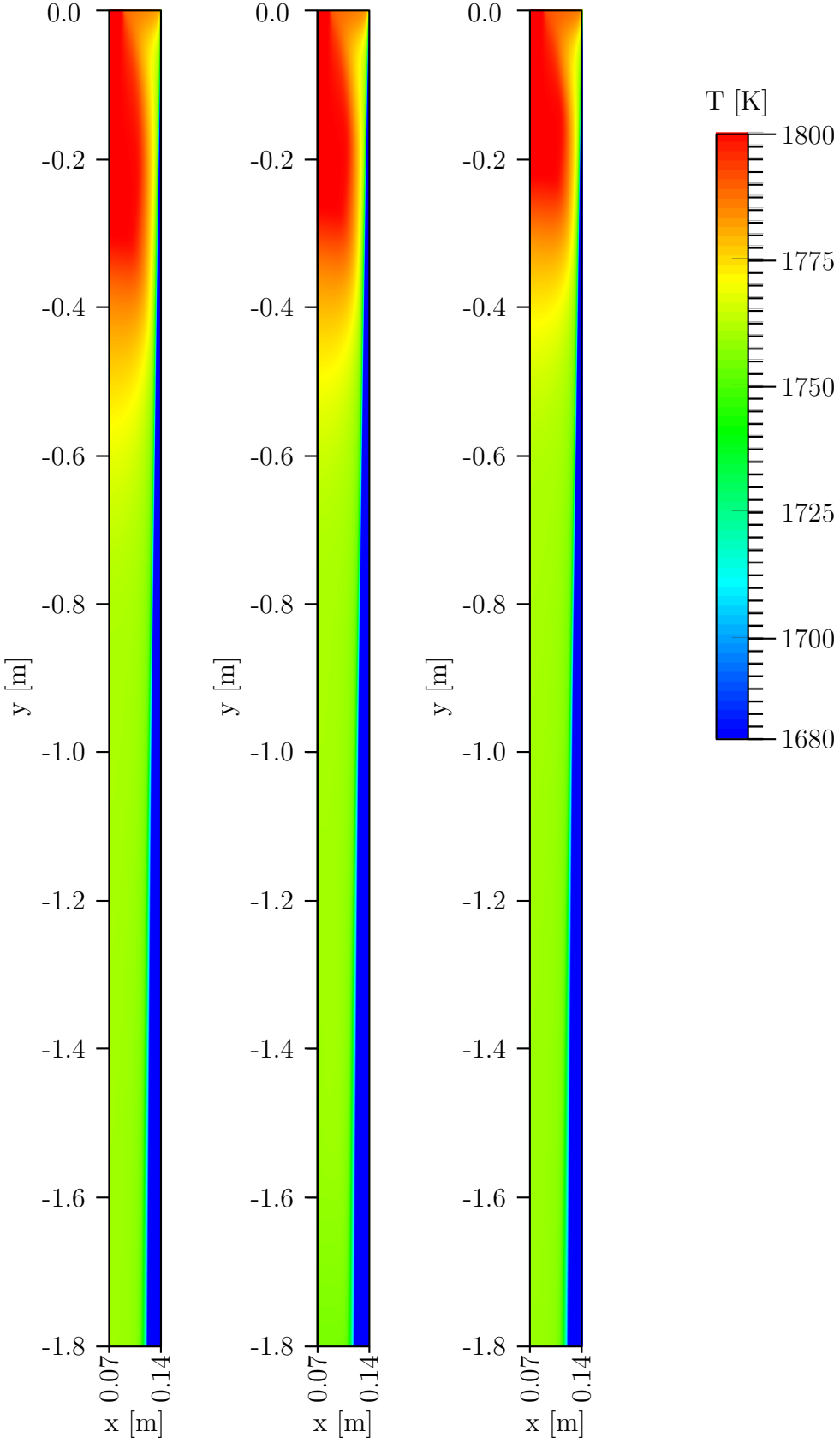

Figure 6.81: Temperature field as a function of N_N. Left: $N_N = 20$. Middle: $N_N = 25$. Right: $N_N = 30$.

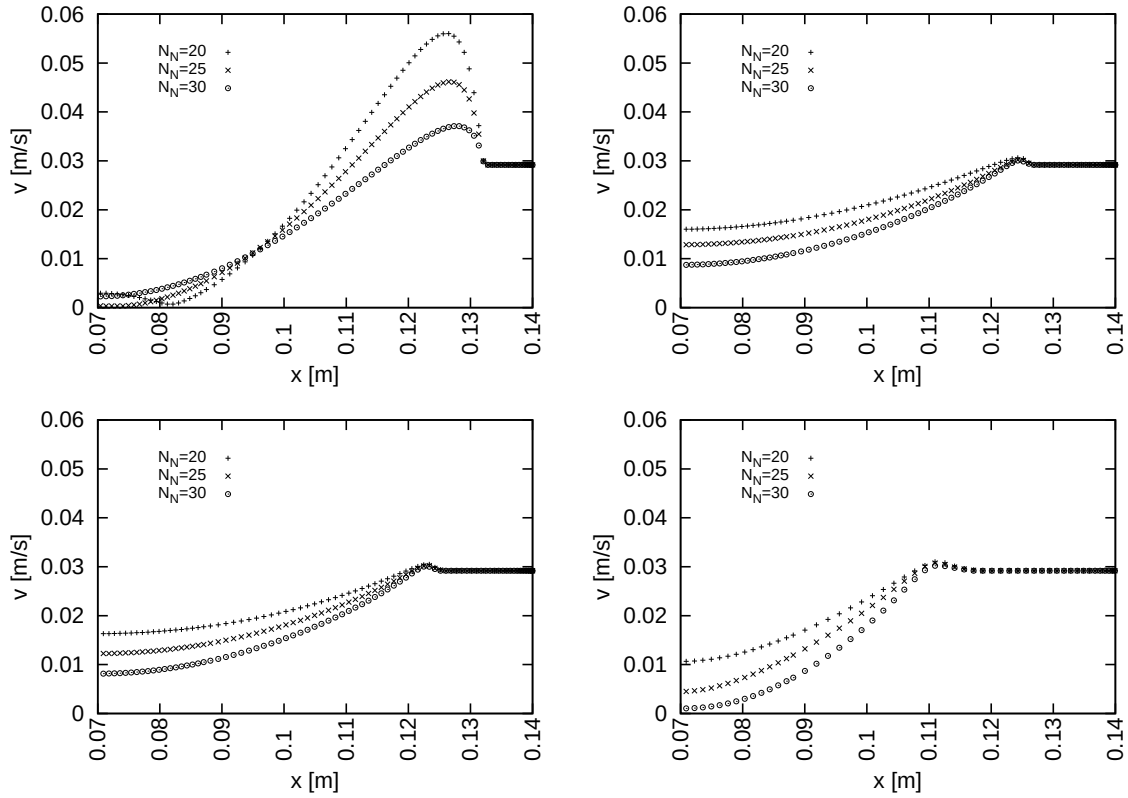

Figure 6.82: Velocity profiles. Top left: -0.4 m. Top right: -0.8 m. Bottom left: -0.9 m. Bottom right: -1.8 m.

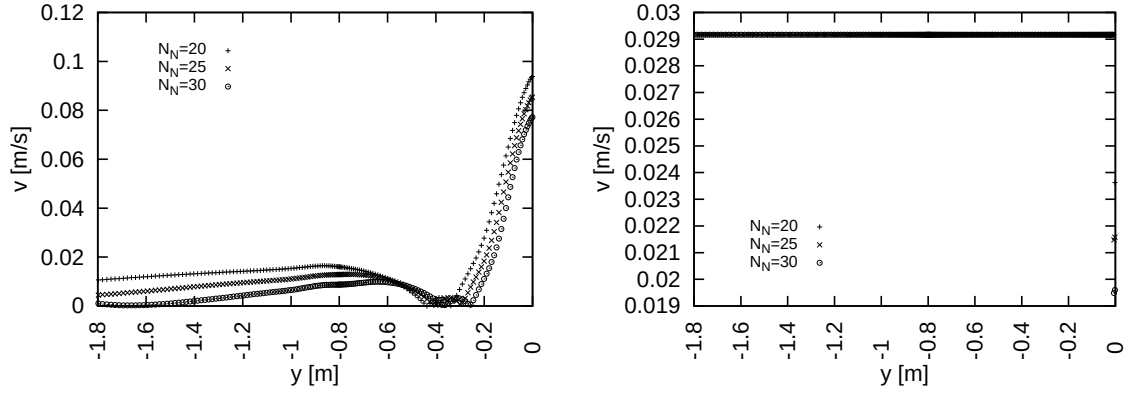

Figure 6.83: Velocity profiles. Left: $x = 0.07$ m. Right: $x = 0.14$ m.

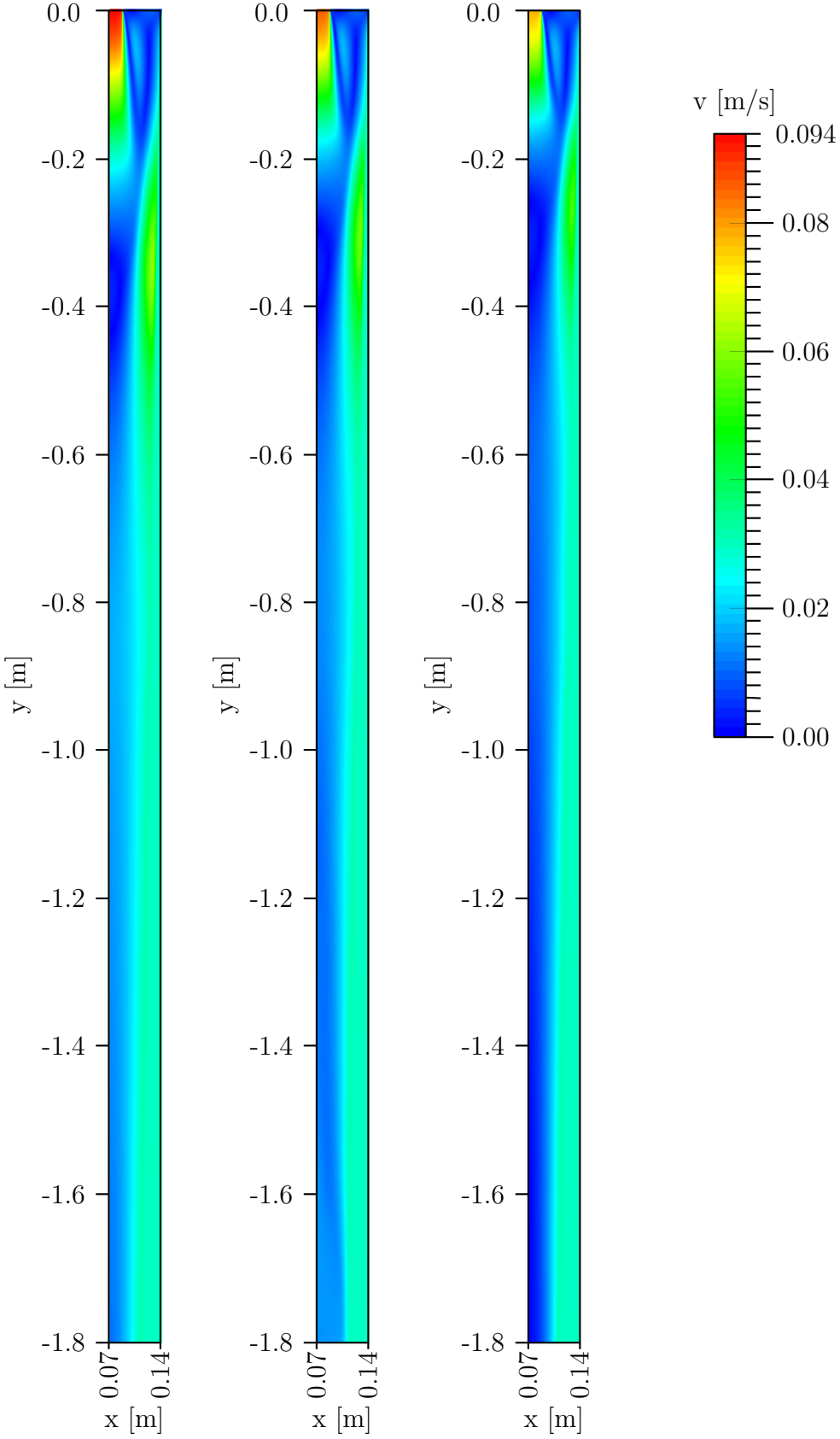

Figure 6.84: Velocity field as a function of N_N. Left: $N_N = 20$. Middle: $N_N = 25$. Right: $N_N = 30$.

The Influence of the N_M

Last but not least, the influence of the number of windings in y direction on the strength of magnetic field and its influence on the temperature and velocity fields is investigated. For each winding in x direction, N_M windings in y direction are added to the coil. The change in magnetic field due to the change in the coil configuration is tested for 9, 10 and 11 windings. In a like manner as in the case of expanding the coils in x direction, the expansion of coils in y direction amplifies the magnetic field. The proof of this can be seen in Fig. 6.85, where the contour plots for $N_M = 9$, 10 and 11 are presented.

The temperature profiles are depicted in Figs. 6.86 and 6.87 for the vertical and horizontal cross-sections respectively. Analogous to the sensitivity study of the number of windings in x direction, the temperature field does not change much. The changes are the most apparent in the vertical cross-section at the center of the strand, where the coil configuration with the largest number of windings (11) exhibits the fastest drop in temperature. Temperature contour plots are depicted in Fig. 6.88 and reconfirm that the largest number of windings produces the largest magnetic field which in turn exhibits the largest effect on the temperature field.

The number of windings in y direction affects the velocity profiles in a similar way as the number of windings in x direction. The velocity profiles for this parametric study are presented in Fig. 6.89 and Fig. 6.90. Again, the statement that the strongest magnetic field slows down the velocity the most is confirmed. This is especially apparent in Fig. 6.89, where the horzontal cross-sections are presented. The values of the velocity magnitudes are much more diminished at the edge of the strand then at the center, as the magnetic field is much stronger at the edge. The change in the velocity magnitudes in the horizontal cross-sections (Fig. 6.90) is not pronounced. However, the profiles still confirm that the increase in the magnetic field causes the velocity to slow down. The velocity of the solidified steel shell moves along with a constant casting velocity for all of the coil arrangements. The velocity contour plots are presented in Fig. 6.91.

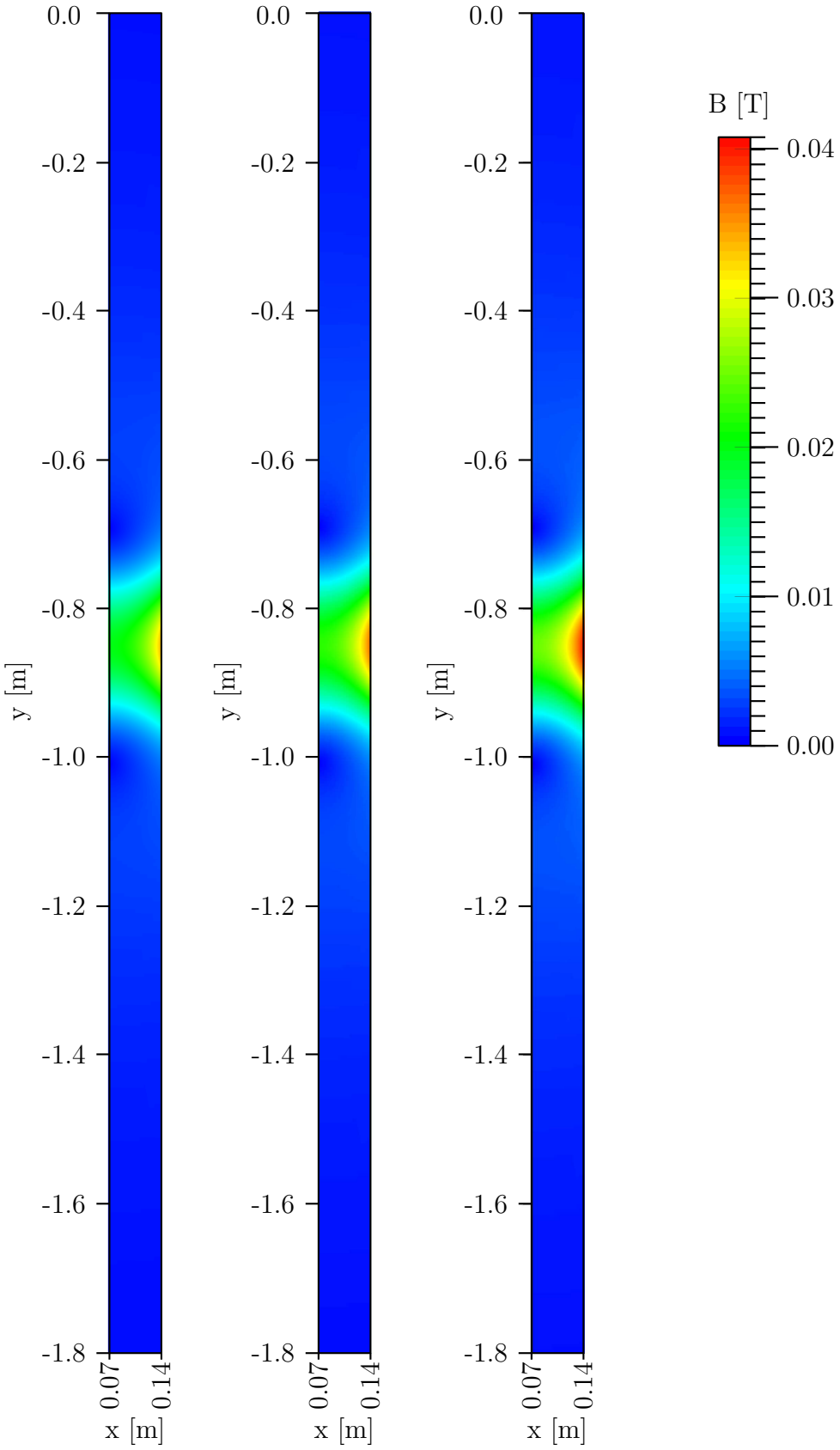

Figure 6.85: Magnetic field as a function of N_M. Left: $N_M = 9$. Middle: $N_M = 10$. Right: $N_M = 11$.

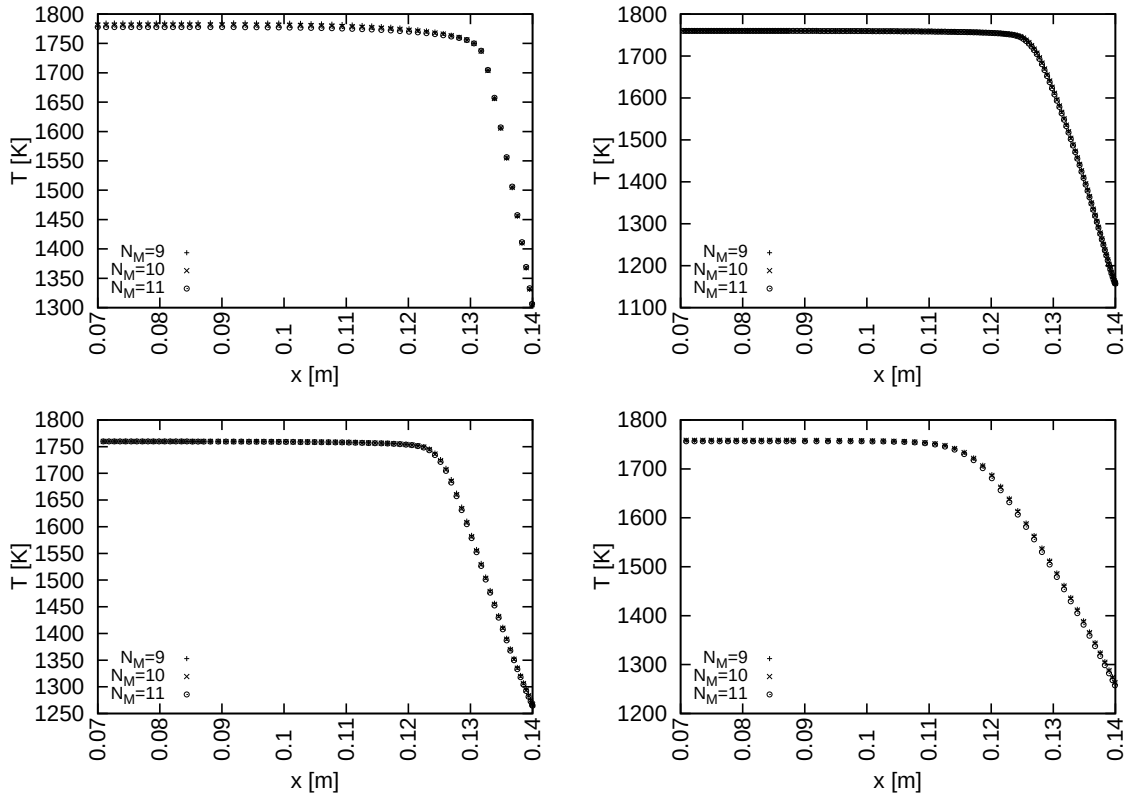

Figure 6.86: Temperature profiles. Top left: -0.4 m. Top right: -0.8 m. Bottom left: -0.9 m. Bottom right: -1.8 m.

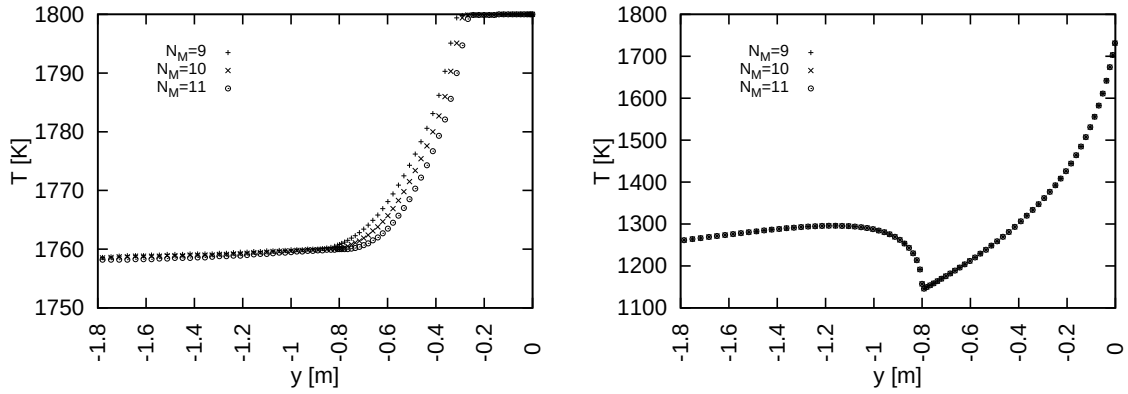

Figure 6.87: Temperature profiles. Left: $x = 0.07$ m. Right: $x = 0.14$ m.

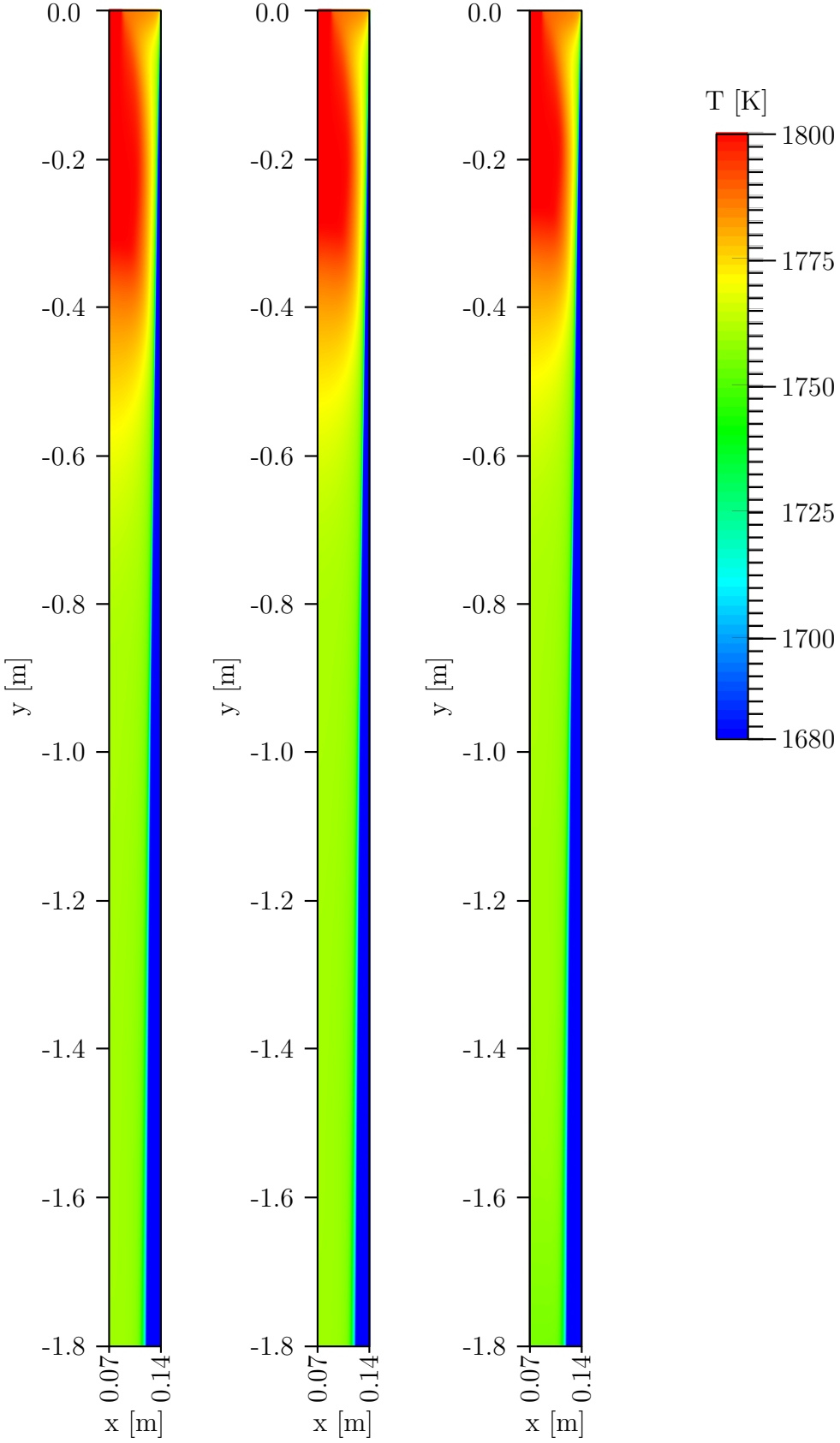

Figure 6.88: Temperature field as a function of N_M. Left: $N_M = 9$. Middle: $N_M = 10$. Right: $N_M = 11$.

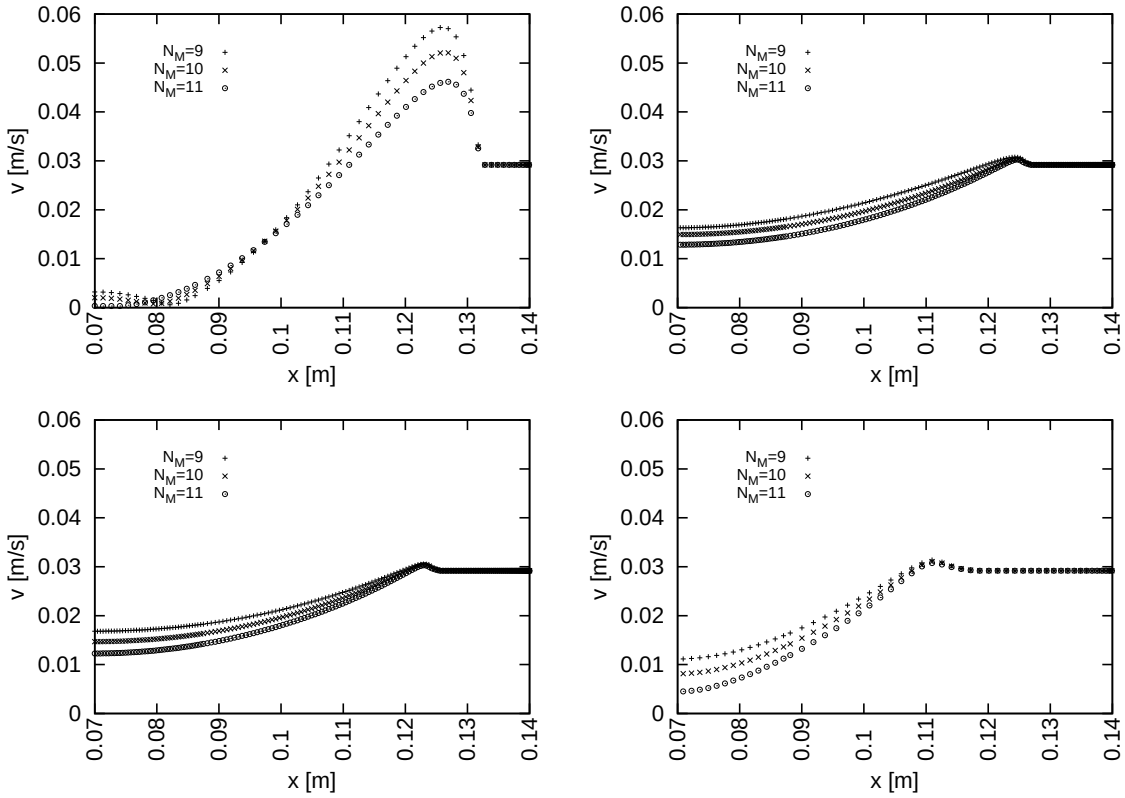

Figure 6.89: Velocity profiles. Top left: -0.4 m. Top right: -0.8 m. Bottom left: -0.9 m. Bottom right: -1.8 m.

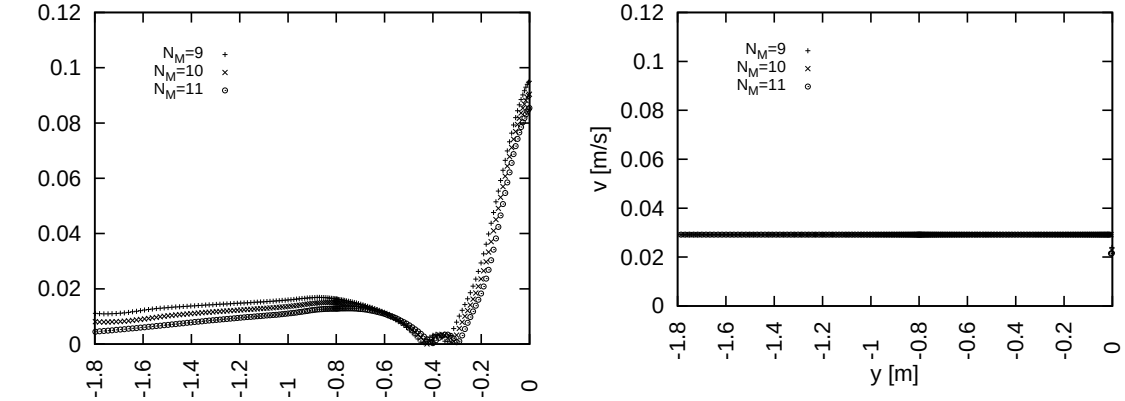

Figure 6.90: Velocity profiles. Left: $x = 0.07$ m. Right: $x = 0.14$ m.

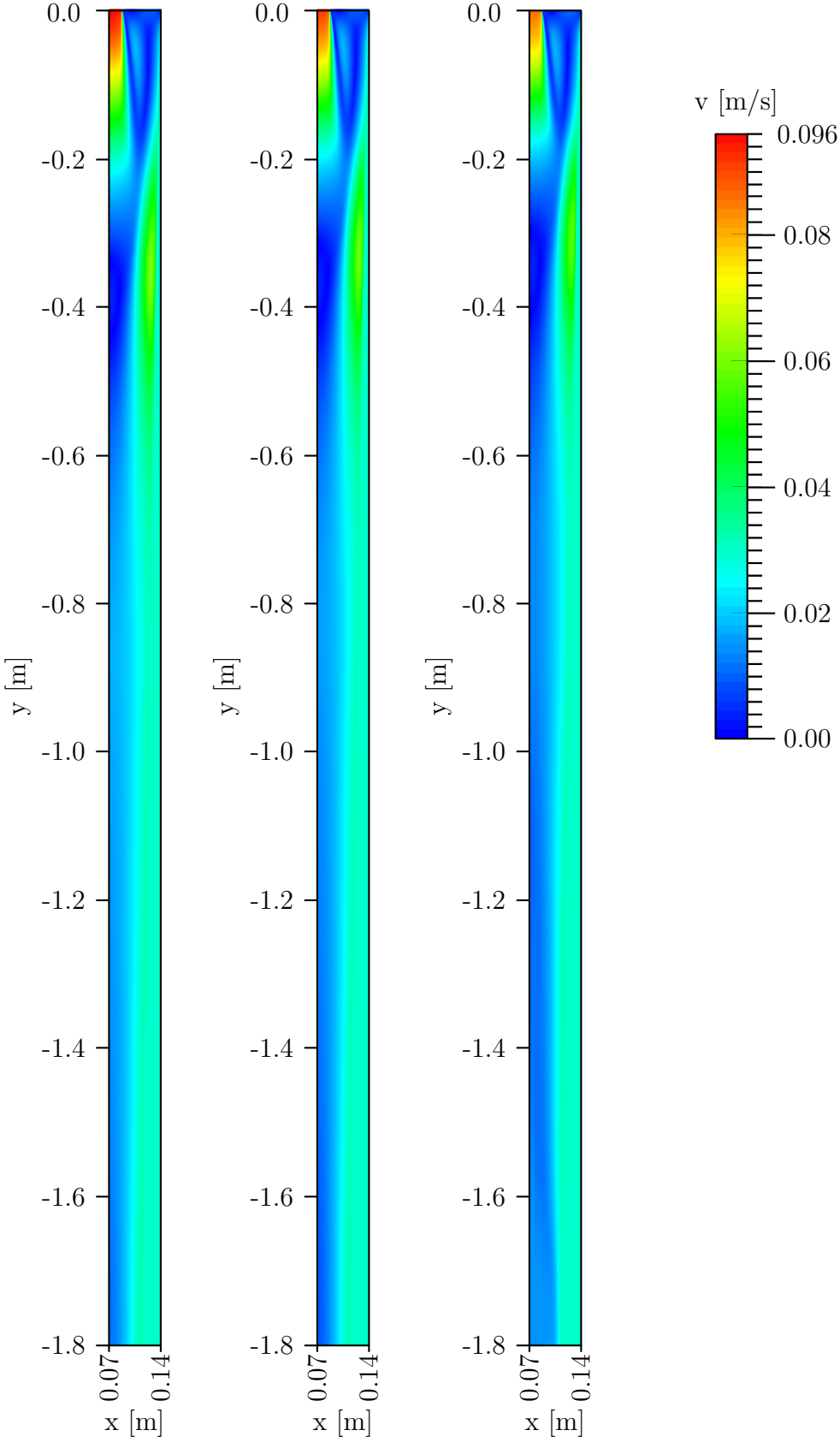

Figure 6.91: Velocity field as a function of N_M. Left: $N_M = 9$. Middle: $N_M = 10$. Right: $N_M = 11$.

The changes of the electrical current, the span distance, the number of windings in x direction and the number of windings in y direction influence the magnetic field magnitude. By keeping constant the rest of the variables and increasing either the electric current in the loops of the coil, the number of coils in either x or y direction, or the span distance between the coils and the strand, the magnetic field is increased according to Eqs. 6.19 and 6.16. The Lorentz force which effectively couples the velocity and the magnetic field opposes the flow and correspondingly, the velocity of the molten steel flow is diminished. The change in the magnetic field also causes the change in the temperature field, as the velocity influences the temperature. Although the decrease in the velocity can be significant, the decrease in the temperature is not so pronounced.

6.7.3 C: Coil Magnetic Field - Temperature, Velocity, Concentration

The third numerical example C deals with the binary alloy under the influence of the magnetic field. The steel consists of 99.2 wt% pure iron and of 0.8 wt% carbon. The coils configuration is the same as the default coils configuration in the numerical example B, and thus the magnetic field stems from the following parameters: $N_N = 25$, $N_M = 11$, $I = 50$ A and $a_d = 0.05$ m. The temperature, velocity and concentration fields are compared for the case with and the case without magnetic field for several different vertical and horizontal cross-sections. Then the streamlines and contour plots for the velocity, temperature, and concentration are presented for both cases.

Comparison between Configuration with and without the Magnetic Field

First the temperature profiles are compared for three different vertical cross-sections at the horizontal positions of 0.07 m (the center of the strand), 0.125 m and 0.14 m (the edge of the strand), and for three different horizontal cross-sections at the vertical positions of -0.8 m (the end of the mould), -0.9 m, and -1.8 m (the end of the calculation domain). The comparisons are shown in Fig. 6.92. In all of the cases, the temperature is slightly lower in the case with the magnetic field.

Next, the vertical and horizontal cross-sections of the velocity magnitude are presented in Fig. 6.93 for vertical cross-sections at the horizontal positions of 0.07 m (the center of the strand), 0.125 m and 0.14 m (the edge of the strand), and for horizontal cross-sections at the vertical positions of -0.8 m (the end of the mould), -0.9 m, and -1.8 m (the end of the calculation domain). The trend of the velocity magnitude for vertical cross-sections (Fig. 6.93 left) is similar for both of the cases, however the velocity magnitude in the case with the magnetic field is shifted to the right and has lower values then in the case without the magnetic field. The horizontal cross-section profiles show (Fig. 6.93 right) that the velocity of the liquid part is indeed diminished. The velocity of the solid part is in both cases the same and equals the casting speed. The amount of solidified

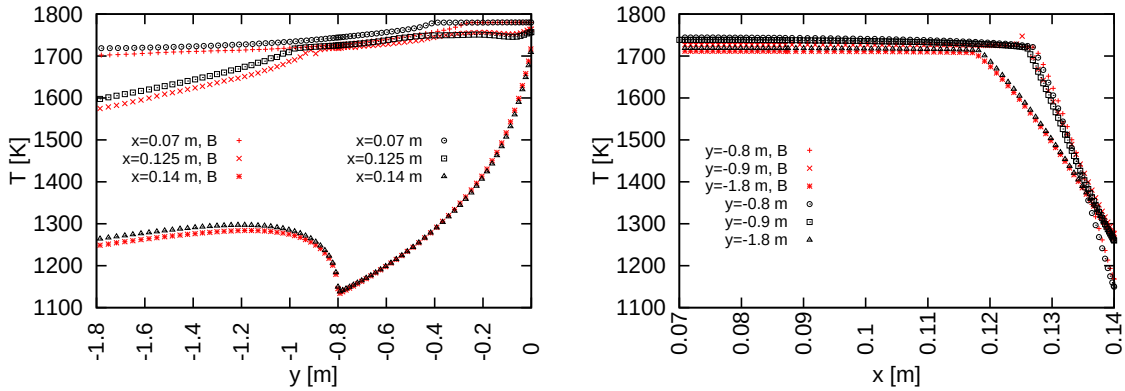

Figure 6.92: Temperature fields. Left: vertical cross-sections of the temperature field. Right: horizontal cross-sections of the temperature field.

material is slightly larger in the case with the magnetic field. To confirm this observation, the vertical and the horizontal cross-sections for liquid fractions are explored. As can be seen in Fig. 6.94, the magnetic field decreases the depth of the liquid part.

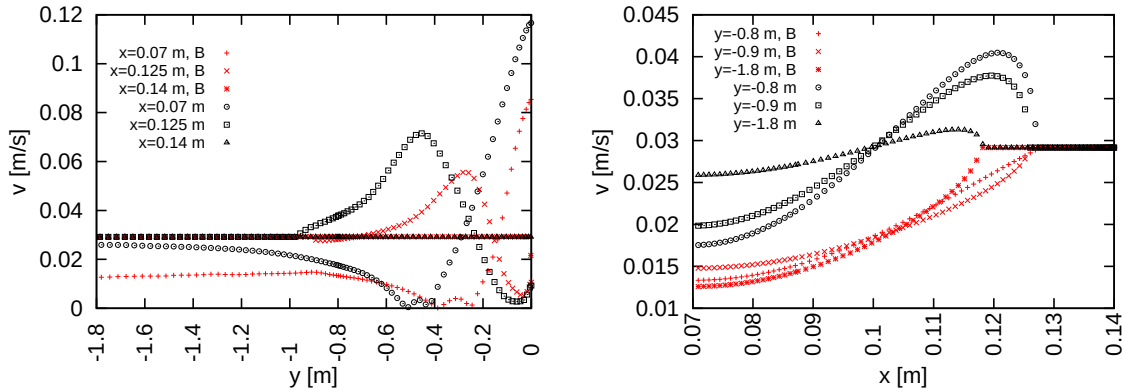

Figure 6.93: Velocity fields. Left: vertical cross-sections of the velocity field. Right: horizontal cross-sections of the velocity field.

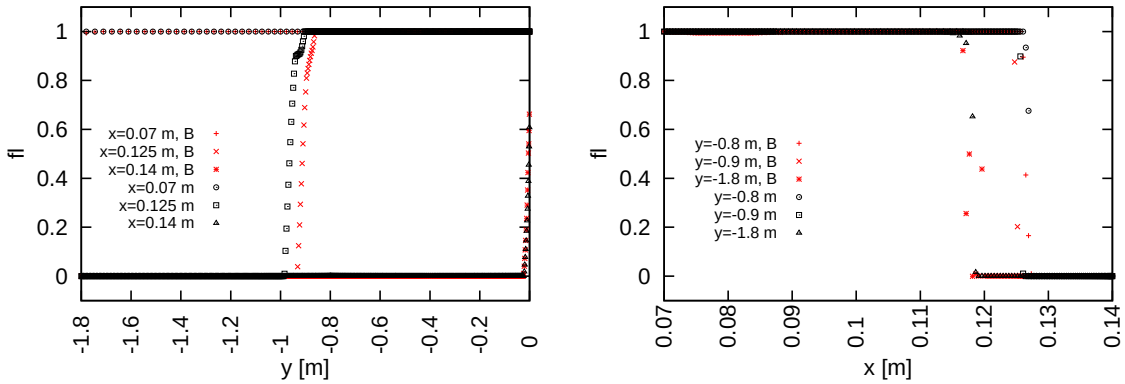

Figure 6.94: Liquid fraction. Left: vertical cross-sections of the liquid fraction. Right: horizontal cross-sections of the liquid fraction.

The normalized concentration of carbon is depicted in Fig. 6.95 for horizontal and vertical cross-sections. The value of $C_0 = 0.8$ wt%. Along the strand the concentration of carbon varies. The application of the magnetic field causes the concentration of carbon in the middle of the strand to increase at a higher vertical position and to a larger values (Fig. 6.95 left). The concentration of the carbon near the liquid-solid interface (0.125 m) exhibits approximately the same trend, however, the values of carbon concentration in the case with the magnetic field are higher for about 0.05 wt%. At the solid edge, the concentration of the carbon is lowered when the magnetic field is applied. The horizontal cross-sections (Fig. 6.95) confirm the above mentioned observation that the solid fraction is slightly increased by applying the magnetic field. In the higher vertical positions, the carbon concentration is increased in the liquid part of the mixture when in presence of the magnetic field. The decrease of the carbon concentration in the solid phase at higher vertical positions of the strand is not so prominent. At the end of the computational domain, the situation is similar but not as significant.

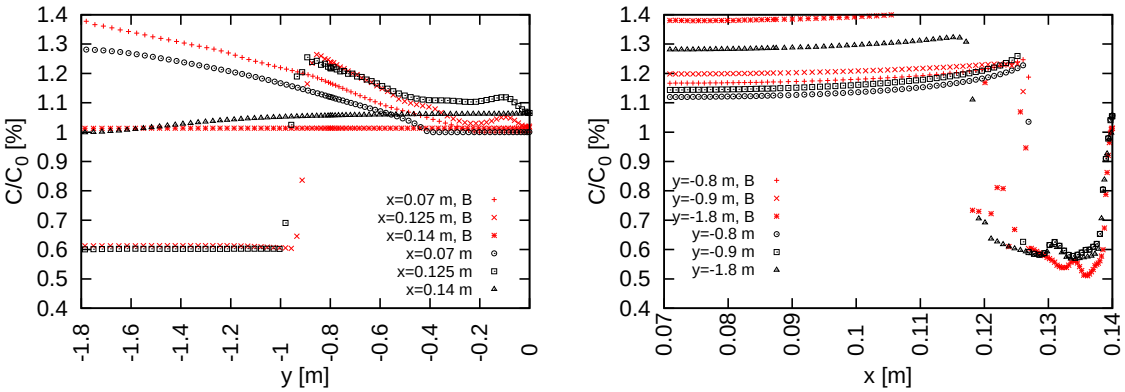

Figure 6.95: Concentration fields. Left: vertical cross-sections of the concentration fields. Right: horizontal cross-sections of the concentration fields.

The streamlines are depicted in Fig. 6.96. The application of the magnetic field moves the vortex to a higher vertical position and the upper recirculation zone is less pronounced.

Temperature-wise the application of the magnetic field in the binary mixture decreases the temperature, especially in the mould, where the zone of the highest temperature values is noticeably decreased. The contour plots of temperature fields are depicted in Fig. 6.97. The trend is similar as in the case with real magnetic field (Sec. 6.7.2).

The velocity magnitude contour plots are presented in Fig. 6.98. In the presence of the magnetic field, the velocity slows down throughout the calculation domain.

The contour plot of the concentration of carbon is depicted in Fig. 6.99. As already mentioned, the concentration of carbon is increased at the center of the strand in the presence of the magnetic field. The concentrations of carbon in the solidified part of the strand are slightly decreased, but the difference between the cases with and without magnetic field is not so pronounced. The overall concentration of the carbon in the strand remains the same.

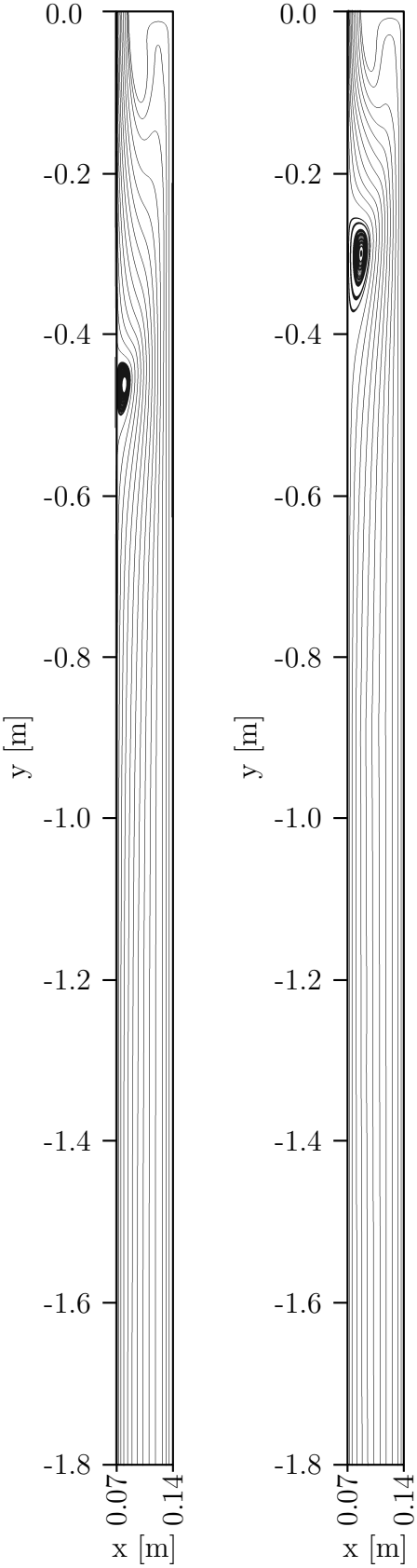

Figure 6.96: Streamlines. Left: without magnetic field. Right: with magnetic field.

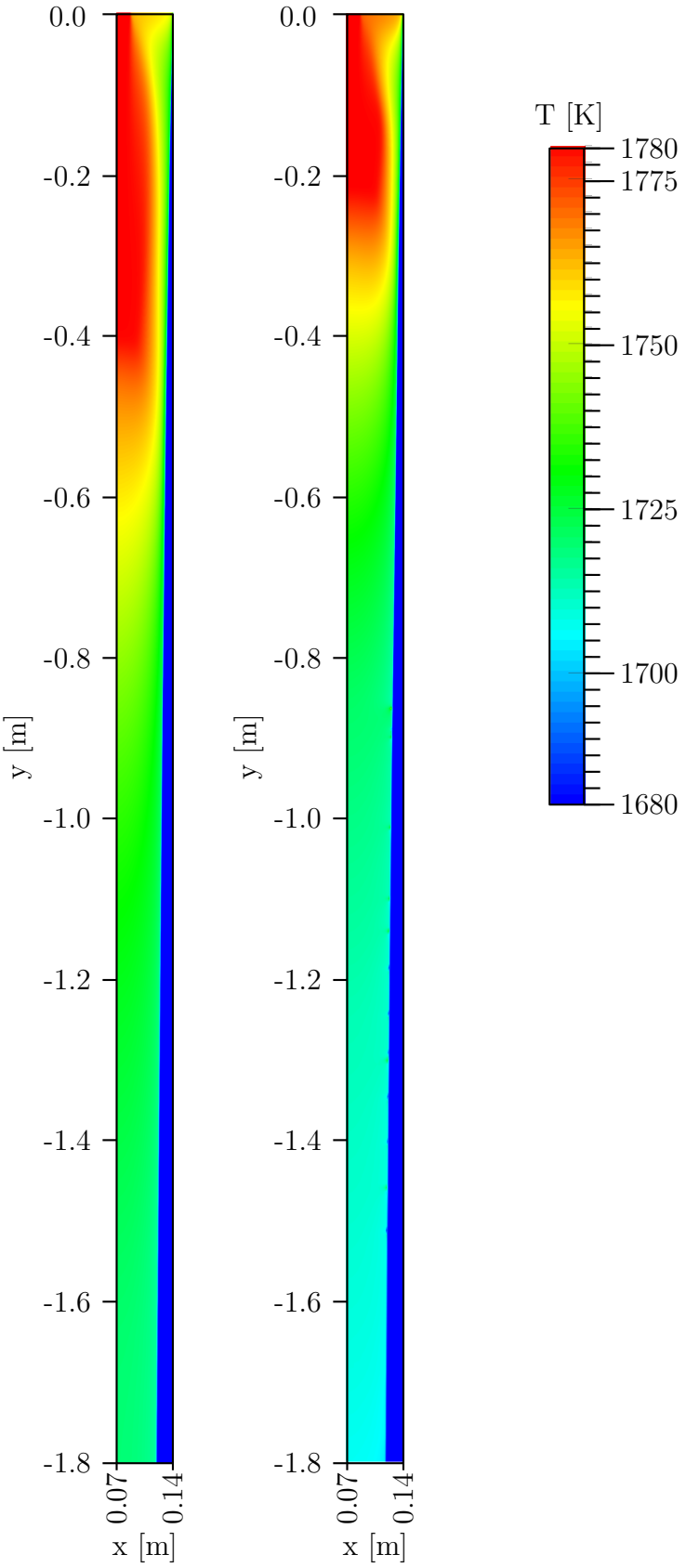

Figure 6.97: Temperature field. Left: without magnetic field. Right: with magnetic field.

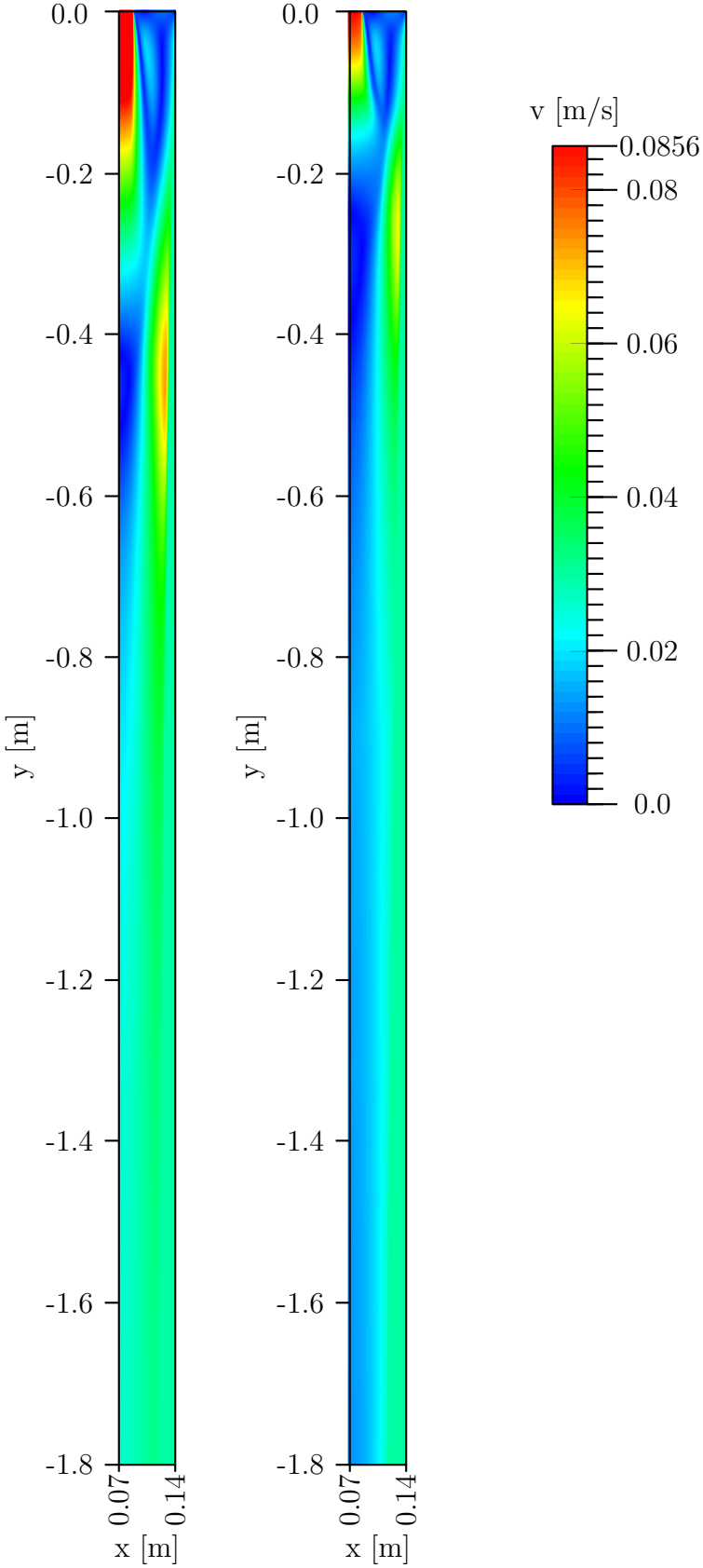

Figure 6.98: Velocity field. Left: without magnetic field. Right: with magnetic field.

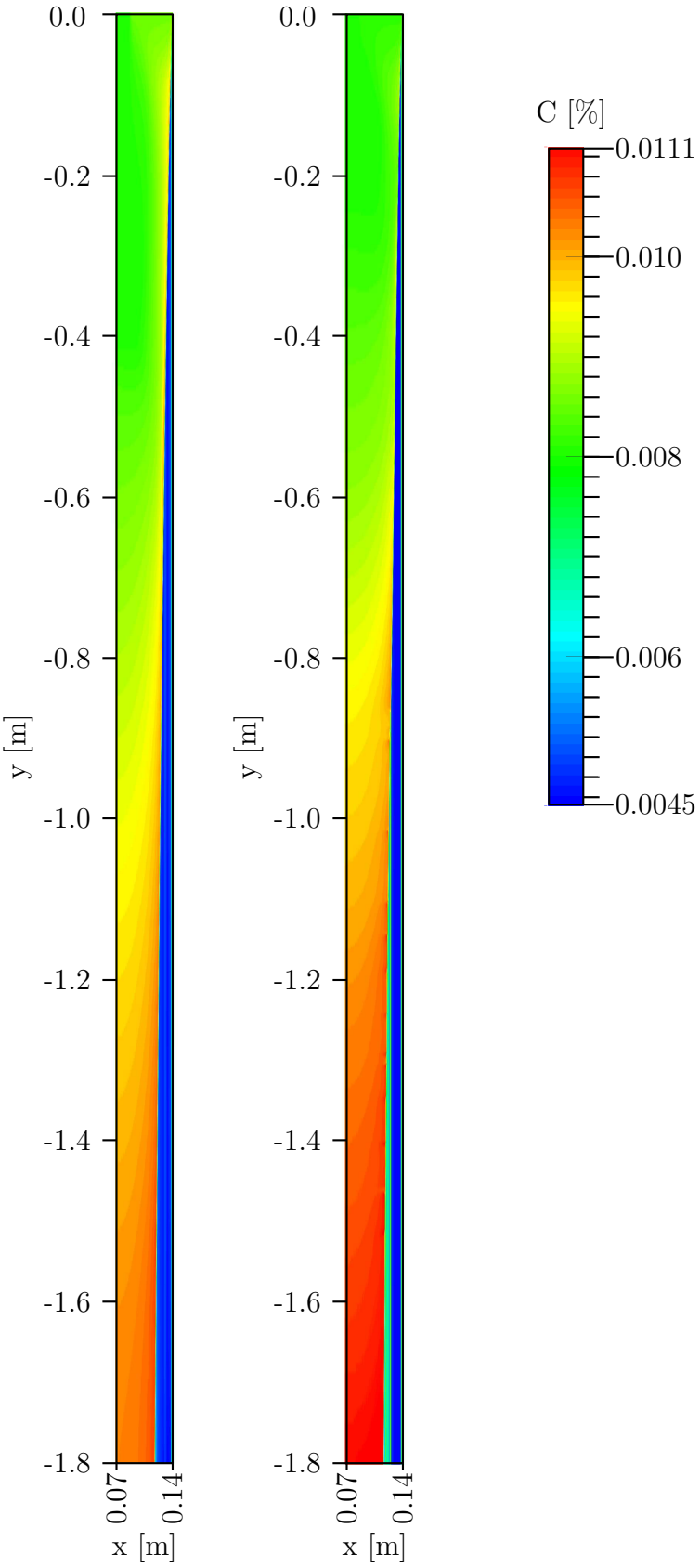

Figure 6.99: Concentration field. Left: without magnetic field. Right: with magnetic field.

Heat flux in the mould and in the spray cooling region is calculated from Eqs. 6.32 and 6.33. As in the case of temperature field, the magnetic field lowers the heat flux in the spray cooling region. The step between the mould and the spray cooling region is due to the difference in heat transfer coefficient for mould cooling h_{mc} and for spray cooling h_{sc}. The influence of the magnetic field is slightly stronger in the spray cooling region, which can be seen in Fig. 6.100.

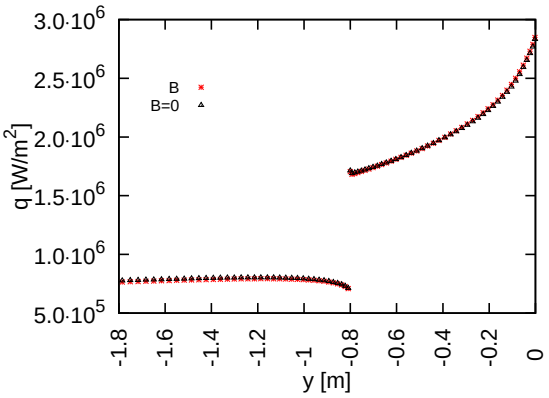

Figure 6.100: Heat flux.

6.8 Overview of Calculated Examples

An overview of the calculated CC cases along with the influence of the parameters is given in Tab. 6.4.

Table 6.4: Overview of calculated examples.

Case	Changed parameter	Influence on magnetic field	Influence of the changed parameter
A	magnetic field magnitude	increase in magnitude	The increased magnitude of **B** causes the decrease in the velocity. The changes in temperature are negligible.
	position	change in vertical position, magnitude remains constant	Velocity extremes are increased at higher vertical positions. The changes in temperature are negligible.
	height	change in **B** range, vertical position and magnitude are constant	The extreme values of velocity are increased over a wider range of vertical positions. The changes in temperature are negligible.
B	span (distance between mould and coils)	increased span causes smaller **B**	Increased span causes smaller magnetic field. Consequently the velocity in the extremes is diminished. Temperature drops at higher vertical position for stronger **B**.
	electric current	higher **I** causes stronger **B**	Velocity in the extremes is diminished for stronger **B**. Temperature drops at higher vertical positions for stronger **I**.
	N_N (number of coils in x direction)	larger N_N causes stronger **B**	Velocity in the extremes is diminished for larger N_N. Temperature drops at higher vertical positions for largerN_N.
	N_M (number of coils in y direction)	larger N_M causes stronger **B**	Velocity in the extremes is diminished for larger N_N. Temperature drops at higher vertical positions for larger N_N.

Continued on next page

Table 6.4 – continued from previous page

Case	**Changed parameter**	**Influence on magnetic field**	**Influence of the changed parameter**
C	magnetic field magnitude	increase in magnitude	Velocity in the extremes, temperature and liquid fraction are decreased at higher vertical positions. Concentration is increased in the middle of the strand and decreased at the edge of the strand at higher vertical positions.

7 Summary and Conclusions

This dissertation presents the application of the LRBFCM to the problem of CC of steel in the presence of an externally applied magnetic field. The main contribution of this work is the extension of the LRBFCM to the problems involving magnetic field. The developed approach is evaluated on several different numerical benchmark test cases and thus successfully proves that the method is applicable to the discussed multi-physics problem.

The first part of the thesis describes the CC process together with various possible electromagnetic field configurations. It also gives an overview of the physical models and the numerical method used to solve them. In the next chapters, first the physical model is explained in detail and then the numerical method is presented along with the numerical implementation. The model, as well as the method, are assessed first for the various benchmark test cases and then for the CC of steel under the influence of the magnetic field.

7.1 Performed Work

The work performed in the scope of this dissertation can be summarized in the following principal contributions:

- The physical model has been extended for the application of the static external magnetic field. An additional source term, accounting for the influence of the magnetic field, was added to the momentum and energy equations.
- The general upgraded transport equations have been dicretisized according to the proposed numerical procedure.
- The below numerical examples have been chosen as benchmark test cases in order to verify the accuracy of the meshless numerical method:
  - the lid-driven cavity [Mramor et al., 2013a]
  - the de Vahl Davis test case (natural convection in a cavity without the magnetic field) [Mramor et al., 2012, 2013b]
  - the natural convection in the presence of the magnetic field [Mramor et al., 2012, 2013b]
  - the Hartmann flow
  - the backward facing step [Mramor et al., 2014b]

  - the backward facing step under the influence of static externally applied magnetic field [Mramor et al., 2014b].

- The above mentioned benchmark test cases served as an elaboration and verification for the following numerical model considerations:
  - the type of the basis function,
  - the pressure-velocity coupling scheme,
  - the boundary conditions for the magnetic field,
  - the boundary conditions for in- and outflow,
  - the initial conditions for magnetic field,
  - the initial conditions for in- and outflow, and
  - the accuracy of the separation and the reattachment positions in channel flow.

- The magnetic field was calculated for multiple different arrangements of square coil systems, both with and without the iron core. Among several different solenoid arrangements that were considered, the configuration with two coils with parallel orientation was chosen.

- The static magnetic field was applied to the simplified geometry and thermophysical quantities of the CC of steel [Mramor et al., 2014a].

- The sensitivity analysis was performed for the simplified magnetic field. The parameters under consideration in this analysis were the magnitude, the position and the range of the magnetic field.

- The realistic magnetic field configuration for EMBR ruler was applied to the simplified geometry and thermo-physical parameters of the CC problem.

- The parametric study of the magnetic field and consequently the influence on the velocity and temperature fields was simulated. The parameters that were used in this study were the magnitude of the electric current, the number of windings in x and in y direction, and the distance between the placement of the coils and the strand.

- The influence of the magnetic field on the species concentration (macrosegregation) was examined for several different magnitudes of the realistic magnetic field.

7.2 Conclusions

Numerous conclusions can be drawn from the results obtained in this work:

- The placement of the magnetic field coils determines the magnitude and the orientation of the magnetic field.

- The magnetic field affects the velocity of the fluid flow as well as the temperature and the species concentration.
- The larger the magnitude of the magnetic field, the stronger the effects on the velocity, temperature and species concentration fields.
- The present configuration of the coils produces the magnetic field that successfully slows the velocity of the flow and decreases the temperature.
- The application of magnetic field affects the pattern of the segregation.

7.2.1 Industrial Relevance

It is shown that the placement, range and magnitude of the magnetic field affect the velocity, temperature and concentration fields in the CC of steel. Even though the present model is 2D, it gives a rough idea as to where the coils should be placed and what the appropriate magnitude of the magnetic field should be in order to enhance the influence of the magnetic field and thus obtain a steel with the desired characteristics. By implementing the realistic boundary and initial conditions, the model can serve as a useful tool in the optimization of the position, range and magnitude of the magnetic field. It thus enables further optimization of the process parameters which in turn enable a better quality of the steel. In the broader context, the present work presents a next step in the process of modelling the entire production chain, from initial casting operations to the final finished product.

7.3 Suggestions for Future Work

Although this thesis covers the most important aspects in the modelling and simulation of the CC process in the presence of the static magnetic field, a lot of work remains to be done, in order to obtain a reasonably predictive and accurate model. The recommendations for further work are divided into two segments: the development of the numerical model and the development of the physical model.

7.3.1 Numerical Modelling Upgrades

As shown in this thesis, as well as in several other related works [Vertnik, 2010], the LRBFCM is not only suitable for the solution of PDEs but performs well even for the solution of more complex physical examples described by coupled PDEs. Despite the good agreement with the reference results, both, those obtained from relevant reference papers and those calculated with other numerical methods, there is still room for further improvement and advancement of the method, especially in the terms of more thorough mathematical definition.

Although the LRBFCM has already been rigorously tested and verified on numerous fluid flow and solidification benchmark test cases as well as reference results, so far not much has been done in the field of segregation and deformation. As the later stages in the process of CC of steel include these phenomena,

additional tests would certainly be advisable. The additional verification and comparison of different PV coupling schemes, as well as the turbulence models would enable further development and understanding of the numerical model. In future, a coupling of other variables such as velocity and magnetic field, and temperature and magnetic field would enable the method to evolve and to be applied to an even more complex problems, such as plasma reactors.

In terms of the numerical development of the method, several numerical parameters, such as the shape parameter, the time step and the distance between the neighbouring nodes, require further in-depth investigation. So far, the correlations between these parameters have been granted only a superficial attention.

Next, the more extensive examination of the influence domain selection would be appropriate. In this regard some initial tests have already been performed [Vertnik et al., 2006]. However, this tests were not very broad as only five and nine nodded sub-domains were considered. By increasing the number of the sub-domain nodes, the number of RBFs has to be increased. The LRBFCM can only solve the problem effectively when the number of the domain nodes corresponds to the number of the basis functions in collocation nodes. If the number of nodes exceeds the number of basis functions the system is predetermined and another procedure, such as weighted least square approximation, has to be used. Many work in this direction has already been made [Nayroles et al., 1992; Sadat et al., 2006].

Another aspect that needs to be addressed and investigated in present numerical model is the domain node adaptation. In this dissertation, the adaptation of the nodes in different parts of the domain has been pre-implemented and fixed. Nonetheless, current implementation does not enable the adaptation of the nodes during the calculation. The effective change in node arrangement density might be beneficial in reducing the calculation time and improve the accuracy.

7.3.2 Physical Modelling Upgrades

Several of the physical phenomena have yet to be completely explained, thus leaving ample space for further development of the physical model. Examples of such phenomena are turbulence and segregation. Although several models exist, none of them can with absolute certainty completely describe the physics behind the phenomena. In order to attempt this type of improvement a large number of very precise experiments would be necessary.

The model should be extended to the application of a time varying magnetic field. Such an extension would enable a broader application of the model, enabling it to include the simulation of the AC current problems. An example of such a problem are the EMS, which can be used in the CC of steel.

Another step in the development of the physical model is the expansion of the model into 3D. As the formulation of the magnetic field module already includes the magnetic field in 3D, such an extension should be straightforward. The initial tests and calculations on the 3D model are currently under way.

Next, the temperature dependence of the thermo-physical quantities such as density, specific heat, and thermal conductivity should be taken into account and

implemented in the model.

The steel consists of several different components. The amount of which is varied according to the desired properties of the finished product. In the present model, steel is considered first as an unary metal and then as a binary alloy of iron and carbon. In order to achieve a more precise realistic composition, a multiple-component steel will be considered.

The solidification in the mushy region should also be addressed more thoroughly. Currently, the mushy region is modelled as a completely porous medium as the floating dendrites in the slurry region are not considered. In the next stage of the physical model development, the slurry region should be considered separately and the movement of floating dendrites should be taken into account.

Last but not least, the present physical model should be extended to include different mushy zones morphologies and segregation models in order to account for the growth of the dendrites on the liquid-solid boundary as well as those floating in the slurry region. This extension is all but straightforward, as it incorporates physical phenomena on two different scales and assumes coupling between models on micro and macro levels. Although the columnar and equiaxed dendrites follow the same macrosegregation model, the solidification on microlevel can be described by several different rules. The simplest linear and lever rules give sufficient results. However, for a more precise results, Scheil and Brody-Flemings models should also be considered.

7.4 Publications

The following articles, scientific conference contributions and studieshave been published or performed during the course of the present dissertation.

Original scientific article

1. MRAMOR, Katarina, VERTNIK, Robert, ŠARLER, Božidar. Simulation of laminar backward facing step flow under magnetic field with explicit local radial basis function collocation method. *Engineering analysis with boundary elements*, ISSN 0955-7997. [Print ed.], 2014, str. 1-11, doi: 10.1016/j.enganabound.2014.04.013. [COBISS.SI-ID 3349243]

2. MRAMOR, Katarina, VERTNIK, Robert, ŠARLER, Božidar. Simulation of continuous casting of steel under the influence of magnetic field using the local-radial basis-function collocation method = Simulacija kontinuirnega ulivanja jekla pod vplivom magnetnega polja na podlagi metode kolokacije z radialnimi baznimi funkcijami. *Materiali in tehnologije*, ISSN 1580-2949, mar.-apr. 2014, letn. 48, št. 2, str. 281-288, ilustr. `http://mit.imt.si/Revija/`. [COBISS.SI-ID 1043114]

3. MRAMOR, Katarina, VERTNIK, Robert, ŠARLER, Božidar. Simulation of natural convection influenced by magnetic field with explicit local radial basis function collocation method. *Computer modeling in engineering & sciences.*

CMES, ISSN 1526-1492. Tiskana izd., 2013, vol. 92, no. 4, str. 327-352. [COBISS.SI-ID 2827003]

4. MRAMOR, Katarina, VERTNIK, Robert, ŠARLER, Božidar. Low and intermediate Re solution of lid driven cavity problem by local radial basis function collocation method. *Computers, materials & continua*, ISSN 1546-2218, 2013, vol. 36, no. 1, str. 1-21. [COBISS.SI-ID 2865659]

Published scientific conference contribution

5. MRAMOR, Katarina, VERTNIK, Robert, ŠARLER, Božidar. Simulation of macrosegregation influenced by magnetic field in continuous casting of steel. V: ŠARLER, Božidar (ur.), MASSAROTTI, Nicola (ur.), NITHIARASU, Perumal (ur.). *ThermaComp2014*. 3rd ed. Napoli: Giannini Editore, 2014, str. 283-286. [COBISS.SI-ID 3380987]

6. ŠARLER, Božidar, VERTNIK, Robert, MRAMOR, Katarina. A numerical benchmark test for continuous casting of steel. V: *MCWASP XIII, International Conference on Modeling of Casting, Welding and Advanced Solidification Processes, 17-22 June 2012, Schladming, Austria*, (IOP Conference Series, ISSN 1757-8981, Materials Science and Engineering, vol. 33). Bristol: IOP Publishing, 2012, vol. 33, str. 1-10, doi: 10.1088/1757-899X/33/1/012012. [COBISS.SI-ID 2417403]

Published scientific conference contribution abstract

7. MRAMOR, Katarina, VERTNIK, Robert, ŠARLER, Božidar. Simulation of continuous casting of steel under the influence of external magnetic field by using local radial basis function collocation method. V: 21. Mednarodna konferenca o materialih in tehnologijah, 13.-15. november 2013, Portorož = 21st International Conference on Materials and Technology, 13-15 November 2013, Portorož, Slovenia. GODEC, Matjaž (ur.), et al. *Program in knjiga povzetkov = Program and book of abstracts*. Ljubljana: Inštitut za kovinske materiale in tehnologije, 2013, str. 132. [COBISS.SI-ID 3067899]

8. ŠARLER, Božidar, VERTNIK, Robert, MRAMOR, Katarina. A benchmark test for continuous casting of steel, II. V: *Sixth International Conference on Solidification and Gravity, Miskolc-Lillafüred, Hungary, September 2-5, 2013*. Miskolc-Lillafüred: [s. n.], 2013, str. 55. [COBISS.SI-ID 2878715]

9. MRAMOR, Katarina, VERTNIK, Robert, ŠARLER, Božidar. Simulation of natural convection under the influence of magnetic field by Explicit Local Radial Basis Function Collocation Method. V: 8th ICCES Special Symposium on Meshless & Other Novel Computational Methods, September 2-6, 2012, Maestral Hotel, Budva, Montenegro. ATLURI, Satya N. (ur.), VUŠANOVIĆ, Igor (ur.), ŠARLER, Božidar (ur.). *Book of abstracts*. Podgorica: University of Montenegro

Press, 2012, str. 27. [COBISS.SI-ID 2535163]

Treatise, preliminary study, study

10. MRAMOR, Katarina, VERTNIK, Robert, ŠARLER, Božidar. *Review of mathematical modelling of magneto-hydrodynamic processes in continuous casting of steel*. V Novi Gorici: Univerza, 2011. [4], 35 str., ilustr. [COBISS.SI-ID 1991931]

A Turbulence Modelling Classification

In the chart A.1 a classification of turbulence modelling is shown. The abbreviations used in the chart are: Reynolds Averaged Navier-Stokes (RANS) models, Large Eddy Simulation (LES), Direct Numerical Simulation (DNS), Linear Eddy Viscosity Model (LEVM), Non-Linear Eddy Viscosity Model (NLEVM), Reynolds Stress Model (RSM), Re-Normalisation Group Large Eddy Simulation (RNG-LES), Wall-Adapting Local Eddy-viscosity (WALE) model, Explicit Non-Linear Constitutive Relation (ENLCR), Explicit Algebraic Reynolds Stress Models (EARSM), Re-Normalisation Group (RNG), and Shear Stress Transport (SST). A short description of each group of turbulence modelling is given below.

Direct Numerical Simulation

In DNS [Fox and Lilly, 1972; Baritaud et al., 1996] N-S equations are solved directly, without any kind of turbulence modelling. This means that all the scales of the turbulence are solved by adjusting the density of computational mesh. DNS is computationally very expensive, since the problem is 3D and time-dependent. Although, several basic flow problems with simple geometries and low-to-medium Re numbers [Kim et al., 1987; Kasagi et al., 1992; Kasagi and Nishimura, 1997; Le et al., 1997] have been successfully implemented with this method, the DNS cannot be used to solve engineering problems [Moin and Mahesh, 1998], where a range of scales required is too wide to be directly computed.

Large-Eddy Simulation

LES [Smagorinsky, 1963; Deardorff, 1970] is a simulation technique in which the large energy carrying eddies are solved explicitly, whereas the effects of smaller eddies are modelled. The technique was designed to overcome difficulties with DNS and RANS and is their intermediate computationally wise. The LES requires 3D transient modelling, however the number of computational nodes is decreased as the smaller eddies are removed and modelled by a Sub-Grid Scale (SGS) model. Perhaps the most important process in LES is the filtering. In this operation, the velocity and pressure are divided into the resolvable scale part and into the SGS part. The decomposed varieties are used to develop the filtered N-S equations; one set describing the resolved field and the other set, which contains the SGS stress term, describing the SGS part. A detailed description of

the procedure can be found in [Pope, 2000]. Several different SGS models are commonly used to solve the filtered N-S equations: Kinetic energy sub-grid scale model, WALE model, Dynamic sub-grid model, Smagorinsky-Lilly model, and Re-Normalisation Group (RNG)-LES model. The LES models' biggest advantage is an improved accuracy compared to the Reynolds stress models especially in cases where the instability of large-scale eddies is substantial.

Reynolds-Averaged Navier-Stokes Based Models

RANS based turbulence models:

- Linear Eddy-Viscosity Model (EVM)
  - algebraic models or zero-equation turbulence models are calculated directly from the flow variables and do not require any additional equations.
  - one-equation models require the solution of one turbulent transport equation, typically the turbulent kinetic energy equation.
  - two-equation models include two additional equations to account for the turbulent properties of the flow (k-ε, k-ω, k-τ)
- Non-Linear Eddy-Viscosity Model (NLEVM)
  - Explicit non-linear constitutive relation
  - v^2-f models
- Differential Stress Model (DSM)

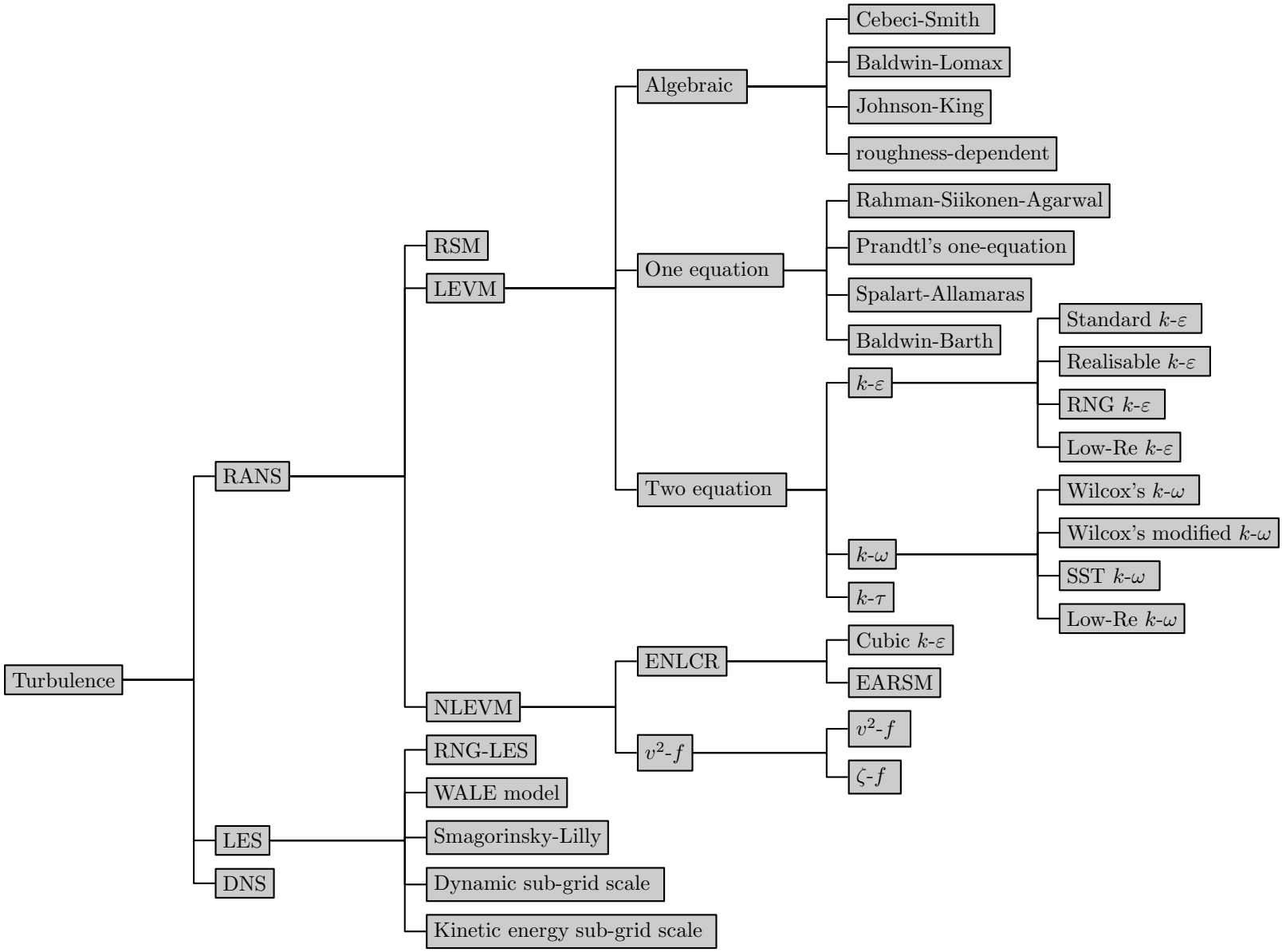

Figure A.1: Classification of turbulence modelling.

B Dimensionless Governing Equations

As the parameter values and dimensions of the computational domain differ from author to author, the easiest way to compare the results is to present them in their dimensionless form.

B.1 Dimensionless Governing Equations for Lid Driven Cavity

The dimensionless variables are defined as follows

$$x' = \frac{x}{L}, \quad y' = \frac{y}{L}, \quad \mathbf{v}' = \frac{\mathbf{v}}{v_c}, \quad t' = \frac{t\, v_c}{L}, \quad p' = \frac{p}{\rho\, v_c^2}. \tag{B.1}$$

By inserting these variables into momentum equation

$$\rho \left(\frac{\partial \mathbf{v}}{\partial t} + \nabla \cdot \left(\mathbf{v}\, \mathbf{v} \right) \right) = -\nabla p + \mu\, \nabla^2\, \mathbf{v}, \tag{B.2}$$

the following dimensionless equation is obtained

$$\frac{\partial \mathbf{v}'}{\partial t'} + \nabla \cdot (\mathbf{v}'\, \mathbf{v}') = -\nabla p' + \frac{1}{\mathrm{Re}} \nabla^2\, \mathbf{v}'. \tag{B.3}$$

The mass continuity equation

$$\nabla \cdot \mathbf{v} = 0, \tag{B.4}$$

becomes

$$\nabla \cdot \mathbf{v}' = 0. \tag{B.5}$$

B.2 Dimensionless Governing Equations for Natural Convection in Cavity under the Influence of External Magnetic Field

The dimensionless variables are defined as follows

$$x' = \frac{x}{L}, \quad y' = \frac{y}{L}, \quad \mathbf{v}' = \frac{\mathbf{v}}{v_c}, \quad t' = \frac{t\,v_c}{L}, \quad p' = \frac{p}{\rho\,v_c^2}, \quad \Theta = \frac{T - T_C}{T_H - T_C}, \tag{B.6}$$

$$\mathbf{g}' = \frac{\mathbf{g}\,L}{v_c^2}, \quad \text{and} \quad \beta_T' = \beta\,(T_H - T_C). \tag{B.7}$$

These variables are inserted into momentum conservation equation

$$\rho\Big(\frac{\partial \mathbf{v}}{\partial t} + \nabla\cdot\big(\mathbf{v}\,\mathbf{v}\big)\Big) = -\nabla p + \mu\nabla^2\,\mathbf{v} + \mathbf{f}_{EM} - \rho\,\mathbf{g}\,\beta_T\,(T - T_{ref}), \tag{B.8}$$

and the following dimensionless equation is obtained

$$\frac{\partial \mathbf{v}'}{\partial t'} + \nabla\cdot(\mathbf{v}'\,\mathbf{v}') = -\nabla p' + \frac{1}{\mathrm{Re}}\nabla^2\,\mathbf{v}' + \frac{\mathrm{Ha}^2}{\mathrm{Re}}\mathbf{v}' - \mathbf{g}'\,\beta_T'\,\Theta. \tag{B.9}$$

The mass conservation equation

$$\nabla\cdot\mathbf{v} = 0, \tag{B.10}$$

becomes

$$\nabla\cdot\mathbf{v}' = 0. \tag{B.11}$$

By inserting the dimensionless variables in

$$\frac{\partial T}{\partial t} + \nabla\cdot\big(\mathbf{v}\,T\big) = \alpha_T\nabla^2\,T, \tag{B.12}$$

the non-dimensional governing equation for temperature is obtained

$$\frac{\partial \Theta}{\partial t'} + \nabla\cdot(\mathbf{v}'\,\Theta) = \frac{\mathrm{Pr}}{\mathrm{Re}}\nabla^2\,\Theta. \tag{B.13}$$

B.3 Dimensionless Governing Equations for Hartmann Flow

The dimensionless variables are defined as

$$x' = \frac{x}{L}, \quad y' = \frac{y}{L}, \quad \mathbf{v}' = \frac{\mathbf{v}}{v_c}, \quad t' = \frac{t\,v_c}{L}, \quad p' = \frac{p\,L}{v_c\,\mu}. \tag{B.14}$$

The momentum conservation equation for the Hartmann flow is written as

$$0 = -\nabla p + \mu\,\nabla^2\,\mathbf{v} + \mathbf{f}_{EM}. \tag{B.15}$$

By inserting the dimensionless variables into the momentum equation, the following dimensionless momentum equation is obtained

$$0 = -\nabla p' + \nabla^2 \mathbf{v}' + \mathrm{H}a^2 \mathbf{v}'. \tag{B.16}$$

The mass conservation equation

$$\nabla \cdot \mathbf{v} = 0, \tag{B.17}$$

becomes

$$\nabla \cdot \mathbf{v}' = 0. \tag{B.18}$$

B.4 Dimensionless Governing Equations for Backward Facing Step

The dimensionless variables are defined as

$$x' = \frac{x}{L}, \quad y' = \frac{y}{L}, \quad \mathbf{v}' = \frac{\mathbf{v}}{v_c}, \quad t' = \frac{t\, v_c}{L}, \quad p' = \frac{p}{\rho\, v_c^2}. \tag{B.19}$$

The momentum conservation equation for the backward facing step is written as

$$\rho\left(\frac{\partial \mathbf{v}}{\partial t} + \nabla \cdot (\mathbf{v}\,\mathbf{v})\right) = -\nabla p + \mu\, \nabla^2 \mathbf{v} + \mathbf{f}_{EM}. \tag{B.20}$$

By inserting the dimensionless variables into the momentum equation, the following dimensionless momentum equation is obtained

$$\frac{\partial \mathbf{v}'}{\partial t'} + \nabla \cdot (\mathbf{v}'\,\mathbf{v}') = -\nabla p' + \frac{1}{\mathrm{Re}} \nabla^2 \mathbf{v}' + \frac{\mathrm{Ha}^2}{\mathrm{Re}} \mathbf{v}'. \tag{B.21}$$

The mass conservation equation

$$\nabla \cdot \mathbf{v} = 0, \tag{B.22}$$

becomes

$$\nabla \cdot \mathbf{v}' = 0. \tag{B.23}$$

C Magnetic Field Square Loop

The magnetic field of a square loop can be calculated as a sum of magnetic fields of individual sides. The components for each of the sides are presented below.

$$B_{0x} = \frac{\mu\,|\mathbf{I}|}{4\,\pi}\left(\frac{-(z+\frac{b}{2})}{\sqrt{x^2+(y+\frac{a}{2})^2+(z+\frac{b}{2})^2}\left(\sqrt{x^2+(y+\frac{a}{2})^2+(z+\frac{b}{2})^2}+(y+\frac{a}{2})\right)}\right.$$
$$\left. - \frac{y-\frac{a}{2}}{\sqrt{x^2+(y+\frac{a}{2})^2+(z+\frac{b}{2})^2}\left(\sqrt{x^2+(y+\frac{a}{2})^2+(z+\frac{b}{2})^2}+(z+\frac{b}{2})\right)}\right)$$

$$B_{90x} = \frac{\mu\,|\mathbf{I}|}{4\,\pi}\left(\frac{z+\frac{b}{2}}{\sqrt{x^2+(y-\frac{a}{2})^2+(z+\frac{b}{2})^2}\left(\sqrt{x^2+(y-\frac{a}{2})^2+(z+\frac{b}{2})^2}-(y-\frac{a}{2})\right)}\right.$$
$$\left. - \frac{y-\frac{a}{2}}{\sqrt{x^2+(y-\frac{a}{2})^2+(z+\frac{b}{2})^2}\left(\sqrt{x^2+(y-\frac{a}{2})^2+(z+\frac{b}{2})^2}+(z+\frac{b}{2})\right)}\right)$$

$$B_{180x} = \frac{\mu\,|\mathbf{I}|}{4\,\pi}\left(\frac{-(z-\frac{b}{2})}{\sqrt{x^2+(y+\frac{a}{2})^2+(z-\frac{b}{2})^2}\left(\sqrt{x^2+(y+\frac{a}{2})^2+(z-\frac{b}{2})^2}+(y+\frac{a}{2})\right)}\right.$$
$$\left. - \frac{y+\frac{a}{2}}{\sqrt{x^2+(y+\frac{a}{2})^2+(z-\frac{b}{2})^2}\left(\sqrt{x^2+(y+\frac{a}{2})^2+(z-\frac{b}{2})^2}+(z-\frac{b}{2})\right)}\right)$$

$$B_{270x} = \frac{\mu\,|\mathbf{I}|}{4\,\pi}\left(\frac{z-\frac{b}{2}}{\sqrt{x^2+(y-\frac{a}{2})^2+(z-\frac{b}{2})^2}\left(\sqrt{x^2+(y-\frac{a}{2})^2+(z-\frac{b}{2})^2}-(y-\frac{a}{2})\right)}\right.$$
$$\left. - \frac{y-\frac{a}{2}}{\sqrt{x^2+(y-\frac{a}{2})^2+(z-\frac{b}{2})^2}\left(\sqrt{x^2+(y-\frac{a}{2})^2+(z-\frac{b}{2})^2}+(z-\frac{b}{2})\right)}\right)$$

$$B_{0y} = \frac{\mu\,|\mathbf{I}|}{4\,\pi}\left(\frac{x}{\sqrt{x^2+(y+\frac{a}{2})^2+(z+\frac{b}{2})^2}\left(\sqrt{x^2+(y+\frac{a}{2})^2+(z+\frac{b}{2})^2}+(z+\frac{b}{2})\right)}\right)$$

$$B_{90y} = \frac{\mu\,|\mathbf{I}|}{4\,\pi}\left(\frac{-x}{\sqrt{x^2+(y-\frac{a}{2})^2+(z+\frac{b}{2})^2}\left(\sqrt{x^2+(y-\frac{a}{2})^2+(z+\frac{b}{2})^2}+(z+\frac{b}{2})\right)}\right)$$

$$B_{180y} = \frac{\mu\,|\mathbf{I}|}{4\,\pi}\left(\frac{x}{\sqrt{x^2+(y+\frac{a}{2})^2+(z-\frac{b}{2})^2}\left(\sqrt{x^2+(y+\frac{a}{2})^2+(z-\frac{b}{2})^2}+(z-\frac{b}{2})\right)}\right)$$

$$B_{270y} = \frac{\mu\,|\mathbf{I}|}{4\,\pi}\left(\frac{-x}{\sqrt{x^2+(y-\frac{a}{2})^2+(z-\frac{b}{2})^2}\left(\sqrt{x^2+(y-\frac{a}{2})^2+(z-\frac{b}{2})^2}+(z-\frac{b}{2})\right)}\right)$$

$$B_{0z} = \frac{\mu\,|\mathbf{I}|}{4\,\pi}\left(\frac{x}{\sqrt{x^2+(y+\frac{a}{2})^2+(z+\frac{b}{2})^2}\left(\sqrt{x^2+(y+\frac{a}{2})^2+(z+\frac{b}{2})^2}+(y+\frac{a}{2})\right)}\right)$$

$$B_{90z} = \frac{\mu\,|\mathbf{I}|}{4\,\pi}\left(\frac{-x}{\sqrt{x^2+(y-\frac{a}{2})^2+(z+\frac{b}{2})^2}\left(\sqrt{x^2+(y-\frac{a}{2})^2+(z+\frac{b}{2})^2}-(y-\frac{a}{2})\right)}\right)$$

$$B_{180z} = \frac{\mu\,|\mathbf{I}|}{4\,\pi}\left(\frac{x}{\sqrt{x^2+(y+\frac{a}{2})^2+(z-\frac{b}{2})^2}\left(\sqrt{x^2+(y+\frac{a}{2})^2+(z-\frac{b}{2})^2}+(y+\frac{a}{2})\right)}\right)$$

$$B_{270z} = \frac{\mu\,|\mathbf{I}|}{4\,\pi}\left(\frac{-x}{\sqrt{x^2+(y-\frac{a}{2})^2+(z-\frac{b}{2})^2}\left(\sqrt{x^2+(y-\frac{a}{2})^2+(z-\frac{b}{2})^2}-(y-\frac{a}{2})\right)}\right)$$

D Sensitivity Study for Simple Magnetic Field

The sensitivity study of temperature and velocity fields are presented in the contour plots below. Fig. D.1 presents the temperature field for different values of magnetic field magnitudes, Fig. D.2 presents the velocity field for different values of magnetic field magnitudes, Fig. D.3 presents the temperature field for different positions of magnetic field, Fig. D.4 presents the velocity field for different positions of magnetic field, Fig. D.5 presents the temperature field for different ranges of magnetic field, and Fig. D.6 presents the temperature field for different ranges of magnetic field.

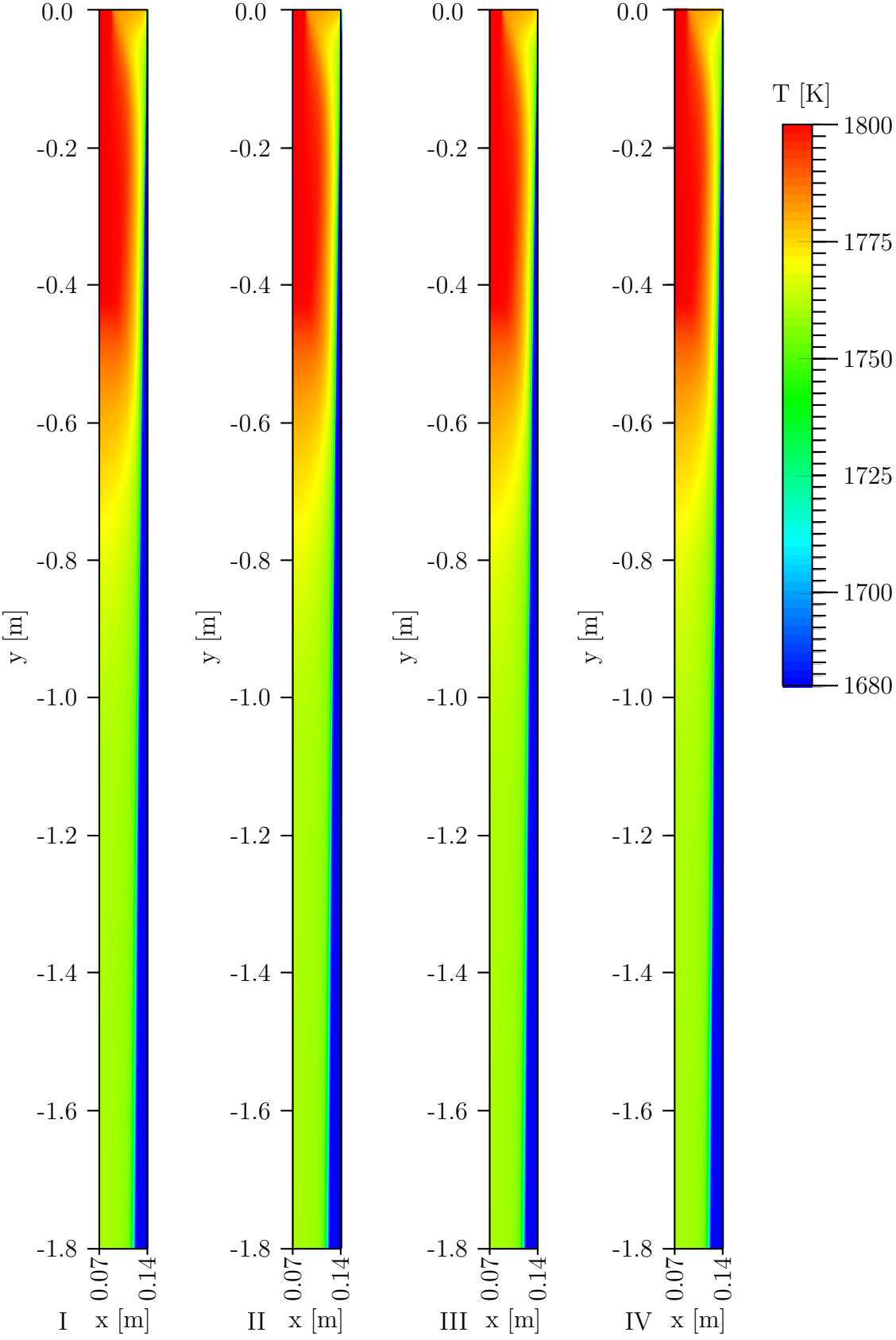

Figure D.1: Temperature field at different EM field magnitudes. I: $B_x = 2.6 \cdot 10^{-3}$ T. II: $B_x = 2.6 \cdot 10^{-2}$ T. III: $B_x = 2.6 \cdot 10^{-1}$ T. IV: $B_x = 2.6$ T.

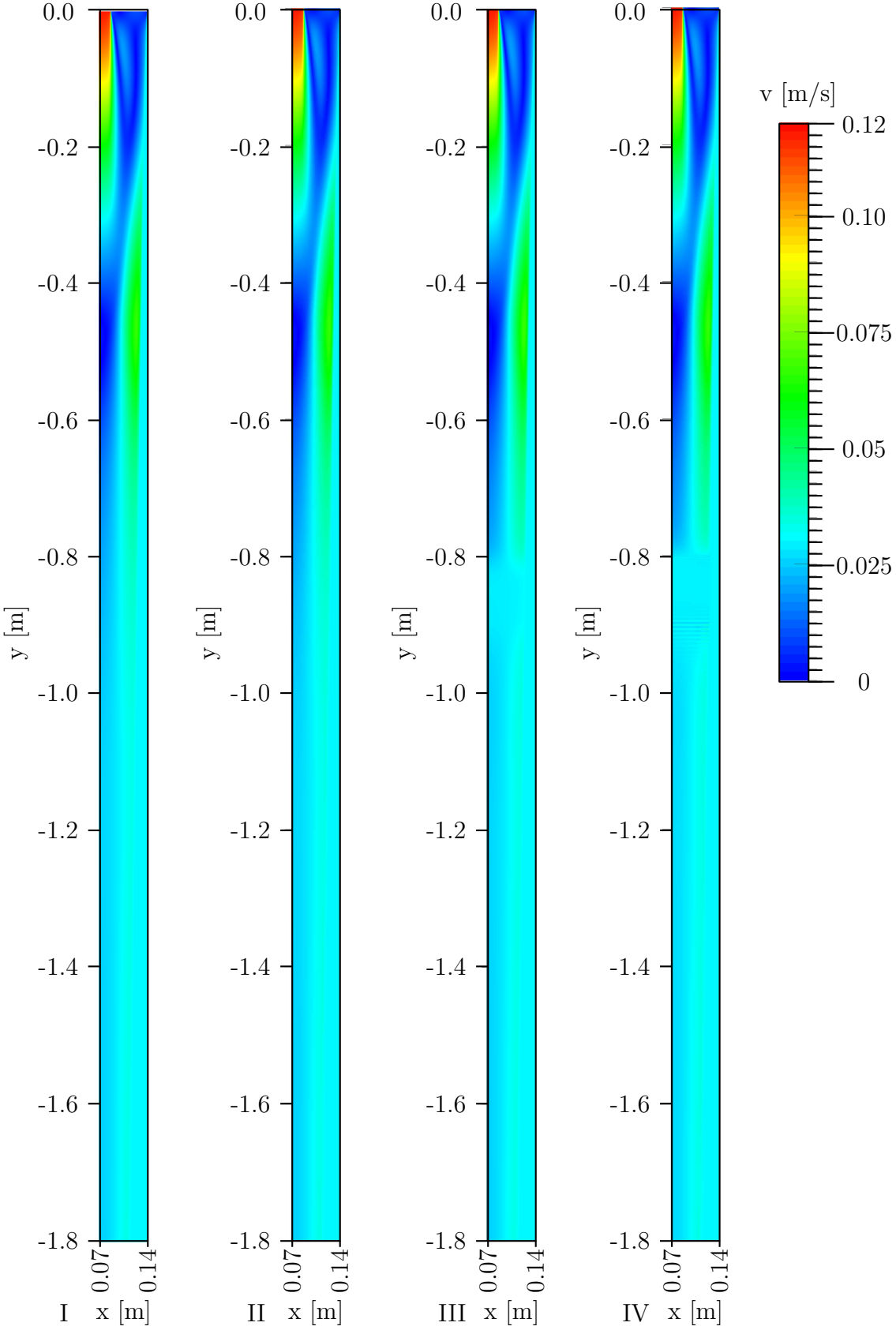

Figure D.2: Velocity field at different EM field magnitudes. I: $B_x = 2.6 \cdot 10^{-3}$ T. II: $B_x = 2.6 \cdot 10^{-2}$ T. III: $B_x = 2.6 \cdot 10^{-1}$ T. IV: $B_x = 2.6$ T.

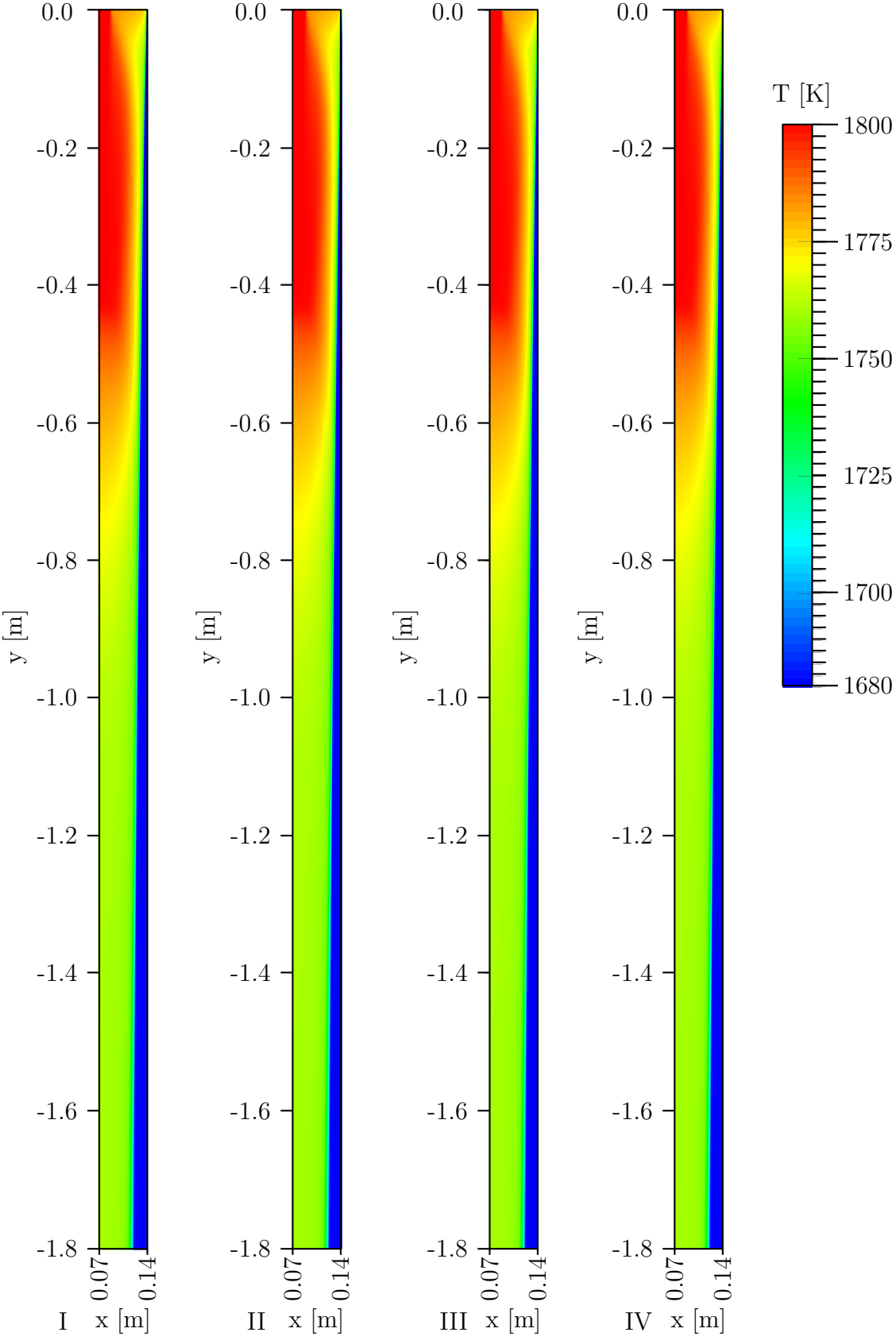

Figure D.3: Temperature field at different EM field positions. I: $l_{mEM} = -0.6$ m. II: $l_{mEM} = -0.7$ m. III: $l_{mEM} = -0.8$ m. IV: $l_{mEM} = -0.9$ m.

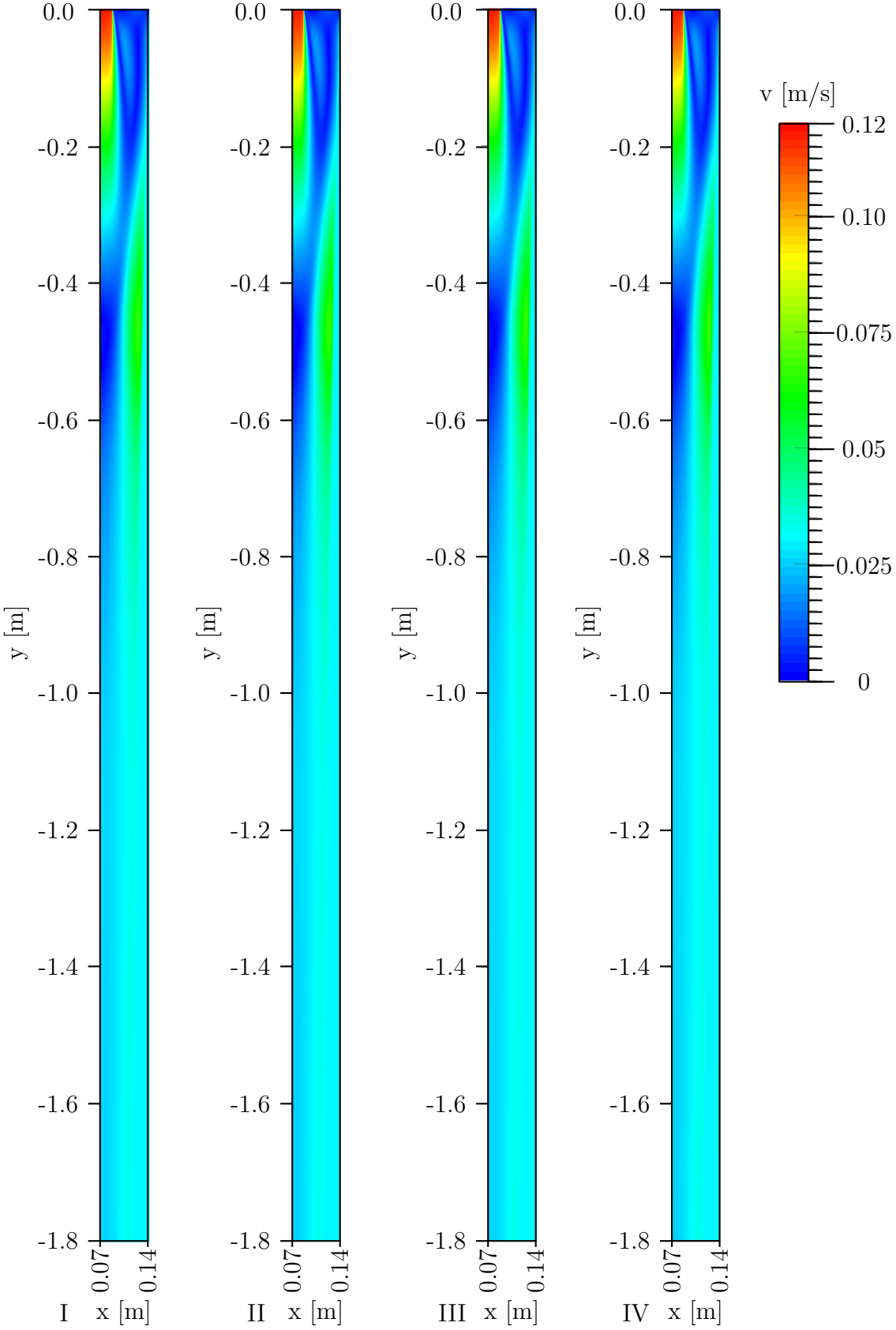

Figure D.4: Velocity field at different EM field positions. I: $l_{mEM} = -0.6$ m. II: $l_{mEM} = -0.7$ m. III: $l_{mEM} = -0.8$ m. IV: $l_{mEM} = -0.9$ m.

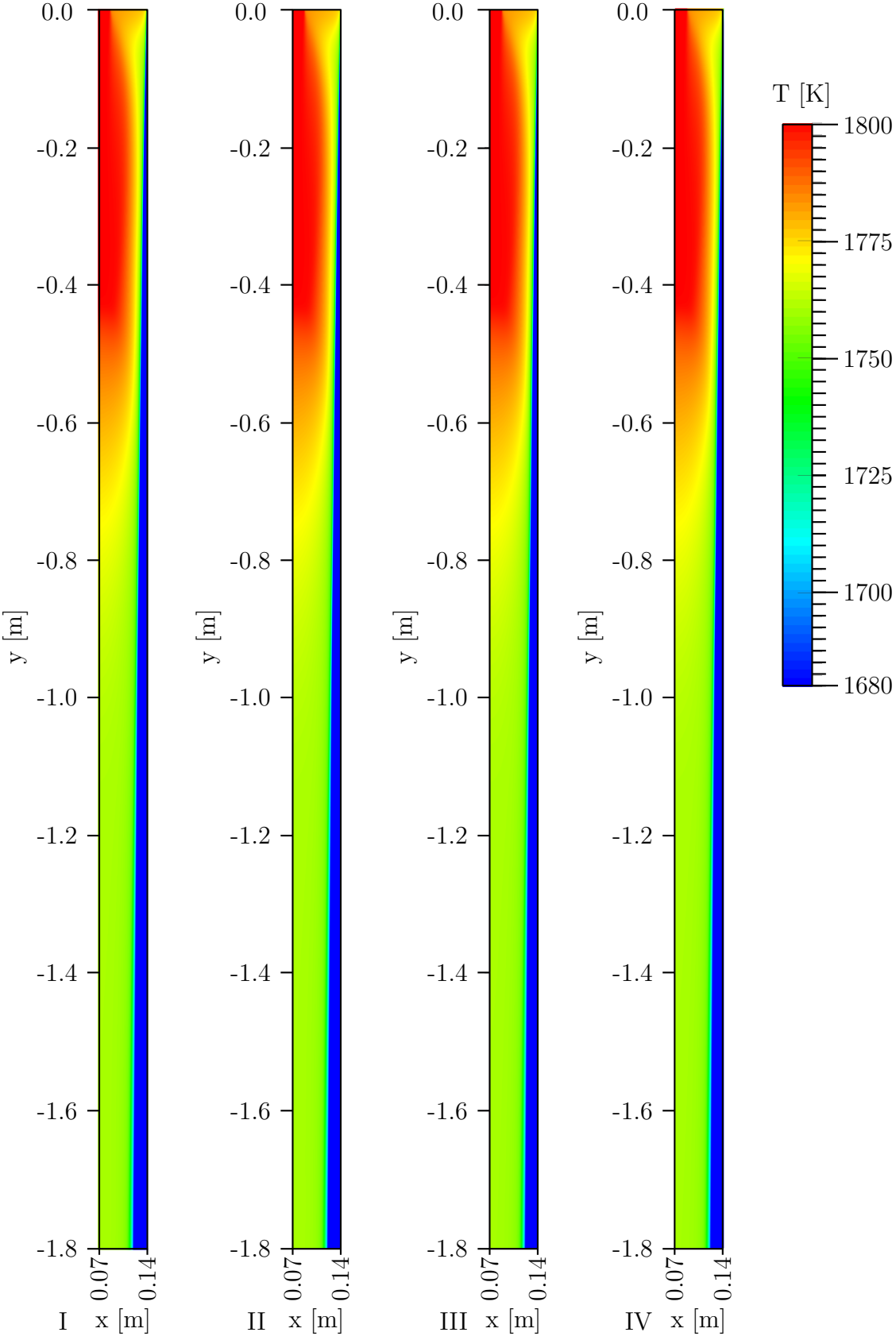

Figure D.5: Temperature field at different EM field ranges. I: -0.8 m $< l_{EM} < -1.0$ m. II: -0.8 m $< l_{EM} < -0.95$ m. III: -0.8 m $< l_{mEM} < -0.9$ m. IV: -0.8 m $< l_{mEM} < -0.85$ m.

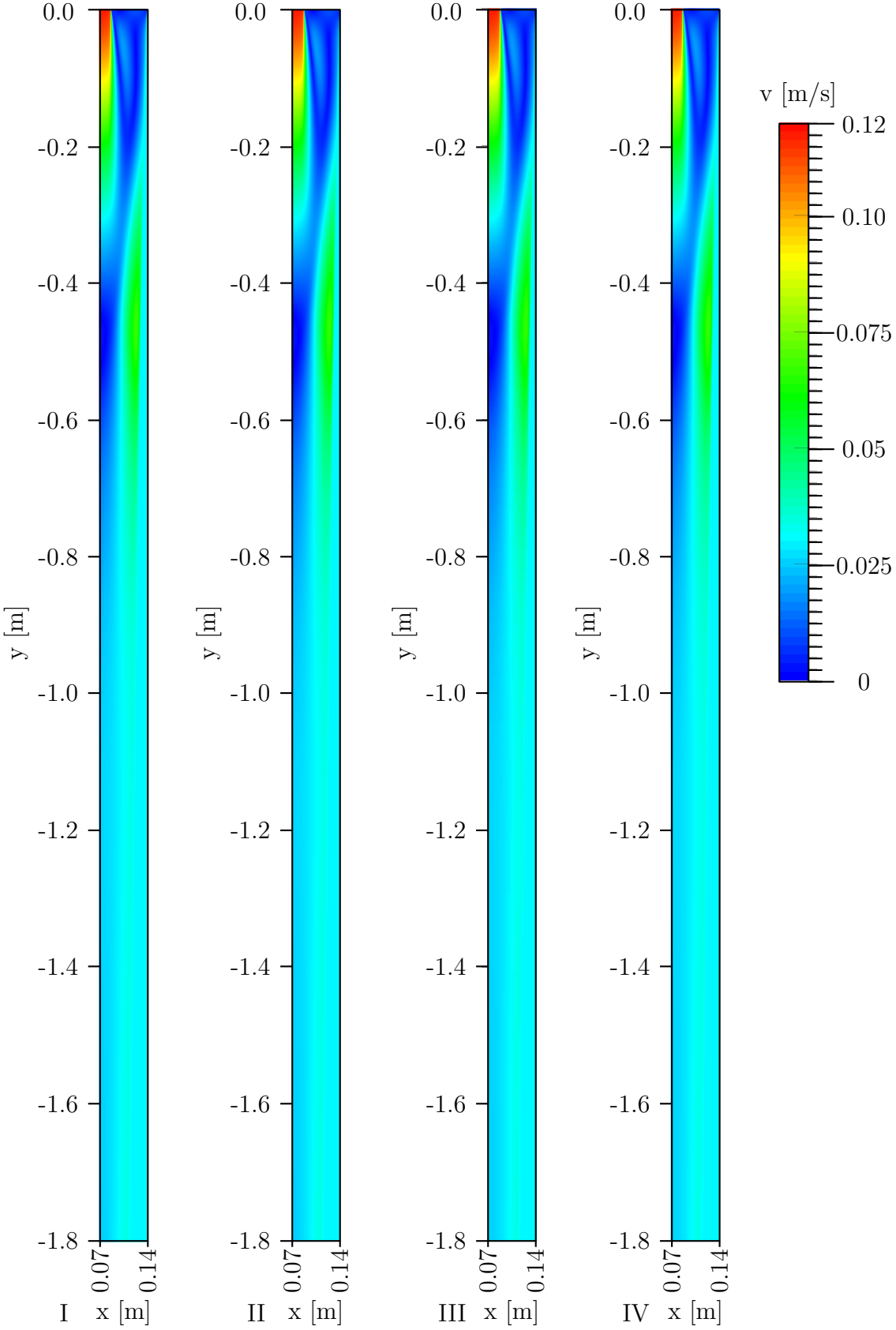

Figure D.6: Velocity field at different EM field ranges. I: -0.8 m $< l_{EM} < -1.0$ m. II: -0.8 m $< l_{EM} < -0.95$ m. III: -0.8 m $< l_{mEM} < -0.9$ m. IV: -0.8 m $< l_{mEM} < -0.85$ m.

Bibliography

ABB (2013). Stirrers and brakers of steel. http://www.abb.si/product/us. Last accessed: April, 2013.

Abbassi, H. and Ben Nassrallah, S. (2007). MHD flow and heat transfer in a backward-facing step. *International Communications in Heat and Mass Transfer*, 34:231–237.

Abe, K., Kondoh, T., and Nagano, Y. (1994). A new turbulence model for predicting fluid flow and heat transfer in separating and reattaching flows–I. Flow field calculations. *International Journal of Heat and Mass Transfer*, 37:139–151.

Abe, K., Kondoh, T., and Nagano, Y. (1995). A new turbulence model for predicting fluid flow and heat transfer in separating and reattaching flows–II. Thermal field calculations. *International Journal of Heat and Mass Transfer*, 38:1467–1481.

Abid, R., Rumsey, C., and Gatski, T. (1995). Prediction of nonequilibrium turbulent flows with explicit algebraic stress models. *The American Institute of Aeronautics and Astronautics Journal*, 33:2026–2031.

Aboutalebi, M. R., Guthrie, R. I. L., and Seyedein, S. H. (2007). Mathematical modeling of coupled turbulent flow and solidification in a single belt caster with electromagnetic brake. *Applied Mathematical Modelling*, 31:1671–1689.

Aboutalebi, M. R., Hasan, M., and Guthrie, R. I. L. (1995). Coupled turbulent flow, heat, and solute transport in continuous casting processes. *Metallurgical and Materials Transactions B*, 26:731–744.

Accolade-Photography (2013). Steel blooms. http://www.accolade-photography.com/industrialphotographer/medium/0024.jpg. Last accessed: April, 2013.

An-Vo, D.-A., Mai-Duy, N., Tran, C. D., and Tran-Cong, T. (2013). ADI method based on C2–continuous two-node integrated–RBF elements for viscous flows. *Applied Mathematical Modelling*, 37:5184–5203.

An-Vo, D.-A., Mai-Duy, N., and Tran-Cong, T. (2011a). A C2–continuous control-volume technique based on Cartesian grids and two–node integrated–RBF elements for second–order elliptic problems. *CMES: Computer Modeling in Engineering & Sciences*, 72:299–334.

An-Vo, D.-A., Mai-Duy, N., and Tran-Cong, T. (2011b). High-order upwind methods based on C2–continuous two–node integrated–RBF elements for viscous flows. *CMES: Computer Modeling in Engineering & Sciences*, 80:141–177.

ANSYS (2013). Academic Research, Release 14.0. http://www.ansys.com/Industries/Academic. Computer Program.

Arefmanesh, A., Najafi, M., and Nikfar, M. (2010). Meshless local Petrov-Galerkin simulation of buoyancy-driven fluid flow and heat transfer in a cavity with wavy side walls. *CMES: Computer Modeling in Engineering & Sciences*, 62:113–149.

Arzani, H. and Afshar, M. H. (2006). Solving Poisson's equations by the discrete least square meshless method. *WIT Transactions on Modelling and Simulation*, 42:23–31.

Atluri, S. N. and Shen, S. (2002). *The Meshless Method*. Tech Science Press, Forsyth, (GA) USA.

Atluri, S. N. and Zhu, T. (1998). A new meshless local Petrov–Galerkin (MLPG) approach in computational mechanics. *Computational Mechanics*, 22:117–127.

Aydin, M. and Fenner, R. (2001). Boundary element analysis of driven cavity flow for low and moderate Reynolds numbers. *International Journal for Numerical Methods in Fluids*, 37:45–64.

Baritaud, T., Poinsot, T., and Baum, M. (1996). *Direct Numerical Simulation for Turbulent Reacting Flows*. Editions Technip, Paris, France.

Barragy, E. and Carey, G. (1997). Stream function-vorticity driven cavity solution using finite elements. *Computers and Fluids*, 26:453–468.

Barton, I. E. (1995). A numerical study of flow over a confined backward-facing step. *International Journal for Numerical Methods in Fluids*, 21:653–665.

Barton, I. E. and Kirby, R. (2000). Finite difference scheme for the solution of fluid flow problems on non-staggered grids. *International Journal for Numerical Methods in Fluids*, 33:939–959.

Bayona, V., Moscoso, M., Carretero, M., and Kindelan, M. (2010). RBF–FD formulas and convergence properties. *Journal of Computational Physics*, 229:8281–8295.

Bayona, V., Moscoso, M., and Kindelan, M. (2011). Optimal constant shape parameter for multiquadric based RBF–FD method. *Journal of Computational Physics*, 230:7384–7399.

Beckermann, C. (2002). Modelling of macrosegregation: applications and future needs. *International Materials Reviews*, 47:243–261.

Bellet, M., Combeau, H., Fautrelle, Y., Gobin, D., Rady, M., Arquis, E., Budenkova, O., Dussoubs, B., Duterrail, Y., Kumar, A., Gandin, C. A., Goyean, B., Mosbah, S., and Založnik, M. (2009). Call for contributions to a numerical benchmark problem for 2D columnar solidification of binary alloys. *International Journal of Thermal Sciences*, 48:2013–2016.

Belytschko, T., Lu, Y. Y., and Gu, L. (1994). Element-free Galerkin methods. *International Journal for Numerical Methods in Engineering*, 37:229–256.

Benard, C., Gobin, D., and Zanoli, A. (1986). Moving boundary problem: heat conduction in the solid phase of a phase-change material during melting driven by natural convection in the liquid. *International Journal of Heat and Mass Transfer*, 29:1669–1681.

Bennon, W. and Incropera, F. (1987a). A continuum model for momentum, heat and species transport in binary solid-liquid phase change systems. I: Model formulation. *International Journal of Heat and Mass Transfer*, 30(10):2161–2170.

Bennon, W. D. and Incropera, F. P. (1987b). A continuum model for momentum, heat and species transport in binary solid-liquid phase change systems. II: Application to solidification in a rectangular cavity. *International Journal of Heat and Mass Transfer*, 30:2171–2187.

Birat, J. P. and Chone, J. (1982). Electromagnetic stirring on billet, bloom, and slab continuous casters: state of the art in 1982. *Ironmaking and Steelmaking*, 10:269–281.

Botella, O. and Peyret, R. (1998). Benchmark spectral results on the lid–driven cavity flow. *Computers and Fluids*, 27:421–433.

Bozkaya, N. and Tezer-Sezgin, M. (2011). The DRBEM solution of incompressible MHD flow equations. *International Journal for Numerical Methods in Fluids*, 67:1264–1282.

Bredberg, J. (1999). Prediction of flow and heat transfer inside turbine blades using EARSM, k-ε and k–ω turbulence models. Technical report, Chalmers University of Technology, Gothenburg.

Bruneau, C.-H. and Jouron, C. (1990). An efficient scheme for solving steady incompressible Navier–Stokes equations. *Journal of Computational Physics*, 89:389–413.

Bruneau, C.-H. and Saad, M. (2006). The 2D lid–driven cavity problem revisited. *Computers and Fluids*, 35:326–348.

Buhmann, M. D. (2000). Radial basis functions. *Acta Numerica*, 9:1–38.

Buhmann, M. D. (2003). *Radial Basis Functions: Theory and Implementations*. Cambridge University Press, Cambridge, UK.

Burgers, J. M. (1948). A mathematical model illustrating the theory of turbulence. *Advances in Applied Mechanics*, 1:171–199.

Bustamante, C. A., Florez, W. F., Power, H., Giraldo, M., and Hill, A. F. (2011). Control Volume–Radial Basis Function solution of 2D driven cavity flow in terms of the velocity vorticity formulation. *CMES: Computer Modeling in Engineering & Sciences*, 79:103–129.

Carman, P. C. (1948). Some physical aspects of water flow in porous media. *Discussions of the Faraday Society*, 3:72–77.

Chaudhary, R., Ji, C., Thomas, B. G., and Vanka, S. P. (2011). Transient turbulent flow in a liquid–metal model of continuous casting, including comparison of six different methods. *Metallurgical and Materials Transactions B*, 42:987–1007.

Chaudhary, R., Thomas, B. G., and Vanka, S. P. (2012). Effect of electromagnetic ruler braking (EMBr) on transient turbulent flow in continuous slab casting using large eddy simulations. *Metallurgical and Materials Transactions B*, 43:532–553.

Chen, C. S., Brebbia, C. A., and Power, H. (1999). Dual reciprocity method using compactly supported radial basis functions. *Communications in Numerical Methods in Engineering*, 15:137–150.

Chiang, T. P., Sheu, T. W. H., and Fang, C. C. (1999). Numerical investigation of vortical evolution in a backward-facing step expansion flow. *Applied Mathematical Modelling*, 23:915–932.

Chinchapatnam, P., Djidjeli, K., and Nair, P. (2007). Radial basis function meshless method for the steady incompressible Navier–Stokes equations. *International Journal of Computer Mathematics*, 84:1509–1521.

Chorin, A. J. (1967). A numerical method for solving incompressible viscous flow problems. *Journal of Computational Physics*, 2:12–26.

Chorin, A. J. (1968). Numerical solution of the Navier-Stokes equations. *Mathematics of Computation*, 22:745–762.

Choudhary, S. K. and Mazumdar, D. (1994). Mathematical modelling of transport phenomena in continuous casting of steel. *Iron and Steel Institute of Japan International*, 34:584–592.

Chow, W. K. and Cheung, Y. L. (1997). Comparison of the algorithms PISO and SIMPLER for solving pressure–velocity linked equations in simulating compartmental fire. *Numerical Heat Transfer, Part A: Applications*, 31:87–112.

Codina, R. and Hernández-Silva, N. (2006). Stabilized finite element approximation of the stationary magneto-hydrodynamics equations. *Computational Mechanics*, 38:344–355.

Colaço, M. J., Dulikravich, G. S., and Orlande, H. R. B. (2009). Magnetohydrodynamic simulations using radial basis functions. *International Journal of Heat and Mass Transfer*, 52:5932–5939.

Cukierski, K. and Thomas, B. G. (2008). Flow control with local electromagnetic braking in continuous casting of steel slabs. *Metallurgical and Materials Transactions B*, 39:94–107.

Cullity, B. D. and Graham, C. D. (2011). *Introduction to Magnetic Materials*. John Wiley & Sons, New York, USA.

Dantzig, J. and Rappaz, M. (2009). *Solidification*. EPFL Press, Lausanne, Switzerland.

Davidson, P. A. (2001). *An Introduction to Magnetohydrodynamics*. Cambridge University Press, Cambridge, UK.

Davidson, P. A. and Boysan, F. (1987). The importance of secondary flow in the rotary electromagnetic stirring of steel during continuous casting. *Applied Scientific Research*, 44:241–259.

Deardorff, J. W. (1970). A numerical study of three–dimensional turbulent channel flow at large Reynolds numbers. *Journal of Fluid Mechanics*, 41:453–480.

Di Piazza, I. and Ciofalo, M. (2002a). MHD free convection in a liquid-metal filled cubic enclosure. I. Differential heating. *International Journal of Heat and Mass Transfer*, 45:1477–1492.

Di Piazza, I. and Ciofalo, M. (2002b). MHD free convection in a liquid-metal filled cubic enclosure. II. Internal heating. *International Journal of Heat and Mass Transfer*, 45:1493–1511.

Divo, E. and Kassab, A. J. (2007). An efficient localized radial basis function meshless method for fluid flow and conjugate heat transfer. *Journal of Heat Transfer*, 129:124–136.

Divo, E. and Kassab, A. J. (2008). Localized meshless modeling of natural–convective viscous flows. *Numerical Heat Transfer, Part B: Fundamentals*, 53:487–509.

van Doormaal, J. P. and Raithby, G. D. (1984). Enhancements of the SIMPLE method for predicting incompressible fluid flows. *Numerical Heat Transfer, Part A: Applications*, 7:147–163.

Dullien, F. A. L. (1991). *Porous Media: Fluid Transport and Pore Structure*. Academic Press, Toronto, Canada.

El-Kaddah, N. and Natarajan, T. T. (1999). Elecromagnetic stirring of steel: effect of stirrer design on mixing in horizontal electromagnetic stirring of steel slabs. In *Book of abstracts: 2nd International Conference on CFD in the Minerals and Process Industries (CSIRO)*, page 27, Melbourne, Australia.

Ergolines (2013). Electromagnetic stirrers. http://www.ergolines.it. Last accessed: April, 2013.

Erturk, E. (2009). Discussions on driven cavity flow. *International Journal for Numerical Methods in Fluids*, 60:275–294.

Erturk, E., Corke, T. C., and Gökçöl, C. (2005). Numerical solutions of 2D steady incompressible driven cavity flow at high Reynolds numbers. *International Journal for Numerical Methods in Fluids*, 48:747–774.

Erturk, E. and Gökçöl, C. (2006). Fourth-order compact formulation of Navier–Stokes equations and driven cavity flow at high Reynolds numbers. *International Journal for Numerical Methods in Fluids*, 50:421–436.

Fairweather, G. and Karageorghis, A. (1998). The method of fundamental solutions for elliptic boundary value problems. *Advances in Computational Mathematics*, 9:69–95.

Fan, C. M., Chien, C. S., Chan, H. F., and Chiu, C. L. (2013). The local RBF collocation method for solving the double-diffusive natural convection in fluid-saturated porous media. *International Journal of Heat and Mass Transfer*, 57:500–503.

Ferziger, J. H. and Perić, M. (1996). *Computational Methods for Fluid Dynamics*. Springer-Verlag, Berlin, Germany.

Fortran (2011). Intel Visual Fortran, standard edition for Windows version 11.

Fox, D. G. and Lilly, D. K. (1972). Numerical simulation of turbulent flows. *Reviews of Geophysics*, 10:51–72.

Gardin, P., Galpin, J. M., Regnier, M. C., and Radot, J. P. (1996). Influence of electromagnetic brake on molten steel flow and inclusion behavior in a continuous casting mold. *Magnetohydrodynamics C/C of Magnitnaia Gidrodinamika*, 32:189–195.

Gartling, D. K. (1990). A test problem for outflow boundary conditions-flow over a backward–facing step. *International Journal for Numerical Methods in Fluids*, 11:953–967.

Ghia, U. K. N. G., Ghia, K. N., and Shin, C. T. (1982). High-Re solutions for incompressible flow using the Navier–Stokes equations and a multigrid method. *Journal of Computational Physics*, 48:387–411.

Gingold, R. A. and Monaghan, J. J. (1977). Smoothed particle hydrodynamics–theory and application to non–spherical stars. *Monthly Notices of the Royal Astronomical Society*, 181:375–389.

Gobin, D. and Le Quere, P. (2000). Melting from an isothermal vertical wall. Synthesis of a numerical comparison exercise. *Computer Assisted Mechanics and Engineering Sciences*, 7:289–306.

Golberg, M. A. and Chen, C. S. (1998). *Boundary Integral Methods-Numerical and Mathematical Aspects*. WIT Press, New Forest, UK.

Gresho, P. M., Gartling, D. K., Torczynski, J. R., Cliffe, K. A., Winters, K. H., Garratt, T. J., Spence, A., and Goodrich, J. W. (1993). Is the steady viscous incompressible two-dimensional flow over a backward–facing step at Re = 800 stable? *International Journal for Numerical Methods in Fluids*, 17:501–541.

Grigoriev, M. and Dargush, G. (1999). A poly-region boundary element method for incompressible viscous fluid flows. *International Journal for Numerical Methods in Engineering*, 46:1127–1158.

Gu, Y. T. and Liu, G.-R. (2006). Meshless techniques for convection dominated problems. *Computational Mechanics*, 38:171–182.

Guermond, J. L., Minev, P., and Shen, J. (2006). An overview of projection methods for incompressible flows. *Computer Methods in Applied Mechanics and Engineering*, 195:6011–6045.

Guermond, J. L. and Shen, J. (2003a). A new class of truly consistent splitting schemes for incompressible flows. *Journal of Computational Physics*, 192:262–276.

Guermond, J. L. and Shen, J. (2003b). Velocity-correction projection methods for incompressible flows. *Society for Industrial and Applied Mathematics Journal on Numerical Analysis*, 41:112–134.

Ha, M. Y., Lee, H. G., and Seong, S. H. (2003). Numerical simulation of three–dimensional flow, heat transfer, and solidification of steel in continuous casting mold with electromagnetic brake. *Journal of Materials Processing Technology*, 133:322–339.

Haiqi, Y., Baofeng, W., Huiqin, L., and Jianchao, L. (2008). Influence of electromagnetic brake on flow field of liquid steel in the slab continuous casting mold. *Journal of Materials Processing Technology*, 202:179–187.

Hall, W. S. (1994). *Boundary Element Method*. Springer-Verlag, Berlin, Germany.

Harada, H., Takeuchi, E., Zeze, M., and Tanaka, H. (1998). MHD analysis in hydromagnetic casting process of clad steel slabs. *Applied Mathematical Modelling*, 22:873–882.

Hardy, R. L. (1971). Multiquadric equations of topography and other irregular surfaces. *Journal of Geophysical Research*, 76:1905–1915.

Hartmann, J. and Lazarus, F. (1937). Hg–dynamics II. *Kongelige Danske Videnskabernes Selskab (Matematisk-Fysiske Meddelelser)*, 15:1–46.

Henderson, A. (2007). ParaView Guide, A Parallel Visualization Application.

Henkes, R. A. W. M., Van Der Vlugt, F. F., and Hoogendoorn, C. J. (1991). Natural–convection flow in a square cavity calculated with low–Reynolds–number turbulence models. *International Journal of Heat and Mass Transfer*, 34:377–388.

Herceg, D., Juhas, A., and Milutinov, M. (2009). A design of a four square coil system for a biomagnetic experiment. *Facta Universitatis-Series: Electronics and Energetics*, 22:285–292.

Ho-Minh, D., Mai-Duy, N., and Tran-Cong, T. (2009). A Galerkin–RBF approach for the streamfunction–vorticity–temperature formulation of natural convection in 2D enclosured domains. *CMES: Computer Modeling in Engineering & Sciences*, 44:219–248.

Hon, Y. C. and Chen, W. (2003). Boundary knot method for 2D and 3D Helmholtz and convection–diffusion problems under complicated geometry. *International Journal for Numerical Methods in Engineering*, 56:1931–1948.

Hon, Y. C. and Schaback, R. (2001). On unsymmetric collocation by radial basis functions. *Applied Mathematics and Computation*, 119:177–186.

Hong, C. P. (2004). *Computer Modelling of Heat and Fluid Flow in Materials Processing*. Institute of Physics Publishing, Bristol, UK.

Hortmann, M., Perić, M., and Scheuerer, G. (1990). Finite volume multigrid prediction of laminar natural convection: Bench-mark solutions. *International Journal for Numerical Methods in Fluids*, 11:189–207.

Hou, S., Zou, Q., Chen, S., Doolen, G., and Cogley, A. (1995). Simulation of cavity flow by the lattice Boltzmann method. *Journal of Computational Physics*, 118:329–347.

Hsu, C., Kung, K., and Hu, S. (2010). Numerical convection of viscoelastic magnetic flows past a backward facing step channel. *International Journal of Geology*, 4:64–74.

Hwang, Y. S., Cha, P. R., Nam, H. S., Moon, K. H., and Yoon, J. K. (1997). Numerical analysis of the influences of operational parameters on the fluid flow and meniscus shape in slab caster with EMBR. *Iron and Steel Institute Journal International*, 37:659–667.

Ilegbusi, O. J. and Szekely, J. (1989). Three–dimensional velocity fields for Newtonian and non–Newtonian melts produced by a rotating magnetic field. *Iron and Steel Institute Journal International*, 29:462–468.

Irving, W. R. (1993). *Continuous Casting of Steel*. The Institute of Materials, London, UK.

Ishii, T., Sazhin, S. S., and Makhlouf, M. (1996). Numerical prediction of magnetohydrodynamic flow in continuous casting process. *Ironmaking and Steelmaking*, 23:267–272.

ul Islam, S., Šarler, B., Vertnik, R., and Kosec, G. (2012). Radial basis function collocation method for the numerical solution of the two–dimensional transient nonlinear coupled Burgers' equations. *Applied Mathematical Modelling*, 36:1148–1160.

ul Islam, S., Vertnik, R., and Šarler, B. (2013). Local radial basis function collocation method along with explicit time stepping for hyperbolic partial differential equations. *Applied Numerical Mathematics*, 67:136–151.

Jang, D. S., Jetli, R., and Acharya, S. (1986). Comparison of the PISO, SIMPLER, and SIMPLEC algorithms for the treatment of the pressure-velocity coupling in steady flow problems. *Numerical Heat Transfer, Part A: Applications*, 10:209–228.

Javurek, M., Barna, M., Gittler, P., Rockenschaub, K., and Lechner, M. (2008). Flow modelling in continuous casting of round bloom strands with electromagnetic stirring. *Steel Research International*, 79:617–626.

Ji, C.-B., Li, J.-S., Yang, S.-F., and Sun, L.-Y. (2013). Large eddy simulation of turbulent fluid flow in liquid metal of continuous casting. *Journal of Iron and Steel Research, International*, 20:34–46.

Johnston, R. L. and Fairweather, G. (1984). The method of fundamental solutions for problems in potential flow. *Applied Mathematical Modelling*, 8:265–270.

Jones, W. P. and Launder, B. E. (1972). The prediction of laminarization with a two–equation model of turbulence. *International Journal of Heat and Mass Transfer*, 15:301–314.

Kansa, E. J. (1990a). Multiquadrics-A scattered data approximation scheme with applications to computational fluid-dynamics. I: surface approximations and partial derivative estimates. *Computers and Mathematics with Applications*, 19:127–145.

Kansa, E. J. (1990b). Multiquadrics-A scattered data approximation scheme with applications to computational fluid-dynamics. II: solutions to parabolic, hyperbolic and elliptic partial differential equations. *Computers and Mathematics with Applications*, 19:147–161.

Karimi, H. R. and Babazadeh, A. (2005). Modeling and output tracking of transverse flux permanent magnet machines using high gain observer and RBF neural network. *The International Society of Automation (ISA) Transactions*, 44:445–456.

Kasagi, N. and Nishimura, M. (1997). Direct numerical simulation of combined forced and natural turbulent convection in a vertical plane channel. *International Journal of Heat and Fluid Flow*, 18:88–99.

Kasagi, N., Tomita, Y., and Kuroda, A. (1992). Direct numerical simulation of passive scalar field in a turbulent channel flow. *American Society of Mechanical Engineers, Transactions Journal of Heat Transfer*, 114:598–606.

Kemeida Electric Co., L. (2013). General description of electromagnetic stirrer. http://www.magnet-lifting.com/electromagnetic-stirrer/electromagnetic-stirrer.html. Last accessed: April, 2013.

Keskar, J. and Lyn, D. A. (1999). Computations of a laminar backward–facing step flow at Re = 800 with a spectral domain decomposition method. *International Journal for Numerical Methods in Fluids*, 29:411–427.

Kim, D. S., Kim, W. S., and Cho, K. H. (2000). Numerical simulation of the coupled turbulent flow and macroscopic solidification in continuous casting with electromagnetic brake. *Iron and Steel Institute of Japan International*, 40:670–676.

Kim, J., Moin, P., and Moser, R. (1987). Turbulence statistics in fully developed channel flow at low Reynolds number. *Journal of Fluid Mechanics*, 177:133–166.

Kim, Y., Kim, D., Jun, S., and Lee, J. (2007). Meshfree point collocation method for the stream-vorticity formulation of 2D incompressible Navier–Stokes equations. *Computer Methods in Applied Mechanics and Engineering*, 196:3095–3109.

Kołodziej, J. A. (2001). *Applications of the Boundary Collocation Method in Applied Mechanics*. Wydawnictwo Politechniki Poznańskiej, Poznań, Poland.

Kosec, G. (2011). *Local Meshless Method for Multi–phase Termo–fluid Problems: Dissertation*. PhD thesis, University of Nova Gorica.

Kosec, G. and Šarler, B. (2008a). Local RBF collocation method for Darcy flow. *CMES: Computer Modeling in Engineering & Sciences*, 25:197–208.

Kosec, G. and Šarler, B. (2008b). Solution of heat transfer and fluid flow problems by the simplified explicit local radial basis function collocation method. *International Journal of Numerical Methods for Heat and Fluid Flow*, 18:868–882.

Kosec, G. and Šarler, B. (2008c). Solution of thermo–fluid problems by collocation with local pressure correction. *International Journal of Numerical Methods for Heat and Fluid Flow*, 18:868–882.

Kosec, G. and Šarler, B. (2009a). Convection driven melting of anisotropic metals. *International Journal of Cast Metals Research*, 1:279–282.

Kosec, G. and Šarler, B. (2009b). Solution of phase change problems by collocation with local pressure correction. *CMES: Computer Modeling in Engineering & Sciences*, 47:191–216.

Kosec, G. and Šarler, B. (2010). Meshless approach to solving freezing with natural convection. *Materials Science Forum*, 649:205–210.

Kosec, G. and Šarler, B. (2011). H-adaptive local radial basis function collocation meshless method. *CMC: Computers, Materials & Continua*, 26:227–254.

Kosec, G. and Šarler, B. (2013). Solution of a low Prandtl number natural convection benchmark by a local meshless method. *International Journal of Numerical Methods for Heat and Fluid Flow*, 23:189–204.

Kosec, G. and Šarler, B. (2014). Simulation of macrosegregation with mesosegregation in binary metallic casts by a meshless method. *Engineering Analysis with Boundary Elements*, 23:189–204.

Kosec, G., Založnik, M., Šarler, B., and Combeau, H. (2011). A meshless approach towards solution of macrosegregation phenomena. *CMC: Computers, Materials & Continua*, 22:169–196.

Kovacevic, I., Poredos, A., and Šarler, B. (2003). Solving the stefan problem with the radial basis function collocation method. *Numerical Heat Transfer, Part B: Fundamentals*, 44:575.

Kozel, K., Louda, P., and Sváček, P. (2004). Numerical solution of flow in backward facing step. In *Numerical Mathematics and Advanced Applications*, pages 596–604. Springer.

Kraft, T. and Chang, Y. (1997). Predicting microstructure and microsegregation in multicomponent alloys. *JOM*, 49:20–28.

Kubo, N., Ishii, T., Kubota, J., and Ikagawa, T. (2004). Numerical simulation of molten steel flow under a magnetic field with argon gas bubbling in a continuous casting mold. *Iron and Steel Institute of Japan International*, 44:556–564.

Kubo, N., Kubota, J., Suzuki, M., and Ishii, T. (2007). Molten steel flow control under electromagnetic level accelerator in continuous casting mold. *Iron and Steel Institute of Japan International*, 47:988–995.

Kurz, W. and Fischer, D. J. (1989). *Fundamentals of Solidification*.

La Rocca, A., Hernandez Rosales, A., and Power, H. (2005). Radial basis function hermite collocation approach for the solution of time dependent convection–diffusion problems. *Engineering Analysis with Boundary Elements*, 29:359–370.

Latimer, B. R. and Pollard, A. (1985). Comparison of pressure–velocity coupling solution algorithms. *Numerical Heat Transfer, Part B: Fundamentals*, 8:635–652.

Launder, B. E. and Sharma, B. I. (1974). Application of the energy–dissipation model of turbulence to the calculation of flow near a spinning disc. *Letters in Heat and Mass Transfer*, 1:131–137.

Le, H., Moin, P., and Kim, J. (1997). Direct numerical simulation of turbulent flow over a backward–facing step. *Journal of Fluid Mechanics*, 330:349–374.

Lee, C. K., Liu, X., and Fan, S. C. (2003). Local multiquadric approximation for solving boundary value problems. *Computational Mechanics*, 30:396–409.

Li, B., Okane, T., and Umeda, T. (2000). Modeling of molten metal flow in a continuous casting process considering the effects of argon gas injection and static magnetic–field application. *Metallurgical and Materials Transactions B*, 31:1491–1503.

Li, J., Wang, B., Ma, Y., and Cui, J. (2006). Effect of complex electromagnetic stirring on inner quality of high carbon steel bloom. *Materials Science and Engineering: A*, 425:201–204.

Li, T. T.-K. (2004). Tri-axial square Helmholtz coil for neutron EDM experiment. *Chinese University of Hong Kong Report*, 1:1–23.

Liao, S. (1992). Higher-order streamfunction-vorticity formulation of 2d steady-state navier-stokes equations. *International Journal for Numerical Methods in Fluids*, 15:595–612.

Liao, S. and Zhu, J. (1996). A short note on high-order streamfunction-vorticity formulations of 2D steady state Navier-Stokes equations. *International Journal for Numerical Methods in Fluids*, 22:1–9.

Lima, J. and Rêgo, M. (2013). On the integral transform solution of low-magnetic MHD flow and heat transfer in the entrance region of a channel. *International Journal of Non-Linear Mechanics*, 50:25–39.

Lin, H. and Atluri, S. N. (2000). Meshless local Petrov–Galerkin(MLPG) method for convection diffusion problems. *CMES: Computer Modeling in Engineering & Sciences*, 1:45–60.

Liu, G. R. (1998). A point assembly method for stress analysis of solids. In *3rd International Symposium on Impact Engineering*, pages 475–480.

Liu, G. R. (2010). *Meshfree Methods: Moving Beyond the Finite Element Method*. CRC Press, , Boca Raton, (FL) USA.

Liu, G. R. and Gu, Y. T. (2001). A point interpolation method for two–dimensional solids. *International Journal for Numerical Methods in Engineering*, 50:937–951.

Liu, G. R. and Liu, M. B. (2003). *Smoothed Particle Hydrodynamics: a Meshfree Particle Method*. World Scientific Publishing Company, Singapore.

Liu, G. R., Yan, L., Wang, J. G., and Gu, Y. T. (2002). Point interpolation method based on local residual formulation using radial basis functions. *Structural Engineering and Mechanics*, 14:713–732.

Liu, G. R. and Zhang, G. Y. (2008). Edge–based smoothed point interpolation methods. *International Journal of Computational Methods*, 5:621–646.

Liu, H., Xu, M., Qiu, S., and Zhang, H. (2012). Numerical simulation of fluid flow in a round bloom mold with in–mold rotary electromagnetic stirring. *Metallurgical and Materials Transactions B*, 43:1657–1675.

Mai-Duy, N., Khennane, A., and Tran-Cong, T. (2007a). Computation of laminated composite plates using integrated radial basis function networks. *CMC: Computers, Materials & Continua*, 5:63–77.

Mai-Duy, N., Mai-Cao, L., and Tran-Cong, T. (2007b). Computation of transient viscous flows using indirect radial basis function networks. *CMES: Computer Modeling in Engineering & Sciences*, 18:59–78.

Mai-Duy, N. and Tanner, R. I. (2007). A collocation method based on one-dimensional RBF interpolation scheme for solving PDEs. *International Journal of Numerical Methods for Heat and Fluid Flow*, 17:165–186.

Mai-Duy, N. and Tran-Cong, T. (2001). Numerical solution of Navier–Stokes equations using multiquadric radial basis function networks. *International Journal for Numerical Methods in Fluids*, 37:65–86.

Mai-Duy, N. and Tran-Cong, T. (2002). Mesh–free radial basis function network methods with domain decomposition for approximation of functions and numerical solution of Poisson's equations. *Engineering Analysis with Boundary Elements*, 26:133–156.

Miao, X., Timmel, K., Lucas, D., Ren, Z., Eckert, S., and Gerbeth, G. (2012). Effect of an electromagnetic brake on the turbulent melt flow in a continuous–casting mold. *Metallurgical and Materials Transactions B*, 43:954–972.

Misakian, M. (2000). Equations for the magnetic field produced by one or more rectangular loops of wire in the same plane. *Journal of Research-National Institute of Standards and Technology*, 105:557–564.

Moffatt, H. (1978). *Field Generation in Electrically Conducting Fluids*. Cambridge University Press, Cambridge, UK.

Moin, P. and Mahesh, K. (1998). Direct numerical simulation: a tool in turbulence research. *Annual Review of Fluid Mechanics*, 30:539–578.

Mramor, K., Vertnik, R., and Šarler, B. (2012). Simulation of natural convection under the influence of magnetic field by explicit local radial basis function collocation method. In *Book of abstracts: 8th ICCES Special Symposium on Meshless and Other Novel Computational Methods*, page 27, Budva, Montenegro. University of Montenegro Press.

Mramor, K., Vertnik, R., and Šarler, B. (2013a). Low and intermediate Re solution of lid driven cavity problem by local radial basis function collocation method. *CMC: Computers, Materials & Continua*, 36:1–21.

Mramor, K., Vertnik, R., and Šarler, B. (2013b). Simulation of natural convection influenced by magnetic field with explicit local radial basis function collocation method. *CMES: Computer Modeling in Engineering & Sciences*, 92:327–352.

Mramor, K., Vertnik, R., and Šarler, B. (2014a). Simulation of continuous casting of steel under the influence of magnetic field using the local-radial basis-function collocation method. *Materials and Technologies*, 48:281–288.

Mramor, K., Vertnik, R., and Šarler, B. (2014b). Simulation of laminar backward facing step flow under magnetic field with explicit local radial basis function collocation method. *Engineering Analysis with Boundary Elements*, in press:1–11.

Na, X. Z., Xue, M., Zhang, X. Z., and Gan, Y. (2007). Numerical simulation of heat transfer and deformation of initial shell in soft contact continuous casting mold under high frequency electromagnetic field. *Journal of Iron and Steel Research, International*, 14:14–21.

Natarajan, T. T. and El-Kaddah, N. (2004). Finite element analysis of electromagnetic and fluid flow phenomena in rotary electromagnetic stirring of steel. *Applied Mathematical Modelling*, 28:47–61.

Nayroles, B., Touzot, G., and Villon, P. (1992). Generalizing the finite element method: diffuse approximation and diffuse elements. *Computational Mechanics*, 10:307–318.

Nield, D. and Bejan, A. (2006). *Convection in Porous Media*. Springer-Verlag, Berlin, Germany.

Oñate, E., Sacco, C., and Idelsohn, S. (2000). A finite point method for incompressible flow problems. *Computing and Visualization in Science*, 3:67–75.

OpenMP (2013). OpenMP Application Program Interface Version 4.0, OpenMP Architecture Review Board.

Ostrowski, Z., Białecki, R. A., and Kassab, A. J. (2008). Solving inverse heat conduction problems using trained POD–RBF network inverse method. *Inverse Problems in Science and Engineering*, 16:39–54.

OutoKumpu (2013). Continuously cast stainless steel slab, bloom and billet. http://www.outokumpu.com/SiteCollectionDocuments. Last accessed: April 2013.

Özişik, M. N. (1994). *Finite Difference Methods in Heat Transfer*. CRC Press, Boca Raton, (FL) USA.

Pardeshi, R., Singh, A. K., and Dutta, P. (2008). Modeling of solidification process in a rotary electromagnetic stirrer. *Numerical Heat Transfer, Part A: Applications*, 55:42–57.

Pass, M. (2013). Continuous casting equipment. http://www.metalpass.com/metaldoc. Last accessed: April, 2013.

Patankar, S. V. (1980). *Numerical Heat Transfer and Fluid Flow*. Hemisphere, Washington, (DC) USA.

Patankar, S. V. and Spalding, D. B. (1972). A calculation procedure for heat, mass and momentum transfer in three-dimensional parabolic flows. *International Journal of Heat and Mass Transfer*, 15:1787–1806.

Pearson, T. (2001). PGPLOT 5.2.2 Graphics Subroutine Library.

Petronetto, F., Paiva, A., Lage, M., Tavares, G., Lopes, H., and Lewiner, T. (2010). Meshless Helmholtz-Hodge decomposition. *IEEE Transactions on Visualization and Computer Graphics*, 16:338–349.

Pope, S. B. (2000). *Turbulent Flows*. Cambridge University Press, Cambridge, UK.

Rappaz, M. and Voller, V. (1990). Modeling of micro-macrosegregation in solidification processes. *Metallurgical and Materials Transactions A*, 21:749–753.

Ravindran, S. (2000). Reduced-order adaptive controllers for fluid flows using POD. *Journal of Scientific Computing*, 15:457–478.

Reynolds, O. (1895). On the dynamical theory of incompressible viscous fluids and the determination of the criterion. *Philosophical Transactions of the Royal Society of London. A*, 186:123–164.

Rudraiah, N., Barron, R., Venkatachalappa, M., and Subbaraya, C. (1995). Effect of a magnetic field on free convection in a rectangular enclosure. *International Journal of Engineering Science*, 33:1075–1084.

Sadat, H., Dubus, N., Gbahoue, L., and Sophy, T. (2006). On the solution of heterogeneous heat conduction problems by a diffuse approximation meshless method. *Numerical Heat Transfer, Part B: Fundamentals*, 50:491–498.

Sadat, S. and Couturier, H. (2000). Performance and accuracy of a meshless method for laminar natural convection. *Numerical Heat Transfer, Part B: Fundamentals*, 37:455–467.

Sahin, M. and Owens, R. G. (2003a). A novel fully implicit finite volume method applied to the lid-driven cavity problem—Part I: High Reynolds number flow calculations. *International Journal for Numerical Methods in Fluids*, 42:57–77.

Sahin, M. and Owens, R. G. (2003b). A novel fully-implicit finite volume method applied to the lid-driven cavity problem—Part II: Linear stability analysis. *International Journal for Numerical Methods in Fluids*, 42:79–88.

Salah, N., Soulaimani, A., and Habashi, W. (2001). A finite element method for magnetohydrodynamics. *Computer Methods in Applied Mechanics and Engineering*, 190:5867–5892.

Sanyasiraju, Y. and Chandhini, G. (2008). Local radial basis function based gridfree scheme for unsteady incompressible viscous flows. *Journal of Computational Physics*, 227:8922–8948.

Šarler, B., Perko, J., Chen, C., and Kuhn, G. (2001). A meshless approach to natural convection. In *International Conference on Computational Engineering and Sciences, CD proceedings*, pages 3–9.

Sarris, I., Kakarantzas, S., Grecos, A., and Vlachos, N. (2005). MHD natural convection in a laterally and volumetrically heated square cavity. *International Journal of Heat and Mass Transfer*, 48:3443–3453.

Sathiyamoorthy, M. and Chamkha, A. (2010). Effect of magnetic field on natural convection flow in a liquid gallium filled square cavity for linearly heated side walls. *International Journal of Thermal Sciences*, 49:1856–1865.

Sathiyamoorthy, M. and Chamkha, A. (2012). Natural convection flow under magnetic field in a square cavity for uniformly (or) linearly heated adjacent walls. *International Journal of Numerical Methods for Heat & Fluid Flow*, 22:677–698.

Schär, C. (2014). The Courant-Friedrichs-Levy (CFL) Stability Criterion. http://www. iac. ethz. ch/edu/courses/bachelor/vertiefung/numerical_methods _in_environmental_physics/Fol_Ch3_CFL-Criterion.pdf.

Schenk, O. and K., G. (2004). Solving unsymmetric sparse systems of linear equations with PARDISO. *Journal of Future Generation Computer Systems*, 20:475–487.

Schwarz, S. and Fröhlich, J. (2014). Numerical study of single bubble motion in liquid metal exposed to a longitudinal magnetic field. *International Journal of Multiphase Flow*, 62:134–151.

Sellountos, E. and Sequeira, A. (2008). An advanced meshless LBIE/RBF method for solving two-dimensional incompressible fluid flows. *Computational Mechanics*, 41:617–631.

Smagorinsky, J. (1963). General circulation experiments with the primitive equations: I. The basic experiment. *Monthly Weather Review*, 91:99–164.

Soleimani, S., Jalaal, M., Bararnia, H., Ghasemi, E., Ganji, D. D., and Mohammadi, F. (2010). Local RBF–DQ method for two–dimensional transient heat conduction problems. *International Communications in Heat and Mass Transfer*, 37:1411–1418.

Spitzer, K. H., Dubke, M., and Schwerdtfeger, K. (1986). Rotational electromagnetic stirring in continuous casting of round strands. *Metallurgical Transactions B*, 17:119–131.

Stevens, D., Power, H., Lees, M., and Morvan, H. (2009). The use of PDE centres in the local RBF Hermitian method for 3D convective-diffusion problems. *Journal of Computational Physics*, 228:4606–4624.

Šarler, B. (2005). A radial basis function collocation approach in computational fluid dynamics. *CMES: Computer Modeling in Engineering & Sciences*, 7:185–193.

Šarler, B. (2007). From global to local radial basis function collocation method for transport phenomena. In *Advances in Meshfree Techniques*, pages 257–282. Springer-Verlag, Berlin, Germany.

Šarler, B., Kosec, G., Lorbicka, A., and Vertnik, R. (2010). A meshless approach in solution of multiscale solidification modeling. *Materials Science Forum*, 649:211–216.

Šarler, B. and Kuhn, G. (1998). Dual reciprocity boundary element method for convective–diffusive solid-liquid phase change problems, Part 1. Formulation. *Engineering Analysis with Boundary Elements*, 21:53–63.

Šarler, B. and Kuhn, G. (1998). Dual reciprocity boundary element method for convective-diffusive solid-liquid phase change problems, Part 2. Numerical examples. *Engineering Analysis with Boundary Elements*, 21:65–79.

Šarler, B. and Kuhn, G. (1999). Primitive variable dual reciprocity boundary element method solution of incompressible Navier–Stokes equations. *Engineering Analysis with Boundary Elements*, 23:443–455.

Šarler, B. and Vertnik, R. (2006). Meshfree explicit local radial basis function collocation method for diffusion problems. *Computers and Mathematics with Applications*, 51:1269–1282.

Šarler, B., Vertnik, R., and Mramor, K. (2012). A numerical benchmark test for continuous casting of steel. In *IOP Conference Series: Materials Science and Engineering*, volume 33, page 012012. IOP Publishing.

Šarler, B., Vertnik, R., and Mramor, K. (2013). A benchmark test for continuous casting of steel, II. In *Proceedings of the 6th International Conference on Solidification and Gravity*, page 55, Miskolc-Lillafüred, Hungary.

Štore Steel, d. o. o. (2013). Steel billets. http://www.store−steel.si/html. Last accessed: October, 2013.

Takeuchi, E., Toh, T., Harada, H., Zeze, M., Tanaka, H., Hojo, M., Ishii, T., and Shigematsu, K. (1994). Advances of applied MHD technology for continuous casting process. *Nippon Steel Technical Report*, 61.

Thomas, B. G. (2001). Continuous casting of steel. In *Modeling for Casting and Solidification Processing*, chapter 15, pages 499–540. Marcel Dekker, Inc., New York, (NY) USA.

Timmel, K., Miao, X., Eckert, S., Lucas, D., and Gerbeth, G. (2010). Experimental and numerical modeling of the steel flow in a continuous mould under the influence of a transverse DC magnetic field. *Magnetohydrodynamics*, 46:337–448.

Trindade, L. B., Vilela, A. C. F., Vilhena, M. T. M. B., Soares, R. B., et al. (2002). Numerical model of electromagnetic stirring for continuous casting billets. *IEEE Transactions on Magnetics*, 38:3658–3660.

de Vahl Davis, G. (1983). Natural convection of air in a square cavity: a bench mark numerical solution. *International Journal for Numerical Methods in Fluids*, 3:249–264.

Versteeg, H. K. and Malalasekera, W. (2007). *An Introduction to Computational Fluid Dynamics: the Finite Volume Method*. Prentice Hall, Upper Saddle River, (NJ) USA.

Vertnik, R. (2010). *Heat and Fluid Flow Simulation of the Continuous Casting of Steel by a Meshless Method: Dissertation*. PhD thesis, University of Nova Gorica.

Vertnik, R. and Šarler, B. (2006). Meshless local radial basis function collocation method for convective-diffusive solid–liquid phase change problems. *International Journal for Numerical Methods for Heat and Fluid Flow*, 16:617–640.

Vertnik, R. and Šarler, B. (2009a). Simulation of continuous casting of steel by a meshless technique. *International Journal of Cast Metals Research*, 1:311–313.

Vertnik, R. and Šarler, B. (2009b). Solution of incompressible turbulent flow by a mesh–free method. *CMES: Computer Modeling in Engineering & Sciences*, 44:65–96.

Vertnik, R. and Šarler, B. (2011). Local collocation approach for solving turbulent combined forced and natural convection problems. *Advances in Applied Mathematics and Mechanics*, 3:259–279.

Vertnik, R. and Šarler, B. (2014). Solution of a continuous casting of steel benchmark test by a meshless method. *Engineering Analysis with Boundary Elements*.

Vertnik, R., Založnik, M., and Šarler, B. (2006). Solution of transient direct–chill aluminium billet casting problem with simultaneous material and interphase moving boundaries by a meshless method. *Engineering Analysis with Boundary Elements*, 30:847–855.

Viskanta, R. (1990). Mathematical modeling of transport processes during solidification of binary systems. *Japan Society of Mechanical Engineers International Journal*, 33:409–423.

Vollhardt, D., Blümer, N., Held, K., and Kollar, M. (2001). Metallic ferromagnetism—an electronic correlation phenomenon. In *Band-Ferromagnetism*, pages 191–207. Springer-Verlag, Berlin, Germany.

Wang, L., Shen, H., and Liu, B. (2004). Effect of electro-magnetic field on fluid flow in continuous casting mold. *Proceedings of MCSP6-2004*, pages 13–20.

Wilcox, D. C. (1998). *Turbulence Modeling for CFD*. DCW Industries, La Canada, (CA) USA.

Williams, T. and Kelley, C. (2010). Gnuplot 4.4: an Interactive Plotting Program.

Wright, G. B. and Fornberg, B. (2006). Scattered node compact finite difference–type formulas generated from radial basis functions. *Journal of Computational Physics*, 212:99–123.

Wrobel, L. C. and Brebbia, C. A. (1987). The dual reciprocity boundary element formulation for nonlinear diffusion problems. *Computer Methods in Applied Mechanics and Engineering*, 65:147–164.

WSA (2013). Statistics of World Steel Association (WSA). http://www.worldsteel.org/. Last accessed: April, 2013.

Wu, X., Tao, W., Shen, S., and Zhu, X. (2010). A stabilized MLPG method for steady state incompressible fluid flow simulation. *Journal of Computational Physics*, 229:8564–8577.

Yang, G., Zhang, Y., Lei, G., Shao, K. R., Guo, Y., Zhu, J., and Lavers, J. D. (2009). A novel superposition RBF collocation method to solve moving conductor eddy current problems. *IEEE Transactions on Magnetics*, 45:3977–3980.

Yang, H., Zhang, X., Deng, K., Li, W., Gan, Y., and Zhao, L. (1998). Mathematical simulation on coupled flow, heat, and solute transport in slab continuous casting process. *Metallurgical and Materials Transactions B*, 29:1345–1356.

Yang, Y., Chang, S., and Chiou, C. (2013). Lattice Boltzmann method and large-eddy simulation for turbulent impinging jet cooling. *International Journal of Heat and Mass Transfer*, 61:543–553.

Yao, G., Šarler, B., and Chen, C. S. (2011). A comparison of three explicit local meshless methods using radial basis functions. *Engineering Analysis with Boundary Elements*, 35:600–609.

Yao, G., Šarler, B., and ul Islam, S. (2010). A comparative study of global and local meshless methods for diffusion-reaction equation. *CMES: Computer Modeling in Engineering & Sciences*, 59:127–154.

Yao, M., Ichimiya, M., Kiyohara, S., Suzuki, K. I., Mesaki, R., and Sugiyama, K. (1992). Three–dimensional analysis of molten metal flow in continuous casting mould. *Iron and Steel Society, Inc., Continuous Casting.*, pages 123–129.

Young, D., Chen, C., and Wong, T. (2005). Solution of maxwell's equations using the mq method. *CMC: Computers, Materials & Continua*, 2:264.

Young, D., Jane, S., Fan, C., Murugesan, K., and Tsai, C. (2006). The method of fundamental solutions for 2D and 3D Stokes problems. *Journal of Computational Physics*, 211:1–8.

Založnik, M. and Šarler, B. (2005). Modeling of macrosegregation in direct–chill casting of aluminum alloys: Estimating the influence of casting parameters. *Materials Science and Engineering: A*, 413:85–91.

Zerroukat, M., Djidjeli, K., and Charafi, A. (2000). Explicit and implicit meshless methods for linear advection-diffusion type of partial differential equations. *International Journal for Numerical Methods in Engineering*, 48:19–35.

Zerroukat, M., Power, H., and Chen, C. (1998). A numerical method for heat transfer problems using collocation and radial basis functions. *International Journal for Numerical Methods in Engineering*, 42:1263–1278.

Zhang, Y., Shao, K. R., Guo, Y., Zhu, J., and Lavers, J. D. (2006). Multiquadrics collocation method for transient eddy current problems. *IEEE Transactions on Magnetics*, 42:3183–3185.

Zhang, Y., Shao, K. R., Guo, Y., Zhu, J., Xie, D. X., and Lavers, J. D. (2007). An improved multiquadric collocation method for 3–D electromagnetic problems. *IEEE Transactions on Magnetics*, 43:1509–1512.

Zhu, M.-Y., Cai, Z.-Z., and Yu, H.-Q. (2013). Multiphase flow and thermomechanical behaviors of solidifying shell in continuous casting mold. *Journal of Iron and Steel Research, International*, 20:6–17.

Zienkiewicz, O. C. and Codina, R. (1995). A general algorithm for compressible and incompressible flow-Part I. the split, characteristic-based scheme. *International Journal for Numerical Methods in Fluids*, 20:869–885.

Zienkiewicz, O. C., Morgan, K., Sai, B. V. K., Codina, R., and Vasquez, M. (1995). A general algorithm for compressible and incompressible flow-Part II. tests on the explicit form. *International Journal for Numerical Methods in Fluids*, 20:887–913.

Zienkiewicz, O. C., Nithiarasu, P., Codina, R., Vazquez, M., and Ortiz, P. (1999). The characteristic-based-split procedure: an efficient and accurate algorithm for fluid problems. *International Journal for Numerical Methods in Fluids*, 31:359–392.

Zienkiewicz, O. C. and Taylor, R. L. (1977). *The Finite Element Method*. McGraw-Hill, New York, (NY) USA.